



Universitat d'Alacant
Universidad de Alicante

LARGE VERSATILITY OF METAL-
ORGANIC FRAMEWORKS (MOFs) IN
GAS/LIQUID ADSORPTION
PROCESSES

Jesús Gandara Loe



Tesis **Doctorales**

UNIVERSIDAD de ALICANTE

Unitat de Digitalització UA

Unidad de Digitalización UA



Universitat d'Alacant
Universidad de Alicante

Departamento de Química Inorgánica
Instituto Universitario de Materiales de Alicante (IUMA)
Laboratorio de Materiales Avanzados (LMA)

***LARGE VERSATILITY OF METAL-ORGANIC
FRAMEWORKS (MOFs) IN GAS/LIQUID
ADSORPTION PROCESSES***

JESÚS GANDARA LOE

Tesis presentada para aspirar al grado de:
DOCTOR POR LA UNIVERSIDAD DE ALICANTE
MENCIÓN DE DOCTOR INTERNACIONAL
DOCTORADO EN CIENCIA DE MATERIALES

Dirigida por:

PROF. JOAQUÍN SILVESTRE ALBERO

Catedrático de la Universidad de Alicante

Financiación: Generalitat Valenciana- Santiago Grisolia (GRISOLIAP/2016/089)

Alicante, octubre 2020

Agradecimientos

Al Prof. Joaquín Silvestre Albero por el apoyo y la ayuda en el desarrollo de esta tesis doctoral.

A David Carpena por toda la ayuda técnica para desarrollar el trabajo experimental de esta tesis, por todos los consejos y por todos los momentos que hicieron estos años una etapa única.

A todos mis compañeros y amigos de doctorado, gracias por todos los momentos y las experiencias compartidas. En especial a Arantxa, Esther, Kike, Eleana, Javi, Nacho y Andrés, por las horas de risas y por convertirse en mi familia en Alicante.

A Laura y Sole, por su amistad y porque desde que llegue a Alicante me han ofrecido su ayuda incondicional, consejos y momentos inolvidables.

A mis compañeros y amigos de despacho por las horas compartidas. A Erika por toda la ayuda y consejos. A Sneza por siempre mantener la alegría del grupo. En especial a Carlos, compañero de doctorado y de viajes durante estos cuatro años.

Agradecer a mis compañeros del LMA y del Departamento de Química Inorgánica por la ayuda brindada.

A todas las buenas personas de las que he tenido la suerte de rodearme en esta etapa: los que siempre han estado, los que llegaron después y los que ya no están. Por cada lección y todo el apoyo, gracias.

A Kevin, por la paciencia, por apoyarme y creer en mí. Por hacer que esta última etapa de la tesis sea única.

A mi familia, porque sin ellos no estaría hoy escribiendo estas líneas, porque este trabajo también es de ustedes. Gracias por enseñarme siempre la humildad, la resiliencia, el respeto a los demás y el amor incondicional.



"Be the change that you wish to see in the world"

-Mahatma Gandhi

Universitat d'Alacant
Universidad de Alicante

A mi Familia

Index of contents

Summary of contents.....	13
CHAPTER 1. Introduction	19
1.1. General Introduction	20
1.1.1. Adsorption process in porous materials	20
1.1.2. Overview of porous materials and their applications.....	22
1.2. Synthesis of Metal organic frameworks.....	24
1.2.1. General overview of MOFs materials and synthesis procedures.....	24
1.2.2. Solvothermal/hydrothermal synthesis	29
1.2.3. Microwave-assited synthesis	29
1.2.4. Electrochemical synthesis.....	30
1.2.5. Mechanochemical synthesis	30
1.2.6. Sonochemical synthesis.....	31
1.3. Application of MOFs	31
1.3.1. Gas storage and separation.....	31
1.3.1.1. H ₂ storage.....	32
1.3.1.2. CH ₄ separation and storage.....	32
1.3.1.3. CO ₂ adsorption	33
1.3.1.4. N ₂ and O ₂ separation.....	34
1.3.1.5. NO storage and release	35
1.3.1.6. Hydrocarbon adsorption.....	37
1.3.2. MOFs for drug delivery.....	38
1.3.2.1. MOFs for drug delivery in ocular therapeutics	40
1.3.2.2. Toxicity and biocompatibility of MOFs.....	41
1.4. Computational modelling and simulation of adsorption in MOFs.....	42
1.5. Flexibility in MOFs.....	43
1.6. MOFs-polymer based composites.....	46
1.7. General objectives of the thesis project	49
CHAPTER 2. Experimental Methods and Techniques Description.....	71
2.1. Methodology and research approach	72
2.2. MOFs synthesis.....	72
2.3. Characterization techniques	73
2.3.1. X-ray diffraction applied in the characterization of MOFs	73
2.3.2. MOFs stability	74

2.3.4.	Synchrotron light for MOFs characterization	75
2.3.5.	Inelastic neutron scattering.....	76
2.3.6.	X-Ray Photoelectron spectroscopy	77
2.3.7.	Scanning electron microscopy.....	79
2.3.8.	Thermogravimetric analysis.....	79
2.3.9.	Gas and liquid adsorption analysis	80
2.3.9.1.	Energy involved in adsorption processes	81
2.3.9.2.	Mathematical models for physisorption in gas phase processes.....	81
2.3.10.	Classification of isotherms and pore shape	83
2.3.11.	Liquid phase isotherms and mathematical models.....	86
2.4.	References.....	87
CHAPTER 3. Structural Flexibility in Zeolitic Imidazolate Frameworks upon Gas Adsorption		
91		
3.1.	Introduction	92
3.2.	Experimental section.....	94
3.2.1.	Synthesis of ZIF-4.....	94
3.2.2.	Characterization of the synthesized ZIF-4	94
3.2.2.1.	Nitrogen and carbon dioxide isotherms	94
3.2.2.2.	Scanning electron microscopy	95
3.2.2.3.	Synchrotron X-ray powder diffraction	95
3.2.2.4.	Inelastic neutron scattering.....	95
3.2.3.	Molecular Simulations of ZIF-4 phase transitions.....	95
3.3.	Results	99
3.3.1.	ZIF-4 characterization.....	99
3.3.2.	ZIF-4 flexibility upon gas adsorption	101
3.3.3.	Molecular simulations of ZIF-4 phase transition	104
3.3.4.	Inelastic neutron scattering.....	111
3.4.	Conclusions	114
3.5.	References.....	115
CHAPTER 4. Gas Adsorption/Separation Properties of Mixed Linker ZIF-62.....		
119		
4.1.	Introduction	120
4.2.	Experimental section.....	122
4.2.1.	ZIF-62 Synthesis.....	122
4.2.2.	Synchrotron powder X-ray diffraction analysis	122
4.2.3.	Termogravimetric Analysis	123

4.2.4.	Scanning electron microscopy	123
4.2.5.	Adsorption isotherms	123
4.2.6.	Molecular modelling and simulations	123
4.3.	Results	125
4.3.1.	Synthesis and characterization of ZIF-62.....	125
4.3.2.	Nitrogen and oxygen adsorption/desorption isotherms.....	127
4.3.3.	Oxygen and nitrogen adsorption simulation in ZIF-62	131
4.3.4.	ZIF-62 structure analysis using synchrotron power X-ray diffraction	135
4.3.5.	Adsorption of bulkier molecules: linear and branched hydrocarbons.....	140
4.4.	Conclusions.....	143
4.5.	References	144
CHAPTER 5. Nitric Oxide Adsorption into Flexible Zeolitic Imidazolate Frameworks (ZIFs).....		
149		
5.1.	Introduction	150
5.2.	Experimental section	152
5.2.1.	MOFs synthesis	152
5.2.2.	MOFs characterization	152
5.2.3.	CO ₂ adsorption isotherm at 273K	153
5.2.4.	ZIFs phase analysis by PXRD	154
5.2.5.	Nitric oxide adsorption/desorption isotherms	154
5.2.6.	Nitric oxide releasing experiments	155
5.3.	Results	155
5.3.1.	Physicochemical evaluation of the synthesized ZIFs	155
5.3.2.	CO ₂ adsorption measurements at 273K	157
5.3.3.	NO adsorption experiments at 298K	159
5.3.4.	NO release experiments under humid conditions	161
5.3.5.	Structural changes upon a thermal treatment under UHV conditions	166
5.3.6.	Phase transition upon gas adsorption.....	169
5.4.	Conclusions.....	171
5.5.	References	172
CHAPTER 6. Metal-Organic Frameworks as Drug Delivery Platforms for Ocular Therapeutics		
175		
6.1.	Introduction	176
6.2.	Experimental section	178
6.2.1.	MOFs synthesis	178
6.2.2.	MOFs characterization	179

6.2.2.1. X-ray diffraction analysis.....	179
6.2.2.2. Nitrogen isotherms at 77 K.....	179
6.2.2.3. Scanning electron microscopy.....	179
6.2.2.4. MOFs structural stability test.....	180
6.2.3. Drug loading and release experiments.....	180
6.2.3.1. Brimonidine loading experiments.....	180
6.2.3.2. Brimonidine release experiments.....	181
6.2.4. Cytotoxicity tests.....	181
6.3. Results.....	182
6.3.1. MOFs characterization.....	182
6.3.2. Brimonidine adsorption isotherms.....	187
6.3.3. MOFs stability test.....	189
6.3.4. Brimonidine release kinetics.....	192
6.3.5. MOFs <i>in vitro</i> toxicity test.....	193
6.4. Conclusions.....	198
6.5. References.....	198
CHAPTER 7. MOF-based Composites as Drug Delivery Platforms.....	203
7.1. Introduction.....	204
7.2. Experimental section.....	206
7.2.1. UiO-67 and films synthesis.....	206
7.2.1.1. UiO-67 synthesis.....	206
7.2.1.2. UiO-67@PU synthesis.....	207
7.2.2. Materials characterization.....	207
7.2.2.1. Synchrotron X-ray powder diffraction (SXRPD) analysis.....	207
7.2.2.2. Thermogravimetric analysis (TGA).....	208
7.2.2.3. Scanning electron microscopy (SEM) evaluation.....	208
7.2.2.4. Nitrogen and ethylene adsorption/desorption isotherms.....	208
7.2.2.5. Loading and release experiments.....	209
7.2.2.5.1. Brimonidine loading experiments.....	209
7.2.2.5.2. Brimonidine release experiments.....	209
7.3. Results.....	210
7.3.1. Characterization of the synthesized films and accessibility of the embedded MOFs.....	210
7.3.2. Brimonidine adsorption and release.....	217
7.3.3. Brimonidine-composite compatibility and stability studies.....	220
7.4. Conclusions.....	227

7.5. References	228
CHAPTER 8. General conclusions	233
Resumen en español	239
Curriculum Vitae	261



Universitat d'Alacant
Universidad de Alicante



Summary of contents

Universitat d'Alacant
Universidad de Alicante

This PhD Thesis is structured in 7 *chapters*, a deep study of adsorption processes in metal-organic frameworks is described through the present work. The research project starts with the adsorption of small molecules in zeolitic imidazolate frameworks (ZIFs) and their structural effect. A second part is dedicated to the study of more complex molecules such as drugs, and finally, an analysis of MOFs based composites for liquid-phase adsorption is explored. Based on this, the abstract of each chapter is summarized in the following lines:

Chapter 1 provides an extensive overview of metal-organic framework materials (MOFs), starting from a detailed description of different synthesis methodologies and potential application of these novel materials in catalysis, gas adsorption, and separation and drug delivery. Chapter 1 also provides a profound description of MOFs structural characteristics, with particular emphasis in structural flexibility as a consequence of external stimuli or the synergy in MOF-based composites materials.

Chapter 2 describes the methodology and research approach developed in this PhD Thesis, and the different experimental techniques used along with the research project. The fundamental principles of each technique, instrumentation and a general description of potential analysis to be applied in the characterization of MOFs are presented in this Chapter.

Chapter 3 reviews the structural changes in ZIFs upon gas adsorption that remain a paradigm due to the sensitivity of the adsorption mechanism to the nature of the organic ligands and gas probe molecules. Synchrotron X-ray diffraction under operando conditions anticipates for the first time that ZIF-4 exhibits a structural reorientation from a narrow-pore (np) to a new expanded-pore (ep) structure upon N₂ adsorption, while it does not for CO₂ adsorption. The existence of an expanded-pore structure of ZIF-4 has also been predicted by molecular simulations. In simulations, the expanded structure was stabilized by entropy at high temperatures and by strong adsorption of N₂ at low temperatures. These results are in perfect agreement with manometric adsorption measurements for N₂ at 77K that show the threshold pressure for the breathing at ~30 kPa. Inelastic neutron scattering (INS)

measurements show that CO₂ is also able to promote structural changes but, in this specific case, only at cryogenic temperatures (5K).

Chapter 4 describes the different approaches applied to understand the structural flexibility upon gas adsorption in mixed linker based ZIFs. ZIF-62 is a MOF formed by the combination of benzimidazole and imidazole as a ligand, and zinc metal centres. Among the 105 ZIFs described in the literature, ZIF-62 has attracted enormous attention due to its unique characteristics and the emerging field in MOFs related to liquid crystals and glass formation. Even so, structural properties upon gas adsorption have not been completely elucidated. Chapter 6 combine different research techniques and methodologies such as synchrotron XRD, gas adsorption-desorption isotherms and, molecular modelling and simulation to create a unique and deep overview of structural changes in ZIF-62 as a consequence of external stimuli. Nitrogen and oxygen isotherms evidenced the presence of specific interactions resulted in a complete affinity for O₂ over N₂ at 77 K in this specific material. SPXRD analysis showed a phase transition upon oxygen and nitrogen adsorption from a contracted phase to an expanded phase. Finally, molecular simulations showed the phase transition and the allocation of molecules in the ZIFs cavities. All this combined opens a wide number of opportunities for applying these materials into the field of gas separation, such as hexane isomers or light hydrocarbon separation (C1-C4).

Chapter 5 reviews the most significant results obtained into the paradigm of structural changes and adsorption capacity in ZIFs upon nitric oxide adsorption and release. Nitric oxide has been called the “molecule of the decade” due to the discovery of its essential role in biological processes. Zeolitic imidazolate frameworks (ZIFs) have been applied for the first time in the adsorption and release of an important biomedical molecule, such as NO. Despite the absence of open metal sites (OMS) and suitable surface chemistry (e.g., amine basic groups) in ZIFs, these materials exhibit excellent performance in terms of total uptake, irreversibility until use and delivery kinetics. These excellent results must be attributed to the presence of specific interactions between the framework and the NO molecules. For instance, ZIF-4 is able to adsorb up to 1.6 mmol/g, whereas its benzyl imidazolate counterpart (ZIF-7) is limited to 0.5 mmol/g. However, despite the lower adsorption

capacity exhibited by ZIF-7, the presence of a narrow pore (np), highly dense structure (phase II) allows to control the NO release under humid conditions for more than 15 h at physiological temperature (310 K).

Chapter 6 reviews the main significative advances achieved into the adsorption and delivery of brimonidine in metal-organic frameworks (MOFs) as potential nanocarriers in ocular therapeutics. Experimental results show that UiO-67 and MIL-100 (Fe) exhibit the highest loading capacity with values up to 50-60 wt.%, while the performance is quite limited for MOFs with narrow cavities (below 0.8 nm, e.g. UiO-66 and HKUST-1). The large loading capacity in UiO-67 is accompanied by an irreversible structural amorphization in aqueous and physiological media that promotes extended release kinetics above 12 days. Compared to the traditional drawbacks associated with the sudden release of the commercial drugs (e.g., ALPHAGAN), these results anticipate UiO-67 as a potential nanocarrier for drug delivery in intra-ocular therapeutics. These promising results are further supported by cytotoxicity tests using retinal photoreceptor cells (661W).

Chapter 7 presents the synthesis of novel MOF-based polymer nanocomposite films using Zr-based UiO-67 as a metal-organic framework (MOF) and polyurethane (PU) as a polymeric matrix. Techniques such as synchrotron X-ray powder diffraction (SXRPD) analysis confirm the improved stability of the UiO-67 embedded nanocrystals, and scanning electron microscopy images confirm their homogeneous distribution (average crystal size ~ 100-200 nm) within the 50 μ m thick film. Accessibility to the inner porous structure of the embedded MOFs has been completely suppressed for N₂ at cryogenic temperatures. However, ethylene adsorption measurements at 25 °C confirm that at least 45% of the MOF crystals are fully accessible for gas phase adsorption of non-polar molecules. Although this partial blockage limits the adsorption performance of the embedded MOFs for ocular drugs (e.g., brimonidine tartrate) compared to the pure MOF, an almost 60-fold improvement in the adsorption capacity was observed for PU matrix after incorporation of the UiO-67 nanocrystals. UiO-67@PU nanocomposite exhibits a prolonged release of brimonidine (up to 14 days were quantified). Finally, the combined use of SXRPD, thermogravimetric analysis (TGA), and FTIR analysis confirmed the presence of the drug in the nanocomposite film, the stability of the

MOF framework and the drug upon loading, and the presence of brimonidine in an amorphous phase once adsorbed.



Universitat d'Alacant
Universidad de Alicante

CHAPTER 1

Introduction

Chapter 1 provides an extensive overview of metal-organic framework materials (MOFs), starting from a detailed description of the different synthesis methodologies and potential application of these novel materials in areas such as catalysis, gas adsorption, and separation and drug delivery. Chapter 1 also provides a profound description of MOFs structural characteristics, with special emphasis in structural flexibility as a consequence of external stimuli or the synergy in MOF-based composites materials.

1.1. General Introduction

Nature has provided human beings with different tools to learn, develop, and optimize activities and, by consequence, gain knowledge. This knowledge attached to the inspiration obtained from nature is what has given humans the capacity to imitate natural processes and apply them for their benefit. Adsorption phenomena and porous materials are present in our daily life, from the adsorption of different essential biomolecules in human cells to the air/water exchange through the semipermeable porous calcium carbonate layer in eggs, to mention some.

1.1.1. Adsorption process in porous materials

Adsorption is defined as a surface phenomenon which occurs due to the accumulation of atoms or molecules coming from the liquid or gas phase into the surface of a solid material (**Figure 1.1**).¹

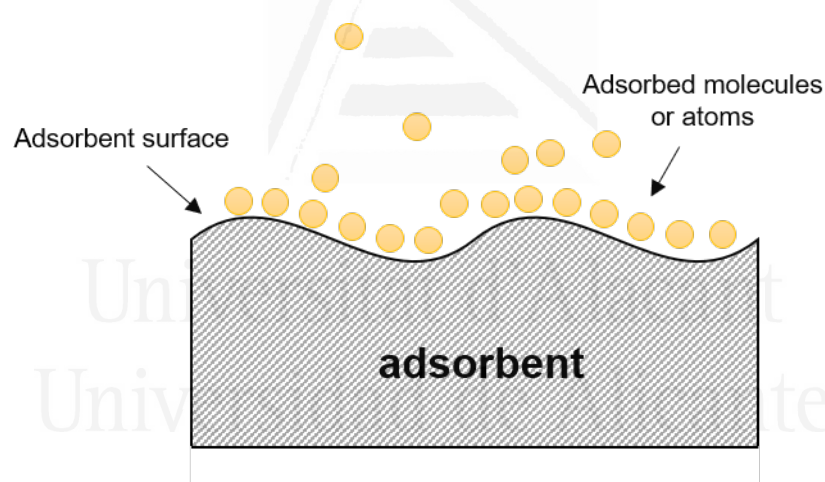


Figure 1.1. Adsorption phenomena in a solid surface.

Adsorption in porous materials is an essential step in a significant number of high-value industrial processes such as wastewater treatment, drying processes, catalytic reactions, gas storage/separation, and biomedical applications.²⁻⁴

Industrially, a large number of materials have been used as adsorbents such as activated carbons, zeolites, clays, fly ash, fibres, silica gel, and activated alumina.⁵ Activated carbon is one of the adsorbents most commonly used in wastewater treatment due to its versatile adsorption capacity of a wide variety of

hazards (i.e. heavy metals, dyes and drugs), availability of raw materials to synthesize and low cost of production.⁶

Adsorption is generally described as physical or chemical phenomena depending on the strength of the adsorbent/adsorbate interactions. The chemisorption is characterized by the formation of strong bonds between adsorbate and adsorbent, and it must be understood as a chemical reaction. For instance, the heat of adsorption and the activation energy are generally similar to those involved in a chemical reaction. This type of adsorption occurs in specific active sites, and it is irreversible.^{7,8} Chemisorption is usually associated with catalytic processes, for instance, the main study of chemisorption in catalysis is related to adsorption process and binding of reactive molecules into the active sites of the catalyst surface.⁹

On the other hand, the physical adsorption or physisorption is a reversible phenomenon resulted from weak intermolecular interactions, mainly of Van der Waals type. Due to the weakness of the interactions between the surface and the adsorbates, the latest can move freely at the interface. The physisorption generally occurs at low temperatures and it is exothermic.⁸ Physisorption is the main principle taking place in gas/liquid phase adsorption and separation processes.

Physical adsorption and adsorptive separation processes in porous materials are generally controlled by one of three mechanisms: steric, kinetic, or equilibrium. The first one is characterized by the molecular sieving properties of certain materials, i.e., only the molecules with the proper size and shape can diffuse into the adsorbent material while the others are excluded. Kinetic separation is achieved due to the different diffusion rates of the molecule to be separated. A large majority of processes operate through the equilibrium adsorption of mixture and hence are called equilibrium separation processes. They work considering the physicochemical properties of the adsorbate in order to assign the optimum adsorbent material.^{5,10}

In order to achieve an optimum in a given adsorption process, different parameters must be considered. Some of them are related to the textural properties of the adsorbent, such as specific surface area, average pore size and pore volume,

and pore shape. However, others are associated with physicochemical characteristics of the adsorbent, i.e., surface charge, active sites, and chemical composition. The adsorbate's physicochemical properties, such as molecular size, polarity, solubility, chemical composition, media pH, adsorption temperature and ionic force, must be taken equally into consideration.¹¹

1.1.2. Overview of porous materials and their applications

Porous architectures have always been present in nature, and they have played a fundamental role in the development of organisms. Porous structures such as molluscs, or corals are a good example. The very first reported example of porous material was the active carbon discovered by the Egyptians around 3000 B.C., and it was used as a sorbent to remove odours.

Activated carbon is an amorphous material constituted by pores or cavities that can be prepared easily from different natural wastes sources such as walnut shells, willow peat, olive stones, etc. Some of the main attractions of activated carbons are their low cost of production and high surface area. Generally, the porosity in activated carbons is a combination of micro, meso- and macropores; the proportion of these cavities is defined by the activation conditions and the nature of the raw material. The International Union of Pure and Applied Chemistry (IUPAC) has classified the pore size as macroporous (diameter > 50 nm), mesoporous (2 < diameter < 50 nm), and microporous (diameter < 2 nm). Through the time different methodologies of activation have been developed, mainly physical and chemical activation. A relationship between the activation method and the number of heteroatoms bonded to the surface (such as oxygen, hydrogen, and nitrogen) has been observed.¹²

Among the different applications described for activated carbon, the main ones are adsorptive removal of colour, odour, taste and other undesirable impurities from the drinking water,^{13,14} solvent recovery,¹⁵ air purification,^{16,17} purification of many chemicals¹⁸ and pharmaceutical products.¹⁹

A significant effort has been devoted to exploring new porous materials for adsorption processes. From zeolites to metal-organic frameworks (MOFs),

crystalline porous materials with higher porosity levels offer a big improvement in terms of functionalities for different industrial processes.²⁰

The first zeolite was discovered by the Swedish mineralogist, Axel F. Cronstedt in northern Sweden. Trying to resemble the natural structures, a big effort has been done in the synthesis of artificial zeolites and their design to adapt these materials for a large number of applications. Zeolite is a crystalline aluminosilicate with a three-dimensional framework structure that forms uniformly sized pores of molecular dimensions. The structure consists of silica frameworks (SiO_2) where at some point Al^{3+} replaces Si^{4+} on the framework, generating a negative charge within the structure that is compensated with the attraction of cations.²¹

Due to the abundance of natural zeolites and the diversity of synthetic zeolites and their inherent capacity to adsorb polar molecules, these materials have been applied in a wide number of applications such as natural gas purification,^{22,23} air separation,²⁴ hydrocarbons desulfurization,^{25,26} refinery gas separation,²⁷ gas drying,²⁸ just to mention some. But more recently, physicochemical versatility in zeolites has placed them in new developing areas such as agriculture, environmental technology, and biological technology.²⁹ Due to the biocompatibility of zeolites in the human body,³⁰ they have found relevance in medical applications for instance, as antibacterial agents,³¹ adjuvant treatment³² or encapsulation/delivery of drugs.³³

Porous materials (mainly activated carbons and zeolites) have played a fundamental role in materials chemistry thanks to the number of industrial processes using tons per year. This has motivated a continuous effort to optimize the synthesis procedures and to minimize the production cost while promoting research related to the development of new porous materials that match the market needs. Based on these premises, novel porous materials such as mesoporous silica, covalent organic frameworks (COFs), or metal-organic frameworks (MOFs) have been discovered in the last decades. Considering the relevance of these materials in the last few years, the next section will focus on a deep description of metal-organic frameworks synthesis and applications.

1.2. Synthesis of Metal organic frameworks

1.2.1. General overview of MOFs materials and synthesis procedures

Metal-organic frameworks (MOFs) have emerged as a new class of crystalline porous materials with exceptional structural characteristics.³⁴ MOFs are crystalline materials formed through the strong interactions between metal ions or cluster and coordinated ligands forming one-, two-, or three-dimensional pore structures (**Figure 1.2.**).³⁵ These materials show an almost infinite number of combinations between organic and inorganic building blocks, offering enormous flexibility in terms of pore size, structure and shape.³⁶ Characteristics such as ultrahigh porosity (up to 90 % free volume), thermal and structural stability, etc., make them of increasing interest for potential application in gas storage, membranes, thin-film devices, gas separation, biomedical imaging and drug delivery.³⁷

Metal-organic frameworks discovery and development have been a consequence of a continuous understanding and research into the assembly of coordination polymers at the beginning of the 1990s. One of the first reports related to the study of extended networks and the influence of metal coordination and geometry of the ligands was done by Robson *et al.* They were able to describe the first 3-D framework with diamond-like structure with molecules of tetra (4-cyanoterepheny) methane connected to tetrahedral Cu(II) metallic centers.³⁸ The term metal-organic framework was first introduced by Yaghi *et al.* in an article where was reported a diamond-like three-dimensional structure formed by 4,4'-bipyridine(4,4'-bpy) as ligand and copper as metallic centre.³⁹ Just a couple of years later, the same authors described the first coordination polymer with permanent porosity using carboxylate-based ligands (terephthalic acid) and Zn²⁺ as metal centre. Compared with the system reported before, this one has the big difference of being a neutral network with only solvent molecules filling the channels. The solvent removal provides a network of accessible and permanent porosity to a range of molecules.⁴⁰

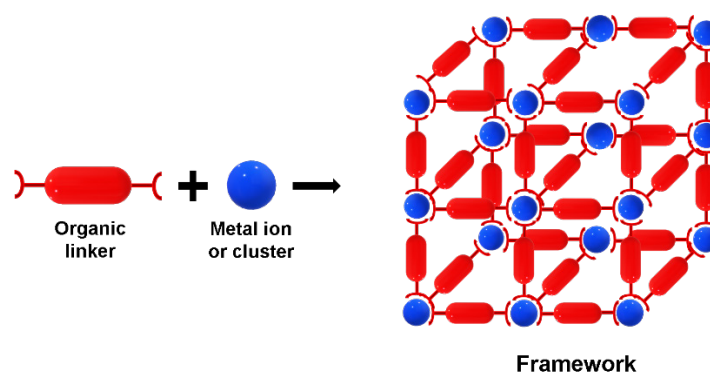


Figure 1.2. Scheme showing MOFs creation.

As a result of the large number of linkers available in the market and the high number of possible combinations for the synthesis of MOFs, in the last decade, there has been an exponential growth in the number of new MOFs structures described in the literature. One of the first materials was HKUST-1, named after the first synthesis at the Hong Kong University of Technology. As it is shown in **Figure 1.3(a)** the framework of this material is formed by paddlewheel clusters of Cu^{2+} and trimesic acid (BTC) as a linker and has the general formula $\text{Cu}_3(\text{BTC})_2(\text{H}_2\text{O})_2$.⁴¹

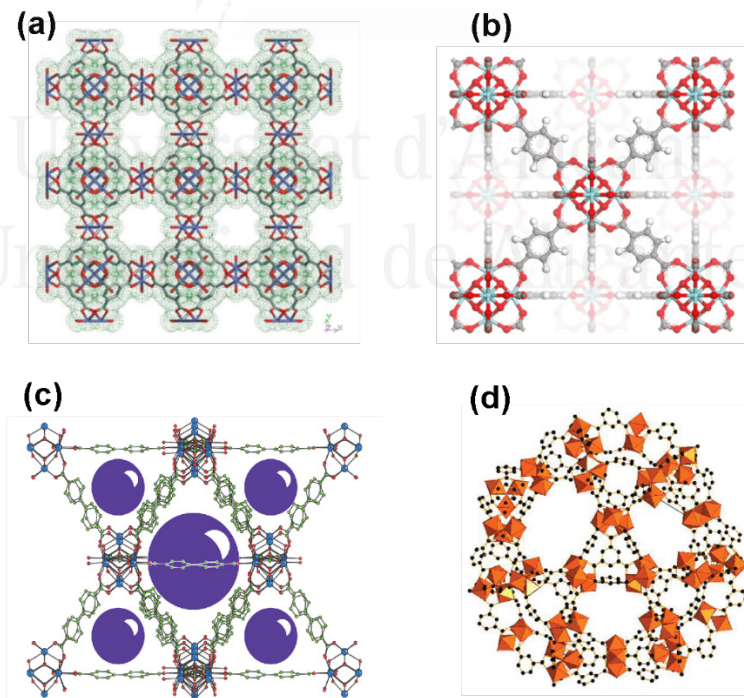


Figure 1.3. Schematic framework of MOFs (a) HKUST-1,⁴¹ (b) UiO-66,⁴² (c) UiO-67⁴³ (d) MIL-100 (Fe).⁴⁴

In the scope of the ongoing investigations of new MOFs, the development of MOFs with a metal cluster of zirconium or iron has attracted considerable interest for different applications such as catalysis or biomedical applications. Within this family, UiO-66 and UiO-67 (Universitetet i Oslo) are the most widely investigated Zr-based MOFs due to their excellent thermal, aqueous and acid stability.⁴⁵⁻⁴⁷ UiO-66 (**Figure 1.3(b)**) is formed by the union of metallic clusters of cationic $Zr_6O_4(OH)_4$ and 1,4-benzenedicarboxylate (BDC) as a linker. UiO-67 has a similar structure, except that it uses biphenyl-4,4'-dicarboxylate (BDPC) as a linker instead of BDC (**Figure 1.3(c)**). Due to the size of BDPC it allows to form a structure with two cage sizes, one octahedral cage (big one) that is facing 8 tetrahedral cages (small ones).⁴³

Iron-based MOFs are emerging as exceptional materials for different applications due to the fact that Fe is an abundant metal on Earth, and Fe-containing complexes have wide applicability in multiple fields such as drug delivery, photocatalysis and environmental remediation.^{48,49} MIL-100 (Materials of Institute Lavoisier) is one of the most widely studied Fe-based MOFs due to its facile synthesis, extensive accessibility, permanent porosity, and easy scale-up. As it is shown in **Figure 1.3(d)**, MIL-100 is formed by the union of tetrahedral iron clusters and benzene-1,3,5-tricarboxylate linkers assembling into zeolitic architecture.⁵⁰

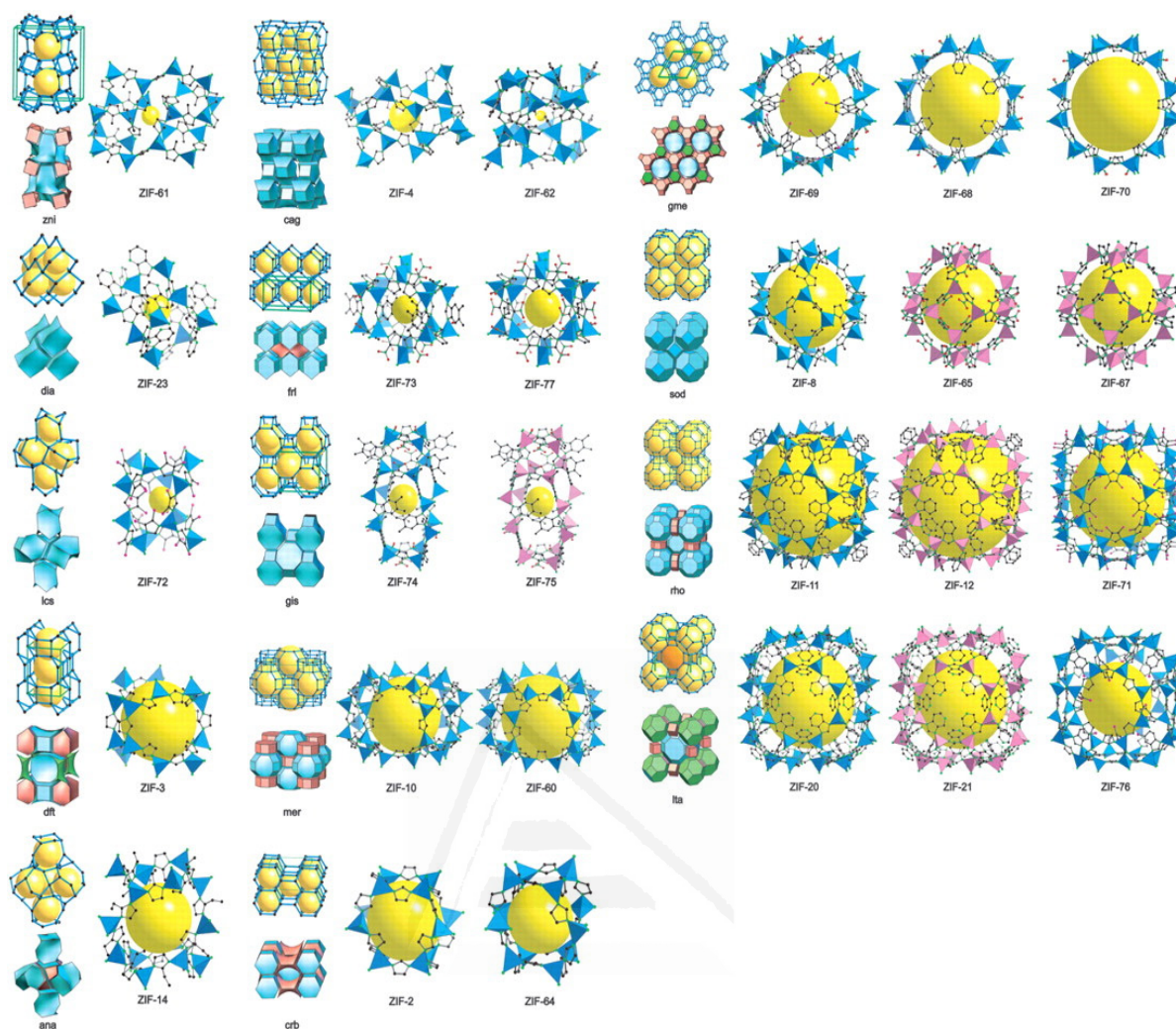


Figure 1.4. Schematic structures of some zeolitic imidazolate frameworks with different topologies. Adapted from ⁵¹

Finally, Zeolitic imidazolate frameworks (ZIFs) are a subfamily of metal-organic frameworks (MOFs) in which tetrahedral zeolitic topologies are formed by the union of imidazolate derived ligands (Im) and divalent metals ($M^{2+} = \text{Zn}, \text{Co}$) exhibiting cage-like subunits.⁵² This group of MOFs has attracted considerable attention due to the high adsorption capacity, thermal stability, and high surface area. Yaghi *et al.* reported different ZIF topologies for the first time by changing the functional group bonded to the imidazole ring and demonstrated their extraordinary gas adsorption capacity.^{51,52} As it is shown in **Figure 1.4**, there is a wide number of configurations between $\text{Zn}^{2+}/\text{Co}^{2+}$ metal centres and the X-Imidazole ligand, giving rise to frameworks made of small cages to structures with large cavities ⁵³.

As it can be appreciated in previous sections, it looks like there is no clear rule about how to name a new MOF structure, and that is true. Even though most of the MOFs reported recently are named with the word “MOF” followed by a number, there is a large group of structures named with the university’s acronym where it was developed, and some called just with the formula unit.

Synthesis optimization in MOFs is an essential step to obtain materials with desirable characteristics of specific surface area, crystal size, crystal shape, etc. Thence, different methods of MOFs synthesis have been developed to fulfil these needs. As it is shown in **Figure 1.5**, synthesis methods for MOFs are generally resumed in two groups: conventional methods, i.e., those that are carried out by conventional electrical heating; and non-conventional synthesis methods where reaction time is decreased using other tools such as microwave irradiation, sonochemistry, etc. Some of the most important are solvothermal, electrochemical, microwave, mechanochemical, sonochemical, and ionothermal method.

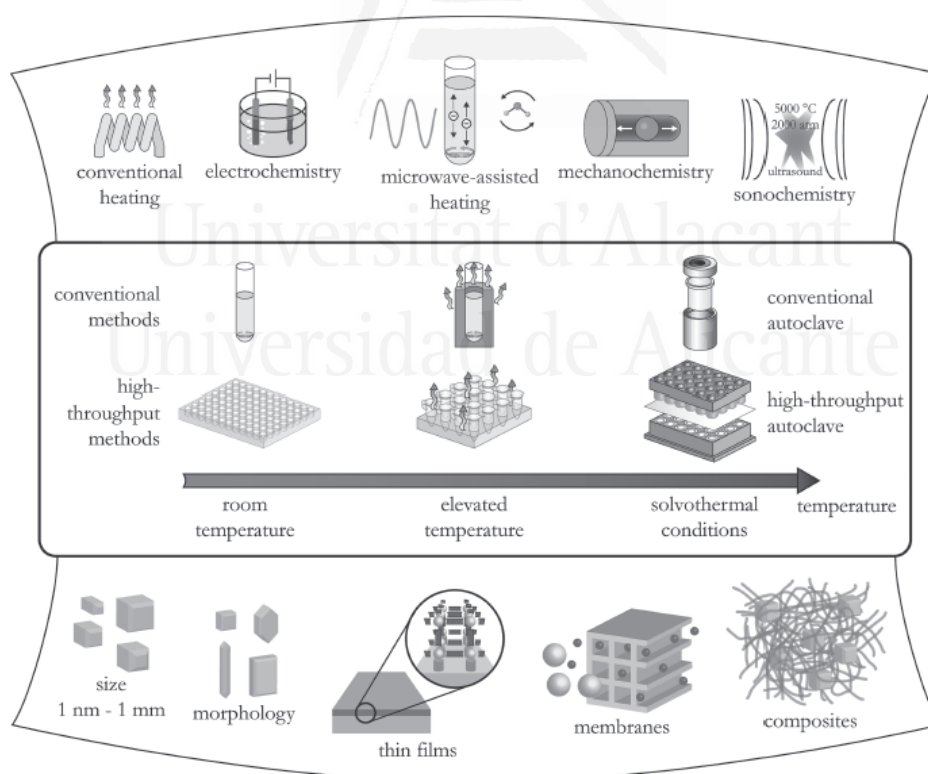


Figure 1.5. Overview of synthesis methods, possible reaction temperatures, and final reaction products in MOFs synthesis.⁵⁴

1.2.2. Solvothermal/hydrothermal synthesis

Solvothermal synthesis of MOFs is one of the most widely used methods due to the easy development and up-scaling. Solvothermal methods are based on reactions taking place in closed containers in non-aqueous (or aqueous) conditions under autogenous pressure and elevated temperature, above the solvent's boiling point.⁵⁵ Heat is the energy applied to the reaction to overcome the activation energy barrier between the metal ions and the ligands. Parameters such as metal/ligand ratio, solvent, modulating reagent and temperature affect greatly the shape, and size (growth) of the crystals. High-throughput methods have demonstrated to be an alternative to optimize all the reaction parameters (miniaturization and automatization of the synthesis procedure to study different variables in a batch of synthesis).⁵⁶ Wide number of MOFs such as ZIFs,⁵¹ HKUST-1,⁵⁷ UiO-66⁵⁸ and UiO-67⁵⁹ have been synthesized for the first time using this method.

1.2.3. Microwave synthesis

Microwave-assisted synthesis has been a widely used method in organic chemistry.^{60,61} Nevertheless, solid-solid and solution-based synthesis have also been described for MW synthesis such as zeolites and MOFs.^{62,63} MW-assisted synthesis works based on the interaction of electromagnetic waves with mobile electric charges (i.e., polar solvent molecules/ions in the solution).⁶⁴ This direct interaction from the energy source-reactants results in more efficient and faster heating. MW-assisted synthesis of MOFs is mainly focused on i) the acceleration of the crystallization, ii) nanoscale products, and the most important iii) to improve the porosity and the selectivity of polymorphs.

One of the first examples of MW-assisted MOFs synthesis was reported by Jhung *et al.* for Cr-MIL-100. In this synthesis, the solution of metallic salts and ligands was sealed in a Teflon autoclave and kept in a MW oven at 220 °C for 1, 2, and 4 h obtaining crystals with a different shape and size.⁶⁵ Nevertheless, a wide variety controlled size crystal of metal (II)-carboxylate-based MOFs have been synthesized with this method such as IRMOF-1 and HKUST-1.^{66,67}

1.2.4. Electrochemical synthesis

In the electrochemical synthesis of MOFs, the metal cations diffuse to the reaction media through the anode, and the organic linkers are dissolved into the electrolyte, where they react with the anode. The advantage of the electrochemical synthesis of MOFs over another is the exclusion of anions coming from the metallic salts (i.e., chloride, nitrate, sulphate, etc.), which has been demonstrated to be beneficial for large scale production.⁵⁴ A wide number of different MOF films and patterned coating have been studied using this synthesis method.⁶⁸

The first synthesis of MOF using electrochemical method was reported by researchers from BASF in 2005. The synthesis was established for different Cu and Zn based MOFs. HKUST-1 (Cu) electrochemical synthesis consisted of the immersion of copper plate into a solution containing the linker (1,3,5-benzenetricarboxylic acid (BTC)), and an electrolyte. When a certain voltage was applied, the copper ions were released from the copper electrode to the solution and reacted. In this patented method the HKUST-1 obtained had a surface area of $1820 \text{ m}^2 \text{ g}^{-1}$, which is higher to the one obtained by solvothermal method ($1550 \text{ m}^2 \text{ g}^{-1}$).^{69,70}

1.2.5. Mechanochemical synthesis

The history of mechanochemistry in synthetic chemistry is long. It has been originally used to develop multicomponent reactions to obtain pharmaceutically active co-crystals, and it has quickly expanded into many areas of research such as inorganic chemistry, organic synthesis, and polymer science.⁷¹⁻⁷³

The synthesis of materials by mechanochemistry consists in the chemical reaction promotion by milling or grinding solids without any or with minimal amounts of solvent.^{74,75} Synthesis of MOFs using mechanochemistry is of great interest due to the advantages in comparison with other synthesis methods such as solvent-free (or minimal amount of solvent), short reaction times and synthesis without external heat supply.⁷⁶ However, the first limitation lies in the scaling-up of the synthesis; for instance, it can be classified as a batch processing technique with a low rate of

production. It is important to mention that even when it is a solvent-free synthesis, a purification step must be added.^{77,78}

The first example of solvent-free MOFs obtained by mechanochemical synthesis was reported by Pichon *et al.* in 2006. In the study, metal salts of Cu and isonicotic acid as a linker were grounded for about 10 minutes to obtain the desired MOF product.⁷⁹

1.2.6. Sonochemical synthesis

Sonochemical synthesis refers to a reaction occurring in an ultrasonic environment, i.e. where the change of pressure from small bubbles and cavities due to a phenomenon called acoustic cavitation.⁸⁰ Cavitation promotes an intimate interaction between molecules and energy. For instance, the pressure and temperature in the hot spot of the bubble may reach 1000 bar and 5000 K (with heating and cooling rates of 10^{10}K s^{-1}), respectively. Using sonochemistry to synthesize MOFs represents an opportunity for a short synthesis time, environmentally friendly and high optimum energy-efficient relations.⁵⁴ The first MOF reported synthesized using sonochemistry was the Zn-BTC, which consisted of MOF nanocrystals synthesized at room temperature and atmospheric pressure in 20% ethanol/water under ultrasound irradiation.⁸¹

1.3. Application of MOFs

MOFs have provided unique opportunities for a wide number of applications. Due to their excellent physicochemical properties mentioned before, these materials have been applied in drug delivery, catalysis, sensor technology, gas storage and separation, water sorption applications, electrical energy storage, luminescent materials, just to mention some.⁸² In this section, some of these applications will be described as a general overview.

1.3.1. Gas storage and separation

Gas storage and separation have become a high importance research topic due to the increasing global concern about industrial activities such as CO₂ capture,

H₂ storage for fuel, gas purification, etc. As it was mentioned before, MOFs present exceptional properties which make them highly attractive for the applications described above. For instance, a great number of publications every year are devoted to topics related to gas adsorption/storage in MOFs.

1.3.1.1. H₂ storage

Hydrogen is a leading candidate to substitute the traditional carbon-based fuels (mainly carbon and petroleum-derivatives) in the near future, thanks to its potential abundance and renewability, high combustion heat (almost triplicate heat of combustion of gasoline, in the case of hydrogen⁸³) and most important, the formation of non-hazardous combustion products (mostly water).⁸⁴ However, this gas presents a high complexity of storage. Different storage technologies are being investigated such as metal hydrides, cryogenic storage and high-pressure storage. Unfortunately, most of them do not present economic and practical advantages compared to fossil fuels energy source.⁸⁵ MOFs are strong candidates to minimize these drawbacks and allow to store large amount of H₂. It has been demonstrated that MOFs formed with open metal sites (preferably M(II) and M(III)) that polarize the molecules in the structure are potential candidates for H₂ storage.⁸⁶

Hydrogen storage in MOFs is based on weak interactions between the surface and the H₂ molecules. This ensures the reversibility of the process and leads to fast kinetics, and manageable heat during hydrogen fueling.⁸⁷ Rosi *et al.* reported for the first time in 2003 the isostructural M-MOF-74 series (M=Mg, Mn, Fe, Co, Ni, Cu, Zn) presenting a promising H₂ storage capacity. Ni-MOF-74 showed a volumetric capacity of 12.1 g/L at 25 °C and 22.3 g/L at -75 °C, both at 100 bars.⁸⁸ Subsequently, several MOFs have been tested for hydrogen uptake capacity.⁸⁹

1.3.1.2. CH₄ separation and storage

Apart from hydrogen, natural gas, whose main component is methane is another energy source with the potential to replace fossil fuels due to its natural abundance.^{90,91} Among all fossil fuels, methane has the highest hydrogen to carbon ratio, and by consequence, the higher research octane number (RON=107), and combustion of methane produces the smallest amount of CO₂ for each unit of heat

that is released.^{92,93} However, methane is a gaseous molecule at ambient temperature and pressure, and the volumetric energy density is rather low (0.04 MJ/L). which exerts constraints on its applications in various possible fields, particularly on-board applications.⁹⁴ Therefore, for large scale usage, it is necessary the development of safe and efficient technology to obtain a competitive volumetric energy density.⁹² Adsorbed natural gas on porous structures presents a safer and costly advantage technique to compressed natural gas storage (CNG).

Metal-organic frameworks (MOFs) have been widely studied for methane adsorption and storage finding important factors controlling the processes in these materials such as Van der Waals and electrostatic interactions, and structural flexibility.⁹¹ One of the first results reported for high-pressure methane adsorption in MOFs ($[\text{Co}_2(4,4'\text{-bipyridine})_3(\text{NO}_3)_4]$) was described for Kitagawa *et al.* in 1997.⁹⁵ Several groups of MOFs have been described in the literature for methane adsorption, pillar-layered MOFs ($\text{M}_2(\text{dicarboxylate})_2(\text{dabco})$) have shown very promising results.^{96–99}

Open unsaturated metal sites MOFs such as MOF-74 series offer a primary binding site to guest molecules showing a promising methane adsorption capacity. Wu *et al.* compared the methane adsorption properties of the MMOF-74 series ($\text{M} = \text{Mg}, \text{Mn}, \text{Co}, \text{Ni}, \text{Zn}$). Their excess adsorption capacities of methane at 298 K and 35 bar range from 149 to 190 cm^3 (STP) g^{-1} , NiMOF-74 exhibiting the highest one.^{100,101}

1.3.1.3. CO₂ adsorption

Global warming is one of the most alarming problems nowadays. Recently, A big effort has been done to reduce greenhouse gas emissions to the atmosphere (mainly CO₂ coming from fossil fuel power plants), and their conversion into value-added products. CO₂ capture at an industrial level is a direct technology that is based on the chemical absorption of CO₂.¹⁰² However, CO₂ adsorption in porous materials is gaining attention in different applications.¹⁰³ Considering the extremely high surface area and the physicochemical surface properties, MOFs have been considered as potential materials for CO₂ capture. Porous shape and size in MOFs can be easily controlled by the use of different ligands. This is an essential

requirement in order to have a preferential selectivity of CO₂ over other similar molecules (H₂, N₂ and CH₄).¹⁰⁴ One of the first studies reported that adsorption of CO₂ in MOFs is enhanced by the presence of unsaturated metal sites working as Lewis acid sites. For instance, these authors reported the highest capacity (27.5 wt.%) ever reported under standard conditions (298 K and 1 bar) for CO₂ adsorbed in Mg-MOF-74.¹⁰⁵ Over the time, the affinity of CO₂ to the surface of MOFs has been increased by introducing ligands with basic Lewis functional groups such as amines, imines, etc. **Table 1.1** summarizes MOFs with high CO₂ capture capacity under standard conditions.

Table 1.1. Representative MOFs CO₂ capacity under standard conditions (adapted from K Sumida *et al*).¹⁰⁶

chemical formula ^a	common name	surface area (m ² /g)		capacity ^b (wt %)	pressure (bar)	temp (K)
		BET	Langmuir			
Mg ₂ (dobdc)	Mg-MOF-74, CPO-27-Mg	1174	1733	27.5	1	298
				27.2	1	298
		1800	2060	26.7	1	298
				26	1.1	298
				1495	1905	26
Cu ₃ (BTC) ₂ (H ₂ O) _{1.5}	HKUST-1, (4 wt % H ₂ O)			27	1	298
Co ₂ (dobdc)	Co-MOF-74	957	1388	24.9	1	298
	CPO-27-Co					
Ni ₂ (dobdc)	Ni-MOF-74 CPO-27-Ni	1080		23.4	1	296
		936	1356	23.9	1	298
		639		22.7	1	298
		1083	1312	22.6	1	303
Zn ₂ (dobdc)	Zn-MOF-74 CPO-27-Zn	1070		20.4	1	296
				19.8	1	296
		816		19.6	1	296
				17.6	1.1	298
Cu ₃ (BTC) ₂	HKUST-1	1400		19.8	1	293
			1492	18.4	1	298
				18.3	1	295
		1781		15.2	1	298
		1482		15	1	295

1.3.1.4. N₂ and O₂ separation

Oxygen is an essential gas for an infinity number of processes in humans and any life form, from blood purification to photosynthesis, just to mention some. However, oxygen has taken importance lately for a high number of industrial processes which are demanding more of this gas every year, for instance, in the oxyfuel combustion process and oxygen-blow gasification to convert coal into an

intermediate synthesis gas that can be processed to obtain electricity, chemicals and fuels.^{107,108} Although O₂ is plenty available in the atmosphere, it is one of the gases with most marketed high prices, associated mainly to the cost of its separation and purification. Different techniques have been developed to obtaining this valuable molecule at a commercial scale. These techniques can be summarized following two approaches for air separation, cryogenic and non-cryogenic separation. Obtaining oxygen under cryogenic distillation conditions is typically reserved for applications that require a high quantity of oxygen at ultra-low temperature. The non-cryogenic separation involves the separation of oxygen at ambient temperature, mainly using molecular sieves. In this field, many porous materials have been studied to separate oxygen.¹⁰⁹

Selective gas adsorption based on the principle of molecular size-exclusion has been successfully studied with several MOFs. For instance, it was reported a high selectivity efficiency in PCN-13 MOF that contain square channels of 3.5 Å x 3.5 Å and a pore volume of 0.3 cm³/g, allowing the oxygen molecules with a kinetic diameter of 3.45 Å to pass through the material and excluding N₂ (kinetic diameter of 3.64 Å).¹¹⁰ Other MOFs such as Mg₃(ndc)₃ with an O₂ uptake capacity of 3.5 mmol/g (77 K and 880 torr)¹¹¹ or PCN-17¹¹² have been studied for this application.

1.3.1.5. NO storage and release

For a long time, nitric oxide (NO) was only perceived as a toxic gas produced from car exhausts. A big effort has been done to understand the chemistry of this molecule in order to reduce NO levels produced from internal combustion engines. Surprisingly, nitric oxide was called in 1992 the “molecule of the year” and subsequently in 1998 the scientists, F. Murad, R. Furchgott and L. Ignarro won the Nobel prize of Physiology for their significant discovery of the uses of NO in the human body, and in particular as a signalling molecule in the cardiovascular system.¹¹³ This small molecule has been the focus of different researches in chemical and medical science. It has been recognized as a versatile player in nearly every physiological system: cardiovascular,¹¹⁴ immune,¹¹⁵ central nervous system¹¹⁶ and outflow physiology.¹¹⁷ In the human body, NO in concentrations of nM and μM is produced intracellularly by the enzymatic action of the NO synthase

(NOS) from amino acid L-arginine.^{118,119} Due to the thereof mentioned biological significance and therapeutic potential of NO, a big achievement has been done on developing feasible systems for effective NO delivery. However, due to the limitations and restrictions that NO delivery has faced, nowadays only a few delivery systems have been approved on the market by the US Food and Drug Administration (FDA). These include nitroglycerine for the treatment of acute angina,¹²⁰ nitroprusside for treatment of congestive heart failure,¹²¹ and VYZULTA (lantanoprostene bunod ophthalmic solution) to lower eye intraocular pressure in glaucoma patient.¹²²

Different NO-releasing platforms have been developed to administrate NO into the body. They can be summarized in non-catalytic, i.e. liposomes, micelles, dendrimers, particles, MOFs, hydrogels, etc., and catalytic such as NO donors (nitrates, diazeniumdiaolates (NONOates) and S-nitrosotiols (RSNOs)).¹²³

Due to their exceptional physicochemical properties, MOFs have been studied as NO delivery platforms. For instance, Lowe *et al.* reported the NO release ability of Cu-TDPAT MOF, which contains 4,6-tris(3,5dicarboxylphenylamino)-1,3,5-triazine (H₆TDPAT) as a ligand.¹²⁴ The NO adsorption process was achieved following two steps: first, NO was adsorbed in the pores and, later on, NO reacted with secondary amine groups of the TDPAT linkers to form NONOates. The maximum release of NO in Cu-TDPAT was about 175 µm/g (after seven days of release). Subsequently, another MOFs has been studied for this application such as iron (II)-based MOF, Fe₂(dobco) (dobco=2,5-dioxido-1,4-benzenedicarboxylate) with a storage capacity of 6.5 mmol/g.¹²⁵

MOFs containing open metal sites are among the most widely studied for NO releasing. For instance, B. Xiao *et al.* reported a high adsorption capacity for NO (up to 9 mmol/g at 196 K) into HKUST-1. These exceptional numbers were attributed mainly to the presence of open metal sites in the walls of the structure.¹²⁶ M-CPO-27 (M= Ni or Co) have shown to present a high storage capacity for NO at room temperature, but even more important, to release almost 100 % of the NO adsorbed under 11 % humid air flow and the feasibility for scaling up the synthesis.¹²⁷

1.3.1.6. Hydrocarbon adsorption

Hydrocarbon separation is one of the most important chemical processes carried out in the petrochemical industry. Hydrocarbons are molecules made exclusively by hydrogen and carbon atoms, and they can be classified depending on their chemical structure as alkanes or paraffins, alkenes or olefins and aromatic hydrocarbons. Some of the most relevant hydrocarbon separation processes receiving great attention due to their essential role in petrochemical and chemical industries are those related to the separation of small molecules, i.e. hydrocarbon C₁-C₄, isomers of hexane and C₈-aromatics (xylene isomers).^{128,129} Thereof mentioned applications play a crucial role in processes such as polymer synthesis, natural gas and petroleum purification, and oil-derived production processes. Cryogenic distillation and molecular sieves, such as zeolites, have been used for these applications. Unfortunately, both present disadvantage due to energy usage and cost.¹³⁰

MOFs have a unique shape and size tuneability and exceptional structural characteristics which make these materials exceptional candidates for adsorption and separation of hydrocarbons. Methane is the simplest hydrocarbon, is the principal component of natural gas and a cleaner alternative fuel to gasoline. MOFs have been widely studied for methane storage in different conditions obtaining relevant results.^{129,131,132}

Research related to larger hydrocarbon separation, such as C₂ or C₃, have been greatly reported due to the importance of these molecules for an almost infinite number of applications. Ethane is a feedstock for ethylene plants while propane and butanes are feedstocks for chemical or petroleum refining processes.¹³³ Separation of olefin/paraffins such as, ethane/ethylene has been studied with different MOFs as an alternative to the costly distillation processes which complexity lies in the similar molecular size and close volatility of the thereof mentioned molecules. One of the first MOFs applied for this separation was the Cu-BTC (Cu₃(btc)₂ or HKUST-1) which showed preferential adsorption of ethylene over ethane. The adsorption preference was associated with the specific interactions between the double bond in ethylene and the partially charged copper atoms in the frameworks.^{134,135}

Moreover, Cu-BTC has been studied for several separations of olefins/paraffins such as isobutane/isobutene¹³⁶ or propane/propylene.¹³⁷

ZIFs present a great thermal and chemical stability, which makes this subgroup of MOFs potential candidates for hydrocarbon separation. For instance, Gascon *et al.* reported an excellent ethylene/ethane separation in ZIF-7 due to the associated breathing phenomena in this material upon adsorption.¹³⁸ ZIF-8 and ZIF-8 based membranes are some of the most popular materials for separation of aromatic and cyclic hydrocarbons such as xylene isomers, benzene or cyclohexane.^{139–141}

1.3.2. MOFs for drug delivery

Nowadays, the need for more efficient drug administration systems to treat a large number of diseases has stimulated a great investment in research related to the design of novel drug delivery platforms. Non-optimal administration of drugs leads to physical side-effects and the rise of economical cost in patients. From the medical, economic and even environmental point of view, there is a clear necessity to developed more efficient drug delivery systems. In the last few years, an extensive number of systems have been developed as novel drug dosage systems, for instance, polymeric nanoparticles,¹⁴² lipid NPs,¹⁴³ dendrimers,¹⁴⁴ liposomes,¹⁴⁵ nanocrystals¹⁴⁶ and carbon nanotubes¹⁴⁷. Nevertheless, porous materials have attracted enormous attention in this application due to their physicochemical properties. Materials like activated carbon, zeolites or porous silicas have been studied for adsorption and release of drugs for cancer treatment,¹⁴⁸ anti-inflammatory agents¹⁴⁹ or antibiotics,¹⁵⁰ just to mention some. More recently, MOFs have also attracted attention as drug delivery systems. The presence of heavy metals may be considered *a priori* as the first limitation to apply these materials in biomedical applications. However, an enormous number of publications have been devoted to finding the appropriate combination of metal clusters and linkers in MOFs (named BioMOFs) to be stable, biocompatible and biodegradable for human drug dosage.¹⁵¹

MOFs containing iron as metal have been widely used for drug delivery. Horcajada *et al.* synthesized Fe(II)-MOFs named as MIL-100 and MIL-101 (Material

Institut Lavoisier) with a well-defined mesoporous structure that are suitable for the adsorption of big pharmaceutical molecules.¹⁵² MIL-100 was found to have a total ibuprofen uptake up to 0.35 g/g whereas MIL-101 was able to uptake 1.4 g/g of ibuprofen. This difference was explained in terms of the ibuprofen molecular size (6 Å x 10.3 Å) which is able to fit in both MIL-101 windows (pentagonal and hexagonal) but not into the smaller pentagonal window of MIL-100. One of the most outstanding results obtained by the MIL family for ibuprofen dosage was related to the delivery process. Ibuprofen in MIL-100 was released mostly in 2 h, but the entire amount was released in the later three days. For MIL-101 the weakly bonded molecules were released in 8 h and the complete release was achieved after six days.^{152,153}

Extensive research in MOFs within the MIL family as drug dosage materials have found potential applications for highly challenging drugs, such as azidothymidine triphosphate (AZT-Tp), cidofovir (CDV), busulfan (Bu), and doxorubicin (Doxo).¹⁵⁴ These drugs are important anticancer and antiviral drugs. Unfortunately, they have therapeutic drawbacks such as poor solubility and/or stability in the biological media, low bioavailability, short half-time and the limited ability to pass biological barriers.¹⁵⁵ Surprisingly, MIL-100 (Fe) was able to successfully adsorb these molecules with encapsulation percentage up to 21.2% for AZT-Tp, 16.1% for CDV, 25.5% for Bu, and 9.1% for Doxo. Meanwhile, MIL-101 (Fe) showed a higher loading capacity for AZT-Tp (42.0%) and CDV (41.9%). Most of the drugs were released within five days, mainly governed by diffusion processes.^{50,152,154}

Materials from the ZIF family have also been evaluated for loading several drugs such as anticancer molecules. ZIF-8 was evaluated for the adsorption of fluorouracil (5-Fu), which is an important anticancer agent used in injection form to treat colon cancer, oesophageal cancer, stomach cancer, just to mention some. ZIF-8 has interesting properties such as high thermal and chemical stability, i.e., exceptional stability in water and alkaline media but poor stability in acid solution. Furthermore, ZIF-8 possesses pores of 11.6 Å and higher surface area of 1630 m²/g.^{51,156} It was reported that around the 45.5 wt.% loading capacity of 5-Fu was achieved in ZIF-8 and the releasing process corresponds to a pH-responsive of the

drug in PBS media. Approximately 50% of the drug was released in about 10 h and the second stage of releasing remained for a week.¹⁵⁷

1.3.2.1. MOFs for drug delivery in ocular therapeutics

In the last decades, optimal drugs dosage in ocular therapeutics has been a challenge for medical researchers. Due to the physical characteristics, the eye is a complex organ formed by several layers which have the function of isolating the internal part of the organ from the exterior. Several materials have been reported in the literature as novel ocular dosage platforms to improve the drug delivery performance. The necessity of these carriers is based on the disadvantages of conventional methods (i.e. eye drops) such as, rapid drainage of the drug from the eye due to the constant lacrimal secretion which leads in more probability of side effects for the patients.

Colloidal dosage forms for ocular drug delivery are one of the most widely studied in the field of ocular drug delivery.¹⁵⁸ These dosage forms include liposomes, nanoparticles, microemulsions, nanoemulsions, etc.¹⁵⁹ Other forms of dosage used in ocular therapeutics are intraocular devices or external devices such as lacrimal duct inserts and drug-loaded contact lenses.^{160,161} Inorganic and organometallic porous materials have been studied as a potential drug delivery material in both colloidal and ocular devices.¹⁶²⁻¹⁶⁴

In ocular therapeutics, metal-organic frameworks (MOFs) have been studied as drug dosage materials due to their structural properties and acceptable biocompatibility. Although, at the moment, the research related to these materials is limited due to the complexity of the eye. One of the first studies reporting the drug delivery in MOFs for ocular therapeutics has been published by Se-Na Kim *et al.* They reported the adsorption and release of brimonidine, an important alpha agonist drug used to treat open-angle glaucoma using iron-based MOFs MIL-88-NH₂. The amount of drug adsorbed was 121.3 mg of brimonidine/g of MOF, and the release was performed up to 12 h. In vitro cytotoxicity tests of the MOF in epithelial cells showed a cell viability of almost 100% after 24h of contact with several numbers of concentration.¹⁶⁵ ZIF-8 has also been studied as drug delivery material for the therapy of endophthalmitis. ZIF-8 was loaded with photosensitizer antibacterial

agents and in vitro and in vivo tests were performed to verify the biocompatibility and cytotoxicity of the materials.¹⁶⁶

1.3.2.2. Toxicity and biocompatibility of MOFs

Toxicity, stability and biocompatibility are trending topics in research related to MOFs for drug delivery systems. As it was reported recently, a certain instability in MOFs is desired in order to help the body in the matrix degradation process after use, and by consequence to avoid the endogenous accumulation of the material in the body.¹⁵⁵ Drug release efficiency is affected by the degradation of the matrix which promotes the diffusion of the drug from the matrix to the body.¹⁵¹ However, a certain level of stability in MOFs for medical application is also required to ensure the proper encapsulation of the molecule and the storage until it is released to the body. For instance, for anticancer drug carriers, the matrix is expected to preserve its structure until the moment it reaches the tumour tissue.

Toxicity of MOFs for biomedical applications depends on different factors, such as the chemical composition of the linker, type of metal and particle size of the nanoparticles. Size of the material determines its cellular uptake, biodistribution, translocation and excretion from the body.^{167,168}

The toxicity of MOF for drug delivery applications is not well established at the moment. There are several publications related to toxicity (in vitro and in vivo analyses) of different MOFs with a large number of linkers and metallic centres. Those MOFs with iron in the structure are some of the most well described in the literature. Tamames-Tabar *et al.* reported an extended research of the toxicity of fourteen MOFs with different metals compositions (Fe, Zn and Zr; carboxylates and imidazolates) on two different cell lines (human epithelial cells foetal cervical carcinoma and murine macrophage cell line). Low toxicity was observed for both cell lines, being the least toxic those composed by Fe-carboxylate (MIL family) and the more toxic the imidazole based family of ZIFs.¹⁶⁹ Recent in-vivo acute toxicity for Fe-based carboxylate MOFs was investigated in rats by evaluating their distribution, metabolism and excretion. The tests have evidenced that the MOFs nanoparticles are rapidly sequenced by the liver and spleen, then further biodegraded and directly eliminated in urine or faeces without metabolization and

substantial toxicity.¹⁶⁷ Even that, there is not a general toxicity process established for MOFs in human bodies. Different research studies have shown that MOFs are potential materials as drug dosage agents and the most feasible way to understand the toxicity, stability and biodegradability of the material is to study each individual case.

1.4. Computational modelling and simulation of adsorption in MOFs

Metal-organic framework (MOFs) have appeared at a time where a wide number of tools can be conducted to characterize and to understand these complex group of porous materials. Due to the almost infinite number of possible combinations of ligands and metals to construct MOFs, computational modelling and simulation have been powerful tools not only to characterize and understand MOFs behaviour; but the most important, to predict possible potential applications with a low economic and time-consuming impact. Computational modelling and simulation are helpful tools to predict adsorption behaviour for several numbers of MOFs and to shortlist materials for experimental synthesis and testing.

To simulate the gas adsorption in a given MOF, its crystal structure must be understood. Several molecular models and methods have been developed to elucidate the crystal structure of MOFs. *Ab initio* calculations can be seen as a mathematical description of the potential energy in the MOF structure and its adsorbed gas molecule. Even when *ab initio* quantum chemical calculations are accurate, they require significant computational resources to be solved. On the other hand, classical force fields models, where interatomic potential parameters are fit by experimental data or *ab initio* calculations, are computationally more efficient but often less accurate.¹⁷⁰

The molecular simulation models most often used for gas adsorption in MOFs are the Monte Carlo and the molecular dynamics. The Markov chain Monte Carlo (MC) method enables efficient sampling of a probability distribution defined on a high-dimensional sample space when a function proportional to the probability

density is known.¹⁷¹ This helps to obtain the probability of each possible microstate of a molecular system composed of a MOF and gas molecules and computing different random variables of interest.¹⁷² On the other hand, molecular dynamics simulates a system comprised of atoms and molecules by propagating Newton's equations of motion on time. In the same way of MC, in MD the user may obtain time average of different variables, and, hence, thermophysical properties of the model system.¹⁷³

1.5. Flexibility in MOFs

MOFs are becoming one of the most rapidly developing fields in chemistry and materials sciences not only for their structural versatility¹⁷⁴ but also for their exploitable applications thereof mentioned. Their crystalline nature, high and permanent porosity, uniform pore size, extraordinary surface area, tunable surface properties, and potential scalability have made MOFs an attractive target for further studies.¹⁷⁵ One of the most studied properties in MOFs is related to the structural reaction to an external stimulus such as gas pressure, temperature of light.^{176,177} Some MOFs possess a unique phenomenon called flexibility as a consequence of the interactions and stimuli of molecules on the MOFs structure. For instance, the first evidence of this property in MOFs was observed when N₂ isotherm at 77 K was performed to determinate the specific surface area. The framework flexibility was associated with drastic changes in the uptake capacity at certain pressures in the adsorption-desorption curve.¹⁷⁸ In order to classify MOFs depending on this new property, MOFs have been grouped as rigid MOFs and flexible MOFs or soft porous crystals¹⁷⁹. Although flexibility in MOFs is commonly associated as the result of a frameworks external stimulus, it is important to mention that this phenomenon may also be caused by the intrinsic composition of the framework.

Intra-framework motives for flexibility in MOFs are related to the structural composition, including the metal ion/cluster and the organic linker. The metallic clusters know as secondary building units (SBU) or molecular building blocks (MBBs) in MOFs are responsible for the movement of the framework. For instance, Férey *et al.* were one of the first to establish a group of empirical rules for the intra-

framework flexibility, such as, MBBs should have a mirror plane with the linker (mostly carboxylates linkers) in a symmetrical position around it; these rules were observed in MIL-88 (Fe, Cr).^{180,181} Another rule was associated with the number of carbon atoms of the carboxylates around the cluster (C) and the number of metal atoms within the cluster (M) must be $C/M \geq 2$. These two rules were observed to be valid for several flexible MOFs, for instance, $[Zn_2(bdc)_2(dabco)]_n$ ¹⁸² and the previously mentioned MIL-88 (Fe, Cr).¹⁸¹ Another approach proposed is related to the utilization of some SBU that induce flexibility to the structure.¹⁸⁰ This approach has been approved in the prismatic SBUs $(M_3O(COO)_6(H_2O)_2 \cdot X)$, $M=Cr, Fe, Al$; $X = F^-, OH^-$) of MIL-88 family, that experience a change in the orientation of the metal trimer and the phenyl rings due to their rotation around O-O axis of the carboxylate groups.¹⁸¹ Similar observations were found in the isostructural DUT-8 (Zn, Co, Ni, CU) (DUT = Dresden University of Technology).^{183,184}

The influence of different functional groups in the linker can promote the expansion/contraction in MOFs.^{180,185,186} As it was proposed by Férey *et al.*, ditopic carboxylate ligands linked to two metal cluster or SBUs are likely for the design of flexible MOFs.¹⁸⁰ Rotation of linkers phenomena has been well described in the ZIF family, especially in ZIF-8 $[Zn(mlm)_2]_n$ (mlm 0 2-methylimidazole, ZIF = Zeolitic Imidazolate Framework).^{187–189}

The external stimuli or the initiator of the flexibility was found to have a great impact on the structural change of the framework, such as phase change or change in unit cell parameters. One of the first reported stimuli in flexible MOFs was that resulted from the removal or incorporation of framework guest molecules, causing a framework expansion/contraction or breathing phenomena (**Figure 1.6A**) which subsequently allows a variety of guest exchange.^{176,190} This can lead to different types of MOFs, such as Pillared MOFs or interpenetrated grids.^{191,192} External pressure is another thermodynamic parameter that is closely related to MOFs flexibility.^{193,194} The effect of the pressure on these porous crystalline materials are directly related to its mechanical stability. Several numbers of researches on MOFs flexibility as a function of pressure are reported in the literature.

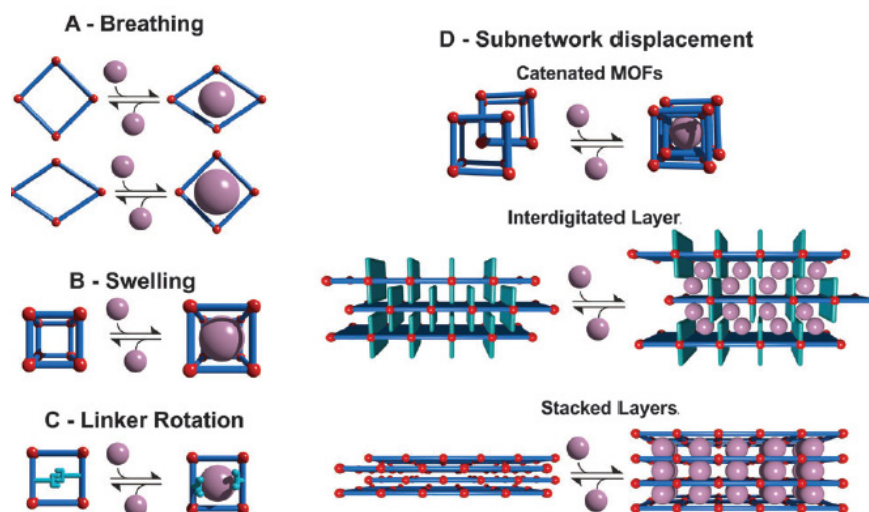


Figure 1.6. Classification of different flexibility modes on MOFs caused by external stimuli.¹⁸⁵

The swelling mode (**Figure 1.6B**) in MOFs is characterized by gradual enlargement of the unit cell volume without a change in the unit cell shape and typically without a change in the space group. One of the most representative MOFs of this mode is the MIL-88 which cell volume is highly is strongly dependant of the guest molecule as it was shown with the adsorption of different alcohols.¹⁸¹ On the other hand, linker rotation (**Figure 1.6C**) is defined as a continuous transition where the spatial alignment of a linker is changed by turning around a rotational axis. A simple prototype of this flexibility mode is ZIF-8.¹⁸⁷

Figure 1.6D shows the scheme of the Subnetwork displacement that is a phenomenon restricted to systems having individual frameworks, which are not connected to each other by strong chemical bonds but interact only by rather weak forces (van der Waals interactions), and thus the subnets can drift, relocate, or shift in regard to each other. This includes interpenetrated three-dimensional (3D) frameworks, as well as interdigitated and stacked two dimensional (2D) frameworks.^{195–198}

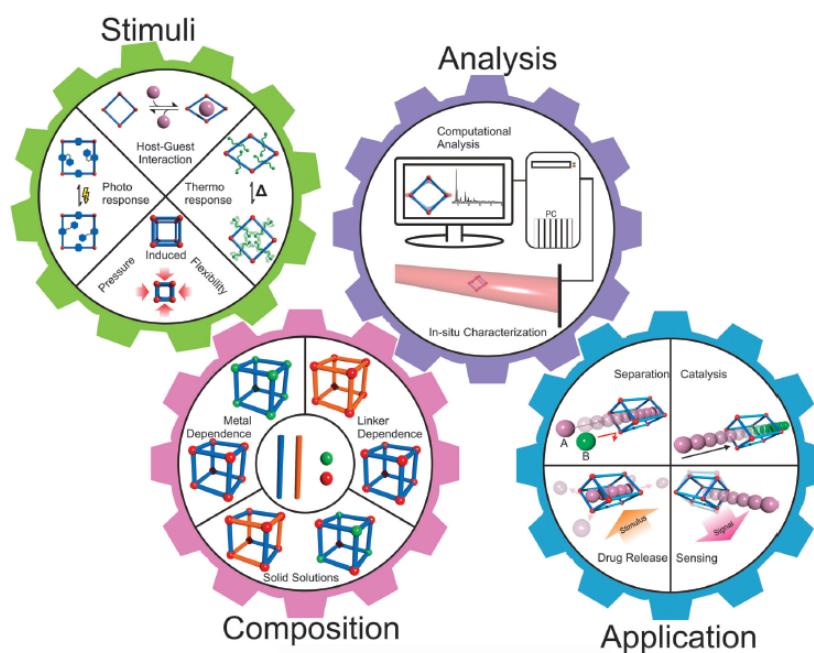


Figure 1.7. Schematic overview of the stimuli and composition in flexible MOFs, in situ analysis methods to determine flexibility and possible future applications.¹⁸⁵

Finally, thermal and photo induction are the responsible of some MOFs structural changes (reversible or irreversible phase transitions).¹⁹⁹ For instance, the heating at 573 K of MIL-53-*as* caused the dynamic movement to the phase MIL-53-*ht*.^{200,201} In the case of the photo induction in MOFs, Modrow *et al.* reported the three-dimensional framework $[\text{Zn}_2(2,6\text{-ndc})_2(\text{azo-bipy})]$ (azo-bipy = 3-azo-phenyl-4,4,0-bipyridine) where azobenzene molecules change their conformation from *trans*- to *cis*- after being exposed to light ($\lambda = 365 \text{ nm}$).²⁰² As it is shown in **Figure 1.7**, there is an ensemble of all the parameters affecting the flexibility in MOFs, their physicochemical characterization techniques and their potential applications.

1.6. MOFs-polymer based composites

The commercialization of MOFs has been limited by their crystalline or microcrystalline form, which limit their incorporation into many applications. A big effort has big done to incorporate and create a synergy of different matrices with MOFs. For instance, composites containing MOFs and polymers have been developed in order to combine the excellent properties of MOFs and easy to handle

of polymers, thus widening the applicability of MOFs. Different approaches have been used to develop elegant methods to synthesize MOF-polymer hybrid materials. Top-down approaches are performed when MOFs are initially synthesized and subsequently incorporated into polymeric materials, contrarily to what it is done in the bottom-up approaches, where hybrid materials are synthesized in conjunction with MOFs formation.²⁰³

As it is summarized in **Figure 1.8**, different approaches for MOF-polymer hybrid materials have been explored by research groups through the synthesis of mixed matrix membranes (MMMs), polymer grafted from MOF particles, polymers grafted through MOFs, polymers templating MOFs growth and MOFs synthesis using polymer ligands.

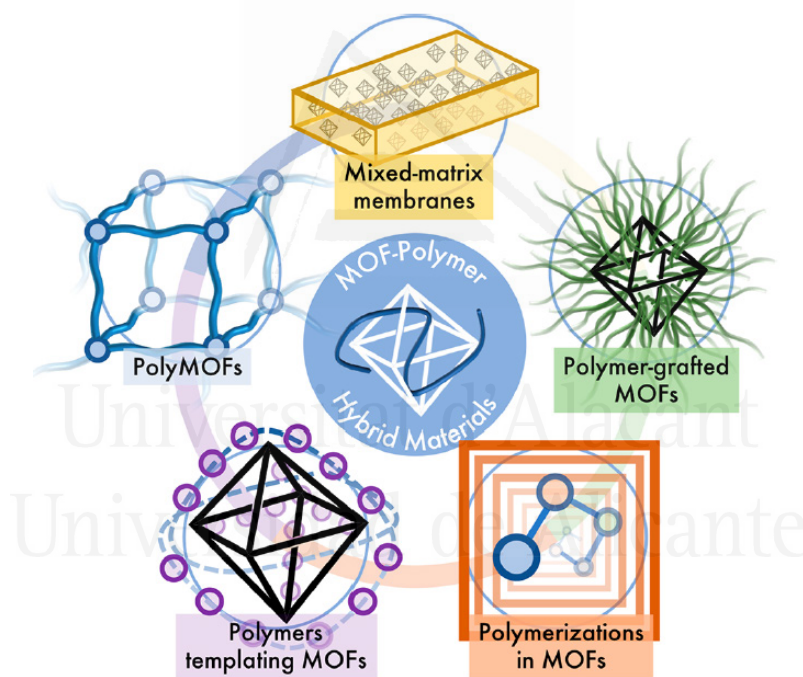


Figure 1.8. Overview of MOF-polymer hybrid materials synthesis approaches.²⁰³

Mixed-matrix membranes (MMMs) consist in the incorporation of rigid materials into flexible, polymeric form.^{204,205} The goal of this method is to create a hybrid material that combines the flexibility of the polymer while the properties of the porous filler remain active.^{204,206} Efforts to synthesize MOF-based MMS have been done toward the potential application of MOFs in gas or liquid separation. It has been shown that the selectivity and the permeability are inversely correlated in

polymer-based membranes, it is important to select the appropriate polymer for each MOF, in order to maximize the permeability and selectivity of the desired molecule and in consequence to avoid nonideal MOF-based MMMs (**Figure 1.9**).^{207,208} For example, more rubbery polymers, such as polydimethylsiloxane (PDMS) promotes higher permeability, whereas glassy polymers, such as polysulfone (PSF), polyimide (PI), and poly(methyl methacrylate (PMMA) tend to display better selectivity.²⁰⁹

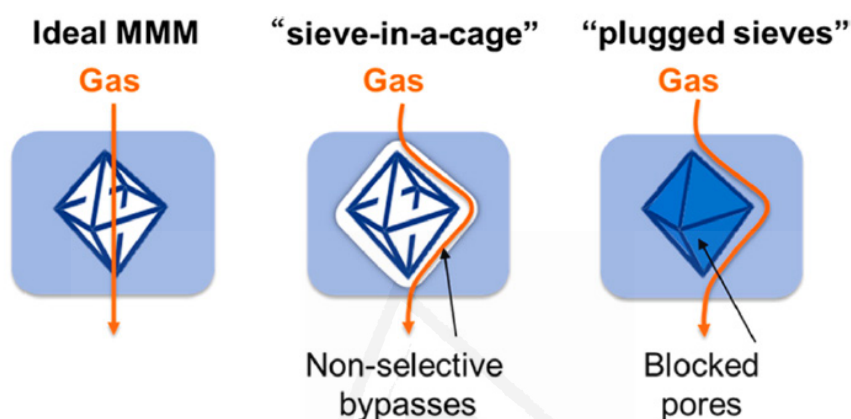


Figure 1.9. Examples of ideal and nonideal MOF-based MMMs²⁰⁹.

The most widely used methods to synthesize MOF-based MMMs are the simple solution, dispersion and casting methods.^{210–212} For example, Urban *et al.* used UiO-66-NH₂ and PSF to obtain MMMs (50 wt.% MOF) with a remarkable selectivity for CO₂ compared to CH₄ and N₂.²¹³ It was reported the differences between MIL-53(Al) and MIL-53(Al)-NH₂ PVDF-based membranes by monitoring their selectivity toward gas combination of He/CH₄ and CO₂/CH₄ which was preferential to He over CH₄ and CO₂ over CH₄ in MIL-53(Al)-NH₂ based composite.²¹⁴ In the last decade there is a high number of publications for MOF-based MMMs, such as PVDF/(UiO-66, UiO-66-NH₂, MIL-53, MIL-101, HKUST-1 and ZIF-8) obtaining a potential application for several separations of gas.²¹²

1.7. General objectives of the thesis project

Taking into consideration the general contextualization described through in chapter 1, this Doctoral Thesis is devoted to exploring the adsorption phenomena in several metal-organic frameworks (MOFs) starting from small gas molecules such as CO₂, O₂ or CH₄ and continuing with the study of more complex ones such as brimonidine tartrate and finally, the effect of the incorporation of MOFs nanoparticles into composite materials. The research includes the study of the external parameters affecting the adsorption process, but also the intraframework characteristics taking place during the uptake process.

With the aim to open the gate towards novel applications of this new group of crystalline porous materials (for instance in research fields such as biomedical applications or gas separation), we develop a synergy between experimental techniques and molecular simulations to elucidate and understand the gas and liquid adsorption phenomena in different MOFs. Based on this, the main objectives proposed for each chapter can be summarized as follow:

2. The flexibility in ZIF-4 is new phenomena not complete explored and understood. Based on this, *Chapter 3* aims to ascertain the nature of these structural changes in ZIF-4 upon gas adsorption by combining synchrotron X-ray diffraction and inelastic neutron scattering studies under operando conditions, and molecular simulation studies.
3. *Chapter 4* is aimed to describe and understand the adsorption phenomena of different molecules such as nitrogen and oxygen in mixed linker ZIF-62 and their structural modifications as a result of guest stimuli. Besides, using molecular simulation, we elucidate the porous accessibility to the cavities of this mixed-linker ZIF.
4. Taking into account the excellent characteristics of ZIFs and the associated structural changes, the main goal *chapter 5* is the evaluation of the performance of two flexible ZIFs, i.e. ZIF-7 and ZIF-4, in the adsorption/delivery of NO under different experimental conditions. The amount of NO adsorbed and the delivery

characteristics under different temperature and dosing conditions will be thoroughly evaluated.

5. The main goal of *chapter 6* is the evaluation of several MOFs in the adsorption and release of brimonidine for glaucoma treatment, the evaluation of their structural stability in the charging/discharging media and, last but not least, the evaluation of the cytotoxicity of the different components (bulk MOF, linker and metallic precursors) in retinal photoreceptor culture cells (661W).
6. *Chapter 7* main goal is to describe an optimal synthesis of functional MOF-based polyurethane thin films and to evaluate the performance of these UiO-67@PU nanocomposites for brimonidine adsorption/release in liquid phase. The successful development of these functional materials (MOF@polymer) will open the gate towards the application of these devices in a number of ocular disorders that require a controlled and prolonged release of drugs, from glaucoma treatment to post-surgical treatments by anti-inflammatory drugs.

6.1. References

1. Desjonquères, M.-C. & Spanjaard, D. Adsorption Phenomena. in *Concepts in Surface Physics* 411–538 (Springer Berlin Heidelberg, 1996). doi:10.1007/978-3-642-61400-2_6
2. Ali, I. & Gupta, V. K. Advances in water treatment by adsorption technology. *Nat. Protoc.* **1**, 2661–2667 (2006).
3. Sayilgan, Ş. Ç., Mobedi, M. & Ülkü, S. Effect of regeneration temperature on adsorption equilibria and mass diffusivity of zeolite 13x-water pair. *Microporous Mesoporous Mater.* **224**, 9–16 (2016).
4. Bonilla-Petriciolet, A., Mendoza-Castillo, D. I. & Reynel-Ávila, H. E. Introduction. in *Adsorption Processes for Water Treatment and Purification* 1–18 (Springer International Publishing, 2017). doi:10.1007/978-3-319-58136-1_1
5. Yang, R. T. Introductory Remarks. in *Adsorbents: Fundamentals and*

- Applications 1–7* (John Wiley & Sons, Inc.). doi:10.1002/047144409X.ch1
6. Çeçen, F. & Aktaş, Ö. Water and Wastewater Treatment: Historical Perspective of Activated Carbon Adsorption and its Integration with Biological Processes. in *Activated Carbon for Water and Wastewater Treatment 1–11* (Wiley-VCH Verlag GmbH & Co. KGaA, 2011). doi:10.1002/9783527639441.ch1
 7. Ibach, H. Physics of Surfaces and Interfaces. in *Physics of Surfaces and Interfaces 245–303* (Springer Berlin Heidelberg, 2006). doi:10.1007/3-540-34710-0
 8. Lüth, H. Adsorption and Solid Surfaces. in *Surfaces and Interfaces of Solids 429–464* (Springer Berlin Heidelberg, 1993). doi:10.1007/978-3-662-10159-9
 9. Muscat, J. P. & News, D. M. Chemisorption on metals. *Prog. Surf. Sci.* **9**, 1–43 (1978).
 10. Yang, R. T. Introductory Remarks. in *Gas Separation by Adsorption Processes 1–8* (Elsevier, 1987). doi:10.1016/B978-0-409-90004-0.50004-0
 11. Day, R. E. & Parfitt, G. D. Factors involved in adsorption at the solid/liquid interface. *Powder Technol.* **1**, 3–10 (1967).
 12. Bansal, R. C. & Goyal, M. Activated Carbon and Its Surface Structure. in *Activated Carbon Adsorption 1–60* (CRC Press, 2005). doi:10.1201/9781420028812
 13. Dias, J. M., Alvim-Ferraz, M. C. M., Almeida, M. F., Rivera-Utrilla, J. & Sánchez-Polo, M. Waste materials for activated carbon preparation and its use in aqueous-phase treatment: A review. *J. Environ. Manage.* **85**, 833–846 (2007).
 14. Mohan, D. & Singh, K. P. Single- and multi-component adsorption of cadmium and zinc using activated carbon derived from bagasse—an agricultural waste. *Water Res.* **36**, 2304–2318 (2002).
 15. Chiang, Y.-C., Chiang, P.-C. & Huang, C.-P. Effects of pore structure and

- temperature on VOC adsorption on activated carbon. *Carbon N. Y.* **39**, 523–534 (2001).
16. Ao, C. H. & Lee, S. C. Indoor air purification by photocatalyst TiO₂ immobilized on an activated carbon filter installed in an air cleaner. *Chem. Eng. Sci.* **60**, 103–109 (2005).
 17. Rege, S. U., T. Yang, R. & Buzanowski, M. A. Sorbents for air prepurification in air separation. *Chem. Eng. Sci.* **55**, 4827–4838 (2000).
 18. Sircar, S., Golden, T. C. & Rao, M. B. Activated carbon for gas separation and storage. *Carbon N. Y.* **34**, 1–12 (1996).
 19. Welch, C. J. *et al.* Adsorbent Screening for Metal Impurity Removal in Pharmaceutical Process Research. *Org. Process Res. Dev.* **9**, 198–205 (2005).
 20. Xie, Z. & Su, B.-L. Crystalline porous materials: from zeolites to metal-organic frameworks (MOFs). *Front. Chem. Sci. Eng.* **14**, 123–126 (2020).
 21. Maesen, T. & Marcus, B. Chapter 1 The zeolite scene—An overview. in *Introduction to Zeolite Science and Practice* 1–9 (2001). doi:10.1016/S0167-2991(01)80242-1
 22. First, E. L., Hasan, M. M. F. & Floudas, C. A. Discovery of novel zeolites for natural gas purification through combined material screening and process optimization. *AIChE J.* **60**, 1767–1785 (2014).
 23. Aguilar-Armenta, G. *et al.* Adsorption Kinetics of CO₂, O₂, N₂, and CH₄ in Cation-Exchanged Clinoptilolite. *J. Phys. Chem. B* **105**, 1313–1319 (2001).
 24. Rege, S. U. & Yang, R. T. Limits for Air Separation by Adsorption with LiX Zeolite. *Ind. Eng. Chem. Res.* **36**, 5358–5365 (1997).
 25. Yang, R. T., Hernández-Maldonado, A. J. & Yang, F. H. Desulfurization of Transportation Fuels with Zeolites Under Ambient Conditions. *Science (80-)*. **301**, 79 LP – 81 (2003).
 26. Hernández-Maldonado, A. J., Yang, F. H., Qi, G. & Yang, R. T.

- Desulfurization of transportation fuels by π -complexation sorbents: Cu(I)-, Ni(II)-, and Zn(II)-zeolites. *Appl. Catal. B Environ.* **56**, 111–126 (2005).
27. Dong, J., Lin, Y. S. & Liu, W. Multicomponent hydrogen/hydrocarbon separation by MFI-type zeolite membranes. *AIChE J.* **46**, 1957–1966 (2000).
28. Suckow, M., Lutz, W., Kornatowski, J., Rozwadowski, M. & Wark, M. Calculation of the hydrothermal long-term stability of zeolites in gas-desulphurization and gas-drying processes. *Gas Sep. Purif.* **6**, 101–108 (1992).
29. Mumpton, F. A. La roca magica: uses of natural zeolites in agriculture and industry. *Proc. Natl. Acad. Sci. U. S. A.* **96**, 3463–70 (1999).
30. Firling, C. E., Evans, G. L., Wakley, G. K., Sibonga, J. & Turner, R. T. Lack of an effect of sodium zeolite A on rat tibia histomorphometry. *J. Bone Miner. Res.* **11**, 254–263 (2009).
31. Zavareh, S., Farrokhzad, Z. & Darvishi, F. Modification of zeolite 4A for use as an adsorbent for glyphosate and as an antibacterial agent for water. *Ecotoxicol. Environ. Saf.* **155**, 1–8 (2018).
32. Pavelić, K. *et al.* Natural zeolite clinoptilolite: new adjuvant in anticancer therapy. *J. Mol. Med.* **78**, 708–720 (2001).
33. Uglea, C. V. *et al.* Drug delivery systems based on inorganic materials: I. Synthesis and characterization of a zeolite-cyclophosphamide system. *J. Biomater. Sci. Polym. Ed.* **6**, 633–637 (1995).
34. Corma, A., García, H. & Llabrés i Xamena, F. X. Engineering Metal Organic Frameworks for Heterogeneous Catalysis. *Chem. Rev.* **110**, 4606–4655 (2010).
35. Rowsell, J. L. C. & Yaghi, O. M. Metal-organic frameworks: A new class of porous materials. *Microporous Mesoporous Mater.* **73**, 3–14 (2004).
36. Llabrés i Xamena, F. X. & Gascon, J. CHAPTER 1. Introduction. in *Metal Organic Frameworks as Heterogeneous Catalysts* 1–5 (2001).
doi:10.1039/9781849737586-00001

37. Zhou, H.-C., Long, J. R. & Yaghi, O. M. Introduction to Metal–Organic Frameworks. *Chem. Rev.* **112**, 673–674 (2012).
38. Hoskins, B. F. & Robson, R. Design and construction of a new class of scaffolding-like materials comprising infinite polymeric frameworks of 3D-linked molecular rods. A reappraisal of the zinc cyanide and cadmium cyanide structures and the synthesis and structure of the diamond-rela. *J. Am. Chem. Soc.* **112**, 1546–1554 (1990).
39. Yaghi, O. M. & Li, G. Mutually Interpenetrating Sheets and Channels in the Extended Structure of [Cu(4,4'-bpy)Cl]. *Angew. Chemie Int. Ed. English* **34**, 207–209 (1995).
40. Yaghi, O. M. *et al.* Reticular synthesis and the design of new materials. *Nature* **423**, 705–714 (2003).
41. Chui, S. S.-Y., Lo, S. M.-F., Charmant, J. P. H., Orpen, A. G. & Williams, I. D. A Chemically Functionalizable Nanoporous Material [Cu₃(TMA)₂(H₂O)₃]_n. *Science (80-.)*. **283**, 1148 LP – 1150 (1999).
42. Kandiah, M. *et al.* Synthesis and Stability of Tagged UiO-66 Zr-MOFs. *Chem. Mater.* **22**, 6632–6640 (2010).
43. Katz, M. J. *et al.* A facile synthesis of UiO-66, UiO-67 and their derivatives. *Chem. Commun.* **49**, 9449 (2013).
44. Eubank, J. F. *et al.* Porous, rigid metal(III)-carboxylate metal-organic frameworks for the delivery of nitric oxide. *APL Mater.* **2**, 124112 (2014).
45. Biswas, S. & Van Der Voort, P. A General Strategy for the Synthesis of Functionalised UiO-66 Frameworks: Characterisation, Stability and CO₂ Adsorption Properties. *Eur. J. Inorg. Chem.* **2013**, 2154–2160 (2013).
46. DeCoste, J. B. *et al.* Stability and degradation mechanisms of metal–organic frameworks containing the Zr₆O₄(OH)₄ secondary building unit. *J. Mater. Chem. A* **1**, 5642 (2013).
47. Wu, H., Yildirim, T. & Zhou, W. Exceptional Mechanical Stability of Highly Porous Zirconium Metal–Organic Framework UiO-66 and Its Important

- Implications. *J. Phys. Chem. Lett.* **4**, 925–930 (2013).
48. Wang, D. & Li, Z. Iron-based metal–organic frameworks (MOFs) for visible-light-induced photocatalysis. *Res. Chem. Intermed.* **43**, 5169–5186 (2017).
49. Liu, X. *et al.* Iron Containing Metal–Organic Frameworks: Structure, Synthesis, and Applications in Environmental Remediation. *ACS Appl. Mater. Interfaces* **9**, 20255–20275 (2017).
50. Horcajada, P. *et al.* Synthesis and catalytic properties of MIL-100(Fe), an iron(II) carboxylate with large pores. *Chem. Commun.* 2820–2822 (2007). doi:10.1039/B704325B
51. Banerjee, R. *et al.* High-Throughput Synthesis of Zeolitic Imidazolate Frameworks and Application to CO₂ Capture. *Science (80-.)*. **319**, 939–943 (2008).
52. Park, K. S. *et al.* Exceptional chemical and thermal stability of zeolitic imidazolate frameworks. *Proc. Natl. Acad. Sci. U. S. A.* **103**, 10186–91 (2006).
53. Wang, B., Côté, A. P., Furukawa, H., O’Keeffe, M. & Yaghi, O. M. Colossal cages in zeolitic imidazolate frameworks as selective carbon dioxide reservoirs. *Nature* **453**, 207–211 (2008).
54. Stock, N. & Biswas, S. Synthesis of Metal-Organic Frameworks (MOFs): Routes to various MOF topologies, morphologies, and composites. *Chem. Rev.* **112**, 933–969 (2012).
55. Rabenau, A. The Role of Hydrothermal Synthesis in Preparative Chemistry. *Angew. Chemie Int. Ed. English* **24**, 1026–1040 (1985).
56. Biemmi, E., Christian, S., Stock, N. & Bein, T. High-throughput screening of synthesis parameters in the formation of the metal-organic frameworks MOF-5 and HKUST-1. *Microporous Mesoporous Mater.* **117**, 111–117 (2009).
57. Küsgens, P. *et al.* Characterization of metal-organic frameworks by water adsorption. *Microporous Mesoporous Mater.* **120**, 325–330 (2009).

58. Garibay, S. J. & Cohen, S. M. Isoreticular synthesis and modification of frameworks with the UiO-66 topology. *Chem. Commun.* **46**, 7700 (2010).
59. Zhu, X. *et al.* Effective Adsorption and Enhanced Removal of Organophosphorus Pesticides from Aqueous Solution by Zr-Based MOFs of UiO-67. *ACS Appl. Mater. Interfaces* **7**, 223–231 (2015).
60. Kappe, P. D. C. O., Dallinger, D. D. & Murphree, P. S. S. Microwave Synthesis - An Introduction. in *Practical Microwave Synthesis for Organic Chemists* 1–9 (Wiley-VCH Verlag GmbH & Co. KGaA, 2008). doi:10.1002/9783527623907.ch1
61. Oliver Kappe, C. Microwave dielectric heating in synthetic organic chemistry. *Chem. Soc. Rev.* **37**, 1127 (2008).
62. Cundy, C. S. & Cox, P. A. The Hydrothermal Synthesis of Zeolites: History and Development from the Earliest Days to the Present Time. *Chem. Rev.* **103**, 663–702 (2003).
63. Seo, Y.-K. *et al.* Microwave synthesis of hybrid inorganic–organic materials including porous Cu₃(BTC)₂ from Cu(II)-trimesate mixture. *Microporous Mesoporous Mater.* **119**, 331–337 (2009).
64. Kappe, C. O. Controlled Microwave Heating in Modern Organic Synthesis. *Angew. Chemie Int. Ed.* **43**, 6250–6284 (2004).
65. Jhung, S. H., Lee, J. H. & Chang, J. S. Microwave Synthesis of a Nanoporous Hybrid Material, Chromium Trimesate. *Bull. Korean Chem. Soc.* **26**, 880–881 (2005).
66. Choi, J. Y. *et al.* Microwave Synthesis of a Porous Metal-Organic Framework, Zinc Terephthalate MOF-5. *Bull. Korean Chem. Soc.* **27**, 1523–1524 (2006).
67. Ni, Z. & Masel, R. I. Rapid Production of Metal–Organic Frameworks via Microwave-Assisted Solvothermal Synthesis. *J. Am. Chem. Soc.* **128**, 12394–12395 (2006).
68. Ameloot, R. *et al.* Patterned Growth of Metal-Organic Framework Coatings

- by Electrochemical Synthesis. *Chem. Mater.* **21**, 2580–2582 (2009).
69. Müller, U. *et al.* Method for Electrochemical Production of a Crystalline Porous Metal Organic Skeleton Material, Patent WO/2005/049892. (2005).
70. Taddei, M., Steitz, D. A., van Bokhoven, J. A. & Ranocchiari, M. Continuous-Flow Microwave Synthesis of Metal-Organic Frameworks: A Highly Efficient Method for Large-Scale Production. *Chem. - A Eur. J.* **22**, 3245–3249 (2016).
71. Boldyrev, V. V & Tkáčová, K. Mechanochemistry of Solids: Past, Present, and Prospects. *J. Mater. Synth. Process.* **8**, 121–132 (2000).
72. Kaupp, G. Mechanochemistry: the varied applications of mechanical bond-breaking. *CrystEngComm* **11**, 388–403 (2009).
73. Garay, A. L., Pichon, A. & James, S. L. Solvent-free synthesis of metal complexes. *Chem. Soc. Rev.* **36**, 846 (2007).
74. Boldyrev, V. V. Mechanochemistry and mechanical activation of solids. *Solid State Ionics* **63–65**, 537–543 (1993).
75. Stolle, A., Szuppa, T., Leonhardt, S. E. S. & Ondruschka, B. Ball milling in organic synthesis: solutions and challenges. *Chem. Soc. Rev.* **40**, 2317 (2011).
76. Friščić, T. New opportunities for materials synthesis using mechanochemistry. *J. Mater. Chem.* **20**, 7599 (2010).
77. James, S. L. *et al.* Mechanochemistry: opportunities for new and cleaner synthesis. *Chem. Soc. Rev.* **41**, 413–447 (2012).
78. Braga, D. & Grepioni, F. Making crystals from crystals: a green route to crystal engineering and polymorphism. *Chem. Commun.* 3635 (2005). doi:10.1039/b504668h
79. Pichon, A., Lazuen-Garay, A. & James, S. L. Solvent-free synthesis of a microporous metal–organic framework. *CrystEngComm* **8**, 211 (2006).
80. Bang, J. H. & Suslick, K. S. Applications of Ultrasound to the Synthesis of

- Nanostructured Materials. *Adv. Mater.* **22**, 1039–1059 (2010).
81. Qiu, L.-G. *et al.* Facile synthesis of nanocrystals of a microporous metal–organic framework by an ultrasonic method and selective sensing of organoamines. *Chem. Commun.* 3642 (2008). doi:10.1039/b804126a
 82. Rungtaweivoranit, B., Diercks, C. S., Kalmutzki, M. J. & Yaghi, O. M. Spiers Memorial Lecture: : Progress and prospects of reticular chemistry. *Faraday Discuss.* **201**, 9–45 (2017).
 83. van den Berg, A. W. C. & Areán, C. O. Materials for hydrogen storage: current research trends and perspectives. *Chem. Commun.* 668–681 (2008). doi:10.1039/B712576N
 84. Bhatia, S. K. & Myers, A. L. Optimum Conditions for Adsorptive Storage. *Langmuir* **22**, 1688–1700 (2006).
 85. Gygi, D. *et al.* Hydrogen Storage in the Expanded Pore Metal–Organic Frameworks M₂(dobpdc) (M = Mg, Mn, Fe, Co, Ni, Zn). *Chem. Mater.* **28**, 1128–1138 (2016).
 86. Suh, M. P., Park, H. J., Prasad, T. K. & Lim, D.-W. Hydrogen Storage in Metal–Organic Frameworks. *Chem. Rev.* **112**, 782–835 (2012).
 87. Orimo, S., Nakamori, Y., Eliseo, J. R., Züttel, A. & Jensen, C. M. Complex Hydrides for Hydrogen Storage. *Chem. Rev.* **107**, 4111–4132 (2007).
 88. Rosi, N. L. *et al.* Hydrogen Storage in Microporous Metal–Organic Frameworks. *Science (80-.)*. **300**, 1127 LP – 1129 (2003).
 89. Zhao, D., Yuan, D. & Zhou, H.-C. The current status of hydrogen storage in metal–organic frameworks. *Energy Environ. Sci.* **1**, 222 (2008).
 90. Armor, J. N. Emerging importance of shale gas to both the energy & chemicals landscape. *J. Energy Chem.* **22**, 21–26 (2013).
 91. Li, H. *et al.* Recent advances in gas storage and separation using metal–organic frameworks. *Mater. Today* **21**, 108–121 (2018).
 92. He, Y., Zhou, W., Qian, G. & Chen, B. Methane storage in metal–organic

- frameworks. *Chem. Soc. Rev.* **43**, 5657–5678 (2014).
93. Celzard, A. & Fierro, V. Preparing a Suitable Material Designed for Methane Storage: A Comprehensive Report. *Energy & Fuels* **19**, 573–583 (2005).
94. Mason, J. A., Veenstra, M. & Long, J. R. Evaluating metal–organic frameworks for natural gas storage. *Chem. Sci.* **5**, 32–51 (2014).
95. Kondo, M., Yoshitomi, T., Matsuzaka, H., Kitagawa, S. & Seki, K. Three-Dimensional Framework with Channeling Cavities for Small Molecules: $\{[M_2(4, 4'\text{-bpy})_3(\text{NO}_3)_4] \cdot x\text{H}_2\text{O}\}_n$ (M = Co, Ni, Zn). *Angew. Chemie Int. Ed. English* **36**, 1725–1727 (1997).
96. Seki, K. Design of an adsorbent with an ideal pore structure for methane adsorption using metal complexes. *Chem. Commun.* 1496–1497 (2001). doi:10.1039/b104204c
97. Seki, K., Takamizawa, S. & Mori, W. Design and Gas Adsorption Property of a Three-Dimensional Coordination Polymer with a Stable and Highly Porous Framework. *Chem. Lett.* **30**, 332–333 (2001).
98. Seki, K. & Mori, W. Syntheses and Characterization of Microporous Coordination Polymers with Open Frameworks. *J. Phys. Chem. B* **106**, 1380–1385 (2002).
99. Wang, H., Getzschmann, J., Senkovska, I. & Kaskel, S. Structural transformation and high pressure methane adsorption of $\text{Co}_2(1,4\text{-bdc})_2\text{dabco}$. *Microporous Mesoporous Mater.* **116**, 653–657 (2008).
100. Wu, H., Zhou, W. & Yildirim, T. High-Capacity Methane Storage in Metal–Organic Frameworks $M_2(\text{dhtp})$: The Important Role of Open Metal Sites. *J. Am. Chem. Soc.* **131**, 4995–5000 (2009).
101. Zhou, W., Wu, H. & Yildirim, T. Enhanced H_2 Adsorption in Isostructural Metal–Organic Frameworks with Open Metal Sites: Strong Dependence of the Binding Strength on Metal Ions. *J. Am. Chem. Soc.* **130**, 15268–15269 (2008).
102. Farla, J. C. M., Hendriks, C. A. & Blok, K. Carbon dioxide recovery from

- industrial processes. *Clim. Change* **29**, 439–461 (1995).
103. Dion, L.-M., Lefsrud, M. & Orsat, V. Review of CO₂ recovery methods from the exhaust gas of biomass heating systems for safe enrichment in greenhouses. *Biomass and Bioenergy* **35**, 3422–3432 (2011).
104. Trickett, C. A. *et al.* The chemistry of metal–organic frameworks for CO₂ capture, regeneration and conversion. *Nat. Rev. Mater.* **2**, 17045 (2017).
105. Bao, Z., Yu, L., Ren, Q., Lu, X. & Deng, S. Adsorption of CO₂ and CH₄ on a magnesium-based metal organic framework. *J. Colloid Interface Sci.* **353**, 549–556 (2011).
106. Sumida, K. *et al.* Carbon Dioxide Capture in Metal–Organic Frameworks. *Chem. Rev.* **112**, 724–781 (2012).
107. Hashim, S. S., Mohamed, A. R. & Bhatia, S. Oxygen separation from air using ceramic-based membrane technology for sustainable fuel production and power generation. *Renew. Sustain. Energy Rev.* **15**, 1284–1293 (2011).
108. Leo, A., Liu, S. & Costa, J. C. D. da. Development of mixed conducting membranes for clean coal energy delivery. *Int. J. Greenh. Gas Control* **3**, 357–367 (2009).
109. Smith, A. . & Klosek, J. A review of air separation technologies and their integration with energy conversion processes. *Fuel Process. Technol.* **70**, 115–134 (2001).
110. Ma, S., Wang, X.-S., Collier, C. D., Manis, E. S. & Zhou, H.-C. Ultramicroporous Metal–Organic Framework Based on 9,10-Anthracenedicarboxylate for Selective Gas Adsorption. *Inorg. Chem.* **46**, 8499–8501 (2007).
111. Dincă, M. & Long, J. R. Strong H₂ Binding and Selective Gas Adsorption within the Microporous Coordination Solid Mg₃(O₂C-C₁₀H₆-CO₂)₃. *J. Am. Chem. Soc.* **127**, 9376–9377 (2005).
112. Ma, S., Wang, X.-S., Yuan, D. & Zhou, H.-C. A Coordinatively Linked Yb Metal–Organic Framework Demonstrates High Thermal Stability and

- Uncommon Gas-Adsorption Selectivity. *Angew. Chemie Int. Ed.* **47**, 4130–4133 (2008).
113. Koshland Jr., D. E. The Molecule of the Year. *Science (80-)*. **258**, 1861 (1992).
114. Lundberg, J. O., Gladwin, M. T. & Weitzberg, E. Strategies to increase nitric oxide signalling in cardiovascular disease. *Nat. Rev. Drug Discov.* **14**, 623–641 (2015).
115. Bogdan, C. Nitric oxide and the immune response. *Nat. Immunol.* **2**, 907–916 (2001).
116. Calabrese, V. *et al.* Nitric oxide in the central nervous system: neuroprotection versus neurotoxicity. *Nat. Rev. Neurosci.* **8**, 766–775 (2007).
117. Chang, J. Y. H. *et al.* Role of nitric oxide in murine conventional outflow physiology. *Am. J. Physiol. Physiol.* **309**, C205–C214 (2015).
118. Radomski, M. W., Palmer, R. M. J. & Moncada, S. The role of nitric oxide and cGMP in platelet adhesion to vascular endothelium. *Biochem. Biophys. Res. Commun.* **148**, 1482–1489 (1987).
119. Vaughn, M. W., Kuo, L. & Liao, J. C. Estimation of nitric oxide production and reaction rates in tissue by use of a mathematical model. *Am. J. Physiol. Circ. Physiol.* **274**, H2163–H2176 (1998).
120. Hambrecht, R., Berra, K. & Calfas, K. J. Managing Your Angina Symptoms With Nitroglycerin. *Circulation* **127**, (2013).
121. Opasich, C., Cioffi, G. & Gualco, A. Nitroprusside in decompensated heart failure: What should a clinician really know? *Curr. Heart Fail. Rep.* **6**, 182–190 (2009).
122. Kaufman, M. B. Pharmaceutical Approval Update. *P T* **43**, 22–60 (2018).
123. Yang, T., Zelikin, A. N. & Chandrawati, R. Progress and Promise of Nitric Oxide-Releasing Platforms. *Adv. Sci.* **5**, 1701043 (2018).

124. Lowe, A., Chittajallu, P., Gong, Q., Li, J. & Balkus, K. J. Storage and delivery of nitric oxide via diazeniumdiolated metal organic framework. *Microporous Mesoporous Mater.* **181**, 17–22 (2013).
125. Bloch, E. D. *et al.* Gradual Release of Strongly Bound Nitric Oxide from Fe₂(NO)₂(dobdc). *J. Am. Chem. Soc.* **137**, 3466–3469 (2015).
126. Xiao, B. *et al.* High-Capacity Hydrogen and Nitric Oxide Adsorption and Storage in a Metal–Organic Framework. *J. Am. Chem. Soc.* **129**, 1203–1209 (2007).
127. Cattaneo, D. *et al.* Water based scale-up of CPO-27 synthesis for nitric oxide delivery. *Dalt. Trans.* **45**, 618–629 (2016).
128. Wu, H., Gong, Q., Olson, D. H. & Li, J. Commensurate Adsorption of Hydrocarbons and Alcohols in Microporous Metal Organic Frameworks. *Chem. Rev.* **112**, 836–868 (2012).
129. He, Y., Zhou, W., Krishna, R. & Chen, B. Microporous metal–organic frameworks for storage and separation of small hydrocarbons. *Chem. Commun.* **48**, 11813 (2012).
130. Banerjee, D., Deibert, B. J., Wang, H. & Li, J. Metal-Organic Frameworks: Adsorption of Hydrocarbons and Alcohols. in *Encyclopedia of Inorganic and Bioinorganic Chemistry* 1–21 (John Wiley & Sons, Ltd, 2014). doi:10.1002/9781119951438.eibc2216
131. Getman, R. B., Bae, Y.-S., Wilmer, C. E. & Snurr, R. Q. Review and Analysis of Molecular Simulations of Methane, Hydrogen, and Acetylene Storage in Metal–Organic Frameworks. *Chem. Rev.* **112**, 703–723 (2012).
132. Konstas, K. *et al.* Methane storage in metal organic frameworks. *J. Mater. Chem.* **22**, 16698 (2012).
133. Herm, Z. R., Bloch, E. D. & Long, J. R. Hydrocarbon Separations in Metal–Organic Frameworks. *Chem. Mater.* **26**, 323–338 (2014).
134. Min Wang, Q. *et al.* Metallo-organic molecular sieve for gas separation and purification. *Microporous Mesoporous Mater.* **55**, 217–230 (2002).

135. Ploegmakers, J., Japip, S. & Nijmeijer, K. Mixed matrix membranes containing MOFs for ethylene/ethane separation—Part B: Effect of Cu₃BTC₂ on membrane transport properties. *J. Memb. Sci.* **428**, 331–340 (2013).
136. Hartmann, M. *et al.* Adsorptive Separation of Isobutene and Isobutane on Cu₃(BTC)₂. *Langmuir* **24**, 8634–8642 (2008).
137. Ferreira, A. F. P. *et al.* Suitability of Cu-BTC extrudates for propane–propylene separation by adsorption processes. *Chem. Eng. J.* **167**, 1–12 (2011).
138. Gücüyener, C., van den Bergh, J., Gascon, J. & Kapteijn, F. Ethane/Ethene Separation Turned on Its Head: Selective Ethane Adsorption on the Metal–Organic Framework ZIF-7 through a Gate-Opening Mechanism. *J. Am. Chem. Soc.* **132**, 17704–17706 (2010).
139. Demessence, A. *et al.* Adsorption properties in high optical quality nanoZIF-8 thin films with tunable thickness. *J. Mater. Chem.* **20**, 7676 (2010).
140. Diestel, L., Bux, H., Wachsmuth, D. & Caro, J. Pervaporation studies of n-hexane, benzene, mesitylene and their mixtures on zeolitic imidazolate framework-8 membranes. *Microporous Mesoporous Mater.* **164**, 288–293 (2012).
141. Peralta, D. *et al.* The separation of xylene isomers by ZIF-8: A demonstration of the extraordinary flexibility of the ZIF-8 framework. *Microporous Mesoporous Mater.* **173**, 1–5 (2013).
142. Soppimath, K. S., Aminabhavi, T. M., Kulkarni, A. R. & Rudzinski, W. E. Biodegradable polymeric nanoparticles as drug delivery devices. *J. Control. Release* **70**, 1–20 (2001).
143. zur Mühlen, A., Schwarz, C. & Mehnert, W. Solid lipid nanoparticles (SLN) for controlled drug delivery – Drug release and release mechanism. *Eur. J. Pharm. Biopharm.* **45**, 149–155 (1998).
144. Liu, M. & Fréchet, J. M. J. Designing dendrimers for drug delivery. *Pharm.*

- Sci. Technolo. Today* **2**, 393–401 (1999).
145. Sharma, A. & Sharma, U. S. Liposomes in drug delivery: Progress and limitations. *Int. J. Pharm.* **154**, 123–140 (1997).
146. Junghanns, J.-U. A. H. & Müller, R. H. Nanocrystal technology, drug delivery and clinical applications. *Int. J. Nanomedicine* **3**, 295–309 (2008).
147. Bianco, A., Kostarelos, K. & Prato, M. Applications of carbon nanotubes in drug delivery. *Curr. Opin. Chem. Biol.* **9**, 674–679 (2005).
148. Fuchigami, T., Kawamura, R., Kitamoto, Y., Nakagawa, M. & Namiki, Y. A magnetically guided anti-cancer drug delivery system using porous FePt capsules. *Biomaterials* **33**, 1682–1687 (2012).
149. Cavallaro, G. *et al.* Drug Delivery Devices Based on Mesoporous Silicate. *Drug Deliv.* **11**, 41–46 (2004).
150. Vallet-Regí, M., Doadrio, J. C., Doadrio, A. L., Izquierdo-Barba, I. & Pérez-Pariente, J. Hexagonal ordered mesoporous material as a matrix for the controlled release of amoxicillin. *Solid State Ionics* **172**, 435–439 (2004).
151. McKinlay, A. C. *et al.* BioMOFs: Metal-Organic Frameworks for Biological and Medical Applications. *Angew. Chemie Int. Ed.* **49**, 6260–6266 (2010).
152. Horcajada, P. *et al.* Metal–Organic Frameworks as Efficient Materials for Drug Delivery. *Angew. Chemie Int. Ed.* **45**, 5974–5978 (2006).
153. Férey, G. Hybrid porous solids: past, present, future. *Chem. Soc. Rev.* **37**, 191–214 (2008).
154. Horcajada, P. *et al.* Porous metal–organic-framework nanoscale carriers as a potential platform for drug delivery and imaging. *Nat. Mater.* **9**, 172–178 (2010).
155. Sun, C.-Y., Qin, C., Wang, X.-L. & Su, Z.-M. Metal-organic frameworks as potential drug delivery systems. *Expert Opin. Drug Deliv.* **10**, 89–101 (2013).
156. Shi, Q., Chen, Z., Song, Z., Li, J. & Dong, J. Synthesis of ZIF-8 and ZIF-67 by Steam-Assisted Conversion and an Investigation of Their Tribological

- Behaviors. *Angew. Chemie Int. Ed.* **50**, 672–675 (2011).
157. Sun, C. *et al.* Zeolitic imidazolate framework-8 as efficient pH-sensitive drug delivery vehicle. *Dalt. Trans.* **41**, 6906 (2012).
158. Gaudana, R., Jwala, J., Boddu, S. H. S. & Mitra, A. K. Recent perspectives in ocular drug delivery. *Pharm. Res.* **26**, 1197–216 (2009).
159. Gaudana, R., Ananthula, H. K., Parenky, A. & Mitra, A. K. Ocular drug delivery. *AAPS J.* **12**, 348–60 (2010).
160. Yellepeddi, V. K. *et al.* Punctal plug: a medical device to treat dry eye syndrome and for sustained drug delivery to the eye. *Drug Discovery Today* (2015). doi:10.1016/j.drudis.2015.01.013
161. Holgado, M. A., Anguiano-Domínguez, A. & Martín-Banderas, L. Contact lenses as drug-delivery systems: a promising therapeutic tool. *Arch. la Soc. Española Oftalmol. (English Ed.)* **95**, 24–33 (2020).
162. Cheng, L. *et al.* Intravitreal properties of porous silicon photonic crystals: a potential self-reporting intraocular drug-delivery vehicle. *Br. J. Ophthalmol.* **92**, 705–711 (2008).
163. McInnes, S. J., Irani, Y., Williams, K. A. & Voelcker, N. H. Controlled drug delivery from composites of nanostructured porous silicon and poly(L-lactide). *Nanomedicine* **7**, 995–1016 (2012).
164. Rawas-Qalaji, M. & Williams, C.-A. Advances in Ocular Drug Delivery. *Curr. Eye Res.* **37**, 345–356 (2012).
165. Kim, S.-N. *et al.* Metal-organic frameworks, NH₂-MIL-88(Fe), as carriers for ophthalmic delivery of brimonidine. *Acta Biomater.* **79**, 344–353 (2018).
166. Chen, H. *et al.* Synergistic Chemotherapy and Photodynamic Therapy of Endophthalmitis Mediated by Zeolitic Imidazolate Framework-Based Drug Delivery Systems. *Small* **15**, 1903880 (2019).
167. Baati, T. *et al.* In depth analysis of the in vivo toxicity of nanoparticles of porous iron(III) metal-organic frameworks. *Chem. Sci.* **4**, 1597 (2013).

168. Sajid, M. Toxicity of nanoscale metal organic frameworks: a perspective. *Environ. Sci. Pollut. Res.* **23**, 14805–14807 (2016).
169. Tamames-Tabar, C. *et al.* Cytotoxicity of nanoscaled metal–organic frameworks. *J. Mater. Chem. B* **2**, 262–271 (2014).
170. Sturluson, A. *et al.* The role of molecular modelling and simulation in the discovery and deployment of metal-organic frameworks for gas storage and separation. *Mol. Simul.* **45**, 1082–1121 (2019).
171. Tijms, H. *Probability: A Lively Introduction*. (Cambridge University Press, 2017). doi:10.1017/9781108291361
172. Shell, M. S. *Thermodynamics and Statistical Mechanics*. (Cambridge University Press, 2015). doi:10.1017/CBO9781139028875
173. Sarkisov, L. Toward Rational Design of Metal–Organic Frameworks for Sensing Applications: Efficient Calculation of Adsorption Characteristics in Zero Loading Regime. *J. Phys. Chem. C* **116**, 3025–3033 (2012).
174. Kim, D., Liu, X. & Lah, M. S. Topology analysis of metal-organic frameworks based on metal-organic polyhedra as secondary or tertiary building units. *Inorganic Chemistry Frontiers* **2**, 336–360 (2015).
175. Furukawa, H., Cordova, K. E., O’Keeffe, M. & Yaghi, O. M. The Chemistry and Applications of Metal-Organic Frameworks. *Science (80-.)*. **341**, 1230444–1230444 (2013).
176. Uemura, K., Matsuda, R. & Kitagawa, S. Flexible microporous coordination polymers. *J. Solid State Chem.* **178**, 2420–2429 (2005).
177. Bureekaew, S., Shimomura, S. & Kitagawa, S. Chemistry and application of flexible porous coordination polymers. *Sci. Technol. Adv. Mater.* **9**, 14108 (2008).
178. Devic, T. *et al.* Functionalization in Flexible Porous Solids: Effects on the Pore Opening and the Host–Guest Interactions. *J. Am. Chem. Soc.* **132**, 1127–1136 (2010).
179. Horike, S., Shimomura, S. & Kitagawa, S. Soft porous crystals. *Nat. Chem.*

- 1, 695–704 (2009).
180. Férey, G. & Serre, C. Large breathing effects in three-dimensional porous hybrid matter: facts, analyses, rules and consequences. *Chem. Soc. Rev.* **38**, 1380 (2009).
181. Mellot-Draznieks, C., Serre, C., Surblé, S., Audebrand, N. & Férey, G. Very Large Swelling in Hybrid Frameworks: A Combined Computational and Powder Diffraction Study. *J. Am. Chem. Soc.* **127**, 16273–16278 (2005).
182. Dybtsev, D. N., Chun, H. & Kim, K. Rigid and Flexible: A Highly Porous Metal–Organic Framework with Unusual Guest-Dependent Dynamic Behavior. *Angew. Chemie Int. Ed.* **43**, 5033–5036 (2004).
183. Klein, N. *et al.* Monitoring adsorption-induced switching by ^{129}Xe NMR spectroscopy in a new metal–organic framework $\text{Ni}_2(2,6\text{-ndc})_2(\text{dabco})$. *Phys. Chem. Chem. Phys.* **12**, 11778 (2010).
184. Klein, N. *et al.* Structural flexibility and intrinsic dynamics in the $\text{M}_2(2,6\text{-ndc})_2(\text{dabco})$ ($\text{M} = \text{Ni}, \text{Cu}, \text{Co}, \text{Zn}$) metal–organic frameworks. *J. Mater. Chem.* **22**, 10303 (2012).
185. Schneemann, A. *et al.* Flexible metal–organic frameworks. *Chem. Soc. Rev.* **43**, 6062–6096 (2014).
186. Murdock, C. R., Hughes, B. C., Lu, Z. & Jenkins, D. M. Approaches for synthesizing breathing MOFs by exploiting dimensional rigidity. *Coord. Chem. Rev.* **258–259**, 119–136 (2014).
187. Fairen-Jimenez, D. *et al.* Opening the Gate: Framework Flexibility in ZIF-8 Explored by Experiments and Simulations. *J. Am. Chem. Soc.* **133**, 8900–8902 (2011).
188. Fairen-Jimenez, D. *et al.* Flexibility and swing effect on the adsorption of energy-related gases on ZIF-8: combined experimental and simulation study. *Dalt. Trans.* **41**, 10752 (2012).
189. Garberoglio, G. & Taioli, S. Modeling flexibility in metal–organic frameworks: Comparison between Density-Functional Tight-Binding and Universal Force

- Field approaches for bonded interactions. *Microporous Mesoporous Mater.* **163**, 215–220 (2012).
190. Kitagawa, S. & Uemura, K. Dynamic porous properties of coordination polymers inspired by hydrogen bonds. *Chem. Soc. Rev.* **34**, 109 (2005).
191. Kitaura, R., Fujimoto, K., Noro, S., Kondo, M. & Kitagawa, S. A Pillared-Layer Coordination Polymer Network Displaying Hysteretic Sorption: [Cu₂(pzdc)₂(dpyg)]_n (pzdc= Pyrazine-2,3-dicarboxylate; dpyg=1,2-Di(4-pyridyl)glycol). *Angew. Chemie Int. Ed.* **41**, 133–135 (2002).
192. Carlucci, L., Ciani, G., Moret, M., Proserpio, D. M. & Rizzato, S. Polymeric Layers Catenated by Ribbons of Rings in a Three-Dimensional Self-Assembled Architecture: A Nanoporous Network with Spongelike Behavior. *Angew. Chemie Int. Ed.* **39**, 1506–1510 (2000).
193. Spencer, E. C. *et al.* Pressure-Induced Bond Rearrangement and Reversible Phase Transformation in a Metal-Organic Framework. *Angew. Chemie Int. Ed.* **53**, 5583–5586 (2014).
194. Gagnon, K. J., Beavers, C. M. & Clearfield, A. MOFs Under Pressure: The Reversible Compression of a Single Crystal. *J. Am. Chem. Soc.* **135**, 1252–1255 (2013).
195. Kitagawa, S., Kitaura, R. & Noro, S. Functional Porous Coordination Polymers. *Angew. Chemie Int. Ed.* **43**, 2334–2375 (2004).
196. Maji, T. K., Matsuda, R. & Kitagawa, S. A flexible interpenetrating coordination framework with a bimodal porous functionality. *Nat. Mater.* **6**, 142–148 (2007).
197. Kanoo, P., Matsuda, R., Higuchi, M., Kitagawa, S. & Maji, T. K. New Interpenetrated Copper Coordination Polymer Frameworks having Porous Properties. *Chem. Mater.* **21**, 5860–5866 (2009).
198. Bureekaew, S. *et al.* Control of Interpenetration for Tuning Structural Flexibility Influences Sorption Properties. *Angew. Chemie Int. Ed.* **49**, 7660–7664 (2010).

199. Mowat, J. P. S. *et al.* A novel structural form of MIL-53 observed for the scandium analogue and its response to temperature variation and CO₂ adsorption. *Dalt. Trans.* **41**, 3937–3941 (2012).
200. Serre, C. *et al.* Very Large Breathing Effect in the First Nanoporous Chromium(III)-Based Solids: MIL-53 or Cr III (OH)·{O₂C–C₆H₄–CO₂}·{HO₂C–C₆H₄–CO₂H}_x·H₂O_y. *J. Am. Chem. Soc.* **124**, 13519–13526 (2002).
201. Millange, F., Serre, C. & Férey, G. Synthesis, structure determination and properties of MIL-53as and MIL-53ht: the first C_{riii} hybrid inorganic–organic microporous solids: C_{riii}(OH)·{O₂C–C₆H₄–CO₂}·{HO₂C–C₆H₄–CO₂H}_x Electronic supplementary information (ESI) available: crystal data, atomic c. *Chem. Commun.* 822–823 (2002). doi:10.1039/b201381a
202. Modrow, A., Zargarani, D., Herges, R. & Stock, N. The first porous MOF with photoswitchable linker molecules. *Dalt. Trans.* **40**, 4217 (2011).
203. Kalaj, M. *et al.* MOF-Polymer Hybrid Materials: From Simple Composites to Tailored Architectures. *Chem. Rev.* acs.chemrev.9b00575 (2020). doi:10.1021/acs.chemrev.9b00575
204. Chung, T.-S., Jiang, L. Y., Li, Y. & Kulprathipanja, S. Mixed matrix membranes (MMMs) comprising organic polymers with dispersed inorganic fillers for gas separation. *Prog. Polym. Sci.* **32**, 483–507 (2007).
205. Bastani, D., Esmaili, N. & Asadollahi, M. Polymeric mixed matrix membranes containing zeolites as a filler for gas separation applications: A review. *J. Ind. Eng. Chem.* **19**, 375–393 (2013).
206. Zimmerman, C. M., Singh, A. & Koros, W. J. Tailoring mixed matrix composite membranes for gas separations. *J. Memb. Sci.* **137**, 145–154 (1997).
207. Semino, R., Moreton, J. C., Ramsahye, N. A., Cohen, S. M. & Maurin, G. Understanding the origins of metal–organic framework/polymer compatibility. *Chem. Sci.* **9**, 315–324 (2018).

208. Katayama, Y., Bentz, K. C. & Cohen, S. M. Defect-Free MOF-Based Mixed-Matrix Membranes Obtained by Corona Cross-Linking. *ACS Appl. Mater. Interfaces* **11**, 13029–13037 (2019).
209. Robeson, L. M., Liu, Q., Freeman, B. D. & Paul, D. R. Comparison of transport properties of rubbery and glassy polymers and the relevance to the upper bound relationship. *J. Memb. Sci.* **476**, 421–431 (2015).
210. Zhang, Y., Feng, X., Yuan, S., Zhou, J. & Wang, B. Challenges and recent advances in MOF–polymer composite membranes for gas separation. *Inorg. Chem. Front.* **3**, 896–909 (2016).
211. Moreton, J. C., Denny, M. S. & Cohen, S. M. High MOF loading in mixed-matrix membranes utilizing styrene/butadiene copolymers. *Chem. Commun.* **52**, 14376–14379 (2016).
212. Denny, M. S. & Cohen, S. M. In Situ Modification of Metal-Organic Frameworks in Mixed-Matrix Membranes. *Angew. Chemie Int. Ed.* **54**, 9029–9032 (2015).
213. Su, N. C. *et al.* Enhanced permeation arising from dual transport pathways in hybrid polymer–MOF membranes. *Energy Environ. Sci.* **9**, 922–931 (2016).
214. Feijani, E. A., Mahdavi, H. & Tavasoli, A. Poly(vinylidene fluoride) based mixed matrix membranes comprising metal organic frameworks for gas separation applications. *Chem. Eng. Res. Des.* **96**, 87–102 (2015).

CHAPTER 2

Experimental Methods and Techniques Description

Chapter 2 describes the methodology and research approach developed in this PhD Thesis, and the different experimental techniques used along with the research project. The fundamental principles of each technique, instrumentation and a general description of potential analysis to be applied in the characterization of MOFs are presented in this Chapter.

2.1. Methodology and research approach

Physicochemical characterization of porous materials is a fundamental step in the understanding of their properties in any given application. Among the different properties, textural details such as specific surface area, pore volume or surface chemistry are highly important to define their final performance. These properties are usually defined by the nature of the raw material and the synthesis approach used.

The techniques most widely applied in the characterization of MOFs for adsorption purposes are X-ray diffraction, scanning electron microscopy, X-ray photoelectron spectroscopy and Nitrogen adsorption isotherms at 77 K, among others. In the present chapter, a general overview of the main techniques applied in the characterization of MOFs (preferentially those applied in this PhD thesis) is described.

2.2. MOFs synthesis

The synthesis of the different MOFs reported in the present PhD thesis was performed using the solvothermal method. As it is shown in **Figure 2.1**, the solvothermal reaction is performed in an autoclave system, made of Teflon, where the mixture of metal salts and linker is transferred. The liner is placed in a metallic autoclaved tightly closed. Generally, once the reaction is completed, the crystals are filtered and washed several times with an appropriate solvent. Finally, an activation procedure is performed to remove the solvent and leave empty cavities. The specific conditions applied for the MOFs synthesized in this PhD thesis are detailed in each individual chapter.

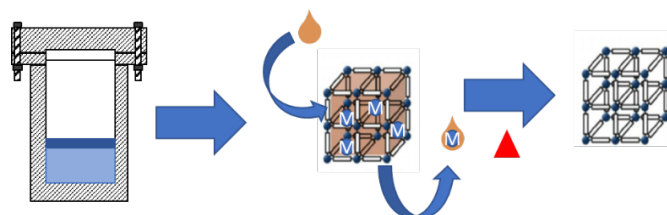


Figure 2.1. Schematic procedure for a MOF synthesis and activation.

2.3. Characterization techniques

2.3.1. X-ray diffraction applied in the characterization of MOFs

X-ray diffraction is a technique based on the diffraction at specific angle of periodic and long-range monochromatic X-ray radiation (generated in an X-ray tube) onto a solid crystalline sample. The X-ray radiation is diffracted according to equation 1 and recorded by a detector and finally condensed as an X-ray diffraction pattern, as it is show in **Figure 2.2(a)**.^{1,2}

$$2d \sin \theta = n\lambda \quad (1)$$

where d is the distance between two layers of diffracting atoms (**Figure 2.2(b)**), θ is the incident angle of the X-ray beam, n is an integer and λ is the wavelength of the X-ray source.

PXRD is a powerful technique to detect crystallographic phases in a sample and, it is essential to evaluate structural changes taking place in a crystallographic system upon an external stimulus. As a result of the exponential development of new metal-organic structures, the necessity of powerful technics to characterize these complex structures is increasing. MOFs are generally crystalline structures that can be determined using X-ray diffraction. However, although this technique is widely used in MOFs characterization, it is important to mention that the structure solution of highly porous materials is not always a straightforward process, i.e. some consideration must be taken to prevent trivial structural elucidation such as, include the presence of occupied pores, disordered solvent molecules or difficulties associated with the growing of quality crystals for diffraction.³

Collected experimental PXRD data are usually compared to a calculated diffraction pattern obtained from a theoretical modelled structure in order to evaluate the purity of the sample. A wide number of published crystals structures (crystallographic information file or CIF format) can be obtained from the Cambridge crystallographic data centre (CCDC).

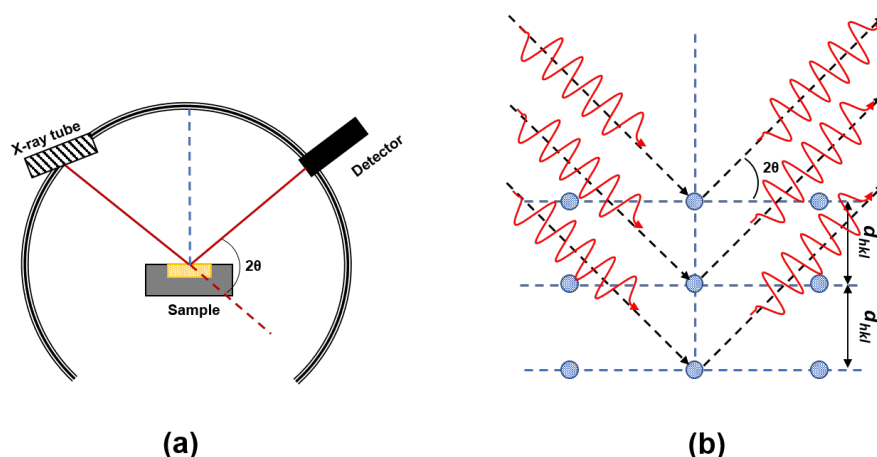


Figure 2.2. (a) Scheme of PXRD technique geometry and (b) scheme of depicting Bragg's law.

If the crystallinity of the MOF obtained is high, and the initial modelled structure is available, the structure of the framework can be refined by the Rietveld method.⁴ However, if the PXRD sensitivity is not enough to perform a structural elucidation, other techniques such as synchrotron X-ray diffraction are still available to this end.

2.3.2. MOFs stability

MOs stability upon gas and liquid adsorption can be directly assessed using PXRD. Depending on the MOF selected, and the adsorbate used, a reaction may occur as a result of the host-guest interactions, especially at the nodes of the MOF crystals. This kind of interactions may lead to a partial or complete collapse of the framework. The collapse is associated with a loss of the periodicity and, therefore, crystallinity, which may be reflected in the PXRD pattern, i.e. a decrease in the intensity or complete disappearance of the diffraction peaks associated with the MOF framework. This feature has been widely reported to assess the stability of MOFs at ambient conditions. For instance, it has been shown that several MOFs adsorb water from the air, and this progressively causes a collapse of the structure or even the transition to a new intermediate crystalline phase. The approach can be extended not only to water but other vapour, liquid or gas adsorbates.^{5,6} It is important to mention that other techniques such as N_2 isotherms at 77 K are

required to complement this analysis, and to quantify the percentage of collapse in these crystalline structures.

2.3.4. Synchrotron light for MOFs characterization

A synchrotron is a cyclic particle accelerator that produces radiation in a beam with continuum wavelengths. At the synchrotron, the electrons are first accelerated with a linear accelerator and further by the booster before being injected into the storage ring where the particles accelerated travels around a fixed closed-loop, thus producing a white beam radiation that is directed to the beamlines (**Figure 2.3**). The white radiation is generated when the accelerated electrons are bent to follow the ring, a process that is assisted by bending magnets. The bending magnets produce a strong electromagnetic field, and then the electron is bent off and electromagnetic radiation is released tangentially to the bending. The bending magnet produces a spray of unfocused electromagnetic waves, including X-rays. To conduct these electromagnetic waves, insertion devices must be placed between magnets in straight distances. Finally, the radiation must be directed through mirrors and windows filtering to discard uninteresting wavelengths and a monochromator which selects electromagnetic radiation with only one energy. The X-ray beam is directed to an experimental hutch where the X-ray passes through the reference detector, the samples and the final detector (which detects the adsorption of the sample).

Synchrotron X-ray diffraction is a high sensitivity technique used in MOFs to elucidate their structure and their performance under non-ambient conditions (i.e. temperature and pressure). Non-ambient conditions allow to observe and elucidate the framework structural changes due to an external stimulus, i.e. after changing temperature or after the introduction of gas molecules. Structural elucidation of gas adsorption induced phase transition (MOFs flexibility) has been widely reported using synchrotron X-ray diffraction.

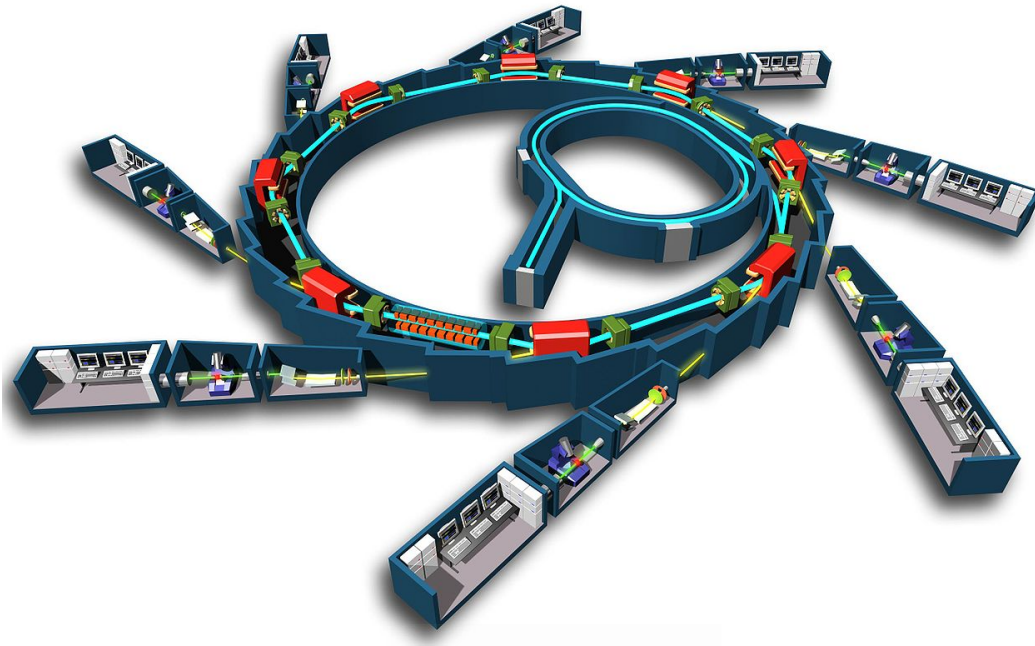


Figure 2.3. Scheme of synchrotron light source facility (SOLEIL, France).⁷

2.3.5. Inelastic neutron scattering

Inelastic neutron scattering (INS) is a technique widely used in material sciences to elucidate the binding of hydrogen atoms in compounds due to its non-invasive behaviour, i.e. they do not change the investigated sample since they do not deposit energy into it.

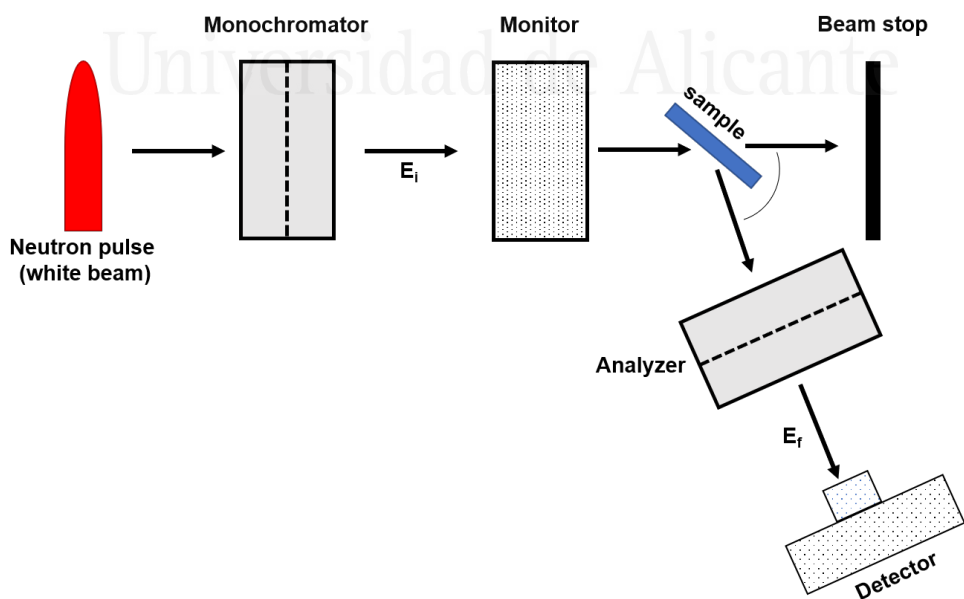


Figure 2.4. Basic scheme of an inelastic neutron scattering experiment.

In the INS experiment, neutrons coming from a fission reactor (U-235 or Pu-239) or spallation source generate a beam that passes through a monochromatization process, collimation, scattering and an energy detection of the scattered neutrons. A crystal analyser (or the time-of-flight method) is required to resolve the energy transfer during the scattering process (**Figure 2.4**).^{8,9}

The process of exchanging energy between the incident neutron beam and the sample produces a shift in energy/wavelength of the exiting neutrons relative to the incident ones. Since the neutron scattering wavelengths vary enormously with the atomic number and are independent of the momentum transfer (Q), detecting the energy shifts of the scattered neutrons much knowledge can be acquired related to the fundamental atomic and molecular motions taking place in materials. In order to have feasible results, it is essential to have fine energy resolutions, i.e. a good quality monochromatization of neutron beam is required or an accurate time-of-flight stamping procedure of the produced neutrons in order to establish the wavelength/energy parameters of the experiment.^{8,9}

INS has been a powerful tool in the characterization of MOFs. A wide number of studies have been published in the literature elucidating structural changes and MOFs flexibility through the energy changes resulted from different hydrogen atoms forming the linkers or the metallic cluster.¹⁰ In the aim of use MOFs as materials for the future to H₂ storage, INS has been a technique very useful to explain the adsorption process of hydrogen in these materials and the mechanism of diffusion and binding to the surface.^{11,12}

2.3.6. X-Ray Photoelectron spectroscopy

X-ray photoelectron spectroscopy (XPS) also known as electron spectroscopy for chemical analysis (ESCA) is the most widely used electron spectroscopy technique for the determination of the elemental composition and/or speciation of the surface (1-10 nm) of any solid substrate. XPS spectrum is obtained when a sample is irradiated by monoenergetic soft X-ray beam and emits photoelectrons from the external surface. The emitted electrons are collected and detected by an electron spectrometer according to their kinetic energy. Generally, the analyser is operated as an energy window, i.e. accepting only those electrons

having an energy within the range of this fixed window. A scanning for different energies is obtained by applying a variable electrostatic field (**Figure 2.5**).^{13,14}

The kinetic energy of the emitted electrons is directly linked to the wavelength of the irradiation source and the binding energy of the electron, which itself depends on the chemical state of the element it originates from.⁵ The determination of surface composition in a solid porous material is a fundamental step in order to elucidate the possible routes of adsorption and the binding mechanism of molecules in the surface. XPS is a powerful tool because it is able to identify almost all the elements (H and He are not detectable due to their extremely low photoelectron cross-sections and the fact that XPs is optimised to analyse core electrons).¹³

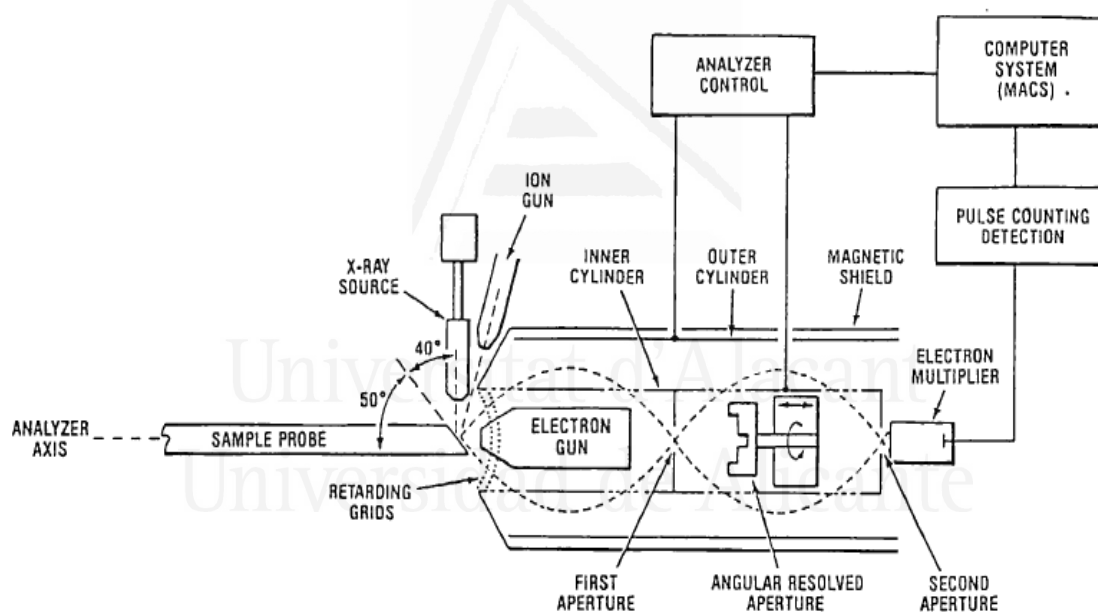


Figure 2.5. Schematic representation of an XPS equipment.¹⁴

XPS is a fundamental tool for the initial characterization of MOFs. It provides important information about the composition, the oxidation states of the elements and the ratio between them.¹⁵ But also it is an important tool to monitor any change in the chemistry of the structure of the MOF as result of adsorption of molecules and by consequence to elucidate its stability.

2.3.7. Scanning electron microscopy

Scanning electron microscopy (SEM) is a high-resolution imaging technique based on the use of an electron beam on a sample to study the external morphology. In a typical SEM equipment, electrons are generated from a heated tungsten wire in an electron gun and accelerated down to the column in high vacuum conditions. Accelerated electrons (typically of 0-30 kV) in the beam produce a vast amount of kinetic energy which is transferred into signals after interacting with the sample. Condenser lens, apertures, and objective lens are used to manipulate the size and the focus of the electron beam.

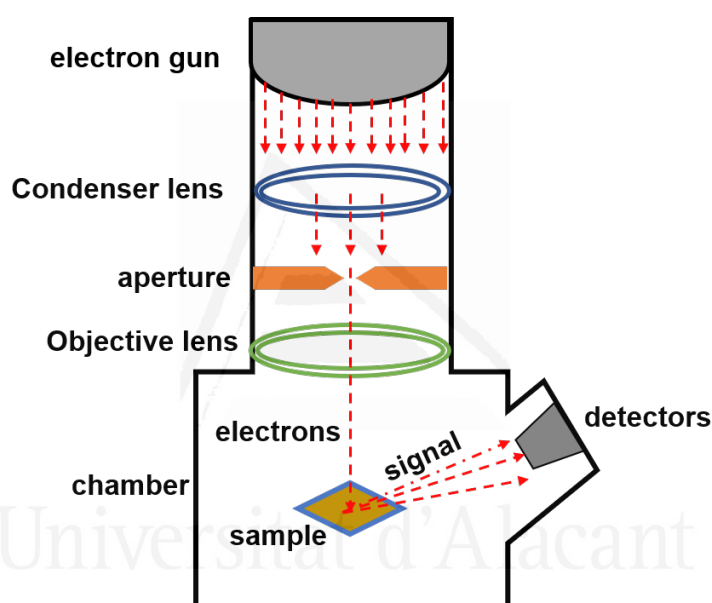


Figure 2.6. Diagram of a typical SEM experimental geometry.

SEM images are produced by the detection of the electron backscattered and secondary electrons resulted from the inelastic interaction between the electron beam and the sample (**Figure 2.6**).

SEM is commonly used to observe the morphology, and to evaluate the phase purity based on the morphology of MOF particles.¹⁶

2.3.8. Thermogravimetric analysis

Thermogravimetric analysis (TGA) monitor the weight change of a sample when it is heated up. The versatility of this analysis allows us to perform a variety of

experiments, including experiments in single or mixed gas streams, heating controlled rates, and analysis of gas species that evolve from the sample during the experiment. Further analysis of the outcoming gas streams may require additional instrumentation, such as mass spectrometer, gas chromatographer or a FTIR spectrometer. It is important to mention that the experiments are performed with a minimum amount of sample (around 10 mg or less), and different phenomena can be evaluated such as desorption/adsorption, phase transition, oxidative and thermal decomposition, oxidation reactions, and reduction reactions.^{5,17,18}

In MOFs the weight does not show significant changes until the structure starts to decompose generally due to the thermal decomposition of the organic linkers; thereof, the major weight losses in the low-temperature range are attributed to the liberation of any guest or entrapped molecules.¹⁹ For instance, TGA analysis is routinely carried out to optimize the sample activation conditions. The ratio of metal ion and organic linker can be proposed from TGA results, assuming that the chemical composition of the residue is known.

2.3.9. Gas and liquid adsorption analysis

As it was detailed in the introductory chapter, adsorption processes are usually described as a concentration of gas or liquid molecules (adsorbate) at the surface of a solid material (adsorbent).

In general, gas adsorption analysis is a technique used to determine the porosity and the textural parameters of a target sample. Gas sorption analysis is generally a volumetric technique that relies on the adsorption of a probe gas (i.e. N₂, Ar, CO₂, etc.) on the external and internal surface of a solid material. The quantification of the amount of gas adsorbed in the material determined by the change of pressure at certain doses allows calculating parameters such as surface area, pore volume and pore size distribution.²⁰ Different important aspects of the adsorption analysis will be detailed in the following sections.

2.3.9.1. Energy involved in adsorption processes

During an adsorption phenomenon, adsorption interactions can be explained as a balance between intermolecular attractive and repulsive forces, which in a scenario of multicomponent adsorption a high complexity is added to the system since interactions adsorbent-adsorbate and adsorbent-adsorbent must be considered in the adsorption energy calculation. To avoid this scenario most of the attention is given to the adsorption of a single component at the adsorbent-adsorbate interface ²¹.

The forces involved in physisorption phenomena always include a wide range of dispersive forces (attractive in nature) and short-range repulsive forces. These forces do not depend on the nature of the adsorbent or adsorbate. As it was described by London in 1930 the attractive interactions can be described as the electrical moment induced by the rapid fluctuations in electron density in one atom surrounded by others. After using quantum-mechanical perturbation theory, London determined the expression of potential energy (eq. 2) of two isolated atoms separated by a distance (r) ²².

$$\varepsilon_D(r) = -C/r^6 \quad (2)$$

The repulsive interactions are often expressed as equation 3 and they are the result of interpenetration of electron clouds.

$$\varepsilon_R(r) = B/r^{12} \quad (3)$$

Finally, the total potential energy can be represented as a relationship of the thereof mentioned forces (equation 4).

$$\varepsilon(r) = B/r^{12} - C/r^6 \quad (4)$$

2.3.9.2. Mathematical models for physisorption in gas phase processes.

As it was mentioned above, the gas adsorption principles combine the theoretical kinetics and statistical mechanical concepts, and they were described by

scientist such as Brunauer, Emmett and Teller (1938), Dubinin (1966), and Langmuir (1918).

As it is shown in **Figure 2.7**, the gas phase adsorption on the internal surface of a porous material is generally described by two models: monolayer adsorption, as the Langmuir model, and multilayer BET model. Langmuir model is the simplest one, and it assumes that only one layer of molecules is adsorbed on the surface ²³. The second mentioned model is a multilayer adsorption model, that results from the Langmuir model after some modifications proposed by Brunauer *et al.* This model considers the effect of a second layer adsorbed as well as third and overlying layers ²⁴. A wide number of modifications of these models have been developed to describe more specific adsorption systems, but these two have been the most commonly used to analyse the adsorption phenomena in a porous material.

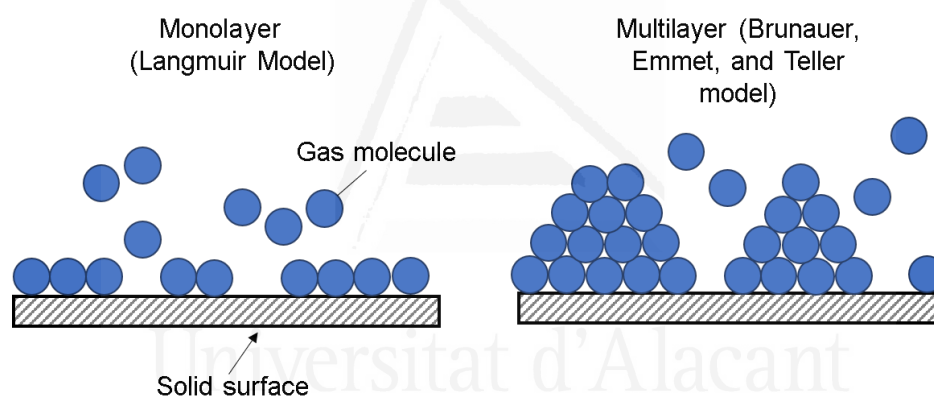


Figure 2.7. Simplified diagram of adsorption mechanisms as proposed by the Langmuir model (left) and Brunauer, Emmett and Teller model (right).

The equation developed by Langmuir describes the relationship between the molecules adsorbed as a monolayer on a solid surface at a given pressure and temperature. This relationship is resumed in equation 5 ²³.

$$\theta = \frac{N}{N_0} = \frac{K \cdot p}{1 + K \cdot p} \quad (5)$$

Where:

θ is the fraction of occupied sites

N is the number of filled sites per area

N_0 is the total number of surface sites per area

K is adsorption equilibrium constant

P is the partial pressure of the adsorbate

Brunauer, Emmett and Teller model (BET) was developed to determine the specific surface area of an adsorbent material. The quantification of specific surface area in porous materials represents a challenge due to the complexity of the surface of these materials combining pores with different shape and size. The model expands the monolayer proposed by the Langmuir model but adding the adsorption of second and subsequent layers. The model allows estimating the monolayer capacity and, by consequence, the specific surface area. Even that BET model was developed considering a flat surface; it is widely used for porous structures obtaining a good estimation of surface area. In the last few years, a different number of refinements in the BET model have been developed, but the basic BET model remains the most commonly used technique for estimation of the specific surface area. The BET model can be resumed as it is shown in equation 6^{24,25}

$$\frac{v}{v_m} = \frac{b \cdot (p/p_s)}{(1-p/p_s)(1-p/p_s + b \cdot p/p_s)} \quad (6)$$

Where:

P_s represents the saturation vapour pressure of the adsorbent

P is the equilibrium pressure of the adsorbate

V is the total volume adsorbed

V_m is the volume of gas adsorbed when the surface is covered by a monolayer

B represents a characteristic constant related to the heat released in the sorption process

2.3.10. Classification of isotherms and pore shape

N_2 and Ar adsorption at cryogenic temperatures are the most widely applied probe molecules to estimate the accessible surface area (N_2 at 77 K and Ar at 87 K). The main reason to use these probe molecules is due to their inert and nontoxic properties, availability in any laboratory, and the possibility to easily maintain the required temperature by the use of liquid nitrogen or argon baths.

The profile of the isotherm is sensitive to the adsorbent material and the probe gas; thereof, the IUPAC recommended classifying the isotherm profiles into six types based on the analysis of a variety of gas/vapour adsorption isotherms.²⁶

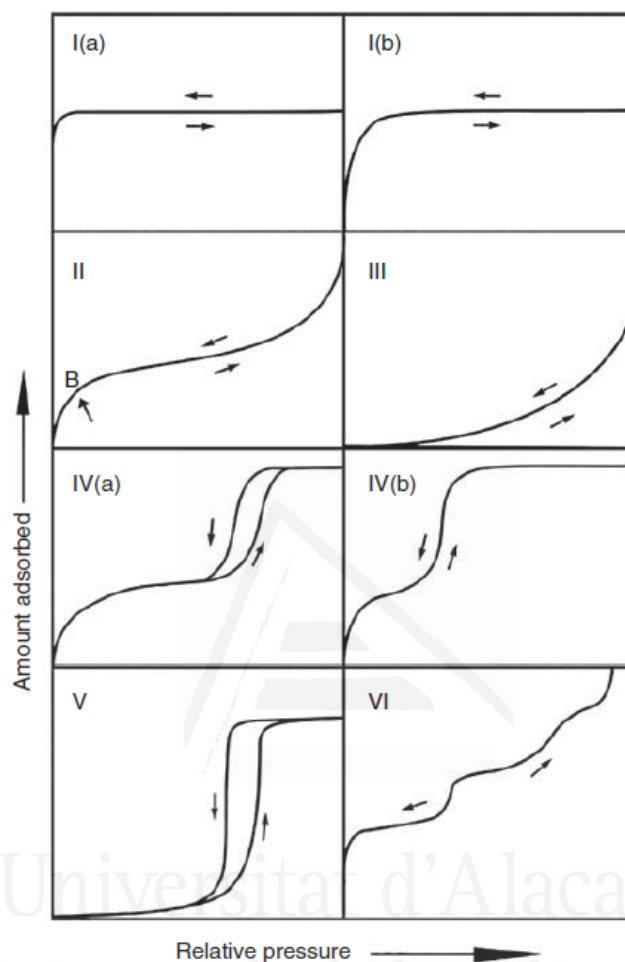


Figure 2.8. IUPAC classification of physisorption isotherms.²⁷

As it is shown in **Figure 2.8**, the isotherm type I is characteristic of microporous materials exhibiting a high uptake step in the low-pressure region due to the strong interactions between adsorbent and adsorbate. Recently, it has been concluded that interactions in narrow micropores play an important role in the filling behaviour at a very low relative pressure (P/P_0) dividing the type I isotherm in two possible scenarios. Type I(a) isotherm is characteristic of microporous materials having mainly narrow micropores of width $< \sim 1$ nm while isotherms type I(B) are found with materials having pore size distribution over a broader range including wider micropores and possibly narrow mesopores ($< \sim 2.5$ nm).²⁷ Type III and V

isotherms result when the gas uptake in the low-pressure range is rather low due to the weak host-guest interactions. When the material contains mesopores, higher pressures are required to promote capillary condensation in these pores, the isotherm obtained is similar to that in type IV, or V. In type IV(a) isotherm occurs when the pore width exceeds a certain critical width, which is dependent on the adsorption system and temperature. With adsorbents having mesopores of smaller widths, completely reversible Type IV(b) isotherms are observed. Isotherm type II and III are also characterized by a gradual increase in the uptake near the saturation pressure due to the interparticle condensation. Finally, stepwise isotherm (type VI) are observed when layer by layer adsorption is observed in the porous material (when using, e.g. krypton as a probe molecule).²⁰

Nitrogen and Argon isotherms can provide information about the textural properties of porous materials, while other probe molecules are used to obtain information about the surface chemistry of the material. For instance, water adsorption isotherms can provide interesting information about the hydrophobicity/hydrophilicity associated with the surface chemistry. Isotherm type III and V are commonly observed in water adsorption as a result of materials with hydrophobic pores.²⁸

The presence of a hysteresis loop in adsorption-desorption isotherm commonly make reference to mesoporous materials, and it provides essential information about the arrangement of the molecules in different zones of the pores, but also about the pore shape. Different loop shapes have been observed in MOFs N₂ isotherms at cryogenic conditions but most of them are produced as a consequence of a different phenomenon called structural flexibility.

In MOFs, the use of gas adsorption analysis can provide valuable information about the porous structure (size, shape and type of pores), structural stability, the presence of structural alterations (flexibility) upon adsorption, and the strength of the adsorption process.

2.3.11. Liquid phase isotherms and mathematical models

Adsorption in a liquid phase is a fundamental step in a high number of industrial processes. Generally, liquid-phase adsorption refers to the separation of dissolved molecules from liquid effluents due to their toxicity or to the necessity to obtain pure liquid streams. Mathematical models for liquid-phase adsorption provide the relationship between the mass of the adsorbed solute per mass of adsorbent and the concentration of the solute in the solution when the adsorption equilibrium has been reached. Different models have been developed to explain the phenomena involved in the adsorption of molecules in liquid phase into the surface of a solid porous material. Some of the most used ones are Langmuir model, Freundlich model and Pausnitz-Radke ²⁹.

The Langmuir model for liquid-phase adsorption is an extrapolation of the model developed for the gas phase. For instance, the liquid adsorption model considers as well that i) the adsorption occurs only in specific sites of the surface of the porous material; ii) only one molecule is adsorbed in one site; iii) the intermolecular interactions do not exist, iv) the molecules adsorbed forms a monolayer in the surface of the material and v) the heat of adsorption is equal for all surface sites. The model is represented by equation 7.

$$q = \frac{q_m \cdot K \cdot C}{1 + K \cdot C} \quad (7)$$

where, C is the concentration of the solute in the final liquid solution in equilibrium (mg/L), q is the mass of the adsorbed solute per mass of adsorbent (mg/l), q_m is the maximum adsorption capacity of the solute in the surface expressed as the mass of the solute per mass of adsorbent (mg/L), and K is the Langmuir constant related to the heat of adsorption (L/mg) ³⁰.

Freundlich isotherm model for liquid adsorption was developed by Herbert Freundlich in 1909 and it is an empirical relationship between the concentration of a solute on the surface of the adsorbent and the concentration of the solute in the solution after the equilibrium was reached. This model can be expressed mathematically as it is shown in equation 8 where, q is the adsorption capacity of

the adsorbent material (mg/g), k is the Freundlich constant that makes relation to the adsorption capacity ($\text{mg}^{1-1/n} \text{L}^{1/n}/\text{g}$) and n is the intensity of the adsorption³¹.

$$q = K \cdot C^{1/n} \quad (8)$$

Finally, the Prausnitz-Radke isotherm model was developed to describe the multicomponent adsorption, and it is a mathematical interpretation can be resumed as it is shown in Equation 9 where a , b and β are constant, C is the concentration of the solute in the final solution and q is the maximum amount adsorbed in the surface of the material. If the constant $\beta=1$, then the model becomes the Langmuir model, but when the fragment bC^β is larger than 1, then the model becomes like the one described by Freundlich³².

$$q = \frac{aC}{1+bC^\beta} \quad (9)$$

2.4. References

1. West, A. R. Crystallography and Diffraction Techniques. in *Solid state chemistry and its applications* 229–269 (Wiley, 2014).
doi:10.1107/s0108768185002476
2. Niemantsverdriet, J. W. Diffraction and Extended X-Ray Absorption Fine Structure (EXAFS). in *Spectroscopy in Catalysis* 147–177 (Wiley-VCH Verlag GmbH & Co. KGaA, 2007). doi:10.1002/9783527611348.ch6
3. Gándara, F. & Bennett, T. D. Crystallography of metal–organic frameworks. *IUCrJ* **1**, 563–570 (2014).
4. Will, G. The Rietveld Method. in *Powder Diffraction* 41–72 (Springer-Verlag, 2006). doi:10.1007/3-540-27986-5_2
5. Petit, C. Characterization Techniques for the Analysis of Metal–Organic Frameworks during and after Adsorption. in *Gas Adsorption in Metal-Organic Frameworks* 327–362 (CRC Press). doi:10.1201/9780429469770-7
6. Huang, L. Synthesis, morphology control, and properties of porous metal–organic coordination polymers. *Microporous Mesoporous Mater.* **58**, 105–

- 114 (2003).
7. SOLEIL. Scheme of synchrotron light radiation-Optimized Light Source of Intermediate Energy-France. Available at: <https://www.synchrotron-soleil.fr/en/about-us/what-soleil/soleil-3-questions>.
 8. Leroy, C. & Rancoita, P.-G. *Principles of Radiation Interaction in Matter and Detection*. (WORLD SCIENTIFIC, 2009). doi:10.1142/6872
 9. Furrer, A., Mesot, J. & Strässle, T. *Neutron Scattering in Condensed Matter Physics*. **04**, (WORLD SCIENTIFIC, 2009).
 10. Casco, M. E. *et al.* Understanding ZIF-8 Performance upon Gas Adsorption by Means of Inelastic Neutron Scattering. *ChemistrySelect* **2**, 2750–2753 (2017).
 11. Rowsell, J. L. C., Eckert, J. & Yaghi, O. M. Characterization of H₂ Binding Sites in Prototypical Metal–Organic Frameworks by Inelastic Neutron Scattering. *J. Am. Chem. Soc.* **127**, 14904–14910 (2005).
 12. Sumida, K. *et al.* Neutron Scattering and Spectroscopic Studies of Hydrogen Adsorption in Cr³⁺(BTC)₂—A Metal–Organic Framework with Exposed Cr²⁺ Sites. *J. Phys. Chem. C* **115**, 8414–8421 (2011).
 13. van der Heide, P. Introduction. in *X-Ray Photoelectron Spectroscopy: An Introduction to Principles and Practices* 1–12 (John Wiley & Sons, Inc., 2011). doi:10.1002/9781118162897.ch1
 14. Wagner, C. D., Riggs, W. M., Davis, L. E. & Moulder, J. F. Introduction. in *Handbook of X-Ray Photoelectron Spectroscopy: A Reference Book of Standard Data For Use in X-Ray Photoelectron Spectroscopy* (ed. Muilenberg, G. E.) (Perkin-Elmer Corporation, 1979).
 15. Rodríguez-San-Miguel, D., Amo-Ochoa, P. & Zamora, F. From Layered MOFs to Structuring at the Meso-/Macroscopic Scale. in *Metal-Organic Frameworks* 81–121 (Wiley-VCH Verlag GmbH & Co. KGaA, 2018). doi:10.1002/9783527809097.ch4
 16. Suga, M. *et al.* Recent progress in scanning electron microscopy for the

- characterization of fine structural details of nano materials. *Prog. Solid State Chem.* **42**, 1–21 (2014).
17. West, A. R. Other Techniques: Microscopy, Spectroscopy, Thermal Analysis. in *Solid State Chemistry and its Applications* 271–321 (Wiley, 2014). doi:10.1107/S0108768185002476
 18. Bottom, R. Thermogravimetric Analysis. in *Principles and Applications of Thermal Analysis* 87–118 (Blackwell Publishing Ltd). doi:10.1002/9780470697702.ch3
 19. Rowsell, J. L. C., Spencer, E. C., Eckert, J., Howard, J. A. K. & Yaghi, O. M. Gas adsorption sites in a large-pore metal-organic framework. *Science* **309**, 1350–4 (2005).
 20. Furukawa, H. Synthesis and Characterization of Metal–Organic Frameworks. in *Gas Adsorption in Metal-Organic Frameworks* 17–81 (CRC Press). doi:10.1201/9780429469770-2
 21. Ibach, H. Adsorption. in *Physics of Surfaces and Interfaces* 245–308 (Springer Berlin Heidelberg, 2006). doi:10.1007/3-540-34710-0_6
 22. Rouquerol, F., Rouquerol, J. & Sing, K. Introduction. in *Adsorption by Powders and Porous Solids* 1–26 (Elsevier, 1999). doi:10.1016/B978-012598920-6/50002-6
 23. Langmuir, I. THE ADSORPTION OF GASES ON PLANE SURFACES OF GLASS, MICA AND PLATINUM. *J. Am. Chem. Soc.* **40**, 1361–1403 (1918).
 24. Brunauer, S., Emmett, P. H. & Teller, E. Adsorption of Gases in Multimolecular Layers. *J. Am. Chem. Soc.* **60**, 309–319 (1938).
 25. Ruthven, D. M. Physical adsorption and the characterization of porous adsorbents. in *Principles of adsorption and adsorption processes* 29–59 (John Wiley and Sons, Inc., 1984).
 26. Thommes, M. *et al.* Physisorption of gases, with special reference to the evaluation of surface area and pore size distribution (IUPAC Technical Report). *Pure Appl. Chem.* **87**, 1051–1069 (2015).

27. Van Der Voort, P., Leus, K. & Canc de, E. Theory of Adsorption and Catalysis. in *Introduction to Porous Materials* 15–73 (Wiley, 2019). doi:10.1007/978-3-662-45456-5_1
28. Furukawa, H. *et al.* Water adsorption in porous metal-organic frameworks and related materials. *J. Am. Chem. Soc.* **136**, 4369–81 (2014).
29. Do, D. D. Fundamentals of Pure Component Adsorption Equilibria. in *Adsorption Analysis: Equilibria and Kinetics* 11–48 (College Press, 1998). doi:10.1142/9781860943829_0002
30. Piccin, J. S., Cadaval, T. R. S., de Pinto, L. A. A. & Dotto, G. L. Adsorption Isotherms in Liquid Phase: Experimental, Modeling, and Interpretations BT - Adsorption Processes for Water Treatment and Purification. in *Adsorption Processes for Water Treatment and Purification* (eds. Bonilla-Petriciolet, A., Mendoza-Castillo, D. I. & Reynel-Ávila, H. E.) 19–51 (Springer International Publishing, 2017). doi:10.1007/978-3-319-58136-1_2
31. Sparks, D. L. Sorption Phenomena on Soils. in *Environmental Soil Chemistry* 133–186 (Elsevier, 2003). doi:10.1016/B978-012656446-4/50005-0
32. Leyva-Ramos, R. & Geankopolis, C. J. Diffusion in liquid-filled pores of activated carbon. I. Pore volume diffusion. *Can. J. Chem. Eng.* **72**, 262–271 (1994).

CHAPTER 3

Structural Flexibility in Zeolitic Imidazolate Frameworks upon Gas Adsorption

Structural changes in ZIFs upon gas adsorption remain a paradigm due to the sensitivity of the adsorption mechanism to the nature of the organic ligands and gas probe molecules. Synchrotron X-ray diffraction under operando conditions clearly anticipates for the first time that ZIF-4 exhibits a structural reorientation from a narrow-pore (np) to a new expanded-pore (ep) structure upon N₂ adsorption, while it does not for CO₂ adsorption. The existence of an expanded-pore structure of ZIF-4 has also been predicted by molecular simulations. In simulations, the expanded structure was stabilized by entropy at high temperatures, and by strong adsorption of N₂ at low temperatures. These results are in perfect agreement with manometric adsorption measurements for N₂ at 77K that show the threshold pressure for the breathing at ~30 kPa. Inelastic neutron scattering (INS) measurements show that CO₂ is also able to promote structural changes but, in this specific case, only at cryogenic temperatures (5K)

Gandara-Loe J. et al., Journal of Materials Chemistry A, 2019, 7(24), 14552-14558. doi: 10.1039/C8TA09713E

3.1. Introduction

Zeolitic-imidazolate frameworks (ZIFs) is a new subfamily of the metal-organic frameworks (MOFs). These structures consist in metallic centers in a tetrahedral coordination (MN₄) linked through imidazolate linkers, the final topology being rather similar to those observed in zeolites (for instance the M-Im-M bond resembles that in zeolites Si-O-Si, i.e. 145°).¹⁻³ One of the most important characteristics of this group of materials is the presence of structural changes/transformations upon an external stimuli (for instance upon gas adsorption, a heat treatment or under high-pressure conditions). Interestingly, the nature of these phenomena highly depends on the kind of functionality present in the imidazolate linker (**Figure 3.1**). Indeed, the nature of the functional group defines the competition within the ZIF structure between strong non-bonding interactions (van der Waals and electrostatic), which favor the formation of highly dense structures (e.g. desolvated ZIF-7), and bonding interactions (mainly torsional and bending), that favors the formation of high symmetry, low-density crystal structure.

For instance, in the specific case of the methyl-based imidazolate, the one present in ZIF-8, previous studies described in the literature have shown that this material exhibits a gate-opening phenomenon upon an external pressure or upon gas adsorption (above ~2 kPa in the specific case of N₂).^{4,5} This gate-opening is associated with the swinging of the imidazolate linkers above a given threshold pressure, and depends on the nature of the probe molecule.⁶ On the contrary, a closely related ZIF with the same SOD topology, sharing the same metal atoms (Zn), the only difference being the nature of the ligand, i.e. benzimidazole in the specific case of ZIF-7, gives rise to a completely different scenario. Recent studies described in the literature have shown that upon gas adsorption there are associated phase-to-phase transitions, the threshold pressure for these changes being also sensitive to the nature of the adsorptive molecule. Experimental results and mathematical modelling clearly anticipate a breathing effect from a narrow-pore highly dense structure, phase I, to a large-pore low-density framework, phase II.^{7,8}

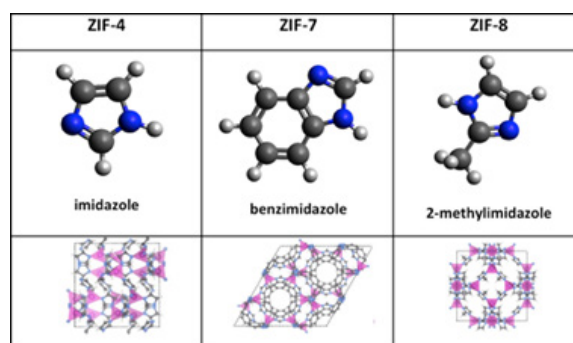


Figure 3.1. Scheme of molecular structure of the organic linker and 3D structure of some ZIFs with structural flexibility.³

As described above, the core structure of these fascinating ZIFs is a network of Zn metallic centers tetrahedrally coordinated through substituted imidazolate linkers. The most basic of these structures, i.e. the one constituted by un-substituted imidazolate linker, corresponds to ZIF-4. This ZIF has an orthorhombic space group with cag network topology of the mineral variscite and pore size windows of 0.21 nm in diameter.⁹ Recent studies have shown that despite the small pore window predicted theoretically, ZIF-4 is indeed able to adsorb N₂ and even small hydrocarbons.^{9,10} N₂ adsorption measurements described by Bennett et al. anticipate structural changes upon N₂ adsorption, although the reason behind these phenomena have never been evaluated. Despite the importance of this specific ZIF to get a better understanding of this sub-class of materials and their associated structural transformation, the number of studies reported in the literature is rather scarce.^{2,9-12}

With this in mind, the aim of this study is to ascertain the nature of these structural changes in ZIF-4 upon gas adsorption by combining synchrotron X-ray diffraction and inelastic neutron scattering studies under *operando* conditions, and molecular simulation studies.

3.2. Experimental section

3.2.1. Synthesis of ZIF-4

ZIF-4 crystals were synthesized following the recipe described by Yaghi et al. with some modifications.² In an initial step, a solid mixture of 0.4 g $\text{Zn}(\text{NO}_3)_2 \cdot 4\text{H}_2\text{O}$ and 0.3 g imidazole was prepared in a 100 ml beaker. Afterwards, 30 ml of N,N-dimethylformamide were added drop wise and the solution was ultrasonicated for 30 min. After ultrasonication, the beaker containing the solution was sealed with silicon stopper and heated to 403 K (heating ramp 5 K/min) for 48h. Since the control of the temperature is crucial to get high-quality crystals, sand-bath was used to control the temperature. Once the thermal treatment is done, the mixture must be cooled down to room temperature very slowly and left for additional 96h at 268 K in the fridge. These crystals must be washed with 30 ml DMF (x2) and methanol (x2). Finally, the crystals are dried at 323 K for 1h. At this point it is important to highlight the necessity of the step at 268 K for 96h to allow time for the growth of micron-size ZIF-4 crystals. If this step is not performed properly, a white powder is obtained with mixtures of nano-crystalline ZIF-4 and an “unknown” phase.

3.2.2. Characterization of the synthesized ZIF-4

3.2.2.1. Nitrogen and carbon dioxide isotherms

Synthesized ZIF-4 crystals have been evaluated using a number of techniques. Textural properties have been evaluated using N_2 adsorption/desorption measurements at cryogenic temperatures. Before the adsorption experiment, ZIF-4 crystals were outgassed at 413 K for 48h under high vacuum (10^{-7} kPa). Nitrogen adsorption measurements at 77 K were performed in a home-made high-resolution manometric equipment designed and constructed by the LMA group. CO_2 adsorption/desorption isotherms were performed at 273 K and 298 K using the same equipment and under the same experimental conditions.

3.2.2.2. Scanning electron microscopy

Scanning electron microscopy images of as synthesized ZIF-4 were performed using a JEOL JSM-840 microscope.

3.2.2.3. Synchrotron X-ray powder diffraction

Synchrotron X-ray powder diffraction data (SXRPD) were collected on the powder-diffraction end station of the MSPD beamline at synchrotron ALBA in Spain, using a MYTHEN detector and a wavelength of 0.4427 Å. The experiments were performed in an *ad hoc* capillary reaction cell (fused silica capillary, inner diameter 0.7 mm, outer diameter 0.85 mm). Before the experiment the ZIF-4 samples were placed inside the capillary connected on-line to a gas-handling and a vacuum line. An Oxford Cryostream 700 was used to control the temperature of the sample. In-situ SXRPD measurements were performed at 298 K and 80 K and varying pressures (vacuum up to 1 bar).

3.2.2.4. Inelastic neutron scattering

Inelastic neutron scattering (INS) measurements were performed at the VISION beamline (BL-16B) of the Spallation Neutron Source (SNS), Oak Ridge National Laboratory (ORNL), USA. About 200 mg of ZIF-4 was loaded in an Al sample holder connected to a gas handling system. The blank sample was first evacuated for 48h at 413 K and subsequently cooled down to 5 K. Once at this temperature, the INS spectrum was collected for several hours (the background for the instrument and sample holder is negligible in this case since the hydrogenous sample scatters neutrons very strongly). After the background measurement, the ZIF-4 was loaded with N₂ at 80 K up to 103 kPa for a few hours. The dosed sample was cooled down to 5 K and the INS was re-measured for several hours. A similar experiment was performed after dosing CO₂ at 298 K up to 103 kPa, followed by cooling down to 5 K.

3.2.3. Molecular Simulations of ZIF-4 phase transitions

Molecular Dynamics simulations were performed with the forcefield based on the forcefield developed by Zhang *et al.*¹³ These authors modified Amber forcefield

to simulate N₂-induced transition in ZIF-8.¹³ The forcefield has been recently adopted by some of us to simulate the temperature-induced transition in ZIF-7.¹⁴ The major modification was to use the QEq charge equilibration scheme¹⁵ to calculate partial atomic charges. The parameters are listed in **Tables 3.1-3.5**. With this modification the forcefield predicts reliable structural properties of ZIF-8. In particular, it predicts anisotropic mechanical properties of ZIF-8 in reasonable agreement with experimental measurements.¹⁶

Table 3.1. Lennard-Jones parameters and partial charges for ZIF-4 simulations

	U, kcal/mol	$R_0 = 2^{1/6} \sigma$, Å	q, e ^a
C_R	0.0567	3.8512	0.207
C_R1	0.0567	3.8512	0.010
H1	0.0238	2.8859	0.119
H2	0.0238	2.8859	0.098
N_R	0.0373	3.6604	-0.303
Zn	0.067	2.7635	0.128

^a Average charges. Charges were calculated using the QEq procedure¹⁵ for the reported ZIF-4(HT) structure¹¹ and were kept constant during subsequent calculations.

Table 3.2. Bond stretch parameters for ZIF-4 simulations

	R_0 , Å	K_0 , kcal/mol/Å ²
C_R1 – C_R1	1.346	1036
C_R – H1	0.929	734
C_R1 – H2	0.929	734
N_R – C_R	1.339	976
N_R – C_R1	1.371	820
Zn – N_R	1.987	172

$$U_{stretch} = \frac{K_0}{2} (R - R_0)^2 \quad \text{Eq. 3.1}$$

Table 3.3. Angle bend parameters for ZIF-4 simulations

	θ_0	K_0 , kcal/mol/rad ²
C_R – N_R – C_R1	105.24	140
C_R1 – C_R1 – H2	125.67	100
N_R – C_R – H1	123.89	100
N_R – C_R – N_R	112.17	140
N_R – C_R1 – C_R1	108.67	140
N_R – C_R1 – H2	125.66	100
N_R – Zn – N_R	109.47	21
Zn – N_R – C_R	127.5	100
Zn – C_R – C_R1	128	70

$$U_{bend} = \frac{K_0}{2}(\theta - \theta_0)^2 \quad \text{Eq. 3.2}$$

Table 3.4. Dihedral torsion parameters for ZIF-4 simulations.

	B, kcal/mol	d	n
Zn - N R - C R - H1	0.2	1	2
Zn - N R - C R - N R	0.2	1	2
Zn - N R - C R1 - C R1	0.2	1	2
Zn - N R - C R1 - H2	0.2	1	2
N R - Zn - N R - C R	0.348	-1	3
N R - Zn - N R - C R1	0.348	-1	3
H2 - C R1 - C R1 - H2	8	1	2
N R - C R1 - C R1 - H2	8	1	2
N R - C R1 - C R1 - N R	8	1	2
C R1 - N R - C R - H1	8.3	1	2
C R1 - N R - C R - N R	9.6	1	2
C R1 - C R1 - N R - C R	9.6	1	2
C R - N R - C R1 - H2	9.6	1	2

$$U_{torsion} = \frac{1}{2} \sum_j B_j (1 - d_j \cos[n_j \phi]) \quad \text{Eq. 3.3}$$

Table 3.5. Improper torsion parameters for ZIF-4 simulations

	K_0 , kcal/mol	n	χ_0
C R - N R - N R - H1	2.2	2	0
C R1 - C R1 - H2 - N R	2.2	2	0
Zn - N R - C R1 - C R	2.0	2	0

$$U_{improper} = \frac{K_0}{2} (1 - \cos[n \chi - \chi_0]) \quad \text{Eq. 3.4}$$

MD simulations were performed using Forcite code from Materials Studio 2018 from BIOVIA. First, we converted ZIF-4 structure to P1 and minimized it to obtain a dense structure at zero temperature. Starting with this structure we performed a series of short NpT simulations with progressively increasing temperature. This procedure mimics the experimental measurements of temperature induced phase transition in ZIF-7¹⁴ and ZIF-4¹¹. MD simulations we performed with 0.2 fs timestep, Nose-Hoover thermostat¹⁷ with Q ratio 0.001, and anisotropic Parrinello-Raman¹⁸ barostat as implemented by Martyna *et al.*¹⁹ with time constant of 0.1 ps. The length of simulations at each temperature was 1 ps. The temperature ramp was from 10 K to 1510 K with 450 steps. We used 3x2x2 supercell. Simulations were also performed with 2x2x2 and single unit cell to confirm the results. The use of a larger 3x2x2 supercell is preferred as it minimize fluctuations in volume and pressure.

GCMC simulations were performed to load the obtained expanded ZIF-4 structure with N₂ molecules at 77 K. To facilitate full loading, we performed simulations at 1000 kPa. We used TraPPE forcefield for N₂ molecules²⁰ and n-pentane²¹ and Lorentz-Berthelot combining rules for LJ interactions with ZIF-4 atoms.

After GCMC simulations we performed NpT simulations for expanded ZIF-4 loaded with N₂ molecules to confirm the stability of the structure and refine the unit cell parameters at 77 K.

Vibrational Density of States (VDOS) was calculated from MD simulations using Fourier transform of the velocity autocorrelation function (VACF).²²

$$VACF(t) = \frac{v(0) \cdot v(t)}{v(0) \cdot v(0)} = \frac{1}{LN} \sum_k^L \sum_i^N v_i(t_k) \cdot v_i(t_k + t) \quad \text{Eq. 3.5}$$

$$g(\omega) = \frac{1}{\sqrt{2\pi}} \int_{-\infty}^{\infty} VACF(t) e^{-i\omega t} dt \quad \text{Eq. 3.6}$$

To capture low frequency modes responsible for the phase transitions between different polymorphs of ZIF-4, the production simulations were performed for 50 ps. VDOS for each individual atom were weighted according to the atomic masses.

$$g(\omega) = \sum_{j=1}^N m_j g_j(\omega) \quad \text{Eq. 3.7}$$

For a given structure simulations were performed in the NVT ensemble at 300 K with a unit cell taken as an average from NPT simulations. We checked that the thermostat and barostat did not affect the calculated VDOS frequencies. Essentially identical results were obtained from NPT simulations, NVT simulations, and from NVE simulations (performed after NVT so that the temperature was close to the desired temperature).

3.3. Results

3.3.1. ZIF-4 characterization

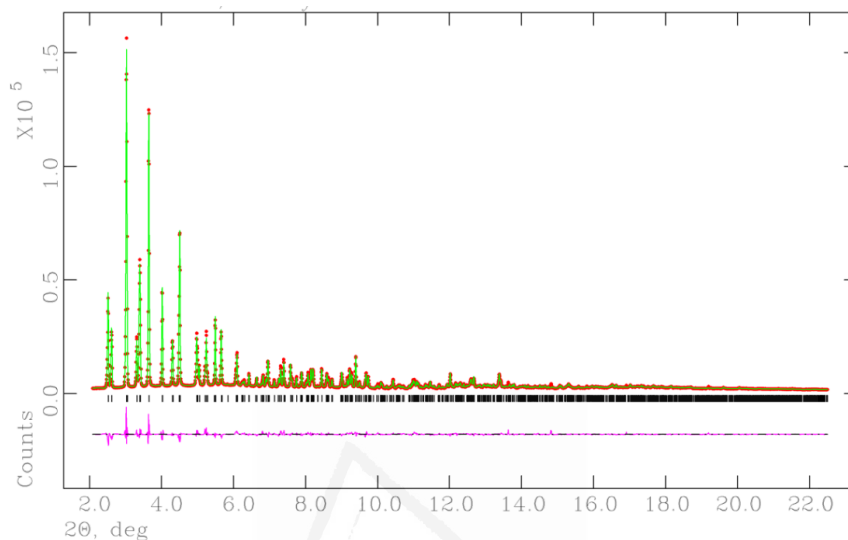


Figure 3.2. Rietveld refinement of the X-ray diffraction pattern of as-synthesized ZIF-4 performed using synchrotron XRD. Initial model taken from Lewis *et al.*²³

The quality of the synthesized ZIF-4 crystals has been evaluated using synchrotron XRD measurements. **Figure 3.2** shows the pattern for the as-synthesized sample and the Rietveld refinement. The XRD pattern of the desolvated sample exhibits a very good agreement with the theoretical one, thus confirming the quality of the synthesized crystals. At this point it is important to highlight the synthesis of ZIF-4 is quite challenging since small variations in the synthesis protocol gives rise to white powders with collapsed structures.

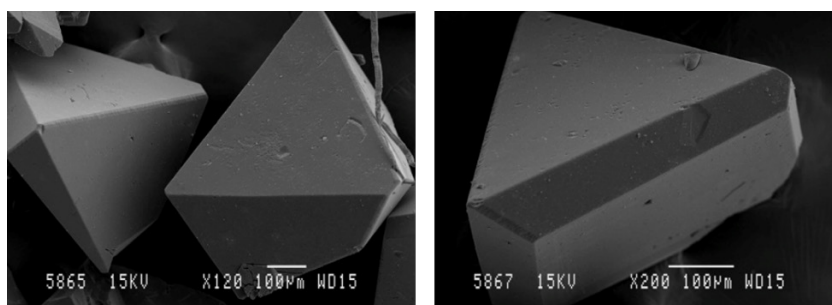


Figure 3.3. SEM images of the synthesized microcrystals of ZIF-4.

The morphology of the synthesized crystals was evaluated using scanning electron microscopy (SEM). **Figure 3.3** shows two representative images of the as-synthesized crystals. As it can be observed, the proposed synthesis approach gives rise to high quality crystals with rhombohedra morphology and with a crystal size in the micrometer-size range (average size ca. $625 \mu\text{m} \pm 137 \mu\text{m}$).

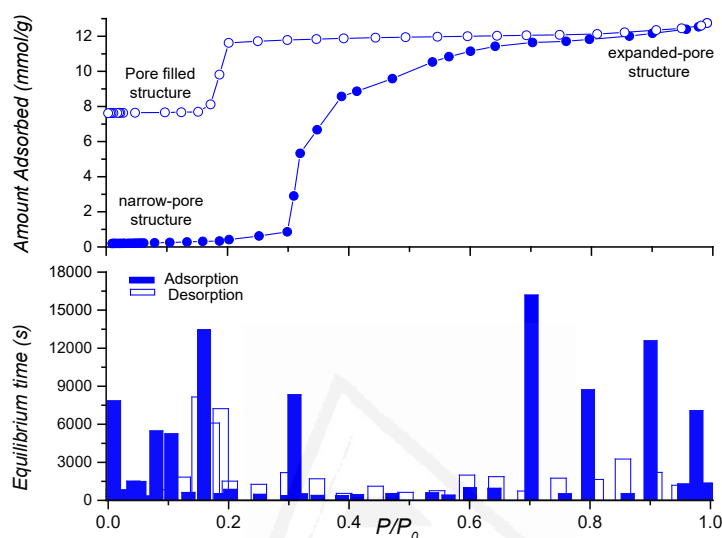


Figure 3.4. N_2 adsorption (filled symbols)/desorption (empty symbols) isotherm for ZIF-4 at 77K (upper panel). Time requested to reach equilibrium for each of the adsorption and desorption points (lower panel).

Figure 3.4 shows the N_2 adsorption/desorption isotherm for ZIF-4 at cryogenic temperatures measured in a fully automated manometric equipment under very strict criteria to reach equilibrium. It is included the kinetic data for each physisorption point. At this point it is important to highlight that the whole nitrogen isotherm for ZIF-4 crystals took approximately one week. As it can be observed, the amount of nitrogen adsorbed below $p/p_0 = 0.3$ is rather zero. Consequently, N_2 adsorption measurement in ZIF-4 does not allow anticipating the monolayer capacity, and consequently, the BET surface area of ZIF-4.

The amount of nitrogen adsorbed below 0.4 relative pressure is rather small due to the inaccessibility of the nitrogen molecules to the inner porous structure. However, above a certain threshold pressure, i.e. above 30 kPa, the nitrogen adsorption capacity experiences a sudden increase in the amount adsorbed up to a

maximum of *ca.* 12.5 mmol g⁻¹ (or 280 cm³ STP g⁻¹) at 103 kPa. Upon desorption the material remains unaltered, i.e. nitrogen is kept entrapped in the inner porosity down to a given pressure, *ca.* 21 kPa, when the material suddenly desorbs partially these nitrogen molecules down to a constant value of ~ 7.6 mmol g⁻¹. The shape of the isotherm and the breathing phenomenon at medium pressures is in close agreement with the N₂ isotherm reported in the literature by Bennett et al. for ZIF-4.⁹ At this point it is important to emphasize that contrary to some assumptions reported in the literature, ZIF-4 isotherm does not allow to estimate the monolayer capacity using the BET equation (due to the absence of nitrogen adsorption in the relative pressure range 0-0.3) and consequently, to estimate the apparent surface area.

3.3.2. ZIF-4 flexibility upon gas adsorption

To gain more knowledge about the breathing phenomenon in ZIF-4, synchrotron X-ray powder diffraction (SXRPD) studies were performed at the MSPD station in ALBA synchrotron (Spain). Desolvated ZIF-4 was cooled down to 80 K under vacuum and N₂ doses were incorporated in the capillary cell up to atmospheric pressure followed by an evacuation step, trying to reproduce the adsorption measurements described above. The Rietveld refinement of the desolvated sample at 298 K showed in **Figure 3.2** confirms that its crystal structure corresponds to ZIF-4 without observable amount of impurities.¹¹ Lattice parameters are $a = 15.4936(7)\text{\AA}$, $b = 15.5110(7)\text{\AA}$, $c = 18.0468(8)\text{\AA}$ ($V = 4337.0(5) \text{\AA}^3$). Afterwards the ZIF-4 sample was cooled down under vacuum to 80 K before the incorporation of N₂. At cryogenic temperatures the unit cell parameters exhibit a small contraction (1%), so that the new lattice parameters at 80 K are $a = 15.507(5)\text{\AA}$, $b = 15.098(2)\text{\AA}$, $c = 18.354(4)\text{\AA}$ ($V = 4297(2) \text{\AA}^3$).

The small contraction in the unit cell at 80 K differs from the values previously reported so far by Wharmby *et al.*, where a porous to dense phase transition with up to 23% contraction in the unit cell was observed at 80 K ($V = 3344.77(4)$).¹¹ These authors observed that this contraction is indeed crystal-size dependent, i.e. larger crystals exhibit a smaller contraction. However, our experiments suggest that the value of 1% is quite reproducible independently of the crystal size evaluated. At this

point it is important to highlight that we could observed a larger unit cell contraction when performing a fast cooling step, i.e. under non-equilibrium conditions.

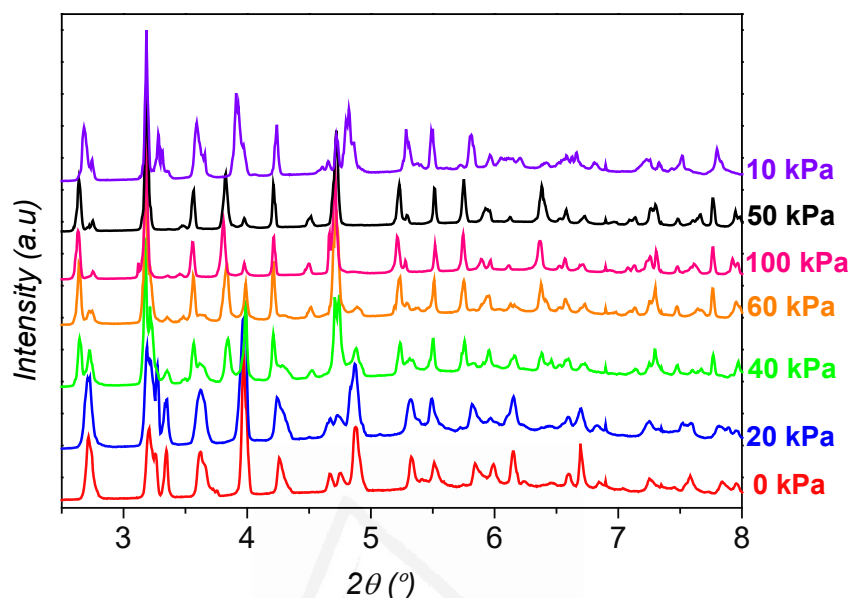


Figure 3.5. Synchrotron X-ray diffraction pattern of ZIF-4 at 80 K after dosing N₂ (adsorption and desorption).

As can be appreciated in **Figure 3.5** the SPXRD pattern of ZIF-4 does not exhibit any significant change after incorporation of 20 kPa of N₂. However, incorporation of 40 kPa gives rise to important changes in the SPXRD pattern that evolve progressively until reaching 103 kPa, i.e. two different phases prevail until saturation. Upon N₂ dosing (only a few minutes were left after dosing N₂ and before recording the spectra) some peaks disappear (for instance 2.72°, 3.35°, 3.62° and 4.88°) and some new peaks emerge (3.55°, 3.80° and 4.72°), among others. These structural changes are associated with the prevalence of two different phases, the low-temperature phase described above, and a new phase characterized by a significant expansion in the unit cell parameters (up to 8-9% vol. expansion). The lattice parameters for the expanded-pore (N₂) ZIF-4 are $a = 15.960(3)\text{Å}$, $b = 15.908(3)\text{Å}$, $c = 18.311(3)\text{Å}$ ($V = 4649(2)\text{Å}^3$).

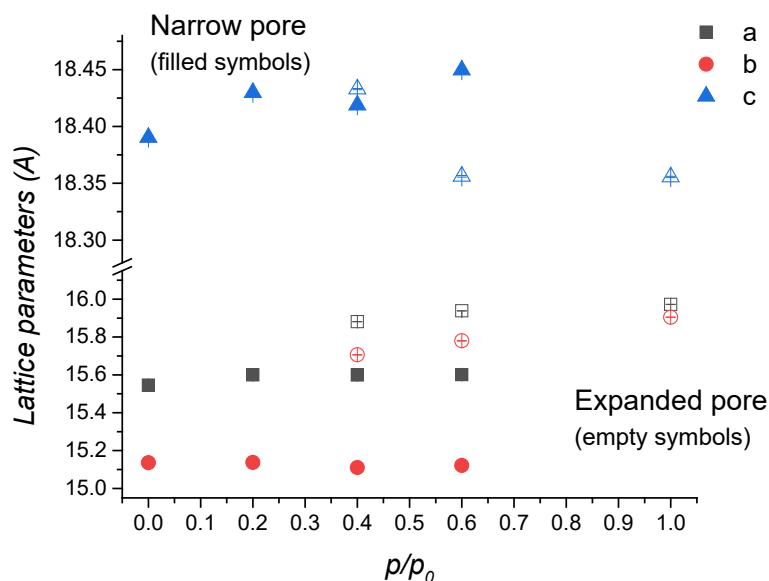


Figure 3.6. Evolution of the unit cell parameters in ZIF-4 before and after dosing N_2 at 80K.

Figure 3.6 shows the evaluation of the unit cell parameters for the ZIF-4 sample upon nitrogen adsorption obtained after Le Bail fitting. These results are perfectly coincident with the nitrogen adsorption measurements described above, i.e. below p/p_0 0.4 only the narrow-pore ZIF-4 structure is present. However, above this threshold pressure both phases (narrow-pore and expanded-pore) prevail up to atmospheric pressure when the expanded-pore (ep) structure is the only phase present. As described above, the unit cell expansion upon N_2 dosing is $\sim 8\text{--}9\%$ or $\Delta V = \sim 350 \text{ \AA}^3$. Taking into account the formula weight for ZIF-4 ($399.0374 \text{ g mol}^{-1}$), this expansion corresponds to an increase of $\sim 0.53 \text{ cm}^3 \text{ g}^{-1}$. A closer look to **Figure 3.4** clearly shows that at atmospheric pressure ZIF-4 is able to adsorb 12.5 mmol g^{-1} or $0.44 \text{ cm}^3 \text{ g}^{-1}$ (as a liquid). The agreement between the adsorption experiments and the crystallographic measurements clearly confirms the validity and reproducibility of these measurements.

Upon expansion, the capillary was evacuated down to $\sim 10 \text{ kPa}$. As observed in **Figure 3.5**, the SPXRD pattern does not exhibit any change, in close agreement with the adsorption values. Only at $\sim 10 \text{ kPa}$ the pattern exhibits important changes, the final pattern having certain similarities with the initial narrow-pore ZIF-4, although

with possible symmetry lowering. According to these results, upon evacuation ZIF-4 exhibits a phase transition from an expanded-pore structure to a pore-filled structure trapping inside up to 7.6 mmol/g of nitrogen. The pore-filled structure have some similarities with the high-temperature (HT) structure reported in the literature for ZIF-4.¹¹ The structural parameters of the pore-filled structure are $a = 15.644(2)\text{\AA}$, $b = 15.140(2)\text{\AA}$, $c = 18.411(2)\text{\AA}$ ($V = 4361(1)\text{\AA}^3$). In summary, these results confirm *for the first time* the presence of two phase-to-phase transitions in ZIF-4, i) from narrow (np) to expanded-pore (ep) upon N₂ adsorption and ii) from expanded-pore (ep) to a pore-filled structure upon nitrogen evacuation at 77K.

3.3.3. Molecular simulations of ZIF-4 phase transition

The existence of an expanded-pore structure of ZIF-4 has been predicted by classical Molecular Dynamics simulation. We followed the procedure and forcefield some of us used earlier to predict temperature-induced phase transition in ZIF-7.¹⁴ This forcefield reproduces well the structural properties of ZIFs, including unit cell constants, mechanical moduli (**Table 3.6**), and vibrational densities of states. In particular, it reproduces the low-frequently vibrational modes identified by INS (described later), e.g., the flapping of the imidazole ligand at ~ 3 meV (**Figure 3.7**).

Table 3.6. Reference calculations of anisotropic mechanical properties of ZIF-8 in comparison with experimental data.

ZIF-8	a (Å) ^[b]	C_{11}	C_{12} (GPa)	C_{44}	K ^[e] (GPa)
B3LYP ^[d]	17.3481	11.04	8.33	0.94	9.23 (9.04)
B3LYP-D*	17.0630	11.03	8.43	0.73	9.30
PBE	17.1907	6.38	10.02	0.94	8.8 (8.7)
	17.1907	9.72	11.05	1.50	10.6 (8.7)
	17.2606	10.14	8.00	0.78	8.7 (8.5)
PBE-D	16.8640	4.98	7.92	0.33	6.9 (8.2)
	16.9264	9.79	7.03	0.53	7.95 (8.00)
	16.9672	9.62	6.53	0.46	7.56
HF ^[e]	17.4548	12.36	9.36	1.40	10.36
	17.4548	13.47	9.30	1.42	10.69
	17.4548	10.17	9.29	1.36	9.59
exper.	16.99	9.52	6.87	0.97	7.75
this work	16.64	11.5	8.6	1.7	9.57

Experimental unit cell parameters (a), anisotropic elastic constants (C_{11} , C_{12} , C_{44}) and bulk modulus (K), *ab initio* HF and DFT calculations (PBE and B3LYP functionals) are from Ref.¹⁶ Forcefield calculations from this work – last row.

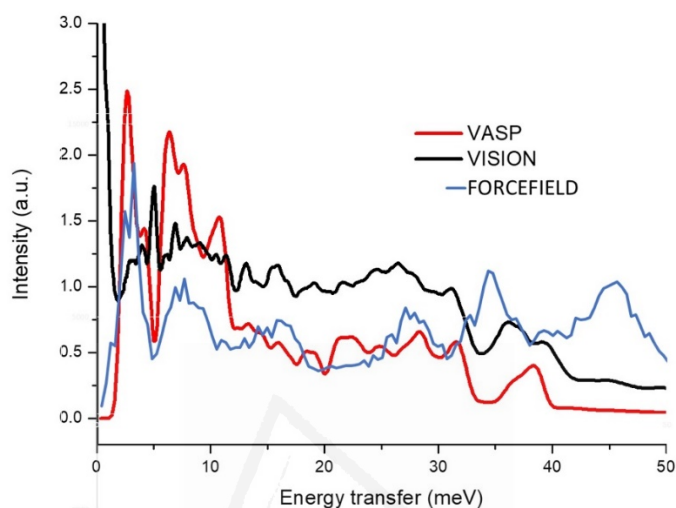


Figure 3.7. Vibrational Density of States calculated from forcefield model of high-density ZIF-4 structure at 50 K in comparison with INS and DFT (VASP)_calculations. Forcefield calculations were performed with the ZIF-4 (LT) structure ($V=3160 \text{ \AA}$).

For the prediction of the pore-expanded ZIF-4 structure we used a series of NpT simulations with anisotropic barostat, and raised the temperature step-wise to gradually increase entropic contributions to the free energy ($F = E - TS$) and drive the system to an expanded phase with a larger entropy, and thus overall lower free energy. **Figure 3.8** and **Figure 3.9** show evolution of the unit cell parameters during MD simulations in comparison with experimental data for the reported low-temperature ZIF-4 transition¹¹ and for the pore expanded ZIF-4.

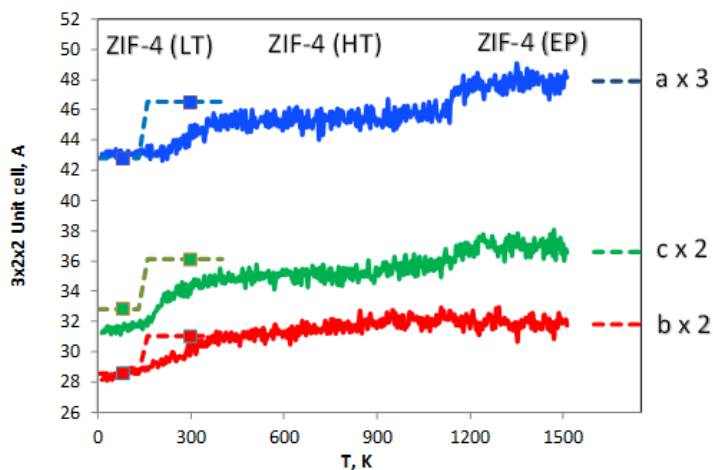


Figure 3.8. Unit cell parameters from Molecular Dynamics simulation of the phase transitions in ZIF-4 upon heating. Shown are unit cell parameters for the 3x2x2 supercell. The narrow pore structure ZIF-4 (LT) transitions first into the open pore structure ZIF-4 (HT) at around 200-300 K, and then into expanded pore ZIF-4 (ep) structure. The dashed lines with points are experimentally measured unit cell parameters from Ref.²⁴ The dashed lines on the right are the unit cell parameters experimentally measured in this work for the expanded pore ZIF-4 (ep) upon N₂ adsorption at 77 K.

Figure 3.8 shows typical simulation results. Starting from low temperature we observe first a transition from the ZIF-4 (LT) phase to ZIF-4 (HT) phase, in close agreement with the experimental measurements [6] for both unit cell parameters as well as the temperature of transition (150 K on the experiment, and ~200 K in simulations). Upon further heating we observe a transition to a pore-expanded ZIF-4 structure at ~1200K. The unit cell parameters of the predicted expanded structure are in very close agreement with the measurements for the N₂ loaded ZIF-4 at 77 K (**Figure 3.6**). Of course, this transition in simulations can't be observed experimentally upon heating because ZIF-4 would either decompose, undergo amorphization²⁵ or transition into a glassy state.²⁴

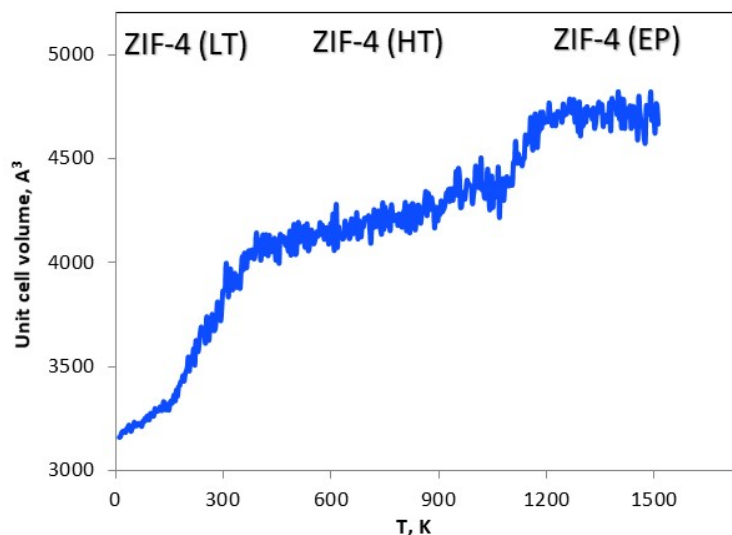


Figure 3.9. Unit cell volume evolution during Molecular Dynamics simulation of the phase transitions in ZIF-4 upon heating. The narrow pore structure ZIF-4 (LT) transitions first into the open pore structure ZIF-4 (HT) at around 200-300 K, and then into expanded pore ZIF-4 (ep) structure.

The results in **Figure 3.10** demonstrate that an expanded-pore ZIF-4 is thermodynamically feasible upon heating despite having higher enthalpy. The resulting unit cell parameters $a = 15.8\text{\AA}$, $b = 16.1\text{\AA}$, $c = 18.9\text{\AA}$ ($V = 4799\text{\AA}^3$) are in very good agreement with the XRD measurements on the expanded-pore (N_2) ZIF-4 obtained experimentally. The predicted total pore volume of an expanded ZIF-4 ($V_p = 0.45\text{ cm}^3/\text{g}$) is also in good agreement with the N_2 adsorption measurements (**Figure 3.4**), assuming the normal liquid density of N_2 in the pores. Moreover, we identify the second step on the desorption branch of N_2 isotherm with the transition back to a pore-filled ZIF-4 structure ($V_p = 0.24\text{ cm}^3/\text{g}$). The expanded ZIF-4 structure has significantly more open channels in the y-direction as compared to the reported ZIF-4 structure.

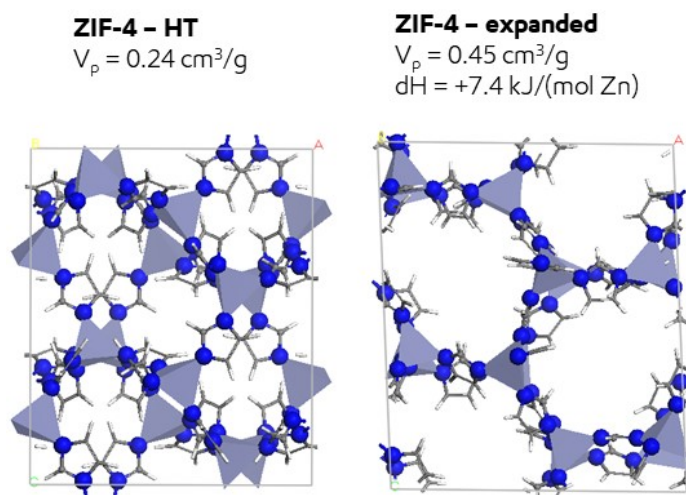


Fig. 3.10. Open ZIF-4 (HT) structure and predicted expanded-pore (ep) ZIF-4 structure. The enthalpy difference was obtained from MD simulations.

We have also simulated expanded ZIF-4 structure with adsorbed N_2 molecules at 77K at a loading of 10.3 mmol/g. We used Grand Canonical Monte Carlo (GCMC) simulations to load the structure with N_2 molecules and, performed NpT simulations, which confirmed stability of the pore-expanded ZIF-4 structure (**Figure 3.11**). The resulting lattice parameters for the simulated (N_2) ZIF-4 $a = 15.7 \text{ \AA}$, $b = 16.0 \text{ \AA}$, $c = 18.6 \text{ \AA}$ ($V = 4655 \text{ \AA}^3$) are in even better agreement with the XRD measurements. Thus, interactions with N_2 also stabilized the expanded ZIF-4 structure even at low temperatures (**Figure 3.11**).

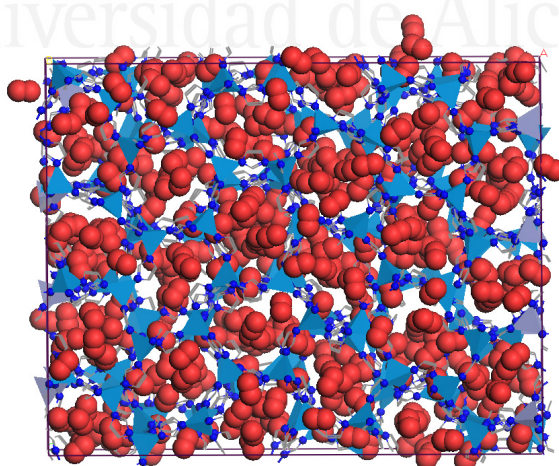


Figure 3.11. Snapshot from the MD simulations of the pore-expanded ZIF-4 (ep) structure with N_2 molecules at the loading of 10.3 mmol/g at 77 K. The structure is viewed from the Y direction.

The adsorption performance of ZIF-4 has also been evaluated for CO₂ as a probe molecule at a much higher adsorption temperature. **Figure 3.12** shows the CO₂ adsorption isotherms at 273 K and up to 103 kPa. As can be appreciated, contrary to N₂, CO₂ is able to access the inner porous structure already at low relative pressures.

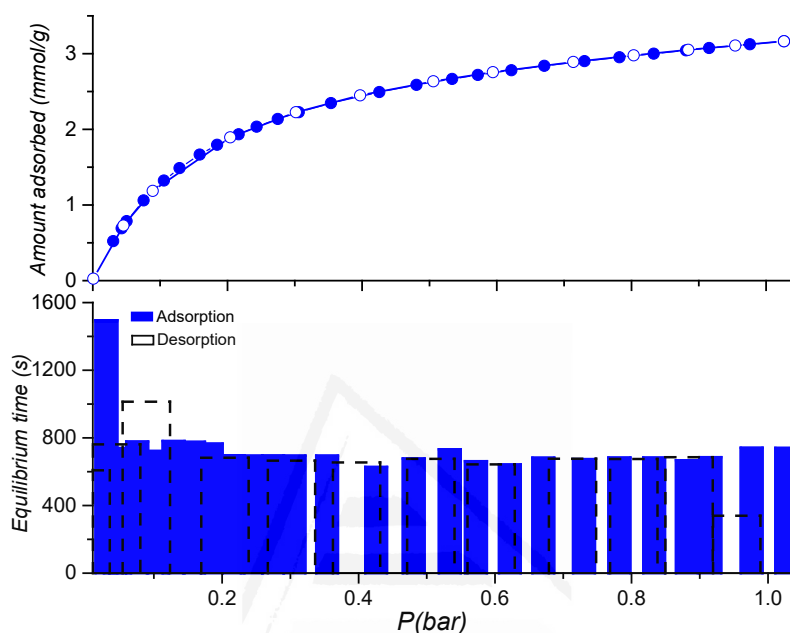


Figure 3.12. (Upper panel) CO₂ adsorption (full symbols)/desorption (empty symbols) isotherms at 273 K for ZIF-4. (Lower panel) Time requested to reach equilibrium for each of the adsorption and desorption points at the isotherm.

The filling of the ZIF-4 cavities with CO₂ is relatively fast compared to N₂ (equilibrium time does not exceed 800 min, independently of the adsorption/desorption branch). The total amount adsorbed at atmospheric pressure is 3.2 mmol g⁻¹ at 273 K. Applying the Dubinin-Radushkevich (DR) equation to the CO₂ adsorption data gives rise to an accessible micropore volume of 0.21 cm³ g⁻¹ (CO₂ liquid density at 273 K is 1.023 g cm⁻³), quite far from the nitrogen adsorbed volume (i.e. 0.43 cm³ g⁻¹). Assuming the Gurvich rule for ZIF-4, the total amount of nitrogen and CO₂ adsorbed as a liquid would be the same, provided that both adsorbates are able to access the same porosity. However, the concave shape of the CO₂ isotherm and the faster kinetics do not anticipate any breathing, expansion or gate-opening phenomena. Taking into account that CO₂ is smaller than N₂ (0.33

nm vs. 0.36 nm) and the higher temperature of the adsorption measurement (298 K vs. 77 K), i.e. associated with faster kinetics, the lower adsorption capacity for CO₂ (3.2 mmol/g vs. 12.5 mmol/g) and the absence of a clear breathing phenomena anticipates that the expansion of the ZIF-4 structure upon gas adsorption is not a kinetic or steric effect but rather an energetic process associated to the phase transition upon CO₂ adsorption from a narrow-pore (np) to an expanded-pore (ep) structure.

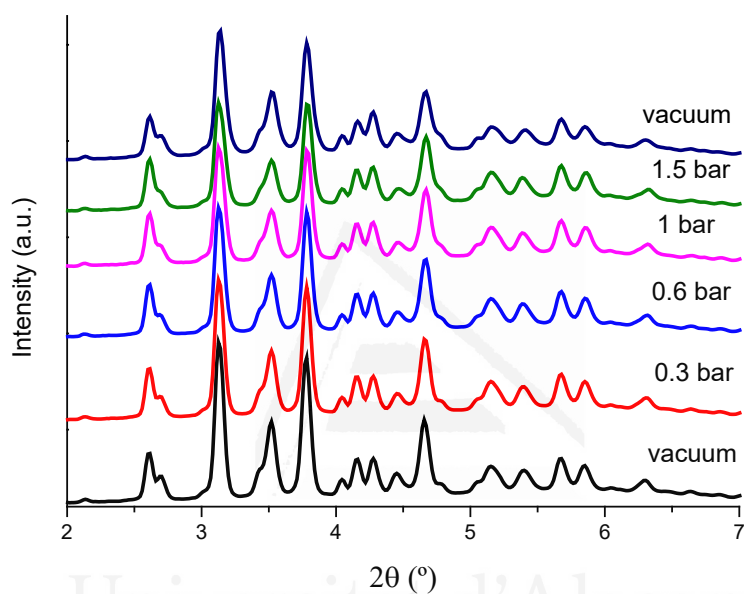


Figure 3.13. Synchrotron XRD pattern for ZIF-4 at 298K before and after introduction of CO₂ up to 103 kPa.

The absence of structural changes upon CO₂ adsorption has been corroborated by synchrotron powder X-ray diffraction measurements. According to **Figure 3.13**, incorporation of CO₂ up to 103 kPa at 298 K and the corresponding desorption step does not produce significant changes in the SPXRD pattern. These results are in close agreement with the CO₂ adsorption isotherms described above and confirm the assumption that CO₂ at atmospheric pressure and 103 kPa is not able to promote in ZIF-4 the phase transition from the narrow-pore to the expanded-pore structure.

3.3.4. Inelastic neutron scattering

Last but not least, the vibrational and rotation modes of ZIF-4 have been evaluated using inelastic neutron scattering measurements. These studies have been performed at the beamline VISION at the Oak Ridge National Laboratory (USA). INS is especially sensitive to the dynamics of hydrogen within a structural network due to the relatively large incoherent neutron cross-section of hydrogen compared to other atomic nuclei. Furthermore, due to the absence of selection rules, all transitions are active in INS, thus providing a powerful tool to evaluate structural deformations in ZIFs.^{3,4,8} Fig. 6 shows the low energy transfer region for the ZIF-4 measured at 5 K and the simulated spectra obtained using VASP model. The theoretical results were then converted to the simulated INS spectra using the aClimax software.²⁶ This low transfer energy region is the terahertz region and contains the most valuable information for ZIFs since it reveals dynamics of open and closed frameworks. The mid-high energy region (50-250 meV) contains the ring deformation modes and the C-C and C-H bending modes from the linker. As it can be observed, the original sample exhibits a rather smooth spectra with a main contribution at 5.05 meV (40.7 cm^{-1}) and two small contributions at 6.90 meV (55.6 cm^{-1}) and 13.10 meV (105.6 cm^{-1}).

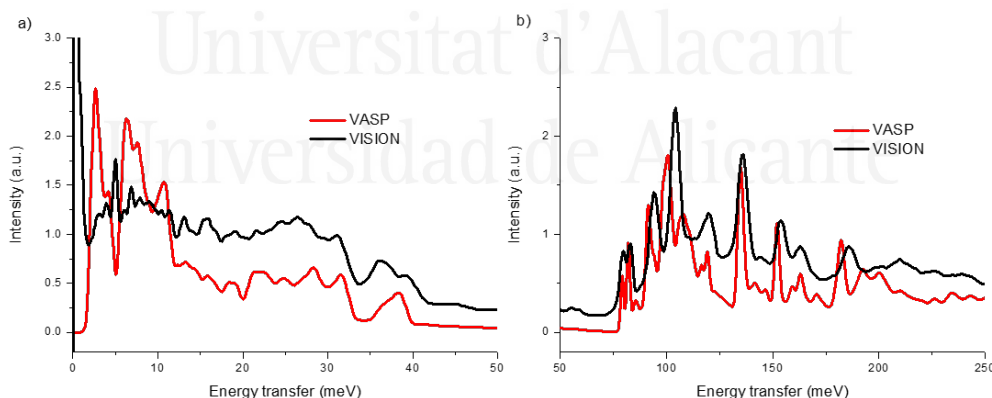


Figure 3.14. Inelastic neutron scattering spectra of ZIF-4 at 5 K in the low (left) and high (right) energy transfer range. The simulated spectra using VASP model is also included (red).

Theoretical results clearly show that VASP allows for a good fitting of the experimental data, including the high energy modes (**Figure 3.14**), except the contribution at 5.05 meV. The higher neutron flux at VISION allows for a higher

resolution of the INS spectra for ZIF-4, thus allowing for a better evaluation of the structural phenomena upon gas adsorption.³

Theoretical predictions anticipate that all contributions below 40 meV are rather similar in nature and involve the libration/flapping of the imidazole ring. More specifically, within this range the lowest energies correspond to the rotation of the rings through the Zn-N axis (see animation in the SI), while higher energies involve the ring libration modes involving Zn-N stretch. The assignment of the low energy peaks (ca. 3-5 meV) to the ring rotation/flapping mode implies that these peaks will be highly affected by the compression/expansion of the unit cell upon an external stimulus (e.g. temperature and pressure change or upon adsorption). Indeed, this could be the reason to explain the differences between simulations and experiments, i.e. whereas simulations are performed using the structure at 80 K (LT structure), at the low temperature of the INS experiment (5 K) an additional unit cell contraction is expected, thus explaining the appearance of this additional peak at 5 meV, not predicted by the models. Classical molecular simulations (**Figure 3.7**) also does not predict the 5 meV peak.

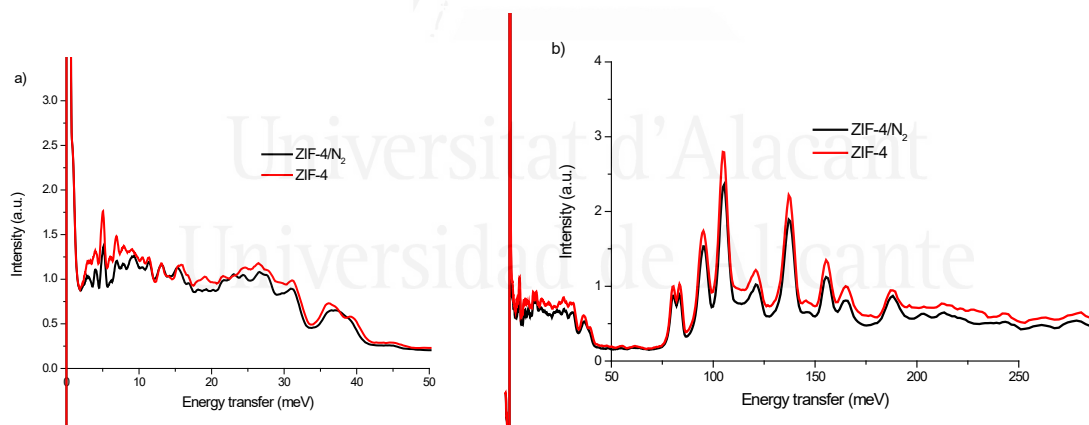


Figure 3.15. Inelastic neutron scattering spectra of ZIF-4 at 5 K before and after the incorporation of 103 kPa of N₂ at 77K. After incorporation of N₂ the sample was cooled down to 5 K before the INS measurement. Low (left) and high (right) energy transfer range are shown.

It is reasonable to assume that in the contracted structure the flapping of the imidazole ligand, theoretically predicted at 3 meV, will be hindered and shifted to a slightly higher energy value (ca. 5.05 meV). Incorporation of 103 kPa of nitrogen to

ZIF-4 at 80 K and subsequent cooling down to 5 K gives rise to the same INS spectra (see **Figure 3.15**). Although this observation is in contradiction with the synchrotron X-ray diffraction measurements, it must be attributed to the instability of N₂ in the cavities of the ZIF-4 at extremely low temperatures (i.e. 5 K). Indeed, a similar instability of N₂ was reported for ZIF-7 upon slight variations in temperature around 80 K.⁸ On the contrary, incorporation of 103 kPa of CO₂ at 298 K and further cooling down to 5 K gives rise to interesting findings. Under these conditions the suppression of the contribution at 5.05 meV can be clearly appreciated (see **Figure 3.16**). Taking into account that the spectra of ZIF-4 filled with CO₂ resembles that predicted by the model at 298 K, this could be an indication of the filling of the cavities by CO₂ at these extremely low temperatures, so that the adsorption of CO₂ produces a structural change, probably from the narrow-pore (*np*) to the certain expanded-pore (*ep*) structure.

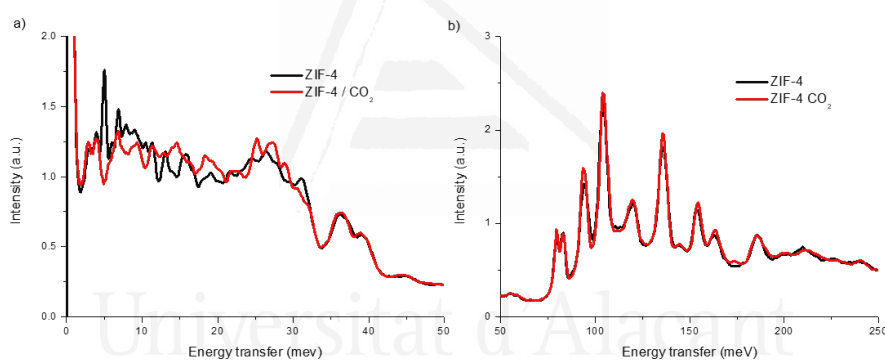


Figure 3.16. Inelastic neutron scattering spectra of ZIF-4 at 5 K before and after the incorporation of 103 kPa of CO₂ at 298 K. After incorporation of CO₂ the sample was cooled down to 5 K before the INS measurement. Low (left) and high (right) energy transfer range are shown.

It should be noted that at least two other publications indirectly confirm the existence of the pore-expanded ZIF-4. In the work of Bennet *et al.*⁹ the measured N₂ adsorption isotherms agree almost perfectly with our isotherm in **Figure 3.4**, thus confirming the validity of our experiments. Recently Hwang *et al.*²⁷ found an unusual dependence for diffusivities of alkanes in ZIF-4. They hypothesized that the structure can expand upon adsorption of pentane. Our experimental and modeling results strongly suggest that this indeed could be the case, and that other molecules

can cause transition to the expanded-pore ZIF-4. In fact, we performed GCMC simulations with the pore-expanded structure and were able to match the experimental loading of pentane of 2.5 mmol/g (**Figure 3.17**).

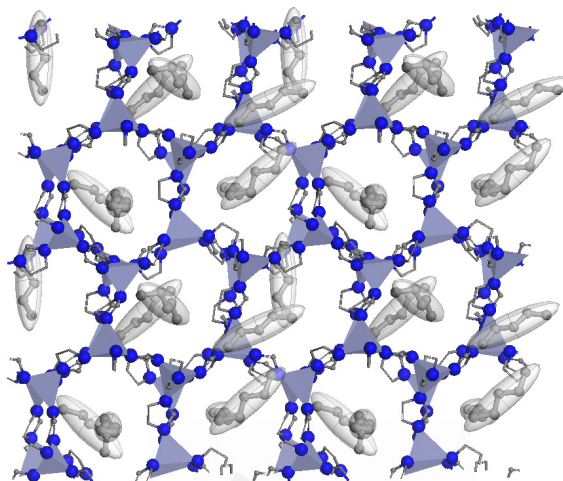


Figure 3.17. Snapshot from the GCMC simulations of the pore-expanded ZIF-4 (*ep*) structure with pentane molecules at the loading of 2.5 mmol/g. The structure is viewed from the Y direction.

3.4. Conclusions

In summary, combination of synchrotron X-ray diffraction and inelastic neutron scattering measurements under operando conditions clearly show that ZIF-4 exhibits a breathing phenomenon upon nitrogen adsorption at ~30 kPa, associated with an 8-9% volume expansion in the unit cell. The transition from a narrow-pore (*np*) to an expanded-pore (*ep*) phase explains the complex behavior of the nitrogen adsorption isotherm at cryogenic temperatures. The existence of an expanded ZIF-4 has been predicted by molecular simulations. First, the expanded ZIF-4 structure was predicted by MD simulations at higher temperatures, which increases entropic contributions to the free energy and stabilizes the expanded structure. Second, the expanded ZIF-4 structure with N₂ molecules was confirmed by MD and GCMC simulations at 77 K. Although CO₂ with a lower kinetic diameter and at a much higher adsorption temperature is able to access in the inner cavities in ZIF-4, this molecule is not able to promote the *np* to *ep* transition at ambient

temperature. However, INS measurements show that only at cryogenic temperatures (5 K) CO₂ is able to promote certain structural changes.

3.5. References

1. Phan, A. *et al.* Synthesis, structure, and carbon dioxide capture properties of zeolitic imidazolate frameworks. *Acc Chem Res* **43**, 58–67 (2010).
2. Park, K. S. *et al.* Exceptional chemical and thermal stability of zeolitic imidazolate frameworks. *Proc. Natl. Acad. Sci. U. S. A.* **103**, 10186–91 (2006).
3. Ryder, M. R. *et al.* Identifying the role of terahertz vibrations in metal-organic frameworks: From gate-opening phenomenon to shear-driven structural destabilization. *Phys. Rev. Lett.* **113**, 1–6 (2014).
4. Casco, M. E. *et al.* Gate-opening effect in ZIF-8: the first experimental proof using inelastic neutron scattering. *Chem. Commun.* **52**, 3639–3642 (2016).
5. Fairen-Jimenez, D. *et al.* Opening the Gate: Framework Flexibility in ZIF-8 Explored by Experiments and Simulations. *J. Am. Chem. Soc.* **133**, 8900–8902 (2011).
6. Casco, M. E. *et al.* Understanding ZIF-8 Performance upon Gas Adsorption by Means of Inelastic Neutron Scattering. *ChemistrySelect* **2**, 2750–2753 (2017).
7. Aguado, S. *et al.* Guest-induced gate-opening of a zeolite imidazolate framework. *New J. Chem.* **35**, 546–550 (2011).
8. Cuadrado-Collados, C. *et al.* Understanding the breathing phenomena in nano-ZIF-7 upon gas adsorption. *J. Mater. Chem. A* **5**, 20938–20946 (2017).
9. Bennett, T. D. *et al.* Facile Mechanochemistry of Amorphous Zeolitic Imidazolate Frameworks. *J. Am. Chem. Soc.* **133**, 14546–14549 (2011).
10. Hartmann, M., Böhme, U., Hovestadt, M. & Paula, C. Adsorptive Separation of Olefin/Paraffin Mixtures with ZIF-4. *Langmuir* **31**, 12382–12389 (2015).
11. Wharmby, M. T. *et al.* Extreme flexibility in a zeolitic imidazolate framework: Porous to dense phase transition in desolvated ZIF-4. *Angew. Chemie - Int. Ed.* **54**, 6447–6451 (2015).

12. Bennett, T. D. *et al.* Reversible pressure-induced amorphization of a zeolitic imidazolate framework (ZIF-4). *Chem. Commun.* **47**, 7983 (2011).
13. Zhang, L., Hu, Z. & Jiang, J. Sorption-Induced Structural Transition of Zeolitic Imidazolate Framework-8: A Hybrid Molecular Simulation Study. *J. Am. Chem. Soc.* **135**, 3722–3728 (2013).
14. Du, Y. *et al.* New High- and Low-Temperature Phase Changes of ZIF-7: Elucidation and Prediction of the Thermodynamics of Transitions. *J. Am. Chem. Soc.* **137**, 13603–13611 (2015).
15. Rappe, A. K. & Goddard, W. A. Charge equilibration for molecular dynamics simulations. *J. Phys. Chem.* **95**, 3358–3363 (1991).
16. Tan, J.-C. *et al.* Exceptionally Low Shear Modulus in a Prototypical Imidazole-Based Metal-Organic Framework. *Phys. Rev. Lett.* **108**, 095502 (2012).
17. Nosé, S. Constant Temperature Molecular Dynamics Methods. *Prog. Theor. Phys. Suppl.* **103**, 1–46 (1991).
18. Parrinello, M. & Rahman, A. Polymorphic transitions in single crystals: A new molecular dynamics method. *J. Appl. Phys.* **52**, 7182–7190 (1981).
19. Martyna, G. J., Tobias, D. J. & Klein, M. L. Constant pressure molecular dynamics algorithms. *J. Chem. Phys.* **101**, 4177–4189 (1994).
20. Potoff, J. J. & Siepmann, J. I. Vapor–liquid equilibria of mixtures containing alkanes, carbon dioxide, and nitrogen. *AIChE J.* **47**, 1676–1682 (2001).
21. Wick, C. D., Siepmann, J. I., Klotz, W. L. & Schure, M. R. Temperature effects on the retention of n-alkanes and arenes in helium–squalane gas–liquid chromatography. *J. Chromatogr. A* **954**, 181–190 (2002).
22. Lin, S.-T., Blanco, M. & Goddard, W. A. The two-phase model for calculating thermodynamic properties of liquids from molecular dynamics: Validation for the phase diagram of Lennard-Jones fluids. *J. Chem. Phys.* **119**, 11792–11805 (2003).
23. Lewis, D. W. *et al.* Zeolitic imidazole frameworks: structural and energetics trends compared with their zeolite analogues. *CrystEngComm* **11**, 2272 (2009).
24. Bennett, T. D. *et al.* Melt-Quenched Glasses of Metal–Organic Frameworks. *J. Am. Chem. Soc.* **138**, 3484–3492 (2016).
25. Bennett, T. D. *et al.* Thermal amorphization of zeolitic imidazolate frameworks. *Angew. Chemie - Int. Ed.* **50**, 3067–3071 (2011).
26. Ramirez-Cuesta, A. J. aCLIMAX 4.0.1, The new version of the software for analyzing and interpreting INS spectra. *Comput. Phys. Commun.* **157**, 226–238 (2004).

27. Hwang, S. *et al.* Anomaly in the Chain Length Dependence of n-Alkane Diffusion in ZIF-4 Metal-Organic Frameworks. *Molecules* **23**, 668 (2018).



Universitat d'Alacant
Universidad de Alicante

CHAPTER 4

Gas Adsorption/Separation Properties of Mixed Linker ZIF-62

Chapter 4 describes the different approaches applied to understand the structural flexibility upon gas adsorption/separation in mixed linker based ZIFs. ZIF-62 is a MOF formed by the combination of benzimidazole and imidazole as a ligand, and zinc metal centres. Among the 105 ZIFs described in the literature, ZIF-62 has attracted enormous attention due to its unique characteristics and the emerging field in MOFs related to liquid crystals and glass formation. Even so, structural properties upon gas adsorption have not been completely elucidated. Chapter 4 combine different research techniques and methodologies such as synchrotron XRD, gas adsorption-desorption isotherms and, molecular modelling and simulation, to create a unique and deep overview of structural changes in ZIF-62 as a consequence of an external stimuli. SPXRD analysis showed a phase transition upon oxygen and nitrogen adsorption from a contracted phase to an expanded phase. Finally, molecular simulations showed the phase transition and the allocation of molecules in the ZIFs cavities. All this combined open a wide number of opportunities for application of these materials into the field of gas separation, such as hexane isomers or light hydrocarbon separation (C1-C4).

4.1. Introduction

Selective adsorption and separation of gases in industrial streams is highly challenging due to the similarity in the physico-chemical properties (size, shape and polarity) of the target molecules in a number of processes.¹ Clear examples of complex separation processes are the discrimination between linear and branched hydrocarbons,² to increase the octane number, O₂/N₂ separation from air,³ and adsorption of CO₂ and N₂ for natural gas upgrading,^{4,5} among others. These separation processes require the design of perfectly tailored 3D porous networks with the proper characteristics to promote these separation processes, for instance, with a proper pore size and shape to allow the selective adsorption of one of the molecules or with a proper polarity to promote specific framework interactions with the target molecules. For these specific processes, zeolites and carbon molecular sieves have been the most widely applied materials due to their intrinsic characteristics such as a high surface area, large pore volume and, in the specific case of the zeolites, a large polarity.^{6,7} Despite their promising performance, these materials are highly limited in terms of composition and associated versatility.

Another kind of materials with highly promising performance for gas separation are zeolitic-imidazolate frameworks (ZIFs). ZIFs are a sub-class of metal-organic frameworks (MOFs) characterized by a high thermal, hydrothermal and chemical stability due to the presence of a 3D network that resembles zeolites (tetrahedral topology), i.e. built up by metal ions (e.g., Zn) linked to four imidazolate molecules with a similar configuration to the Si-O-Si angle in zeolites.⁸ Contrary to traditional porous materials, including MOFs, ZIFs exhibit unique characteristics due to the intrinsic flexibility of their 3D network and the associated structural changes, for instance, gate-opening phenomena, breathing ability, amorphization, phase transition processes, among others.⁹⁻¹⁸ These structural changes are usually associated with an external stimulus, for instance, a high-temperature treatment, application of high pressure or upon exposure to a given gas atmosphere. Interestingly, these structural responses open the gate towards the application of these ZIFs in gas adsorption and separation processes, based not only on steric effects (size and shape of the pore cavities), but also on the presence of specific

adsorbent-adsorbate interactions able to induce structural changes, i.e. able to compete with the bonding and non-bonding interactions within the MOF structure. These principles have been widely explored in the literature for instance in ZIF-8 and ZIF-7 to promote selective hydrocarbon separation,^{17,19} and highly selective processes for H₂, CO₂, O₂, N₂ and CH₄.^{20,21} These results clearly anticipate that despite having a similar structure and sometimes even the same topology (e.g., ZIF-8 vs ZIF-7), the nature of the imidazolate ligand defines a completely different adsorption performance (see for instance the completely different nitrogen adsorption performance in ZIF-8 and ZIF-7, with sod topology, and the prototypical ZIF-4, with cag topology).^{9,11,13,16,22} As described above, the different performance has been attributed to the different interactions between the target molecules and the ZIF framework and the nature of the intranet interactions, defined by the organic imidazolate linker.

The versatility of ZIFs has been tremendously expanded upon the discovery of mixed-linker networks, i.e. the preparation of completely new porous networks through the combination of different imidazolate-based linkers. This is, for instance, the case of ZIF-62 [Zn(imidazolate)_{2-x}(benzimidazolate)_x], which is isostructural of ZIF-4, sharing the same imidazolate linker but with a small proportion ($x \sim 0.25$) of the bulkier benzimidazolate (bim-) linker.²³ Despite sharing the same space group (cag topology) and similar unit cell parameters as ZIF-4, recent studies have shown that the physico-chemical properties of these two ZIFs are rather different (for instance ZIF-62 exhibits a lower melting point and a wider melting range than ZIF-4 due to the higher electron donating properties and larger steric hindrance of bim-).^{24,25} Interestingly, ZIF-62 is able to form glasses with accessible porosity upon a melt-quenching treatment with very good selectivity values for H₂/CH₄, CO₂/N₂ and CO₂/CH₄ mixtures, although associated with a low adsorption capacity.²⁶ Despite the high interest in the glasses, the number of studies dealing with the adsorption and structural properties of the parent ZIF-62 is rather limited.

Taking into account the unique adsorption performance of these ZIFs and the intrinsic structural properties upon adsorption, the main goal of this manuscript is the understanding of the adsorption performance of ZIF-62 and the associated structural changes. Despite being analogous to ZIF-4, gas adsorption studies clearly

show a completely different behaviour, associated with distinct structural phenomena.

4.2. Experimental section

4.2.1. ZIF-62 Synthesis

ZIF-62 was synthesized using a solvothermal method similar to those reported in the literature ²⁷. Imidazole (0.525 g, 7.72 mmol) and benzimidazole (0.130 g, 1.10 mmol) were mixed with $\text{Zn}(\text{NO}_3)_2 \cdot 4\text{H}_2\text{O}$ (0.8 g, 3.06 mmol) in a solid mixture. The mixture was dissolved in 60 mL of N,N-Dimethylformamide and kept under agitation for half an hour. Subsequently, the liquid solution was transferred in a Teflon vessel (100 mL) and heated in an autoclave to 403 K with a heating rate of 5 K min⁻¹ and held to that temperature for 48 h. After the autoclave was at room temperature, the sample was washed several times with 30 mL of DMF (x2) and then with 30 mL of methanol (x2). Finally, the sample was exposed to a solvent exchange process with methanol (30 mL/day) for two days. The resulting white solid was filtered and activated under dynamic vacuum at 493 K for 8 h.

4.2.2. Synchrotron powder X-ray diffraction analysis

Synchrotron X-ray powder diffraction data (SXRPD) were collected on the powder diffraction end station of the MSPD beamline at synchrotron ALBA in Spain, using a MYTHEN detector and a wavelength of 0.4227 Å. The experiments were performed in an ad hoc capillary reaction cell (fused silica capillary, inner diameter 0.7 mm, outer diameter 0.85 mm). SXRPD measurements were performed at 90 K in ZIF-62 material, after the blank pattern was measured, oxygen or nitrogen was dosed to the capillary on amount of 0.3 bar, 0.6 bar and 1 bar and the pattern was measured. Finally, the sample with 1 bar of gas (oxygen or nitrogen) was heated up from 90 K to 300 K and the XRD pattern was measured.

4.2.3. Thermogravimetric Analysis

TGA analysis was carried out in air, with samples placed in ceramic crucibles and heated to 1000 °C (ramp rate of 10 °C min⁻¹). All results were recorded TG-DTA METTLER TOLEDO equipment model TG/SDTA851e/SF/1100

4.2.4. Scanning electron microscopy

ZIF-62 micrographs were recorded using a field emission scanning electron microscope (FESEM) Merlin VP Compact from Zeiss equipped with an EDS microanalysis system Quantax 400 from Bruker. This equipment has resolution of 0.8 nm at 15 kV and 1.6 nm at 1 kV. ZIF-62 sample was kept in methanol until measurement.

4.2.5. Adsorption isotherms

N₂ and O₂ isotherms at 77 K, 195 K and 298 K were performed in a homemade fully automated manometric equipment designed and constructed by the Advanced Materials Group (LMA), now commercialized as N2GSorb-6 (Gas to Materials Technologies; www.g2mtech.com). The samples were previously degassed for 8 h at 493 K under vacuum (10⁻³ Pa). Gas hydrocarbon and vapor molecules adsorption isotherms at 298 K were carried out in under similar conditions (equilibrium points, 10; interval time, 30 s; sorption rate limit, 0.01 Torr/ min). These measurements were performed in a homemade fully automated manometric equipment, now commercialized by Quantachrome as VStar.

4.2.6. Molecular modelling and simulations

Monte Carlo simulations were performed using RASPA software³⁷. First, grand canonical Monte Carlo (GCMC) simulations were carried out to compute adsorption isotherms of O₂ and N₂ in ZIF-62 at 77, 195 and 298 K, and to estimate the saturation loading at 0.8 bar and 77, 97, 117, 137, 157, 177, 195, 215, 235, 255, 275 and 298 K. Then, Monte Carlo simulations in the canonical ensemble (CMC) were run to compute the energy histograms of 100, 150 and 200 molecules of O₂ and N₂ in ZIF-62 at 77K. Simulations were arranged in cycles of trial moves, including translations and rotations of molecules for CMC and GCMC simulations,

and insertions and deletions of molecules for GCMC simulations. Results were obtained after 30 000 initialization cycles and 100 000 production cycles. Pore size distribution for ZIF-62 was computed with RASPA software as well, and the porosity of the framework was studied with PoreBlazer³⁸.

Van der Waals interactions in the system were described by 12-6 Lennard-Jones (LJ) potentials with a cut-off at 12.8 Å, and Lorentz-Berthelot mixing rules were used to calculate adsorbate-adsorbate and adsorbate-adsorbent interactions. Electrostatic interactions were described by Coulomb potentials and computed using Ewald summations. The simulation box was at least twice the cut-off, for which a 2 x 2 x 2 supercell was chosen, and periodic boundary conditions were applied. TraPPE force field was used to model O239 and N240 molecules. ZIF-62 was modelled as rigid with its framework atoms fixed at their crystallographic positions, which were taken from CCDC-671070.²⁷ The LJ parameters and partial charges for the framework atoms of ZIF-62 were derived from previously published force fields for ZIF materials^{28,29}. All these force field parameters are summarised in **Table 4.1** and **4.2**.

Table 4.1. Lennard-Jones parameters and partial charges for framework atoms.

Atom	$\epsilon \text{ k}_B^{-1} /$	$\sigma / \text{Å}$	Charge
C1	33.58	3.431	0.2593
C2	33.58	3.431	-0.0839
C3	33.58	3.431	0.0391
C4	33.58	3.431	-0.1179
H1	15.10	2.42	0.1128
H2	14.047	2.571	0.1128
H4	14.047	2.571	0.1128
N1	22.05	3.261	-0.3879
Zn	39.62	2.462	0.6918

Table 4.2. Lennard-Jones parameters and partial charges for adsorbates.

Atom	ϵ	$\sigma / \text{Å}$	Charge (e-)
Oxygen			
O_O2	49.0	3.020	-0.113
O_com	0	0	0.226
Nitrogen			
N_N2	36.0	3.310	-0.482
N_com	0	0	0.964

4.3. Results

4.3.1. Synthesis and characterization of ZIF-62.

The crystal structure of ZIF-62 synthesized by solvothermal method has been reported before in the literature by Banerjee *et al.*²⁷ The first approach of the research was to synthesize a material with high crystallinity and reproducibility. **Figure 4.1** shows the comparative SPXRD pattern of as-synthesized ZIF-62 (green line) which closely match to the simulated pattern (dotted line) verifying the crystalline nature, the reproducibility of the synthesis method and the quality of the ZIF-62. The unit cell parameters obtained after Rietveld refinement are $a = 15.4659(4)\text{\AA}$, $b = 15.5981(3)\text{\AA}$ and $c = 17.9667(4)\text{\AA}$, with a volume $V = 4334.3(2)\text{\AA}^3$ (orthorhombic space group $Pbca$). These values are similar to those reported before in the literature.^{23,27}

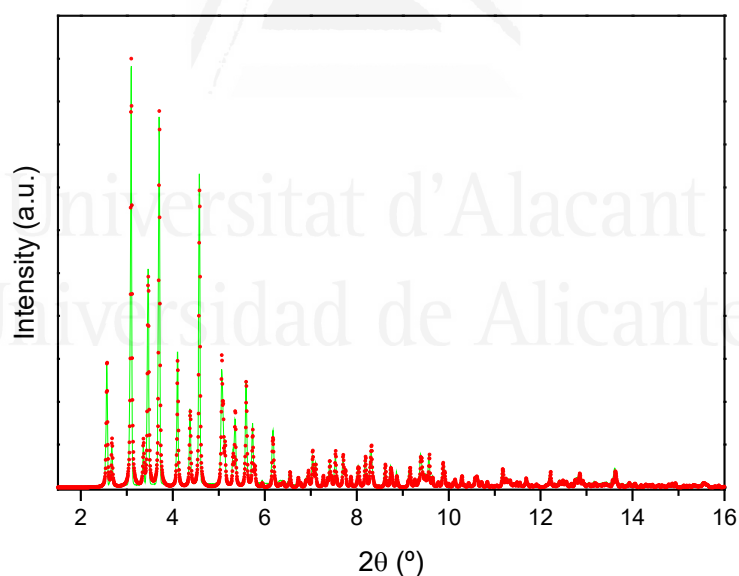


Figure 4.1. SPXRD pattern of as synthesized ZIF-62 (green line) and simulated pattern (dotted line).

The morphology of the synthesized ZIF-62 nanoparticles is shown in **Figure 4.2**. The morphology of the synthesized crystals is of well-defined corner-shared octahedral shape crystals with a heterogeneous particle size among 5 μm and 20

μm . As it has been reported in the literature, the blm:lm ratio may have a considerable influence in the shape and size of ZIF-62 nanoparticles.²³

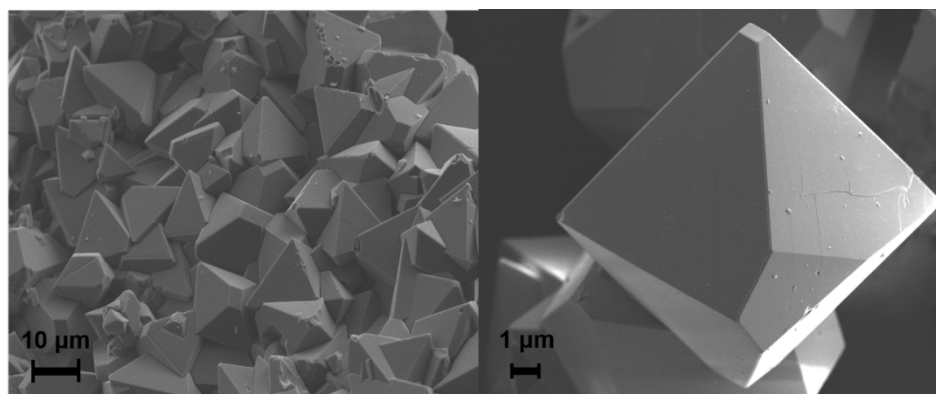


Figure 4.2. FESEM images of as-synthesized ZIF-62

The thermal stability of ZIF-62 has been evaluated using thermogravimetric analysis (TGA). As it can be observed in **Figure 4.3**, the as-synthesized material exhibits a first weight-loss of ca. 10% between 400 K and 650 K due to the removal of the solvent (DMF) and a second weight loss of ca. 55% between 700 K and 1273 K due to the decomposition of the framework. As it has been well described in the literature, close to 700 K an interesting phenomena called melt quenching glass formation is observed in ZIF-62.²⁴

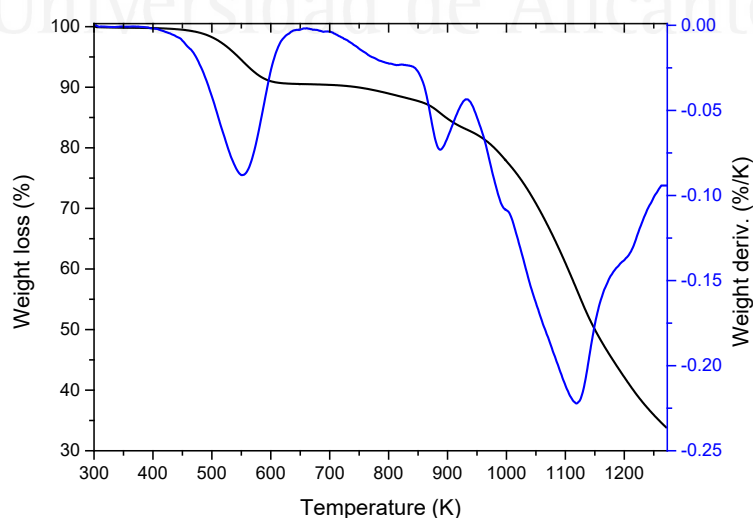


Figure 4.3. TG-DTA thermogram of as-synthesized ZIF-62.

At this point, it is important to highlight the high temperature required to remove the DMF from the ZIF-62 structure, i.e. around 550 K. Compared to other ZIFs (e.g., ZIF-7 and ZIF-4), where activation temperatures around 373 K - 423 K are usually sufficient to empty the cavities, in the specific case of ZIF-62 TG-DTA analysis anticipate that higher temperatures are required. This can be clearly reflected in the TG-DTA analysis (**Figure 4.4**) of the ZIF-62 sample performed after an outgassing treatment under ultra-high vacuum conditions at 413 K and 493 K for 12 h, the complete removal of the solvent being effective only at 493 K.

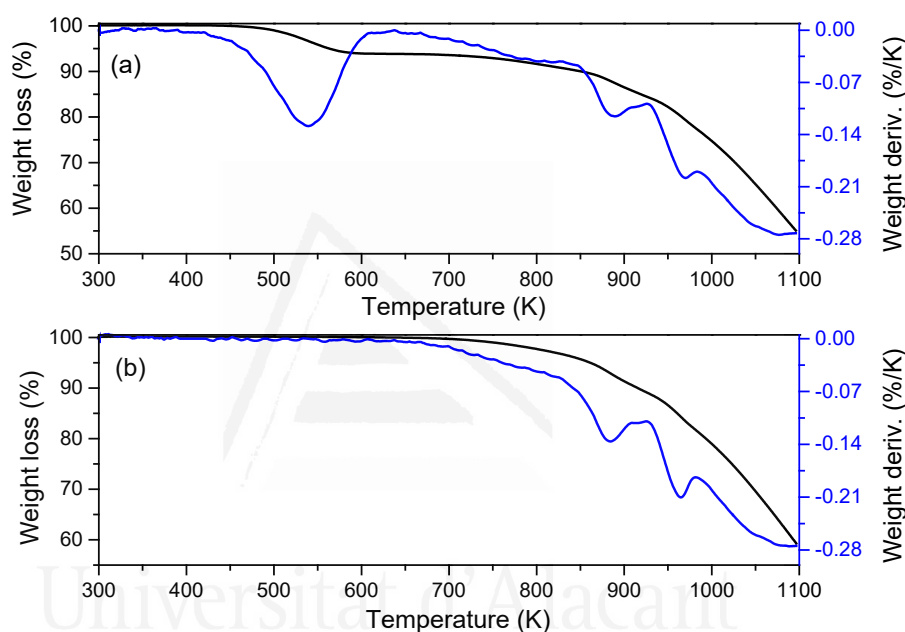


Figure 4.4. TG-DTA thermograms of high-vacuum outgassed ZIF-62 at (a) 413 K and (b) 293 K

4.3.2. Nitrogen and oxygen adsorption/desorption isotherms.

The adsorption performance of ZIF-62 has been evaluated towards N_2 and O_2 at different temperatures. The separation of these two molecules is a challenging process using porous materials due to their similar size and shape (kinetic diameter for N_2 , 0.364 nm, and for O_2 , 0.346 nm). Traditionally their separation using zeolites and MOFs is based on the faster adsorption kinetics for O_2 over N_2 .^{30,31}

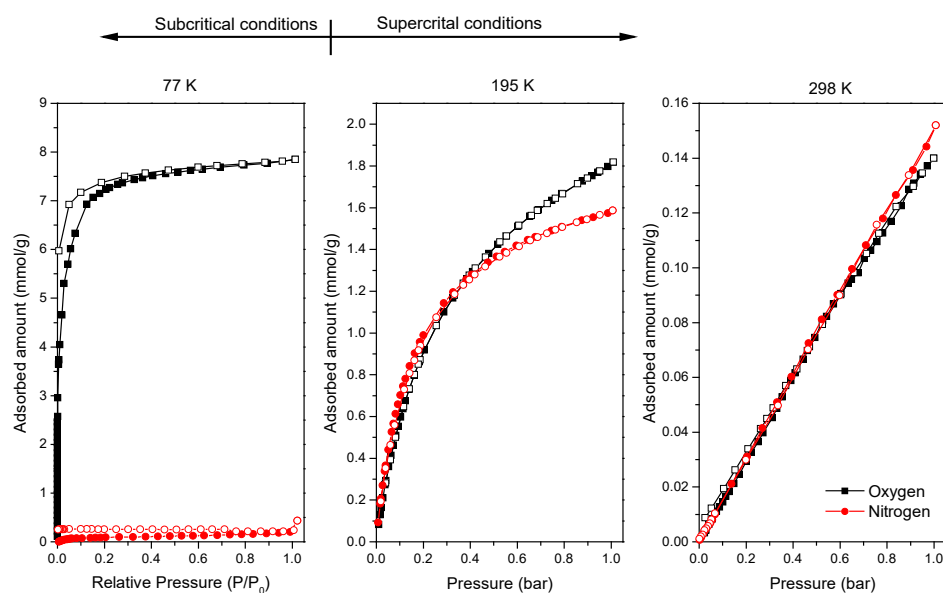


Figure 4.5. Nitrogen and oxygen adsorption-desorption isotherms in ZIF-62 at 77 K, 195 K and 298 K.

As it can be appreciated in **Figure 4.5**, at cryogenic temperatures ZIF-62 exhibits a large adsorption capacity for O₂ (up to 8 mmol/g at saturation pressure). This value is among the best values reported and predicted in the literature for O₂ adsorption under subcritical conditions.³² For instance, Dinca *et al.* reported an adsorption capacity for Cu(BDT) of 14 mmol/g at 77K and Humphrey *et al.* reported up to 6 mmol/g for CUK-1 at 87K.^{33,34} Interestingly, ZIF-62 is able to selectively adsorb O₂ over N₂ with high selectivity at cryogenic temperatures over the whole relative pressure range evaluated (selectivity above 68 at $p/p_0 = 0.4$). These selectivity values are among the best reported in the literature for O₂/N₂ separation in MOFs at 77K.^{33,34} Unfortunately, these excellent adsorption properties vanish under less energy-intensive experimental conditions, i.e. at 195K and 298K. At 195K both probe molecules exhibit a type I isotherm with full accessibility to the inner porous structure, slightly favoured for O₂ at 1 bar (1.8 mmol/g vs 1.6 mmol/g for N₂; O₂/N₂ ratio of 1.14). In any case, the adsorption performance and the preferential adsorption of O₂ vanish at 298K with a total uptake lower than 0.15 mmol/g and no selectivity. Although under equilibrium conditions, both probe molecules exhibit similar accessibility to the

inner porous structure at 195K and 298K, O₂ diffusion is always favoured over nitrogen (**Figure 4.6**).

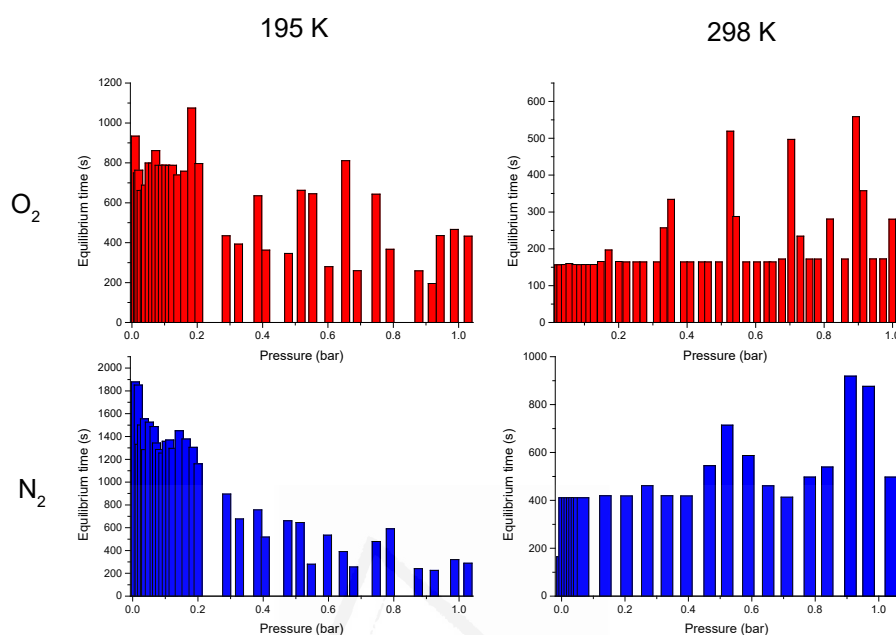


Figure 4.6. Time requested for each specific adsorption point at the N₂ and O₂ isotherms to reach equilibrium. Values are reported only for isotherms performed at 195K and 298K.

The problems of accessibility for nitrogen in ZIFs at 77K have been widely reported in the literature. For instance, in the specific case of ZIF-8 computational studies combined with synchrotron X-ray diffraction data and inelastic neutron scattering (INS) have shown that, upon nitrogen adsorption, ZIF-8 structure experience a gate-opening effect through the swinging of the imidazolate linker.^{9,13} In the case of ZIF-7 and ZIF-4, although nitrogen adsorption is kinetically restricted and requires large equilibration times, synchrotron X-ray diffraction measurements have clearly shown a phase transition from a highly dense narrow pore phase to an expanded phase, i.e. these ZIFs are able to breathe.^{16,22} Contrary to these ZIFs, nitrogen adsorption in ZIF-62 at cryogenic temperatures is rather zero over the whole pressure range evaluated. Even when the N₂ isotherms are performed under strict equilibrium conditions (**Figure 4.7**), although nitrogen uptake improves, the obtained values are far from the adsorption capacity for a similar molecule such as O₂.

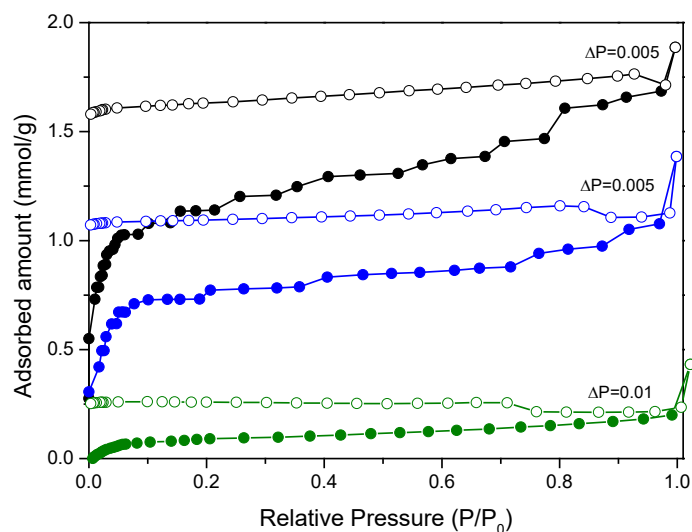


Figure 4.7. Nitrogen adsorption-desorption isotherms at 77 K in ZIF-62 performed under different equilibrium conditions (ΔP = pressure variation allowed between consecutive pressure readings before reaching equilibrium).

A similar performance is observed after a milling process to decrease the ZIF-62 crystal size (**Figure 4.8**). In this specific case, N_2 adsorption slightly increases, thus reflecting the kinetic problems of N_2 to access the inner porous structure in ZIF-62.

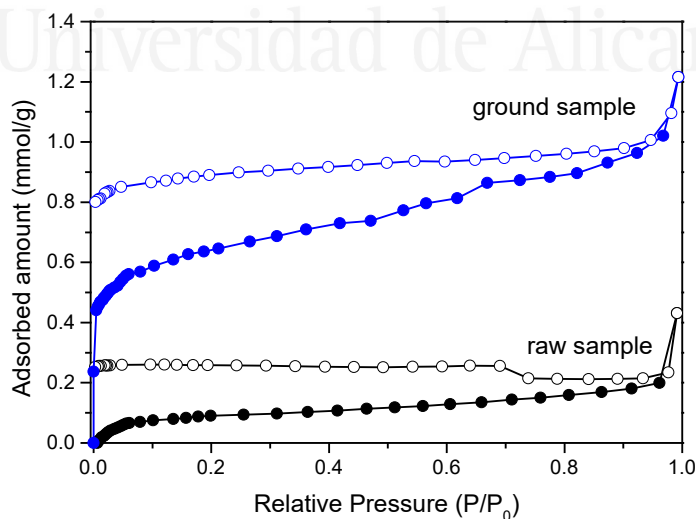


Figure 4.8. Comparative nitrogen adsorption-desorption isotherms in as-synthesized and grounded ZIF-62 at 77K.

4.3.3. Oxygen and nitrogen adsorption simulation in ZIF-62

The adsorption performance of the ZIF-62 material has been modelled using Grand-canonical Monte Carlo simulation in a rigid model. **Figure 4.9** and **Figure 4.10** compare the computational data for O₂ and N₂ adsorption at the three temperatures evaluated (77K, 195K and 298K) with the experimental data described above (**Figure 4.5**).

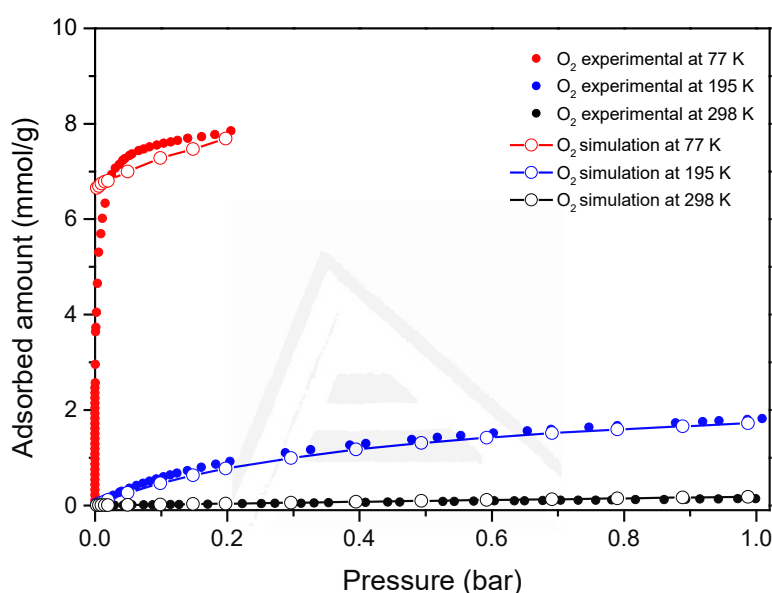


Figure 4.9. comparative adsorption oxygen isotherms at 77 K, 195 K and 298 K (filled symbol experimental value and empty symbol simulated value).

As it can be appreciated in **Figure 4.9**, simulations are able to predict the O₂ adsorption performance in ZIF-62 for the three temperatures evaluated, thus validating the model framework used. However, the scenario changes significantly for nitrogen. Whereas the adsorption performance at 195 K and 298 K can be easily predicted by the model, simulations highly overestimate the adsorption performance for nitrogen at 77 K. In fact, the predicted uptake at cryogenic temperatures for N₂ was close to 6 mmol/g, far from the experimental value (0.43 mmol/g).

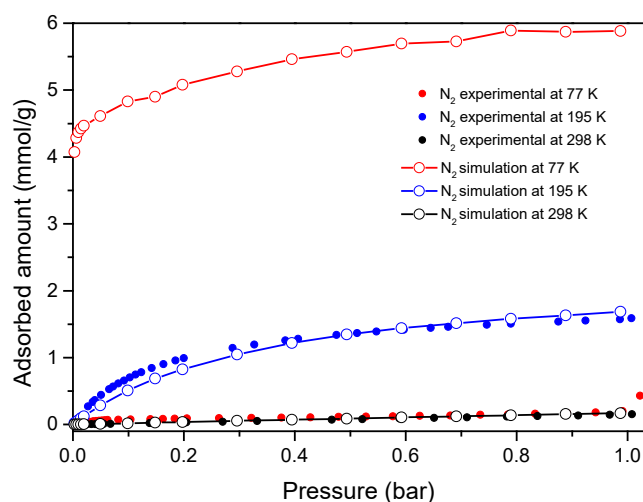


Figure 4.10. Experimental and simulated nitrogen adsorption isotherms at 77 K, 195 K and 298 K (filled symbol experimental value and empty symbol simulated value).

The variation in the uptake for these two probes at different temperatures can be clearly appreciated in **Figure 4.11**. Based on the simulation, two well-defined regions can be appreciated. Above 190 K N_2 and O_2 exhibit a similar adsorption behaviour with a progressive decay with temperature. Below 190 K both probes exhibit an exponential increase in the accessibility, the increase being more marked for O_2 with a total uptake predicted at 77 K of 7.8 mmol/g for O_2 and 5.9 mmol/g for N_2 (theoretical selectivity ratio 1.3).

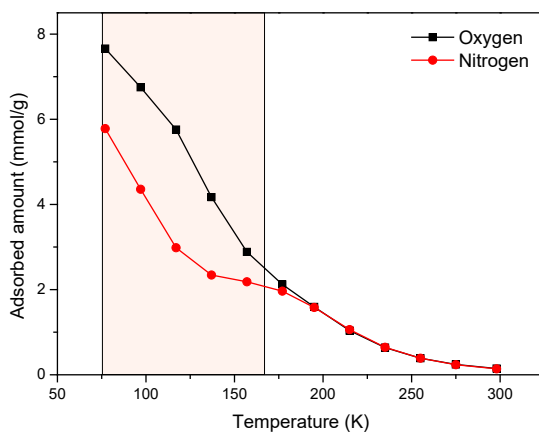


Figure 4.11. ZIF-62 loaded with oxygen and nitrogen at 0.2 bar as a function of the temperature.

Table 4.3 summarises the host-guest and guest-guest contributions per molecule to the system energy at saturation pressure obtained from the computed adsorption isotherms. In the region where adsorption performances are comparable and well predicted by the model, at 298 and 195K, there are no significant differences in the host-guest and guest-guest interactions. At 77K the host-guest interaction of O₂ molecules (-14.436 kJ mol⁻¹) and N₂ (-14.041 kJ mol⁻¹) are very similar. However, the guest-guest contribution per molecule to the system energy is 3.3 times higher for O₂ (-1.25 kJ mol⁻¹) than for N₂ (-0.38 kJ mol⁻¹), suggesting that a higher interaction between molecules of O₂ as the possible reason for the adsorption trends in this region.

Table 4.3. Energy computed in the ZIF-62 system per molecule at saturation (1 bar) at 77, 195 and 298 K, in a 2 x 2 x 2 simulation box.

T / K	O ₂ data			N ₂ data		
	Loading	Host-Guest	Guest-Guest	Loading	Host-Guest	Guest-Guest
77	217 molec.	-14.436 kJ mol ⁻¹	-1.25 kJ mol ⁻¹	169 molec.	-14.041 kJ mol ⁻¹	-0.38 kJ mol ⁻¹
195	49 molec.	-14.268 kJ mol ⁻¹	-0.06 kJ mol ⁻¹	47 molec.	-15.443 kJ mol ⁻¹	-0.05 kJ mol ⁻¹
298	5 molec.	-14.127 kJ mol ⁻¹	-0.005 kJ mol ⁻¹	4 molec.	-14.423 kJ mol ⁻¹	-0.005 kJ mol ⁻¹
77*	220 molec.	-14.366 kJ mol ⁻¹	-1.25 kJ mol ⁻¹	145 molec.	-14.485 kJ mol ⁻¹	-0.34 kJ mol ⁻¹

(*) Energies computed in the system at 0.2 bar and 77K, in a 2 x 2 x 2 simulation box, where oxygen adsorption is already at saturation.

Figure 4.12 shows the energy histograms for the system containing 100, 150 and 200 molecules of O₂ and N₂ at 77 K to explore the behaviour of the adsorbate at analogous conditions. The total energy of the systems sit around -1500 kJ mol⁻¹ for a loading of 100 molecules, and these values increase (in absolute values) at a higher rate for O₂ when the loading increases. Here, the negligible difference found in the host-guest contribution per molecule at 77K (**Table 4.3**) becomes significant, resulting in a difference of 300 kJ mol⁻¹ when the ZIF-62 model is loaded with 200 molecules of O₂ (-2959.18 kJ mol⁻¹) or N₂ (-2648.89 kJ mol⁻¹). Similarly, the values of the guest-guest contribution are 3.8 times higher for O₂ (-239.77 kJ mol⁻¹), generating a shift to the left of 177.12 kJ mol⁻¹. Although host-guest interactions account for roughly the 90% of the total energy in the system, guest-guest interactions are responsible for a third of the differences in the energies between the systems loaded with 200 molecules of O₂ or N₂. Thus, host-guest and guest-guest interactions combined generate an overall difference of 500 kJ mol⁻¹, with a total energy of -3202.28 and -2701 kJ mol⁻¹ for O₂ and N₂, respectively. In addition,

comparing the loading at saturation pressure of O₂ (~200 molecules) and N₂ (~150 molecules), the ZIF-62 model with adsorbed O₂ shows a total energy 1000 kJ mol⁻¹ higher than the model with N₂.

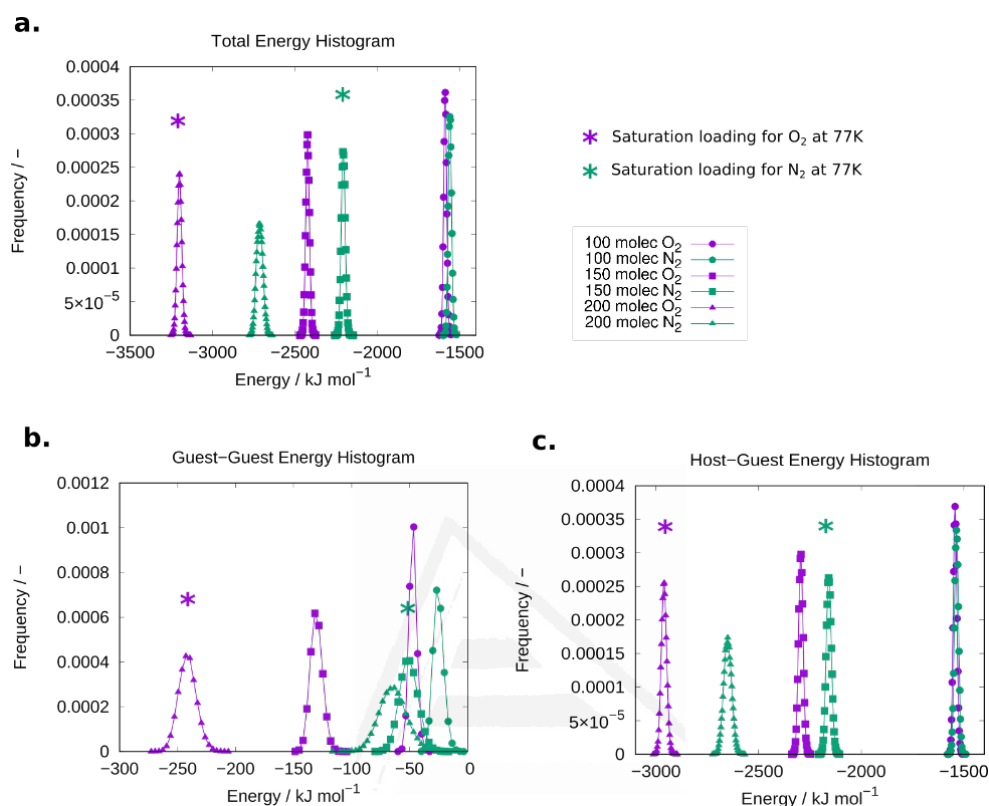


Figure 4.12. Computed energy histograms of total energy of the system (a) and guest-guest (b) and host-guest (c) contributions for O₂ and N₂ in ZIF-62 at 77K.

The porosity of ZIF-62 was studied computationally and is shown in **Figure 4.13**. The pore space within the framework (**Figure 4.13, left**) is characterised by cages with three windows that connect them to the other two cages. According to PoreBlazer³⁵ the pore limiting diameter (PLD) and largest cavity diameter (LCD) are 1.4 Å and 4.57 Å, respectively. These values agree with those observed in the computed pore size distribution (PSD), which shows a high and narrow peak around 4.6 Å, and a wider and lower peak around 1.5 Å (**Figure 4.13, right**). Thus, the cages observed in the pore space of ZIF-62 correspond to the size of the LCD and the higher peak in the PSD. Similarly, the PLD and the lower peak of the PSD mark the size of the channels that connect the cages and therefore limit the diffusion of molecules. Given that this pore opening is smaller than the size of the molecules, a

structural distortion must occur, at least locally, leading to the gate opening that will allow the diffusion of the adsorbates, regardless of the temperature.

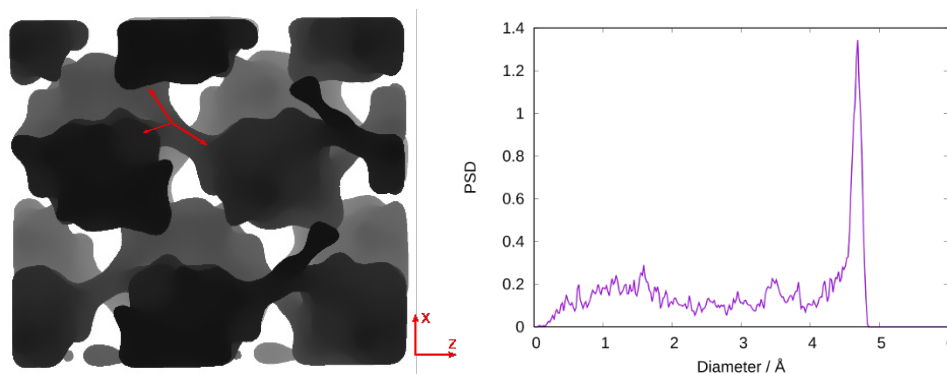


Figure 4.13. Porosity observed from xz-view (left) and pore size distribution (right) of ZIF-62.

GCMC simulations performed in the rigid ZIF-62 do not consider kinetic effects in the ZIF-62 model and thus, cannot reproduce deviations in the adsorption caused by kinetic reasons. However, they capture the different behaviour of O₂ and N₂ within the structure at different temperatures and suggest that the lower interactions between N₂ molecules at 77K and its lower interaction with the framework underlie the kinetic problems of N₂ to access the pores of ZIF-62.

4.3.4. ZIF-62 structure analysis using synchrotron power X-ray diffraction

The presence of structural changes upon adsorption has been evaluated using synchrotron X-ray powder diffraction measurements under operando conditions. To this end, ZIF-62 was cooled down to 90 K and dosed with O₂ or N₂ from low pressures up to 1 bar. Activated ZIF-62 at 90 K under vacuum exhibits an orthorhombic structure with $a = 15.3978(6)$, $b = 15.4138(6)$, $c = 17.9555(6)$, and $v = 4261.5(4)$. These values correspond to a unit cell contraction upon cooling of ca. 1.7%, in close agreement with previous data with ZIF-4.¹⁶ Once at 90 K the reaction cell was pressurized with O₂ up to 1 bar. **Figure 4.14** shows that upon oxygen incorporation there is a decrease in the intensity of the main diffraction peaks at 3.0, 3.4, 3.7, 4.0 and 4.5° and the appearance of new peaks as a shoulder at 2.9, 3.9 and 4.4°.

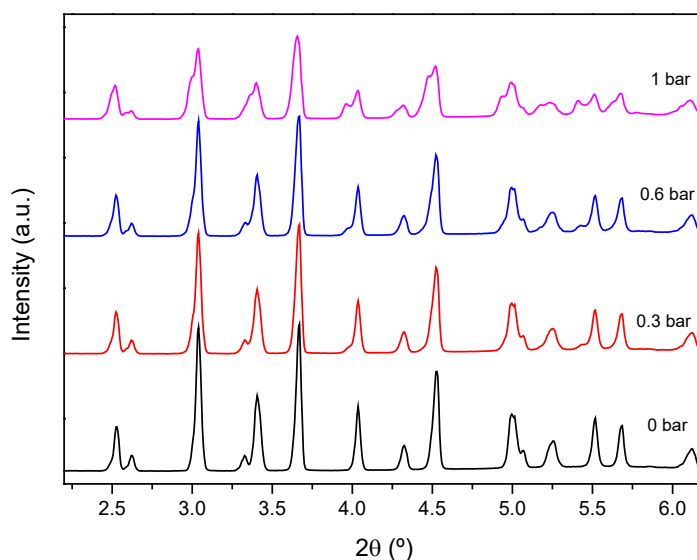


Figure 4.14. SPXRD patterns of ZIF-62 at 90 K loaded with 0.3, 0.6 and 1 bar of O₂.

Rietveld refinement analysis of the sample exposed to 1 bar at 90K show the presence of two phases, an expanded phase (ep) with unit cell parameters $a = 15.697(1) \text{ \AA}$, $b = 15.470(1) \text{ \AA}$, $c = 18.221(1) \text{ \AA}$, and $v = 4424.6(5) \text{ \AA}^3$ (solid symbols in **Figure 4.15**), and a contracted phase (cp) with cell parameters $a = 15.4279(8) \text{ \AA}$, $b = 15.4104(7) \text{ \AA}$, $c = 17.9604(9) \text{ \AA}$, and $v = 4270.1(4) \text{ \AA}^3$ (empty symbols in **Figure 4.15**).

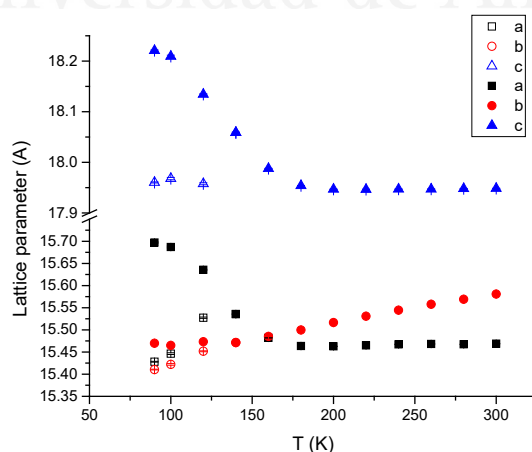


Figure 4.15. Variation in the unit cell parameters for ZIF-62 at different temperatures and 1 bar of O₂.

The expanded phase corresponds to ca. 3.8% volume expansion upon O₂ dosing. **Figure 4.16** shows the structural change upon the heating of the sample loaded with 1 bar of O₂. It is observed the peaks attributed to the prevalence of the two phases in the low temperature region up to 140K, the contracted phase disappearing afterwards. The remaining phase exhibits a certain contraction down to 175 K (**Figure 4.20**), followed by a slight expansion up to 300 K with unit cell parameters $a = 15.4688(4) \text{ \AA}$, $b = 15.5810(4) \text{ \AA}$, $c = 17.9484(6) \text{ \AA}$, and $v = 4325.9(2) \text{ \AA}^3$ at 300K. These values are rather similar to those described above for the activated ZIF-62 structure at 300K under vacuum, thus reflecting the scarce uptake of O₂ at room temperature in this system, in close agreement with the adsorption isotherms in **Figure 4.5**. The presence of these two regions in ZIF-62 with the expanded phase (ep) vanishing at 160-170 K perfectly correlates with the theoretical predictions and the large oxygen uptake below 160 K (see **Figure 4.11**).

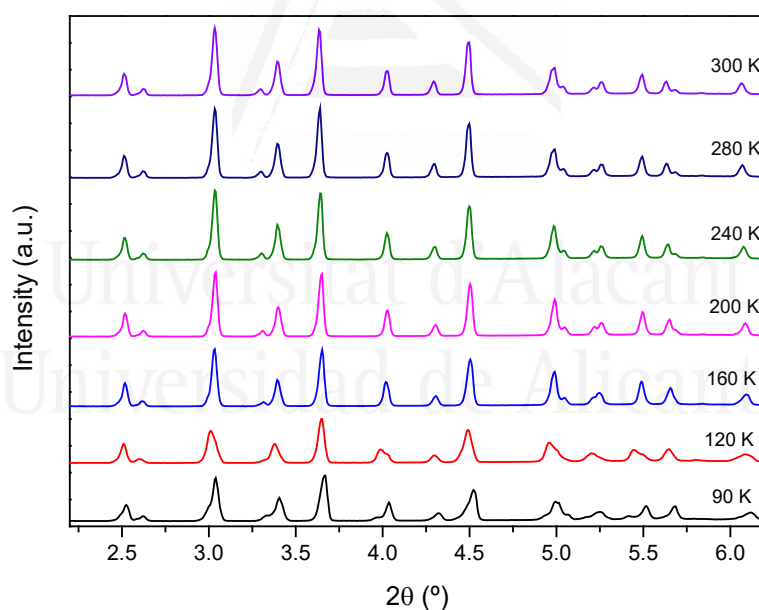


Figure 4.16. SPXRD patterns of ZIF-62 loaded with 1 bar of oxygen from 90 K to 300

Similar experiments have been performed for ZIF-62 at 90K dosing N₂ up to 1 bar (**Figure 4.17**). Contrary to the adsorption isotherms described above, N₂ at 90 K is able to produce significant changes in the XRD pattern upon adsorption.

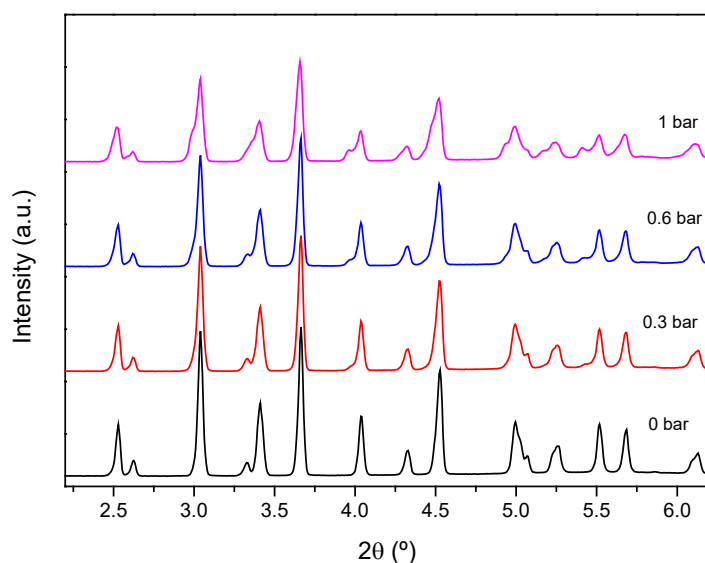


Figure 4.17. SPXRD patterns of ZIF-62 at 90 K loaded with 0.3, 0.6 and 1 bar of nitrogen.

Similar to oxygen, incorporation of nitrogen at 90K and 1 bar gives rise to the development of two phases, an expanded phase (ep) with unit cell parameters $a = 15.677(1) \text{ \AA}$, $b = 15.459(1) \text{ \AA}$, $c = 18.206(1) \text{ \AA}$, and $v = 4412.4(5) \text{ \AA}^3$, and a contracted phase (cp) with parameters $a = 15.4035(5) \text{ \AA}$, $b = 15.4285(5) \text{ \AA}$, $c = 17.9603(6) \text{ \AA}$, and $v = 4268.3(3) \text{ \AA}^3$ (**Figure 4.18**).

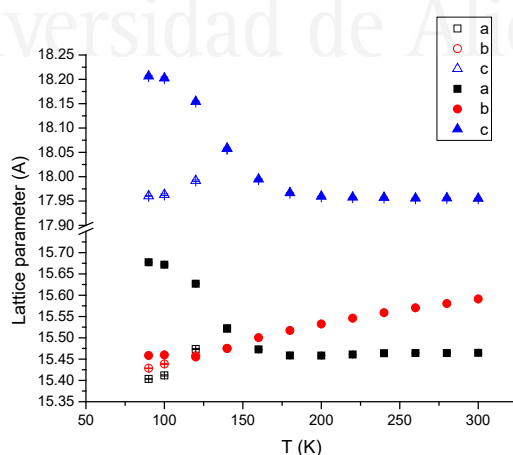


Figure 4.18. Variation in the unit cell parameters for ZIF-62 at different temperatures and 1 bar of N_2 .

The expanded phase observed after nitrogen dosing corresponds to a 3.5% unit cell expansion (**Figure 4.20**). As described above for O₂, the two phases prevail only at low temperatures, the contracted phase disappearing at 140 K (**Figure 4.19**). These results clearly show that the performance of ZIF-62 under operando conditions is rather similar for O₂ and N₂, as described in **Figure 4.20** (although slightly favoured for O₂). These results can be explained due to the different experimental conditions used in the synchrotron XRPD measurements and the gas adsorption isotherms performed at cryogenic temperatures. These differences include a slightly different adsorption temperature (90K vs 77K), a slightly smaller particle size (samples for SXRPD must be finely grounded) and the different dimensions of the reactor (experiments at the synchrotron are performed using a thin capillary reactor). These results confirm that the inaccessibility of nitrogen to the inner porous structure of ZIF-62 at 77 K is not due to a pore size and shape restriction but rather to kinetic restrictions due to the nature of the nitrogen-framework interactions. Larger temperatures are needed to overcome these kinetic limitations.

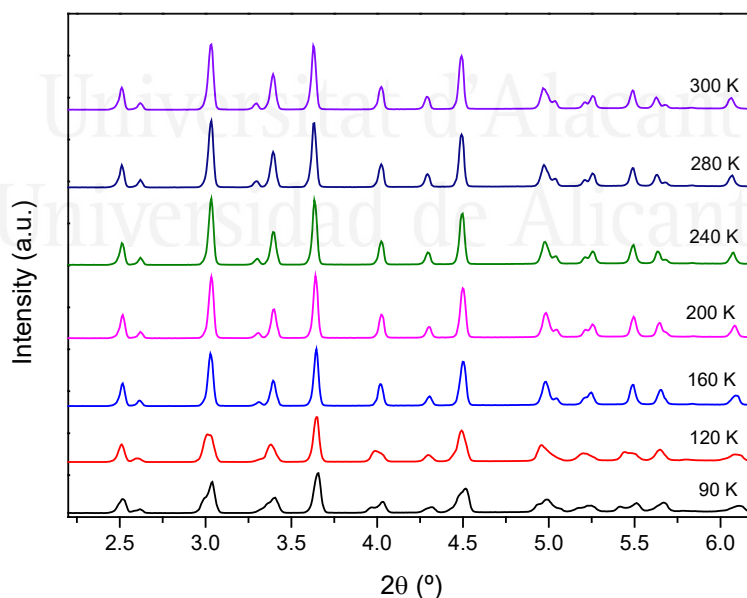


Figure 4.19. SPXRD patterns of ZIF-62 loaded with 1 bar of nitrogen from 90 K to 300 K.

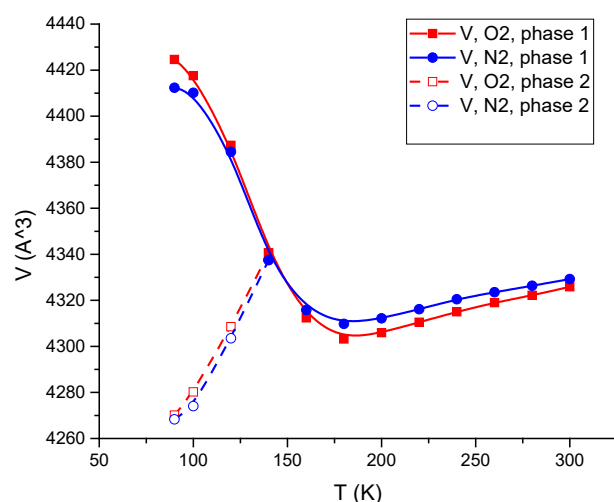


Figure 4.20. Temperature scanning of cell volume in ZIF-62 filled with 1 bar of oxygen (red lines) nitrogen (blue lines) from 90 K to 300 K.

4.3.5. Adsorption of bulkier molecules: linear and branched hydrocarbons

Although ZIFs are characterized by a small pore aperture (e.g., predicted limiting pore size window for ZIF-4 ~ 0.21 nm³⁶, ZIF-7 ~ 0.3 nm²⁷, and ZIF-8 ~ 0.34 nm³⁷), previous studies reported in the literature have shown that these systems are able to adsorb larger molecules, e.g., hydrocarbons, due to the presence of structural effects, for instance, gate-opening phenomena, responsible for the promoted accessibility to the inner porous structure to "unexpected" molecules. Although to our knowledge there are no studies in the literature dealing with hydrocarbon adsorption in ZIF-62, its glass counterpart a_g ZIF-62 has been reported to adsorb linear hydrocarbons (e.g., n-butane) with a significant uptake (up to 0.8 mmol/g), although with certain irreversibility due to the restricted accessibility of these molecules through the reduced pore size aperture of the glass (i.e., 0.25 nm).^{25,38} These studies have anticipated that a_g ZIF-62 is also able to separate alkanes/alkenes based on the faster diffusion of the unsaturated hydrocarbon.

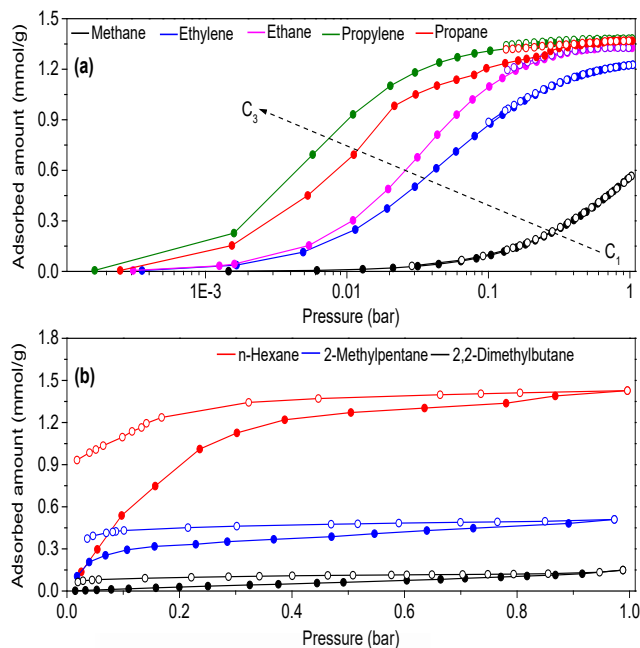


Figure 4.21. Adsorption isotherms for (a) linear and (b) branched hydrocarbons in ZIF-62 at 298 K.

Figure 4.21 shows the adsorption performance of ZIF-62 for (a) linear (C₁-C₃) and (b) linear/branched (C₆) hydrocarbons at 298 K and up to atmospheric pressure. In the specific case of the linear hydrocarbons, these studies have been extended to alkane/alkene adsorption processes to observe the effect of the unsaturated double bonds in ZIF-62. **Figure 4.21a** shows that all hydrocarbons tested are able to access the inner cavities in ZIF-62, independently of the kinetic diameter of the probe molecule (up to 0.43 nm for propane). This observation reinforces the hypothesis that the lack of accessibility for nitrogen at 77K is not due to pore size inaccessibility but rather to kinetic restrictions. Adsorption uptake for hydrocarbon increases with the number of carbon atoms in the aliphatic chain from C₁ (~ 0.6 mmol/g) up to C₃ (~ 1.4 mmol/g). This behaviour has also been observed for other ZIFs, and it must be attributed to the lower condensation pressure of C₃ hydrocarbons versus their lower molecular mass counterparts (e.g., CH₄).¹⁷ Taking a closer look to the C₂ series, experimental results show that ethane exhibits an improved uptake compared to ethylene over the whole pressure range evaluated. The preferential adsorption of the saturated hydrocarbon can be associated with its slightly larger kinetic diameter (~ 0.2 Å) compared to its unsaturated counterpart,

thus having a better fitting in the ZIF cavities and a larger adsorption potential.³⁹ However, the diffusion of the C₂ hydrocarbons follows an opposite trend with the smaller alkene (ethylene) exhibiting a shorter equilibration time (faster diffusion), in close agreement with previous results in a_gZIF-62 (see **Figure 4.22**).²⁵ In any case, the adsorption uptake for hydrocarbons is much larger in the parent ZIF-62 compared to the glass counterpart. The adsorption uptake further increases for propylene (C₃) and shifts to lower pressures compared to C₂ hydrocarbons, following the expected tendency. Only propane with a larger chain length and a larger kinetic diameter experiences problem to access the porosity, the adsorption isotherm exhibiting unexpected steps (e.g., at p ~ 0.1-0.2 bar) and marked irreversibility.

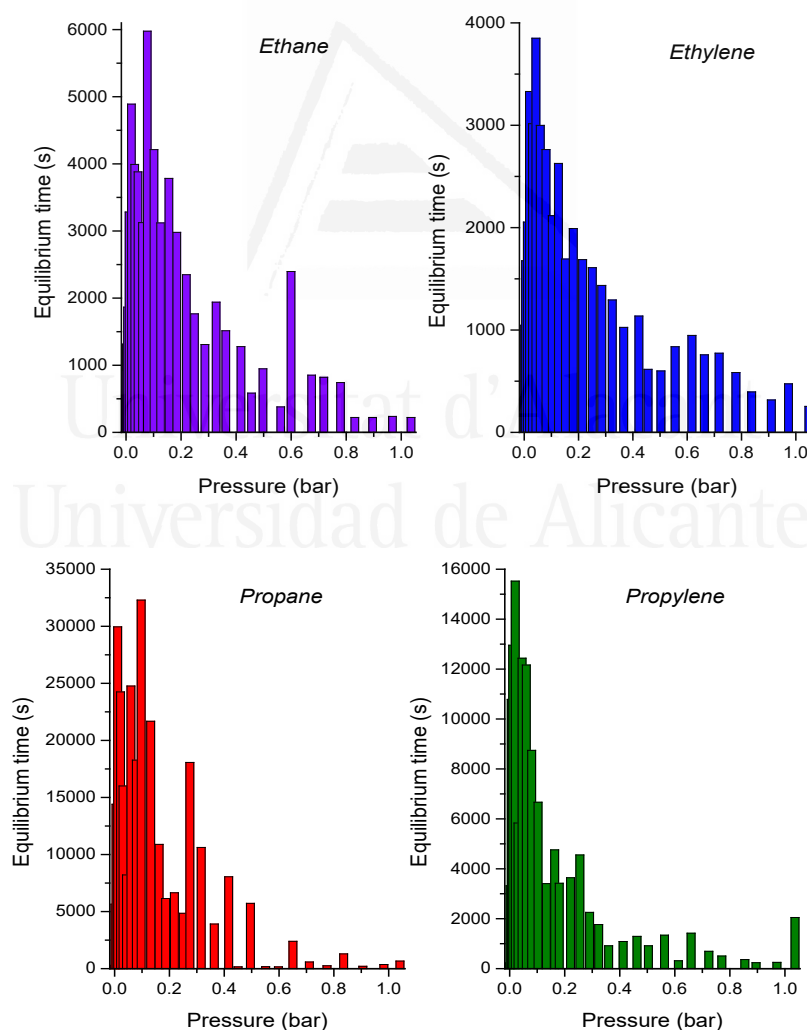


Figure 4.22. Time requested to reach equilibrium for each specific point at the alkane/alkene adsorption isotherms performed in ZIF-62 at 298K.

Last but not least, the adsorption performance has been tested for bulkier hydrocarbons, i.e., mono and di-branched C₆ hydrocarbons (**Figure 4.21b**). In accordance with the observations described above, n-hexane exhibits severe problems to access the inner cavities in ZIF-62, compared to propane, with the associated steps at specific points of the isotherm and the irreversible hysteresis loop. The mono-branched C₆ isomer (2-methyl pentane; kinetic diameter 0.50 nm) exhibits a sudden decrease in the amount uptake (down to ~ 0.5 mmol/g), whereas the di-branched isomer (2,2-dimethyl butane; kinetic diameter 0.62 nm) is mainly excluded. These results confirm that pore size aperture and pore accessibility in ZIF-62 is larger than the crystallographic pore opening predicted and close to the kinetic diameter of C₃-C₆ saturated hydrocarbons, i.e. ca. 0.43 nm. The unexpected accessibility for bulkier hydrocarbons and the variation of the pressure threshold for each individual molecules (C₁-C₂-C₃ selectivity and alkane/alkene selectivity) can only be understood due to the presence of specific interactions between the hydrocarbon molecules and the ZIF framework with the associated structural changes (e.g., a *gate-opening* effect).

4.4. Conclusions

ZIF-62 was synthesized by solvothermal method, and textural and morphological characteristics were evaluated through different physicochemical techniques. It was observed big tetrahedral crystals with an average size of 5-20 μm and strong solvent-surface interactions in the structure evacuation process. Nitrogen and oxygen adsorption-desorption isotherm showed at similar behavior at 298 K and 195 K but not at 77 K where ZIF-62 showed a not adsorptive behavior for nitrogen while the maximum adsorbed amount of oxygen was close to 8 mmol/g. Monte Carlo simulations for a rigid structure of ZIF-62 showed a framework with a big cavity of 4.3 Å and a small one of 1 Å. Simulated nitrogen and oxygen adsorption isotherm elucidate a similar adsorptive behavior for both gases at 77 K, 195 K and 298 K and fitted in good agreement with the experimental data at 195 K and 298 K. Nitrogen adsorption isotherm at 77 K showed a non-adsorptive behavior in the experimental isotherm while simulation suggests there should be a similar maximum of nitrogen and oxygen (close to 5 mmol/g), this may suggest a diffusional barrier.

SXRD experiment showed a structural transformation when the framework was loaded with oxygen or nitrogen at 90 K, suggesting a structural flexibility.

The Rietveld refinement performed in the SPXRD patterns at 90 K suggested a mixture of an expanded phase (phase I) and a contracted phase (phase II), this two phases prevailed until 150 K, after this point the contracted phase disappears and the cell parameter were close to those described for the blank structure. Even at first look experimental and simulated results could be contradictory, synchrotron, and particle size experiments are essential to understand the difference between those results. Even that nitrogen is not adsorbed as simulation experiments predicted, particle size and kinetic barriers experiments confirm the accessibility of nitrogen to the structure. However, the number of molecules accessing to the frameworks depends on external parameters such as, as kinetic barriers caused by particle size or equilibrium time. Expanding the potential applications of ZIF-62 for different industrial interest molecules, isotherms of small molecules such as methane or carbon dioxide where were performed at 298 K.

C1-C4 paraffins and olefins adsorption isotherms in ZIF-62 at 298 K showed an inverse preferential adsorption behavior which has been observed in other ZIF structures. Finally, ZIF-62 appeared to be an excellent material for separation of hexane isomers, showing a high preference for linear alkane and non-adsorptive preference for bi-branched isomers.

4.5. References

1. Yang, R. T. Introductory Remarks. in *Gas Separation by Adsorption Processes* 1–8 (Elsevier, 1987). doi:10.1016/B978-0-409-90004-0.50004-0
2. Baker, R. W. Future Directions of Membrane Gas Separation Technology. *Ind. Eng. Chem. Res.* **41**, 1393–1411 (2002).
3. Chong, K. C., Lai, S. O., Thiam, H. S., Teoh, H. C. & Heng, S. L. Recent progress of oxygen/nitrogen separation using membrane technology. *J. Eng. Sci. Technol.* **11**, 1016–1030 (2016).
4. Andriani, D., Wresta, A., Atmaja, T. D. & Saepudin, A. A Review on Optimization Production and Upgrading Biogas Through CO₂ Removal

- Using Various Techniques. *Appl. Biochem. Biotechnol.* **172**, 1909–1928 (2014).
5. Chen, X. Y., Vinh-Thang, H., Ramirez, A. A., Rodrigue, D. & Kaliaguine, S. Membrane gas separation technologies for biogas upgrading. *RSC Adv.* **5**, 24399–24448 (2015).
 6. Palomino, M., Corma, A., Rey, F. & Valencia, S. New Insights on CO₂–Methane Separation Using LTA Zeolites with Different Si/Al Ratios and a First Comparison with MOFs. *Langmuir* **26**, 1910–1917 (2010).
 7. Bae, Y.-S. & Snurr, R. Q. Development and Evaluation of Porous Materials for Carbon Dioxide Separation and Capture. *Angew. Chemie Int. Ed.* **50**, 11586–11596 (2011).
 8. Park, K. S. *et al.* Exceptional chemical and thermal stability of zeolitic imidazolate frameworks. *Proc. Natl. Acad. Sci. U. S. A.* **103**, 10186–91 (2006).
 9. Fairen-Jimenez, D. *et al.* Opening the Gate: Framework Flexibility in ZIF-8 Explored by Experiments and Simulations. *J. Am. Chem. Soc.* **133**, 8900–8902 (2011).
 10. Moggach, S. A., Bennett, T. D. & Cheetham, A. K. The Effect of Pressure on ZIF-8: Increasing Pore Size with Pressure and the Formation of a High-Pressure Phase at 1.47 GPa. *Angew. Chemie Int. Ed.* **48**, 7087–7089 (2009).
 11. Ania, C. O. *et al.* Understanding Gas-Induced Structural Deformation of ZIF-8. *J. Phys. Chem. Lett.* **3**, 1159–1164 (2012).
 12. Zhang, L., Wu, G. & Jiang, J. Adsorption and Diffusion of CO₂ and CH₄ in Zeolitic Imidazolate Framework-8: Effect of Structural Flexibility. *J. Phys. Chem. C* **118**, 8788–8794 (2014).
 13. Casco, M. E. *et al.* Gate-opening effect in ZIF-8: the first experimental proof using inelastic neutron scattering. *Chem. Commun.* **52**, 3639–3642 (2016).
 14. Bennett, T. D. *et al.* Reversible pressure-induced amorphization of a zeolitic imidazolate framework (ZIF-4). *Chem. Commun.* **47**, 7983 (2011).
 15. Wharmby, M. T. *et al.* Extreme flexibility in a zeolitic imidazolate framework: Porous to dense phase transition in desolvated ZIF-4. *Angew. Chemie - Int. Ed.* **54**, 6447–6451 (2015).
 16. Gandara-Loe, J. *et al.* New insights into the breathing phenomenon in ZIF-4. *J. Mater. Chem. A* **7**, 14552–14558 (2019).
 17. Gücüyener, C., van den Bergh, J., Gascon, J. & Kapteijn, F. Ethane/Ethene Separation Turned on Its Head: Selective Ethane Adsorption on the Metal–Organic Framework ZIF-7 through a Gate-Opening Mechanism. *J.*

- Am. Chem. Soc.* **132**, 17704–17706 (2010).
18. Zhao, P. *et al.* Phase Transitions in Zeolitic Imidazolate Framework 7: The Importance of Framework Flexibility and Guest-Induced Instability. *Chem. Mater.* **26**, 1767–1769 (2014).
 19. Kwon, H. T., Jeong, H.-K., Lee, A. S., An, H. S. & Lee, J. S. Heteroepitaxially Grown Zeolitic Imidazolate Framework Membranes with Unprecedented Propylene/Propane Separation Performances. *J. Am. Chem. Soc.* **137**, 12304–12311 (2015).
 20. Song, Q. *et al.* Zeolitic imidazolate framework (ZIF-8) based polymer nanocomposite membranes for gas separation. *Energy Environ. Sci.* **5**, 8359 (2012).
 21. Li, Y., Liang, F., Bux, H., Yang, W. & Caro, J. Zeolitic imidazolate framework ZIF-7 based molecular sieve membrane for hydrogen separation. *J. Memb. Sci.* **354**, 48–54 (2010).
 22. Cuadrado-Collados, C. *et al.* Understanding the breathing phenomena in nano-ZIF-7 upon gas adsorption. *J. Mater. Chem. A* **5**, 20938–20946 (2017).
 23. Gustafsson, M. & Zou, X. Crystal formation and size control of zeolitic imidazolate frameworks with mixed imidazolate linkers. *J. Porous Mater.* **20**, 55–63 (2013).
 24. Bennett, T. D. *et al.* Melt-Quenched Glasses of Metal–Organic Frameworks. *J. Am. Chem. Soc.* **138**, 3484–3492 (2016).
 25. Frentzel-Beyme, L., Kloß, M., Kolodzeiski, P., Pallach, R. & Henke, S. Meltable Mixed-Linker Zeolitic Imidazolate Frameworks and Their Microporous Glasses: From Melting Point Engineering to Selective Hydrocarbon Sorption. *J. Am. Chem. Soc.* **141**, 12362–12371 (2019).
 26. Wang, Y. *et al.* A MOF Glass Membrane for Gas Separation. *Angew. Chemie Int. Ed.* **59**, 4365–4369 (2020).
 27. Banerjee, R. *et al.* High-Throughput Synthesis of Zeolitic Imidazolate Frameworks and Application to CO₂ Capture. *Science (80-.)*. **319**, 939–943 (2008).
 28. Gutiérrez-Sevillano, J. J. *et al.* Strategies to Simultaneously Enhance the Hydrostability and the Alcohol–Water Separation Behavior of Cu-BTC. *J. Phys. Chem. C* **117**, 20706–20714 (2013).
 29. Wu, X., Huang, J., Cai, W. & Jaroniec, M. Force field for ZIF-8 flexible frameworks: atomistic simulation of adsorption, diffusion of pure gases as CH₄, H₂, CO₂ and N₂. *RSC Adv.* **4**, 16503–16511 (2014).
 30. Liu, Q., Wang, T., Qiu, J. & Cao, Y. A novel carbon/ZSM-5 nanocomposite membrane with high performance for oxygen/nitrogen separation. *Chem.*

- Commun.* 1230 (2006). doi:10.1039/b516519a
31. Park, Y.-J., Lee, S.-J., Moon, J.-H., Choi, D.-K. & Lee, C.-H. Adsorption Equilibria of O₂, N₂, and Ar on Carbon Molecular Sieve and Zeolites 10X, 13X, and LiX. *J. Chem. Eng. Data* **51**, 1001–1008 (2006).
 32. Moghadam, P. Z. *et al.* Computer-aided discovery of a metal–organic framework with superior oxygen uptake. *Nat. Commun.* **9**, 1378 (2018).
 33. Dincă, M. *et al.* Hydrogen Storage in a Microporous Metal–Organic Framework with Exposed Mn²⁺ Coordination Sites. *J. Am. Chem. Soc.* **128**, 16876–16883 (2006).
 34. Humphrey, S. M., Chang, J.-S., Jung, S. H., Yoon, J. W. & Wood, P. T. Porous Cobalt(II)–Organic Frameworks with Corrugated Walls: Structurally Robust Gas-Sorption Materials. *Angew. Chemie Int. Ed.* **46**, 272–275 (2007).
 35. Sarkisov, L. & Harrison, A. Computational structure characterisation tools in application to ordered and disordered porous materials. *Mol. Simul.* **37**, 1248–1257 (2011).
 36. Bennett, T. D. *et al.* Facile Mechanochemistry of Amorphous Zeolitic Imidazolate Frameworks. *J. Am. Chem. Soc.* **133**, 14546–14549 (2011).
 37. Hobday, C. L. *et al.* A Computational and Experimental Approach Linking Disorder, High-Pressure Behavior, and Mechanical Properties in UiO Frameworks. *Angew. Chemie Int. Ed.* **55**, 2401–2405 (2016).
 38. Longley, L. *et al.* Flux melting of metal–organic frameworks. *Chem. Sci.* **10**, 3592–3601 (2019).
 39. Krokidas, P., Castier, M., Moncho, S., Brothers, E. & Economou, I. G. Molecular Simulation Studies of the Diffusion of Methane, Ethane, Propane, and Propylene in ZIF-8. *J. Phys. Chem. C* **119**, 27028–27037 (2015).

CHAPTER 5

Nitric Oxide Adsorption into Flexible Zeolitic Imidazolate Frameworks (ZIFs)

Chapter 5 reviews the most significant results obtained into the paradigm of structural changes and adsorption capacity in ZIFs upon nitric oxide adsorption and release. Nitric oxide has been called the “molecule of the decade” due to discovery of its essential role in biological processes. Zeolitic imidazolate frameworks (ZIFs) have been applied for the first time in the adsorption and release of an important biomedical molecule, such as NO. Despite the absence of open metal sites (OMS) and suitable surface chemistry (e.g., amine basic groups) in ZIFs, these materials exhibit an excellent performance in terms of total uptake, irreversibility until use and delivery kinetics. These excellent results must be attributed to the presence of specific interactions between the framework and the NO molecules. For instance, ZIF-4 is able to adsorb up to 1.6 mmol/g, whereas its benzyl imidazolate counterpart (ZIF-7) is limited to 0.5 mmol/g. However, despite the lower adsorption capacity exhibited by ZIF-7, the presence of a narrow pore (np), highly dense structure (phase II) allows controlling the NO release under humid conditions for more than 15h at physiological temperature (310K).

5.1. Introduction

Nowadays, one of the main challenges in materials science is the design of functional nano porous solids for biomedical applications. For instance, a porous material to be applied in drug delivery processes must fulfil a series of stringent requirements, i.e. a high loading capacity, a "strong" adsorption potential so that the drug can be stored until use, prolonged delivery over time and, the most important, a proper biocompatibility. One of these biomedical challenges concerns the adsorption and release of nitrogen monoxide (NO). NO is a highly reactive molecule, that for a long period was considered just a toxic gas produced from cars exhaust. However, when a Nobel prize was awarded to scientist who discover the essential role of this small molecule into many physiological functions (for instance, in the cardiovascular system) a big attention was focused in the development of nano porous materials able to store and deliver NO constitutes a promising approach for instance to avoid thrombosis formation upon incorporation of medical devices (e.g., stents or catheters) in human body.^{1,2} However, due to the low intermolecular interactions, the saturation vapor pressure of NO is high, i.e. 64.83 bar, with the associated complexity to store a considerable amount of NO at atmospheric pressure. Nanoporous materials such as zeolites and porous organic polymers containing immobilized metal complexes have been reported in the literature as promising platforms to overcome these limitations for NO adsorption and release.^{3,4} The presence of metal cations (or extra-framework cations in the specific case of the zeolite) able to chemisorb NO has been identified through X-ray diffraction and IR spectroscopy. Despite these promising results, these materials suffer from a small adsorption capacity for NO at 298 K, i.e. below 1 mmol/g.

Recent studies described in the literature have shown the improvement of these number by using metal-organic frameworks (MOFs) as a host structure. Cu-, Co- and Ni-MOFs among others have shown adsorption values as high as ~ 7 mmol/g at 25°C, with a proper irreversibility, required to retain the adsorbed NO until use.⁵⁻⁷ The presence of coordinatively unsaturated metal sites (CUSs) on the evaluated MOFs able to bind NO molecules explains the optimum performance in terms of storage values and release characteristics. Despite the irreversible nature

of the adsorbed NO, these studies have shown that it can be partially desorbed using humid air, NO delivery ranging from 1h up to 40h, depending on the metal and porous network. Another approach to store NO in MOFs is based in the formation of NONOates. Recent studies described in the literature have shown that the incorporation of amine groups in the organic linker (for instance IRMOF-3 and UMCM-1-NH₂) allows to improve the NO adsorption performance, even in the absence of open metal sites (OMS).^{8,9}

A potential approach for NO storage not explored till date is the use of flexible MOFs such as, zeolitic-imidazole frameworks (ZIFs). These materials are a subclass of the MOFs family characterized by the presence of structural phenomena upon adsorption, i.e., swinging of the linker and the associated gate-opening or breathing phenomena.^{10–14} Although ZIFs does not possess CUS or a properly designed surface chemistry, the structural changes taken place upon adsorption/desorption can be anticipated *a priori* as a potential tool to control/modify the delivery kinetics for NO. Furthermore, these materials possess high thermal and mechanical stability, with the associated advantages in terms of minimizing structural deterioration and metal leaching in biomedical applications.

ZIF-4 and ZIF-7 are 2 out of 105 ZIFs reported in the literature so far.¹⁵ ZIF-4 is formed by the simplest linker unit, imidazole, and zinc metal clusters. This material shares a remarkable structural flexibility and phase transitions upon external stimulus (pressure and/or temperature changes).^{14,16,17} These properties have attracted great attention for applications in gas separation and storage.^{18,19} On the other hand, ZIF-7 has sodalite topology and is formed by benzimidazole linkers connected to zinc metal clusters.¹² In ZIF-7 the linkers have some freedom to rotate over certain angles promoting structural flexibility, mainly a phase transition from a narrow pore (np) to a large pore (lp) structure.²⁰

Taking into account the excellent characteristics of ZIFs and the associated structural changes, the main goal of this manuscript is the evaluation of the performance of two flexible ZIFs, i.e. ZIF-7 and ZIF-4, in the adsorption/delivery of NO under different experimental conditions. The amount of NO adsorbed and the

delivery characteristics under different temperature and dosing conditions will be thoroughly evaluated.

5.2. Experimental section

5.2.1. MOFs synthesis

ZIF-4 and ZIF-7 were synthesized by solvothermal method using procedures reported before in the literature.^{14,18} For ZIF-4, 0.4 g of $\text{Zn}(\text{NO}_3)_2 \cdot 6\text{H}_2\text{O}$ were mixed with 0.3 g of imidazole and dissolved in 30 mL of N,N-dimethylformamide (DMF). The liquid mixture was placed in a glass jar, sealed tightly and placed in the oven for 48 h at 403 K. For ZIF-7 a similar procedure was followed mixing 0.4135 g of $\text{Zn}(\text{NO}_3)_2 \cdot 6\text{H}_2\text{O}$ and 0.3764 g of benzimidazole. The solid mixture was dissolved in 30 mL of DMF, transferred in a glass jar and placed in the oven for 48 h at 403K. The solid crystals were washed with 30 mL of DMF (x2) and exposed to a solved exchange process with 30 mL of methanol (x) for 24 hours. Finally, the samples were dried at room temperature for 6 hours and stored for further characterization.

5.2.2. MOFs characterization

X-ray powder diffraction (XRPD) patterns of ZIF-4 and ZIF-7 were obtained using a Bruker D8-Advance equipment with mirror Goebel with high temperature Chamber and a generator of X-ray KRISTALLOFLEX K 760-80F with a tube of RX with copper anode. Spectra were registered between 3 and 80° (2 θ) with a step of 0.05° and a time per step of 3 s. XRPD of the samples were obtained under different outgassing temperatures (423 K and 523 K).

Scanning electron microscopy (SEM) images of ZIF-4 and ZIF-7 were obtained using an JSM-6700F that is a high-resolution SEM with a field emission gun (FEG) electron source. It is equipped with a secondary electron detector for topographic contrast imaging, a retractable backscattered electron detector for atomic number contrast imaging and an Oxford Inca EDX system for compositional analysis.

Thermogravimetric analysis (TG) were obtained using the scientific facilities available in the technical services of the University of Alicante. ZIF-4 and ZIF-7 TG-DTA were recorded using an equipment TG-DTA METTLER TOLEDO model TGA/SDTA851e/SF/1100. The samples were measured using an alumina sample holder and temperature range from 298K up to 1073K with step of 5 K/min under N₂ flow.

X-ray photoelectron spectroscopy (XPS) spectra were recorded in a XPS K-ALPHA Thermo Scientific. All spectra were collected using an Al-K radiation (1486.6 eV), monochromatized by a twin crystal monochromator, yielding focused X-ray spot elliptical shaped with a major axis length of 400 μm at 3 mA x 12 kV. The alpha hemispherical analyser was operated at the constant energy mode with survey scan pass energies of 200 eV to measure the whole energy band and 50 eV in a narrow scan to selectively measure the desired elements. Charge compensation was achieved with the system flood gun that provides low energy electrons and low energy argon ions from a single source. The CH_x in carbon 1s score level was used as reference binding energy (284.6 eV). The powder samples were pressed and mounted on the sample holder and placed in the vacuum chamber. Before the spectrum recording, the samples were maintained in the analysis chamber until a residual pressure of ca. 5×10^{-7} Nm⁻². The peaks deconvolution was performed by a quantitative analysis calculating the integral of each peak, after subtracting the S-shaped background, and by fitting the experimental curve to a combination of Lorentzian (30%) and Gaussian (70%) model.

5.2.3. CO₂ adsorption isotherm at 273K

CO₂ adsorption/desorption isotherms were performed at 273 K using a home-made high-resolution manometric equipment designed and constructed by the LMA group. Before the adsorption experiment, ZIF-4 and ZIF-7 crystals were outgassed using two different temperatures, 423 K and 523 K, for 48h under high vacuum (10⁻⁷ kPa).

5.2.4. ZIFs phase analysis by PXRD

ZIF-4 and ZIF-7 structural transition upon outgassing temperature was evaluated through powder X-ray diffraction. A PANalytical Empyrean multi-functional system for analysis by X-ray diffraction was used. The basic configuration has a goniometer with an X-ray tube cathode Cu K α , and a 3D Pixcel detector. The configuration allows the installation of different modules (SAX, reflectometry, etc.) easy to install with prefix positions. The system has a reaction chamber for analysis of the phase change material during heating to a maximum temperature of 900 ° C and an entrance to control gas atmosphere in the chamber. ZIF-4 and ZIF-7 outgassed at 423 K and 523 K were analyzed at room temperature first obtain a blank of the evacuated structure and secondly, a pattern of the material exposed to 1 bar of NO or CO₂.

5.2.5. Nitric oxide adsorption/desorption isotherms

Nitric oxide adsorption/desorption experiments on ZIF-4 and ZIF-7 were measured using a gravimetric equipment bespoke in Russell Morris' research group. In the gravimetric method a CI instrument microbalance was thermally stabilized to eliminate external environmental effects (sensitivity of 0.1 μ g and reproducibility of 0.01% of the load). The adsorption pressure was monitored by two gauges in the ranges of 1×10^{-8} - 1×10^{-2} and 1×10^{-4} - 1×10^3 mbar, respectively. The samples were outgassed either at 423K or 523K under vacuum until no weight loss was observed. For each sample the temperature was decreased to 298K and kept constant using a water bath. To minimize the influence of temperature differences on weight readings, the counterbalance temperature was kept at the same temperature and the sample temperature was monitored using a thermocouple located close to the sample bucket. The nitric oxide was introduced to the system until the desired pressure was reached. Kinetic data was recorded in each point measuring the mass uptake as a function of time. In this manner absorption/desorption isotherm was collected by increasing or decreasing the pressure and the mass gain or loss was noted after the equilibrium had been achieved.

5.2.6. Nitric oxide releasing experiments

NO release measurements were performed using an NOA 280i chemiluminescent nitric oxide analyser. The analyser was calibrated by passing air through a zero filter and 89.82 ppm NO gas flow. The flow rate was set to 180 mL/min with a cell pressure of 8.5 torr and an oxygen pressure of 6.1 psig. To measure the NO released from ZIF-4 and ZIF-7, a nitrogen flow with a controlled humidity (11 % RH) was passed through the powders at different temperature conditions, the final NO concentration being recorded until a NO outlet concentration below 20 ppb is obtained. To observe the effect of the kinetics in the NO adsorption, 1h and 24 h of exposure were used in both materials.

5.3. Results

5.3.1. Physicochemical evaluation of the synthesized ZIFs

Figure 5.1 shows the XRD pattern of the as-synthesized ZIF-4 and ZIF-7. Both patterns perfectly fit with the simulated X-ray diffraction data available at the Cambridge Database. ZIF-4 exhibits the so-called high-temperature phase (HT) described by Wharmby et al. and characterized by a *Pbca* space group and a unit cell volume around 4344 Å³.²¹ Concerning ZIF-7, the obtained XRD pattern corresponds to the rhombohedral phase I (the so-called large-pore (lp)) commonly associated with pore occupation with guest molecules (e.g., solvent).¹²

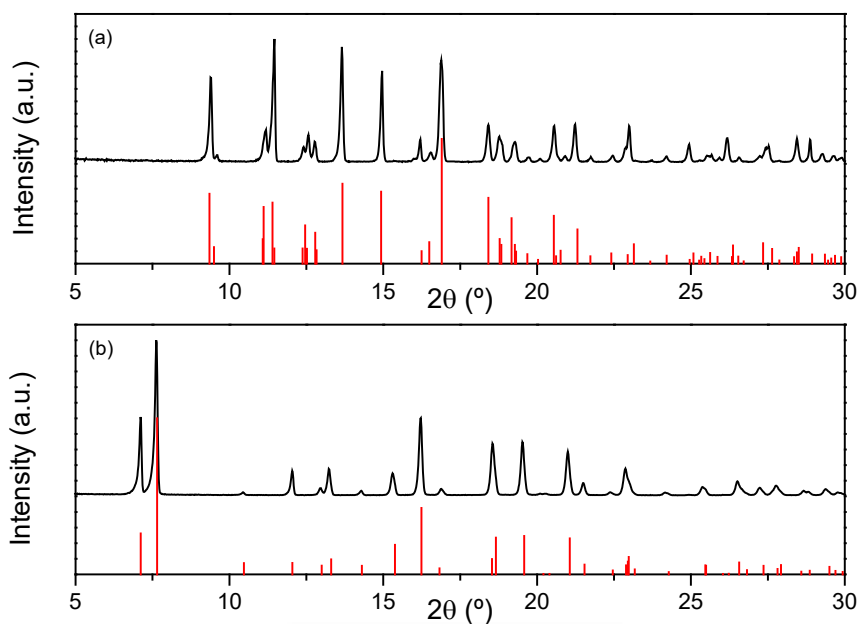


Figure 5.1. XRD pattern of the as-synthesized (a) ZIF-4 and (b) ZIF-7 samples in comparison with the simulated patterns (red), obtained from Cambridge Structural Database, Cambridge Crystallographic Data Centre, Cambridge CB2 1EZ, United Kingdom.

Based on the literature, the volume of the ZIF-7 phase I structure is 7214 \AA^3 , whereas the desolvated structure (phase II) is triclinic with a volume of 7917 \AA^3 .²²

Figure 5.2 shows the SEM images of the synthesized ZIFs. Both samples exhibit octahedral morphology with an average crystal size of ca. $300 \mu\text{m}$ for ZIF-4 and ca. $40 \mu\text{m}$ for ZIF-7.

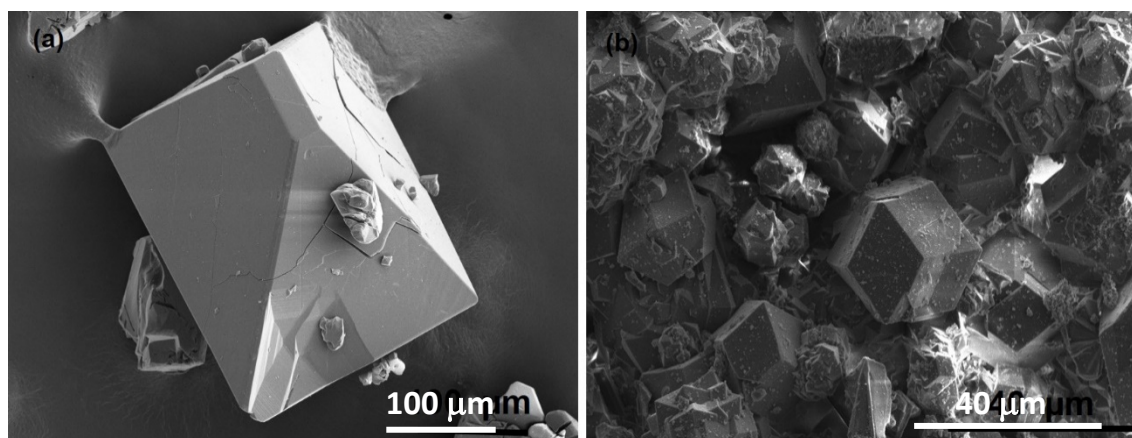


Figure 5.2. SEM images of the as-synthesized (a) ZIF-4 and (b) ZIF-7.

The thermal behaviour of ZIF-4 and ZIF-7 was evaluated using thermogravimetric analysis (TG) under an air flow up to high temperature. As observed in **Figure 5.3**, ZIF-4 exhibits a weight loss (ca. 8%) at 473 K due to the removal of the solvent, and a second weight loss of ca. 34% at 893 K due to the decomposition of the linker. ZIF-7 exhibits a similar profile with a first weight loss due to the removal of the solvent at 470 K (ca. 12%) and a second weight loss at 836K of ca. 41% due to the decomposition of the material. Based on these measurements, 423 K and 523 K were selected temperatures for the thermal treatment before each adsorption evaluation.

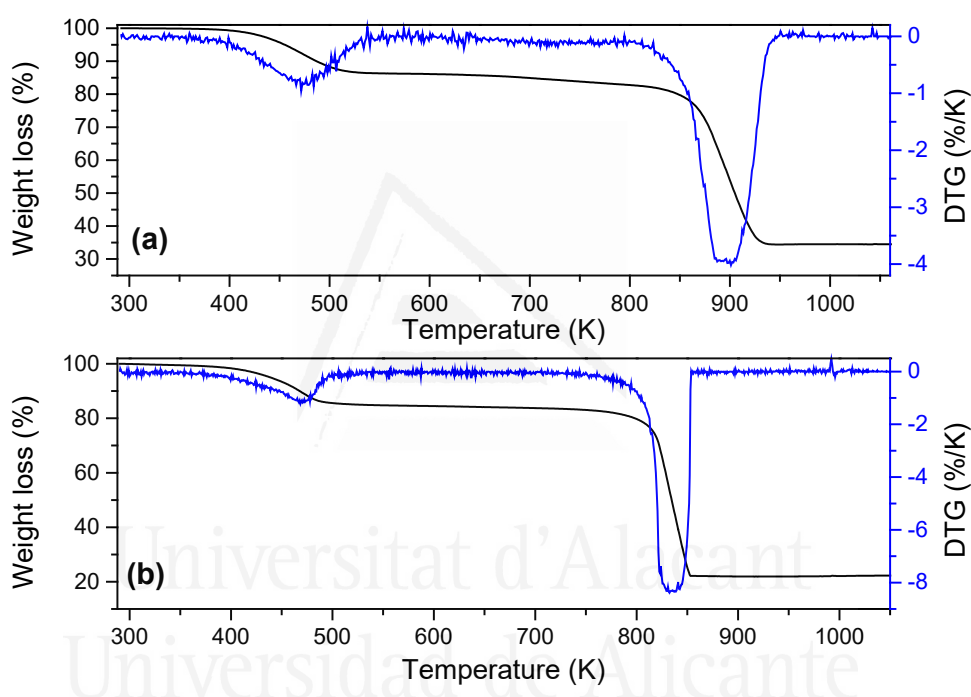


Figure 5.3. TGA-DTA patterns of the as-synthesized (a) ZIF-4 and (b) ZIF-7 samples under air flow.

5.3.2. CO₂ adsorption measurements at 273K

Previous studies described in the literature have shown that N₂ adsorption at 77K in ZIF-7 and ZIF-4 is a kinetically restricted process and extended equilibrium times are required to achieve proper equilibrium conditions (isotherms take several days to be completed).^{12,14} On the contrary, CO₂ adsorption at a higher adsorption temperature (273 K) constitutes a proper alternative to N₂ to evaluate the porous

structure in ZIFs due to the absence of kinetic restrictions and/or specific interactions between the probe molecule and the structural framework that preclude gas adsorption. To evaluate the success of the synthesis process and the nature of the developed structural network, CO₂ adsorption/desorption isotherms have been evaluated for both samples after an outgassing treatment at 423 K and 523 K (**Figure 5.4**).

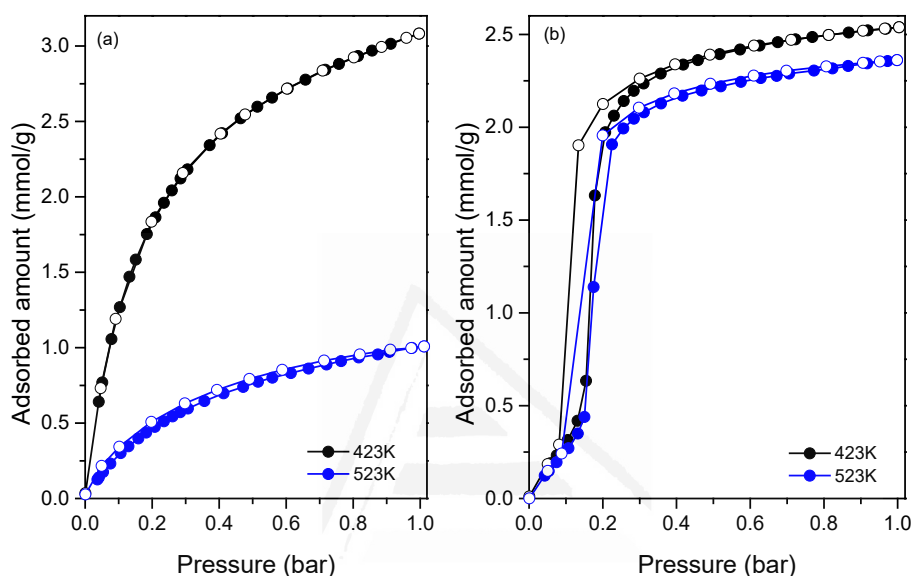


Figure 5.4. Carbon dioxide adsorption/desorption isotherms in (a) ZIF-4 and (b) ZIF-7 at 273 K. Samples were outgassed at 423 K (black) and 523 K (blue).

The CO₂ adsorption isotherm of the ZIF-4 sample exhibits a type I adsorption performance, attributed to the filling of the inner cavities, excluding any structural expansion or gate-opening effect, in close agreement with previous studies described in the literature.¹⁴ CO₂ adsorption in ZIF-4 is fully reversible with a total amount adsorbed of ~3.1 mmol/g, after a thermal treatment at 423 K. An increase in the temperature of the outgassing treatment up to 523 K gives rise to an important decrease in the adsorption performance down to a final uptake of ~1.0 mmol/g. The adsorption performance is different in the case of ZIF-7. In this case, an S-shape isotherm is clearly observed due to the filling of the inner cavities with CO₂, and the associated phase transition from the closed-packed phase II (obtained after removing the solvent), to an expanded, low density, phase I. The total uptake at 1.0

bar is ~ 2.5 mmol/g, in close agreement with previous studies from our research group.¹⁴ The presence of a phase transition associated with a structural expansion can be clearly reflected in the desorption branch, with an associated hysteresis loop at low pressures (*ca.* 0.1-0.2 bar). An increase in the outgassing temperature in the ZIF-7 does not give rise to significant changes, except a small decrease in the total uptake ($\sim 8\%$ decrease). These results confirm the proper removal of the solvent even after a thermal treatment at 423 K under ultra-high vacuum conditions (UHV), together with the presence of some structural changes after an increase in the temperature to 523 K, these changes being detrimental for the final adsorption performance. In any case, these changes in ZIF-7 are rather small compared to ZIF-4. In the specific case of ZIF-4, the drastic decrease in the amount adsorbed must be attributed to the partial amorphization of the ZIF-4 structure after the thermal treatment at 523K to the so-called α_T -ZIF-4, in close agreement with previous findings from Bennett *et al.*¹⁶ However, the presence of further re-crystallization to the dense zni phase cannot be excluded at this point.

5.3.3. NO adsorption experiments at 298K

Previous studies described in the literature have shown that the structural changes taken place in ZIFs highly depend on the nature of the probe molecule, i.e. it is usually an energetic process that depends on the balance between the inner framework interactions and the interactions of the ZIF framework with the corresponding gas molecule. NO is a slightly polar molecule with more electron density over oxygen atom. A priori, one would expect to find specific interactions between the NO molecule and the ZIF framework due to the presence of a permanent dipolar moment able to open the porous network.

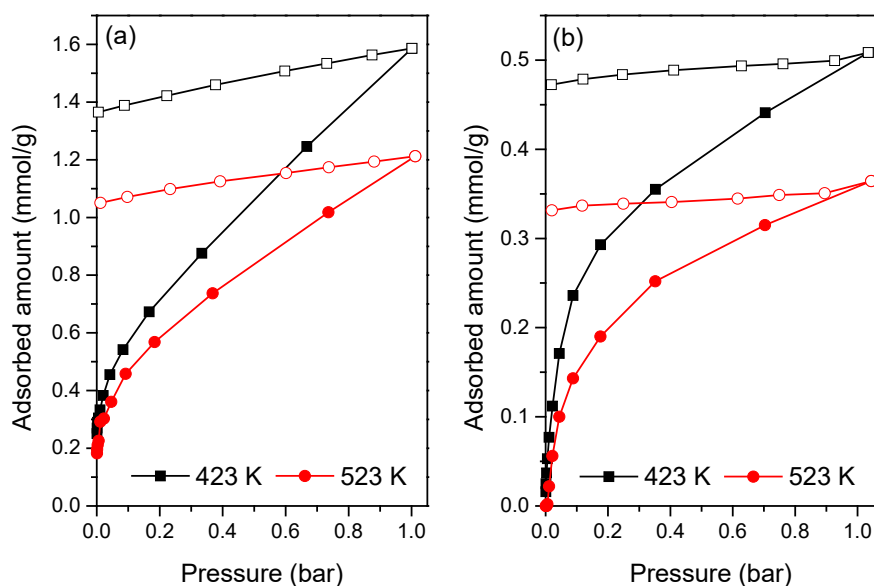


Figure 5.5. Nitric oxide isotherms in (a) ZIF-4 and (b) ZIF-7 at 298 K. Samples outgassed at 423 K (black square) and 523 K (red circles).

Figure 5.5 shows the NO adsorption/desorption isotherms for both ZIFs up to 1.0 bar, for the two outgassing temperatures evaluated. In both cases, the amount of NO adsorbed is larger after a thermal treatment at 423K, in close agreement with CO₂ described above. However, the adsorption performance is extremely different among ZIFs.

Both samples exhibit a concave isotherm characteristic of microporous materials with a strong adsorption potential at low pressures. However, whereas ZIF-4 is able to achieve a large adsorption capacity for NO, up to ~1.6 mmol/g, ZIF-7 has a limited capacity, close to 0.5 mmol/g. These results confirm that NO has a proper accessibility to the inner porous structure in ZIF-4, with an adsorption uptake in the range of the values obtained with CO₂. On the contrary, ZIF-7 has limited accessibility. A closer look to the NO and CO₂ isotherms in ZIF-7 clearly shows that 0.5 mmol/g corresponds roughly to the amount of CO₂ adsorbed in the initial step of the isotherm, i.e. before the phase transition from np to lp. This observation will demonstrate that NO is indeed not able to promote the breathing of ZIF-7 at 1.0 bar and 298 K. At this point it is important to highlight that despite the type I isotherm obtained for both samples, NO adsorption is completely irreversible under ultrahigh

vacuum conditions for both samples, the remaining amount of gas adsorbed being ~ 1.37 mmol/g and ~ 0.47 mmol/g, for ZIF-4 and ZIF-7, respectively. Despite the absence of exposed covalent unsaturated metallic sites (CUS) in ZIFs and the absence of basic functionalities in the organic linker, both samples exhibit a perfect irreversibility. Although the irreversible adsorption of gases can be *a priori* a handicap, it can indeed be very useful for biomedical applications to preserve adsorbed the active component until use, provided that the NO can be properly desorbed upon request.

5.3.4. NO release experiments under humid conditions

Among the different approaches to release NO from inorganic porous materials, the most promising one concerns the use of a humid air flow. This is also the most realistic approach taking into account that, in human body, the loaded MOF will be in contact with physiological media, i.e., upon implantation there will be a competition between H₂O and NO for the adsorption sites in the corresponding material. Previous studies using MOFs and zeolites have shown that this is a proper approach to release, although partially, the retained NO. Only under specific circumstances, for instance for sample CPO-27-Co and CPO-27-Ni, the total amount of NO retained can be properly released.⁶ **Figure 5.6** and **Figure 5.7** show the delivery profiles for ZIF-4 and ZIF-7, respectively, after exposure to NO for 1h and 24h (see experimental section for further details). In all cases, the NO signal was recorded over time under humid flow conditions (11% RH) until the final NO concentration was lower than 20 ppb. At this point, the experiment was stopped.

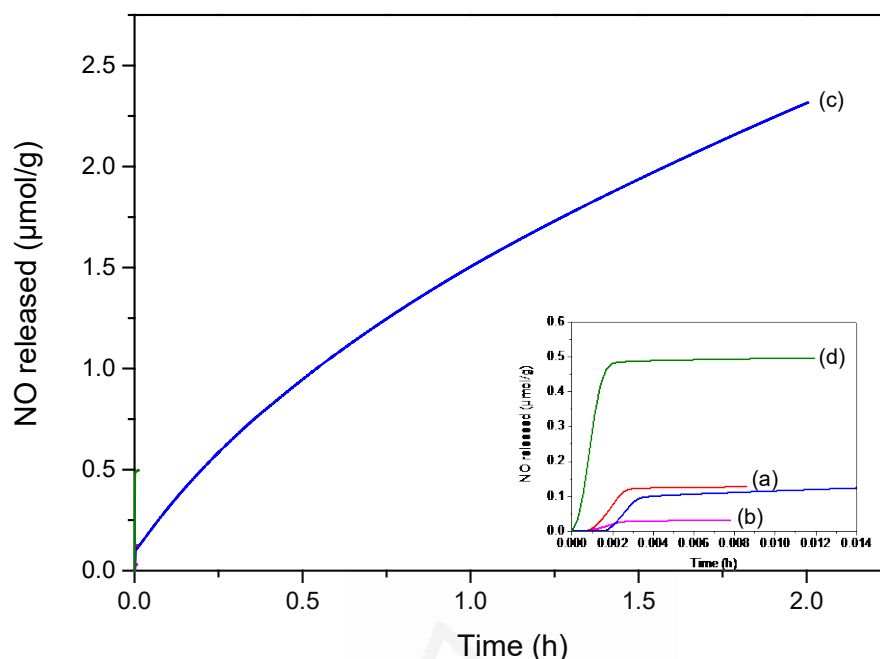


Figure 5.6. Chemiluminescence analysis of total NO delivery at 298K on contact with humid atmosphere (11 % RH) for (a) ZIF-4 outgassed at 423K and 1 h NO exposure, (b) ZIF-4 outgassed at 523K and 1 h NO exposure, (c) ZIF-4 outgassed at 423K and 24 h NO exposure and (d) ZIF-4 outgassed at 523K and 24 h NO exposure. Data collection was stopped when NO levels reached 20 ppb.

Figure 5.6 (inset) shows that NO delivery in ZIF-4 exhibits an initial induction period (less than 1 min), the total amount released reaching a plateau in the first 20s. The total amount desorbed after the plateau is rather small ($\leq 0.5 \mu\text{mol/g}$). As expected, the amount released is much larger for ZIF-4 exposed to NO for 24h, whereas the thermal treatment at 523 K becomes detrimental due to the amorphization of the structure and the low adsorption capacity of the denser material. An exception to this behaviour is the ZIF-4 treated at 423 K and exposed to NO for 24h. Under these conditions, the NO is released continuously for more than 2h until the limit of 20 ppb is reached. Interestingly, under these conditions the total amount of NO released is one-order of magnitude larger and close to $2.4 \mu\text{mol/g}$.

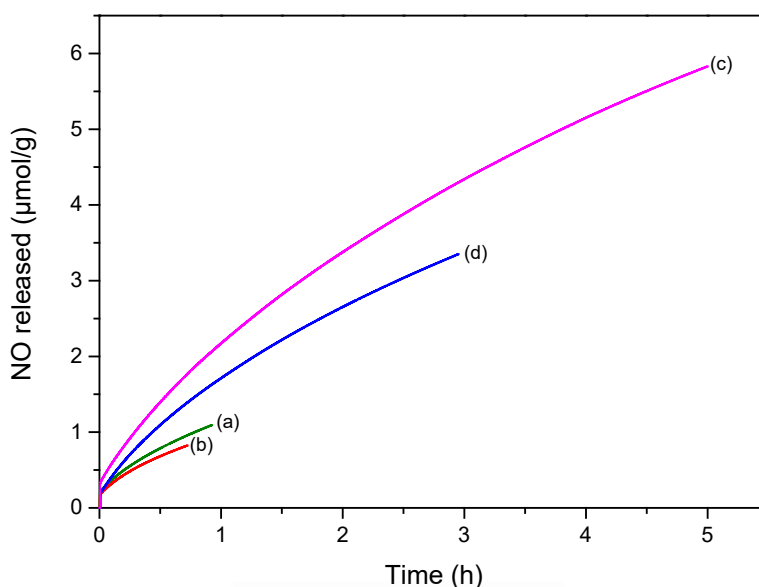


Figure 5.7. Chemiluminescence analysis of total NO delivery at 298 K on contact with humid atmosphere (11 % RH) for (a) ZIF-7 outgassed at 423 K and 1 h NO exposure, (b) ZIF-7 outgassed at 523 K and 1 h NO exposure, (c) ZIF-7 outgassed at 423 K and 24 h NO exposure and (d) ZIF-7 outgassed at 523 K and 24 h NO exposure. Data collection was stopped when NO levels reached 20 ppb.

Although the adsorption performance of ZIF-7 is worse in terms of total NO uptake (**Figure 5.7**) compared to ZIF-4, the performance observed during NO desorption is drastically different. Compared to ZIF-4, the total amount delivered for ZIF-7 is much larger (up to 6 $\mu\text{mol/g}$) and with extended delivery kinetics (up to 5h). These results suggest that NO adsorbed in ZIF-7 with phase II (the so-called low-pore (lp) phase or highly dense phase) gives rise to an optimum performance for NO delivery, i.e., the presence of a folded structure allows to decrease the delivery kinetics with a significant improvement in the time-scale length. As expected, this improvement is more significant after 24h NO exposure and after a thermal treatment at lower temperatures (423 K).

Another important parameter able to define the delivery kinetics in ZIFs is the temperature of the surrounding media. Experiments described above were performed at 298 K, slightly below the temperature of the human body. In order to get a more realistic picture of the ZIFs performance, delivery experiments were

evaluated at 298 K, 310 K (temperature of the human body) and 318 K using the most promising conditions reported before, i.e., an outgassing treatment at 423 K and NO exposure for 24h. **Figure 5.8** and **Figure 5.9** shows the delivery profile for ZIF-4 and ZIF-7, respectively, at the three temperatures evaluated. As it can be appreciated, the performance changes drastically after an increase in the temperature of the delivery media of only 12 K. In the specific case of ZIF-4, the amount desorbed increases from 2.4 $\mu\text{mol/g}$ up to 8.5 $\mu\text{mol/g}$ at 310 K and 11.8 $\mu\text{mol/g}$ at 318 K. Concerning time scale, the system is able to release NO with a concentration above 20 ppb for more than 6h, as compared to 2h in the ZIF-4 at 298 K.

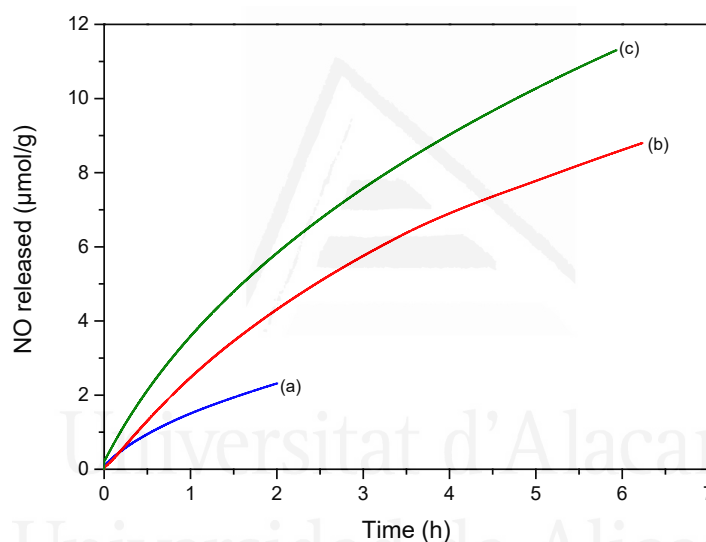


Figure 5.8. Chemiluminescence analysis of total NO delivery on contact with humid atmosphere (11 % RH) for ZIF-4 at analysis temperature of (a) 298 K, (b) 310 K and (c) 318 K. Samples were outgassed at 423 K overnight and exposed to NO for 24 hours. Data collection was stopped when NO levels reached 20 ppb.

Concerning ZIF-7, the scenario also changes after an increase in the desorption temperature. As appreciated in **Figure 5.9**, the total amount of NO released exhibits a drastic change at 310 K (more than 25 $\mu\text{mol/g}$ released) and even larger (more than 70 $\mu\text{mol/g}$) at 318 K. Compared to the amount released at 298K (6 $\mu\text{mol/g}$), this result constitutes a tremendous increase (up to one order of magnitude) after an increase of released temperature of only 20 K. Furthermore, the

delivery process can be extended in time with a total of 18h with more than 20 ppb released.

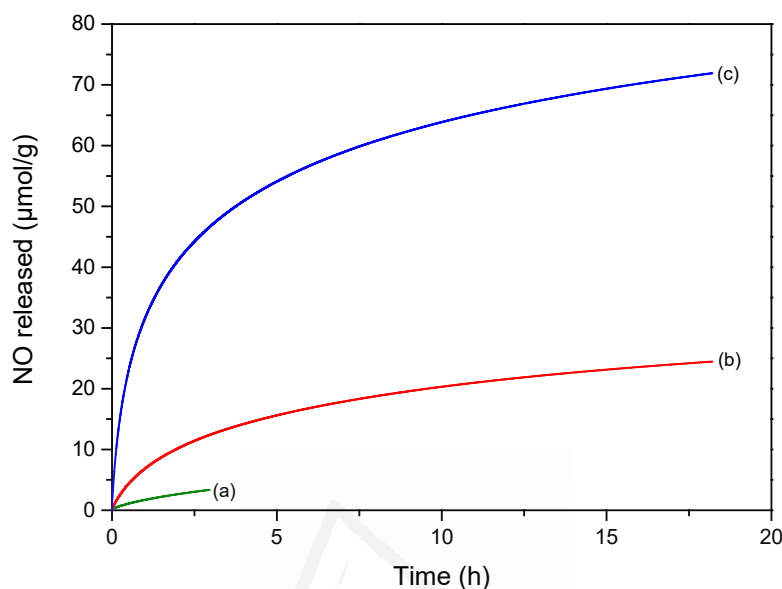


Figure 5.9. Chemiluminescence analysis of total NO delivery on contact with humid atmosphere (11 % RH) for ZIF-7 at analysis temperature of (a) 298 K, (b) 310 K and (c) 318 K. Samples were outgassed at 423 K overnight and exposed to NO for 24 hours. Data collection was stopped when NO levels reached 20 ppb.

Previous studies described in the literature have shown that complete release of the adsorbed NO is rather difficult and depends on the nature of the MOF framework (nature of the metal species and organic linker). Whereas materials with open metal sites (e.g., HKUST-1) exhibit a low release (ca. 2.4 $\mu\text{mol/g}$) for only 1h,^{5,23} materials such as CPO-27-M (M=Co, Ni) are able to deliver close to 100% of the retained NO ($\approx 7 \text{ mmol/g}$) under humid flow conditions.⁶ Amine functionalization of linkers also allows to improve the NO adsorption and released performance (e.g., UMH materials) with a similar performance to ZIF-7, i.e. ca. 60 $\mu\text{mol/g}$ delivered but limited to 6h.²³ Compared to previous approaches described in the literature for NO adsorption using MOFs, this manuscript shows that ZIFs exhibit a similar or even improved behaviour in terms of storage and delivery kinetics with some additional advantages compared to the reported MOFs, i) an easy synthesis process, avoiding complex functionalization of the organic linker to increase its basic character and, ii)

absence of open metal sites, with the associated structural stability even in physiological solution.²⁴ For instance, in the specific case of HKUST-1, DFT calculations predict a binding energy for water to the open metal sites as high as ~ 47.3 kJ/mol, a value that allows water to compete with the majority of the target molecules (e.g., NO with a binding energy of 28.9 kJ/mol). The strong water-framework interaction in HKUST-1 explains the associated structural deterioration of this material (and associated copper leaching) under humid environments.^{25,26} This is a crucial aspect since the structural stability in ZIFs will prevent any structural deterioration and the associated release of toxic metal species into the organism.

5.3.5. Structural changes upon a thermal treatment under UHV conditions

To end up, the structural characteristics of both ZIFs have been evaluated after a thermal treatment under UHV conditions at 423 K and 523 K. The main goal was to ascertain the reasons behind the changes observed in the adsorption performance of ZIFs, preferentially for ZIF-4. **Figure 5.10** shows the XPS spectra corresponding to the N1s region for the two samples after the two thermal treatments applied.

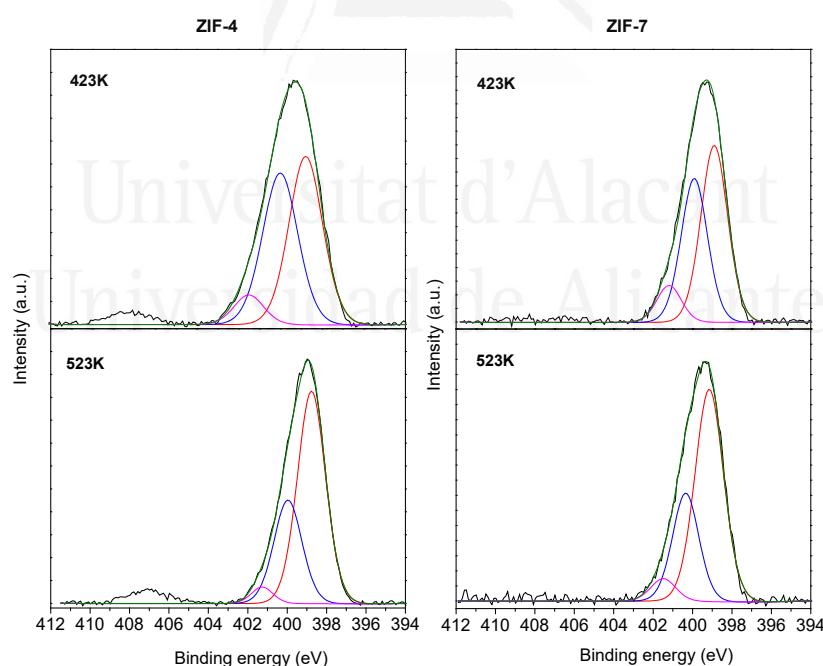


Figure 5.10. XPS spectra of N1s for ZIF-4 and ZIF-7 outgassed at 423 K and 523 K.

As it can be observed, the XPS profiles are rather similar for both samples, independently of the thermal treatment applied. Each nitrogen signal can be deconvoluted into three components corresponding to pyridinic N at 398.9 eV, pyrrolic N at 400.2 eV and a third small contribution at 401.7 eV, most probably due to quaternary or graphitic nitrogen species.^{27,28} Whereas at low degassing temperatures pyridinic and pyrrolic nitrogen signals are rather similar (~50%), an increase in the degassing temperature to 523 K gives rise to a sudden increase in the pyridinic contribution (~67%) in both samples, most probably due to the creation of structural defects. However, these changes are similar for both samples and does not allow to justify the changes observed in the adsorption performance between ZIF-4 and ZIF-7. A similar scenario takes place in the Zn 2p region (**Figure 5.11**) with a similar profile for both materials, independently of the thermal treatment applied. XPS spectra for Zn show two main contributions at 1021.9 eV and 1045.2 eV, attributed to Zn 2p_{3/2} and 2p_{1/2}, respectively. In addition there were two small contributions at 1046.6 eV and 1023.9 eV, most probably due to the presence of metal oxide and hydroxide.²⁷ In any case, these results confirm that the structural changes taken place in these ZIFs at higher temperatures are not related with changes in the chemical structure and elemental state of the materials.

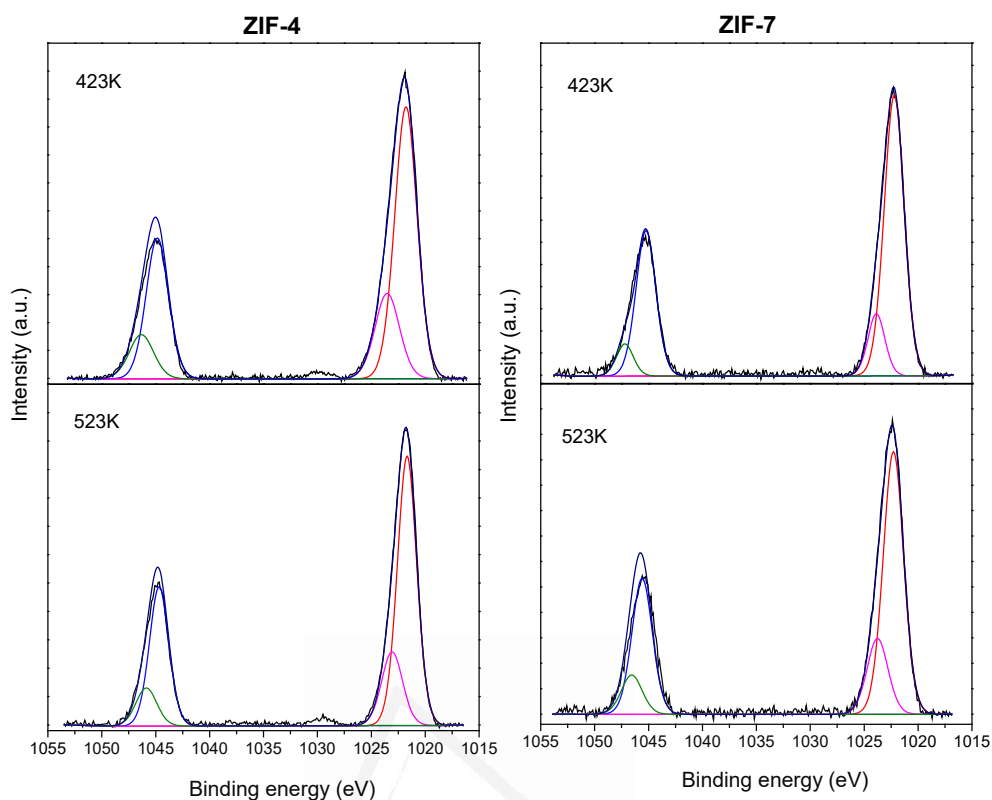


Figure 5.11. XPS spectra in the Zn 2p region for ZIF-4 and ZIF-7 samples after a thermal treatment under UHV conditions at 423 K (a and c) and 523 K (b and d).

To further characterize these materials, XRD patterns have been evaluated in the two ZIFs evaluated after a thermal treatment under UHV conditions at 423 K and 523 K (**Figure 5.12**). In the specific case of the ZIF-7, the XRD pattern corresponds to the narrow pore (np) structure, the so-called phase II, independently of the thermal conditions applied. However, in the specific case of ZIF-4 the scenario is different. Whereas a thermal treatment at 423 K under UHV conditions preserves the so-called high-temperature (HT) phase, an increase in the temperature of this treatment to 523 K gives rise to a completely new phase. Previous studies from Bennett et al. have shown that ZIF-4 is a unique material under a thermal stimulus.¹⁷ Upon heating ZIF-4 can go through an amorphization step (ca. 573K) to the so-called a_T -ZIF-4, and further on, it can suffer a recrystallization to the dense phase zni-ZIF-4, at around 673 K. A closer look to **Figure 5.12** clearly anticipates that ZIF-4 evolved to the dense amorphous ZIF-4 phase.²⁹ Apparently, under UHV conditions

all these thermal changes are shifted to lower temperatures, compared to the previous observations described in the literature.^{17,29}

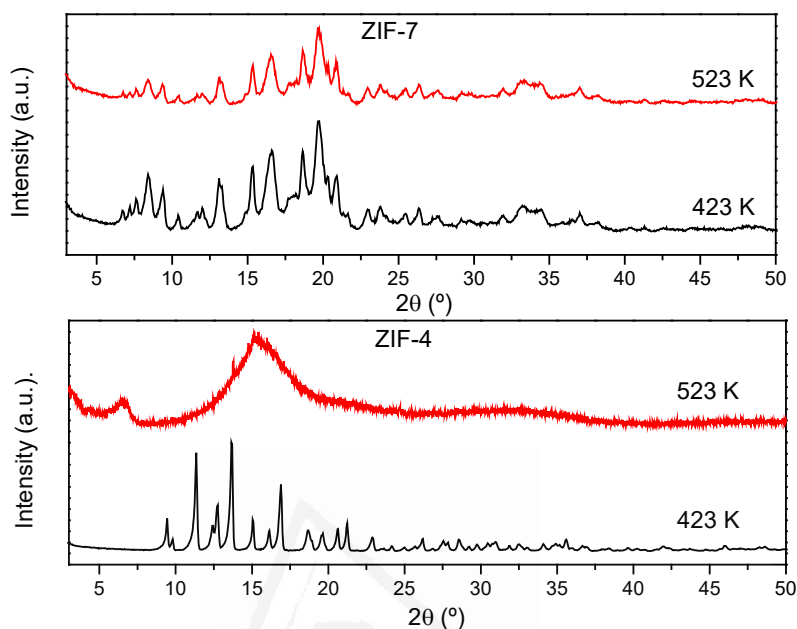


Figure 5.12. XRD patterns of ZIF-4 and ZIF-7 after a thermal treatment under UHV conditions at 423 K (a and c) and 523 K (b and d).

5.3.6. Phase transition upon gas adsorption

Breathing phenomena in ZIF-4 upon nitrogen adsorption at 77 K has been widely described in the literature.^{14,21,30} As it was observed in the isotherms showed in **Figure 5.4**, CO₂ adsorption at 298 K does not promote any phase transition in ZIF-4 as it does in ZIF-7, where CO₂ forces a transition from a narrow pore phase to an expanded pore phase. In situ PXRD measurements were performed under CO₂ atmosphere to confirm the possible phase transitions in the samples outgassed at 423 K and 523 K. **Figure 5.13** resumes the PXRD patterns of the ZIF-4 and ZIF-7 under an atmosphere of CO₂ at room temperature. It can be observed that in case of ZIF-7, outgassing temperature does not influence the phase transition phenomena. In both cases, transition from a narrow pore to an expanded phase is observed since new peaks appears in the pattern. On the other hand, CO₂ is not able to promote a phase transition in ZIF-4 outgassed at 423 K. As it was mentioned

before, ZIF-4 outgassed at 523 K suffer a temperature induced phase transition from a crystalline phase to an amorphous phase which makes a complex process to identify possible structural transition due to the adsorption process.

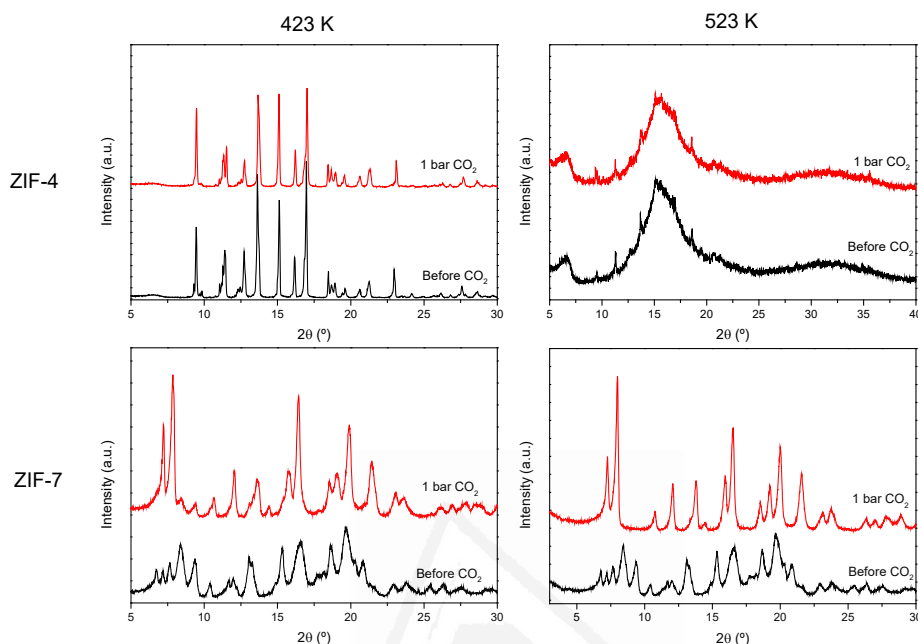


Figure 5.13. X-ray diffraction patterns of ZIF-4 and ZIF-7 under a CO₂ atmosphere.

Figure 5.14 shows the PXRD patterns of the ZIF-4 and ZIF-7 samples exposed to NO atmosphere at room temperature. As it was observed in the case of CO₂ in-situ measurements in ZIF-4, outgassing temperature does not have an influence in structural phase transition promoted by NO adsorption. Although, at 423 K ZIF-4 is a crystalline structure with a close pore phase and the sample outgassed at 523 K shifts to an amorphous phase. PXRD patterns of the ZIF-7 samples shows the peaks typical of the so called ZIF-7 phase II (narrow pore phase) which at difference of CO₂ patterns where a phase transition is observed, the adsorption of NO in ZIF-7 occurs only in the narrow pore phase and non-phase transition is performed.

The in-situ PXRD experiments confirms that nitric oxide adsorption in ZIF-4 is performed in a opposite structures produced from the outgassing temperature,

while the NO adsorption in ZIF-7 occurs in a narrow pore phase (phase II) and this molecule is not able to promote any phase transition.

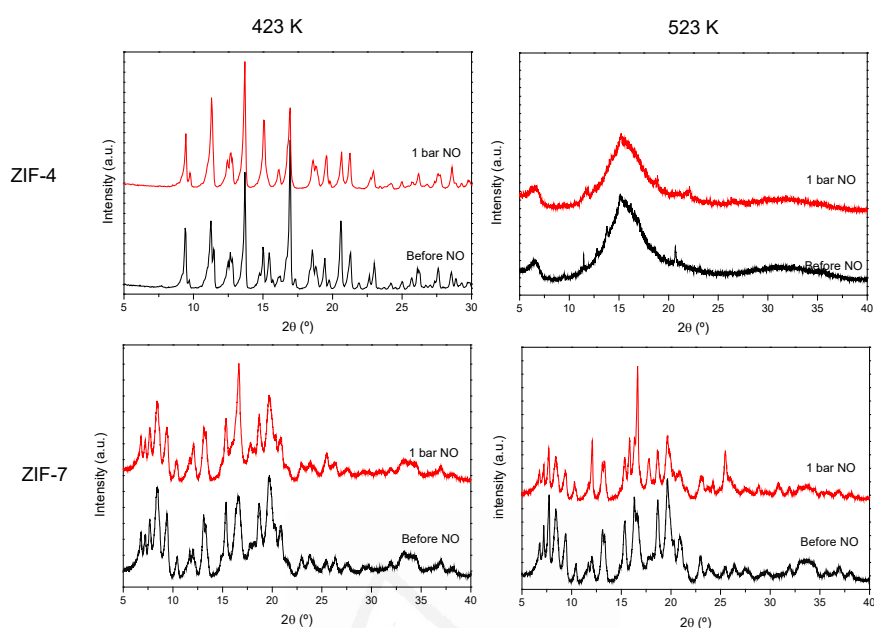


Figure 5.14. X-ray diffraction patterns of ZIF-4 and ZIF-7 under a NO atmosphere.

5.4. Conclusions

Compared to the traditional approaches to improve the interaction of NO with nanoporous structures, i.e., the incorporation of open metal sites or the functionalization of the material with basic moieties, this study anticipates a third approach based on flexible MOFs. The presence of structural changes upon adsorption in ZIFs and the transition from low-to-high density phases constitutes a promising alternative to store and deliver NO in a controlled way. By taking advantage of these phenomena, ZIF-4 can store up to 1.6 mmol/g and deliver it under humid conditions for more than 6h. Unfortunately, these excellent properties vanish after a thermal treatment at higher temperature (523K) due to the partial amorphization and re-crystallization of ZIF-4 into the amorphous structure. In the specific case of ZIF-7, although the amount adsorbed is lower due to the inability of NO to breathe the structure, the presence of a dense-phase allows to control the

delivery kinetics for more than 18h with a total amount released of more than 70 $\mu\text{mol/g}$ at 318K. These excellent results together with the excellent structural stability of ZIFs, even under physiological solution, opens the gate towards the application of ZIFs in biomedical processes (e.g., NO storage and delivery).

5.5. References

1. Keefer, L. K. Twarding Thrombosis. *Nat. Mater.* **2**, 357–358 (2003).
2. Moncada, S., Palmer, R. M. & Higgs, E. A. Nitric oxide: physiology, pathophysiology, and pharmacology. *Pharmacol. Rev.* **43**, 109 LP – 142 (1991).
3. Padden, K. M., Krebs, J. F., MacBeth, C. E., Scarrow, R. C. & Borovik, A. S. Immobilized Metal Complexes in Porous Organic Hosts: Development of a Material for the Selective and Reversible Binding of Nitric Oxide. *J. Am. Chem. Soc.* **123**, 1072–1079 (2001).
4. Wheatley, P. S. *et al.* NO-releasing zeolites and their antithrombotic properties. *J. Am. Chem. Soc.* **128**, 502–509 (2006).
5. Xiao, B. *et al.* High-Capacity Hydrogen and Nitric Oxide Adsorption and Storage in a Metal–Organic Framework. *J. Am. Chem. Soc.* **129**, 1203–1209 (2007).
6. McKinlay, A. C. *et al.* Exceptional Behavior over the Whole Adsorption–Storage–Delivery Cycle for NO in Porous Metal Organic Frameworks. *J. Am. Chem. Soc.* **130**, 10440–10444 (2008).
7. Cattaneo, D. *et al.* Tuning the nitric oxide release from CPO-27 MOFs. *RSC Adv.* **6**, 14059–14067 (2016).
8. Nguyen, J. G., Tanabe, K. K. & Cohen, S. M. Postsynthetic diazeniumdiolate formation and NO release from MOFs. *CrystEngComm* **12**, 2335 (2010).
9. Lowe, A., Chittajallu, P., Gong, Q., Li, J. & Balkus, K. J. Storage and delivery of nitric oxide via diazeniumdiolated metal organic framework. *Microporous Mesoporous Mater.* **181**, 17–22 (2013).
10. Fairen-Jimenez, D. *et al.* Opening the Gate: Framework Flexibility in ZIF-8 Explored by Experiments and Simulations. *J. Am. Chem. Soc.* **133**, 8900–8902 (2011).
11. Casco, M. E. *et al.* Gate-opening effect in ZIF-8: the first experimental proof using inelastic neutron scattering. *Chem. Commun.* **52**, 3639–3642 (2016).

12. Cuadrado-Collados, C. *et al.* Understanding the breathing phenomena in nano-ZIF-7 upon gas adsorption. *J. Mater. Chem. A* **5**, 20938–20946 (2017).
13. Aguado, S. *et al.* Guest-induced gate-opening of a zeolite imidazolate framework. *New J. Chem.* **35**, 546–550 (2011).
14. Gandara-Loe, J. *et al.* New insights into the breathing phenomenon in ZIF-4. *J. Mater. Chem. A* **7**, 14552–14558 (2019).
15. Phan, A. *et al.* Synthesis, structure, and carbon dioxide capture properties of zeolitic imidazolate frameworks. *Acc Chem Res* **43**, 58–67 (2010).
16. Bennett, T. D. *et al.* Facile Mechanochemistry of Amorphous Zeolitic Imidazolate Frameworks. *J. Am. Chem. Soc.* **133**, 14546–14549 (2011).
17. Bennett, T. D. *et al.* Structure and properties of an amorphous metal-organic framework. *Phys. Rev. Lett.* **104**, 2–5 (2010).
18. Park, K. S. *et al.* Exceptional chemical and thermal stability of zeolitic imidazolate frameworks. *Proc. Natl. Acad. Sci. U. S. A.* **103**, 10186–91 (2006).
19. Hartmann, M., Böhme, U., Hovestadt, M. & Paula, C. Adsorptive Separation of Olefin/Paraffin Mixtures with ZIF-4. *Langmuir* **31**, 12382–12389 (2015).
20. Gücüyener, C., van den Bergh, J., Gascon, J. & Kapteijn, F. Ethane/Ethene Separation Turned on Its Head: Selective Ethane Adsorption on the Metal–Organic Framework ZIF-7 through a Gate-Opening Mechanism. *J. Am. Chem. Soc.* **132**, 17704–17706 (2010).
21. Wharmby, M. T. *et al.* Extreme flexibility in a zeolitic imidazolate framework: Porous to dense phase transition in desolvated ZIF-4. *Angew. Chemie - Int. Ed.* **54**, 6447–6451 (2015).
22. Tan, J. C., Bennett, T. D. & Cheetham, A. K. Chemical structure, network topology, and porosity effects on the mechanical properties of Zeolitic Imidazolate Frameworks. *Proc. Natl. Acad. Sci.* **107**, 9938–9943 (2010).
23. Peikert, K. *et al.* Tuning the nitric oxide release behavior of amino functionalized HKUST-1. *Microporous Mesoporous Mater.* **216**, 118–126 (2015).
24. Gandara-Loe, J. *et al.* Metal–Organic Frameworks as Drug Delivery Platforms for Ocular Therapeutics. *ACS Appl. Mater. Interfaces* **11**, 1924–1931 (2019).
25. Watanabe, T. & Sholl, D. S. Molecular chemisorption on open metal sites in Cu₃(benzenetricarboxylate)₂: A spatially periodic density functional theory study. *J. Chem. Phys.* **133**, 094509 (2010).
26. Álvarez, J. R. *et al.* Structure stability of HKUST-1 towards water and

- ethanol and their effect on its CO₂ capture properties. *Dalt. Trans.* **46**, 9192–9200 (2017).
27. Sankar, S. S., Karthick, K., Sangeetha, K. & Kundu, S. In Situ Modified Nitrogen-Enriched ZIF-67 Incorporated ZIF-7 Nanofiber: An Unusual Electrocatalyst for Water Oxidation. *Inorg. Chem.* **58**, 13826–13835 (2019).
 28. Guo, D. *et al.* Observation of Landau levels in potassium-intercalated graphite under a zero magnetic field. *Nat. Commun.* **3**, 1068 (2012).
 29. Li, K., Xiao, H., He, J. & Jiang, H. Differences in Phase Change Processes Upon Heating Between Co and Zn-ZIF-4 Compounds. *Nano* **13**, 1850025 (2018).
 30. Bennett, T. D. *et al.* Thermal amorphization of zeolitic imidazolate frameworks. *Angew. Chemie - Int. Ed.* **50**, 3067–3071 (2011).



Universitat d'Alacant
Universidad de Alicante

CHAPTER 6

Metal-Organic Frameworks as Drug Delivery Platforms for Ocular Therapeutics

Chapter 6 reviews main significant advances achieved into the adsorption and delivery of brimonidine in metal-organic frameworks (MOFs) as potential nanocarriers for ocular therapeutics. Experimental results show that UiO-67 and MIL-100 (Fe) exhibit the highest loading capacity with values up to 50-60 wt.%, while the performance is quite limited for MOFs with narrow cavities (below 0.8 nm, e.g. UiO-66 and HKUST-1). The large loading capacity in UiO-67 is accompanied by an irreversible structural amorphization in aqueous and physiological media that promotes extended release kinetics above 12 days. Compared to the traditional drawbacks associated with the sudden release of the commercial drugs (e.g., ALPHAGAN), these results anticipate UiO-67 as a potential nanocarrier for drug delivery in intra-ocular therapeutics. These promising results are further supported by cytotoxicity tests using retinal photoreceptor cells (661W).

Gandara-Loe J. et al., ACS Applied Materials and Interfaces, 2019, 11(2), 1924-1931, doi:10.1021/acsami.8b20222.

6.1. Introduction

Glaucoma is the second leading cause of irreversible blindness worldwide with millions of people, aged 40 and older, affected by its common form, open-angle glaucoma.¹ After an initial diagnosis, medication is the main treatment nowadays to halt further loss of vision. Glaucoma is a multifactorial disease, usually associated to an increased pressure within the eye, and the associated damage in the optical nerve, resulting in vision impairment and even blindness. Among the different drugs available in the market, brimonidine is one of the most widely applied.² Brimonidine is an alpha-adrenergic receptor agonist that, upon topical administration, can reduce intraocular pressure (IOP) by reducing aqueous humour production and increasing uveoscleral outflow. Recent studies have shown that brimonidine has no adverse effects on different retinal cells, but rather it shows neuroprotective effects on retinal ganglion cell degeneration in glaucoma.^{3,4} In fact, these and other results together with clinical trials have derived in the commercialization of brimonidine for the treatment of glaucoma under European medication agency (EMA) mandate (REF: EMA/366180/2017). Despite the high benefits of the drug, topical administration is usually associated with important drawbacks such as poor bioavailability (only 5% of the administered drug reaches the interior of the eye), side effects due to rapid drainage through nasolacrimal duct, and the necessity for multiple administration (2-3 eye drops daily for many years). Taking into account the low compliance of patients to strictly follow the treatment and the detrimental effects in case of breach, new therapies are required to improve the quality of life in patients and to decrease their dependence on external medication.

One of the most promising alternatives for a long-term treatment of glaucoma consist in the incorporation of the drug in platforms or vehicles able to concentrate the drug and release it at the target in a controlled way, increasing the bioavailability and avoiding the traditional “burst effects”. These delivery systems include hydrogels⁵, microspheres⁶, nano-vesicles⁷, nanoparticles⁸, microfilms⁹, among others. Unfortunately, these formulations based on macromolecules or polymers suffer from low loading capacity (gravimetric < 1 wt. % and/or volumetric <0.1 wt./vol. %) and fast release of the drug (within minutes/hours).¹⁰⁻¹² These numbers can be

improved through the incorporation of denser inorganic matrices in the formulation, for instance montmorillonite clay and layered double hydroxides (LDH).^{13,14} Montmorillonite/chitosan nanoparticles have been evaluated as delivery systems for betaxolol hydrochloride, a selective beta-adrenergic blocking agent, with excellent values of drug loading capacity (up to 14.5 wt.%) and delivery kinetics between 6-10h.¹³ Sun *et al.* reported the synthesis of composites using a thermogel incorporated with brimonidine-loaded LDH nanoparticles with a significant loading capacity (up to 0.125 mg/g), although lower than the original LDH (25.0 mg/g or 2.5%), and an improved release profile (up to 2 days are required to release 75%) compared to the original LDH.¹⁴ These studies mainly focused in pre-corneal administration, thus keeping the concerns about bioavailability in the interior of the eye (low penetration of the drug through the cornea; < 1-7%).

Taking into account the limited volume of the ocular cavity (< 3-4 cm³) and the limited allowance of fluid (human eye can hold only 7-10 ml of fluid), any intraocular delivery platform for ocular therapeutics needs to fulfil even more stringent requirements compared to pre-corneal devices such as i) extremely large loading capacity (in gravimetric (wt.%) and volumetric (w/v %) basis) to mitigate any interference in the visual field after dosing, ii) slow delivery kinetics (within days or weeks) to allow long-term therapy, iii) high biocompatibility for retinal cells and, last but not least, iv) structural instability once the material has completed the job.

Potential candidates able to fulfil these requirements are metal-organic frameworks (MOFs). The proper combination of metallic nodes or clusters and organic ligands allows to design a wide variety of 1-3D networks characterized by an extremely large surface area and pore volume.¹⁵ Previous studies described in the literature have shown that MOFs are potential candidates for drug delivery with excellent results for a wide variety of drugs such as antitumoral, retroviral, etc.^{16,17} Furthermore, *in vitro* and *in vivo* cytotoxicity assays have anticipated a promising performance with low toxicity and inflammatory activity.¹⁶⁻¹⁸ To our knowledge, MOFs have never been tested as potential drug delivery platforms for ocular therapeutics.

Based on these premises, the main goal of the present study is the evaluation of several MOFs in the adsorption and release of brimonidine for glaucoma treatment, the evaluation of their structural stability in the charging/discharging media and, last but not least, the evaluation of the cytotoxicity of the different components (bulk MOF, linker and metallic precursors) in retinal photoreceptor culture cells (661W).

6.2. Experimental section

6.2.1. MOFs synthesis

UiO-66, UiO-67 and MIL-100(Fe) MOFs have been synthesized based in previous works reported in the literature. UiO-66 and UiO-67 were synthesized based in the procedure reported by Katz *et al.*¹⁹ For UiO-66, 0.5 g of ZrCl₄ were dissolved in 20 mL of DMF and 4 mL of concentrated HCl. In a second vessel, 0.492 g of terephthalic acid (BDC) were dissolved in 40 mL of DMF. The two solutions were mixed and maintain under stirring for 30 min. The transparent final solution was transferred to a 200 mL jar, closed tightly and kept at 353 K overnight. The synthesis procedure for UiO-67 was similar to the one described for UiO-66. Briefly, 0.360 g of 4,4'-biphenyldicarboxylic acid (BDPC) were added to a mixture of 20/2 mL of DMF/concentrated HCl and 0.268 g of ZrCl₄ were dissolved into 40 mL of DMF. The two solutions were mixed and stirred for 30 min. The white colored final solution was placed into a 200 mL jar, closed tightly and kept at 353 K overnight. The resulting solid was filtered and washed first with DMF (2x30 mL) and then with ethanol (2x30 mL). Samples were activated under low vacuum ($13 \cdot 10^3$ Pa) until a temperature of 363 K was reached. The samples were then subjected to an outgassing treatment at 423 K for 3 h under ultra-high vacuum conditions. MIL-100 (Fe) was prepared using the facile low temperature synthesis procedure reported in the literature by Zhang *et al.*²⁰ Briefly, 4.04 g of Fe(NO₃)₃·9H₂O and 1.89 g of trimesic acid (H₃BTC) were dissolved in 6 mL of distillate water and kept under reflux at 368 K overnight. The solid was purified three times using a solvent extraction treatment with deionized water (350 ml) and ethanol (350 ml) at 343 K for 24 h, and

finally dried in vacuum at 423 K for 10 h. HKUST-1 (Cu) has been used as received from the Sigma-Aldrich, labelled and commercialize as Basolite C 300.

6.2.2. MOFs characterization

6.2.2.1. X-ray diffraction analysis

X-ray diffraction patterns of the samples were recorded using a Bruker D8-Advance equipment with mirror Goebel with high temperature Chamber and a generator of X-ray KRISTALLOFLEX K 760-80F with a tube of RX with copper anode. Spectra were registered between 3 and 80° (2θ) with a step of 0.05° and a time per step of 3 s.

6.2.2.2. Nitrogen isotherms at 77 K

Textural properties of the samples were evaluated by gas physisorption of nitrogen at 77 K. Gas adsorption measurements were performed in a homemade fully automated manometric equipment designed and constructed by the Advanced Materials Group (LMA), now commercialized as N2GSorb-6 (Gas to Materials Technologies; www.g2mtech.com). The samples were previously degassed for 8 h at 423 K under vacuum (10^{-3} Pa). Nitrogen adsorption data were used to determine: (i) the total pore volume (V_t) at a relative pressure of 0.95, (ii) the BET specific surface area (S_{BET}) and (iii) the micropore volume (V_{N_2}) by application of Dubinin-Radushkevich equation. The difference between V_t and V_{N_2} is considered to be the mesopore volume (V_{meso}).

6.2.2.3. Scanning electron microscopy

The size and shape of the synthesized crystals was evaluated using field emission scanning electron microscopy (FESEM). These analyses were performed in a Merlin VP Compact system from ZEISS with a resolution of 0.8 nm at 15 kV and 1.6 nm at 1 kV. FTIR spectra were recorded on a JASCO FTIR 4700 spectrometer with a resolution of 2 cm^{-1} .

6.2.2.4. MOFs structural stability test.

Structural stability of the MOFs was evaluated by immersing 0.1 g of each MOF in 50 mL of an aqueous solution or a phosphate-based solution (PBS) for 1h, 1 day, 7 days and 30 days. After this time intervals, the material was washed with ultrapure water and filtered in vacuum. After an evacuation at 393 K for 8 h, the crystallinity of the materials was checked using XRD analysis.

6.2.3. Drug loading and release experiments

Brimonidine tartrate quantification was done based on the spectrometric method developed by Bhagav *et al.*²¹ A 1500 ppm stock solution of brimonidine tartrate was prepared dissolving 1.5 g of brimonidine tartrate in 1000 mL of ultrapure water. The calibration curve was constructed measuring concentrations from 2 to 15 ppm using a UV-Vis spectrophotometer (double-beam spectrophotometer with a photomultiplier tube detector JASCO V-650 UV-VIS) at wavelengths of $\lambda_1 = 247$ nm and $\lambda_2 = 320$ nm. High performance liquid chromatography (HPLC) was used to certify the precision of the UV-Vis method in brimonidine quantification.²² Both methods gave an accuracy above 97%, thus confirming the validity of the UV-vis technique for brimonidine determination.

6.2.3.1. Brimonidine loading experiments

For the loading tests, a group of aqueous solutions with an initial concentration of 200 ppm, 500 ppm, 750 ppm, 1000 ppm and 1500 ppm of brimonidine tartrate were prepared from the stock solution. The MOFs samples were outgassed at 423 K overnight prior to the adsorption measurement. 100 mg of each MOF were placed in contact with 50 mL of each concentration and left under stirring until equilibrium was reached. Aliquots were taken in different periods of time in order to evaluate the kinetic behaviour of each MOF. All samples reached complete equilibrium after 7 h.

The quantification of brimonidine tartrate was determined by UV-Vis spectrophotometry diluting each aliquot 1:100 and using the method described above. A MOF-loaded blank experiment was measured to determine possible

interferences in the UV-vis signal due to the MOF degradation. However, no interferences were observed at the wavelengths selected for brimonidine for all MOFs evaluated.

6.2.3.2. Brimonidine release experiments

In an initial step the MOFs were loaded by contacting 100 mg of a degassed MOF with 50 mL of a 500 ppm brimonidine tartrate aqueous solution. The system was left under stirring for 7 h to ensure full equilibrium. After this time, the sample was collected by filtration and an aliquot was saved to determine the maximum loading amount. The brimonidine-loaded MOF was washed several times with ultrapure water and dried under vacuum at 333 K for 6 h. The dried brimonidine-loaded MOF was immersed in 50 mL of physiological solution (PBS) and aliquots were taken at different times up to 12 days. Brimonidine determination has been performed in a similar procedure to that described above. All the dilutions (1:100) and calibration curve were measured using PBS as a solvent instead of ultrapure water.

6.2.4. Cytotoxicity tests

661W cell line, derived from mouse retinoblastoma and considered a photoreceptor cell line, was employed in the cytotoxicity tests. To assess MOFs toxicity in retinal cells, 611W cells were incubated with MOFs and MOFs components at different concentrations for 24h or 48h. A death control was also included in each study to be sure that cells die with a noxious stimulus (0.4 mM sodium nitroprusside, SNP; 228710, Sigma-Aldrich, St Louis, MO, USA).

First, for cell viability assays at 24h or 48h after adding the MOFs, cells were plated in 96-well plates at a density of 10000 or 4000 cells per well respectively. They were incubated in Dulbecco's modified Eagle's medium (DMEM High Glucose; L0106, Biowest, Nuaille, France) supplemented with 10% fetal bovine serum (FBS; SV30160, GE Healthcare, Pasching, Austria), 1% penicillin/streptomycin (P9781, Sigma-Aldrich) and 1% L-Glutamine (25030-081, Gibco, Paisley, UK), and maintained during the whole experiment at 310 K in a humidified atmosphere with 5% CO₂. 24 h after seeding, medium was replaced and 0.4 mM SNP or MOF

concentrations of 0, 10, 20, 30, 40 and 50 $\mu\text{g/ml}$ in supplemented DMEM were added. Each condition was done at eight replicates per plate. MOFs and their respective components were maintained in the medium and cell viability was assessed at 24 and 48 hours using the XTT cell viability assay (X4626, Sigma-Aldrich). Briefly, this kit consists of a colorimetric assay dependent of a redox reaction that measures mitochondrial activity and thus is an estimate of cell quantity. 100 μl of XTT was added to each well, incubated at 310 K and 5% CO_2 for 2 hours and absorbance measured at 492 nm in a Beckman Coulter AD340 plate reader (Beckman Coulter Inc., Nyon, Switzerland). Absorbance was transformed into viability percentage considering the value of the 0 $\mu\text{g/ml}$ concentration (positive control) as 100% cell viability. All these procedures were done in sterile conditions, using sterile materials and solutions, and MOFs were heat-sterilized at 423 K for 3 hours prior to use.

6.3. Results

6.3.1. MOFs characterization

Four different MOFs have been selected for this study, i.e. HKUST-1, MIL-100 (Fe), UiO-66 and UiO-67. The main goal is to evaluate systems with a different porous structure (from purely microporous to micro/mesoporous systems) and different surface chemistry to evaluate the role of these parameters in the loading and delivery performance. Furthermore, these MOFs have been selected based in the *a priori* low toxicity of the metal species incorporated: zirconium chloride lethal dose LD_{50} ~ 3500 mg/kg (for UiO-66 and UiO-67), and iron nitrate lethal dose LD_{50} ~ 3250 mg/kg (for MIL-100(Fe)), except HKUST-1 with a potential toxicity due to the copper nitrate used (LD_{50} ~ 940 mg/kg).²³ The selection of HKUST-1 is based on the excellent performance that has been reported in the literature for this material for a wide range of applications, e.g. methane and hydrogen storage,^{24–26} hydrocarbon separation,²⁷ etc. Briefly, HKUST-1 is assembled from $\text{Cu}_2(\text{H}_2\text{O})_2$ dimer units and tridentate trimesate groups to form 3D channels with alternating cavities of diameter ~ 1.4 nm and ~ 1.1 nm connected through pore windows of ~ 1.0 nm.²⁸ There are also smaller diameter cavities of ~ 0.5 nm between the larger cavities. MIL-100 (Fe)

consist on trimers of metal octahedra and trimesic acid as a linker.¹⁶ This material possesses cages in the mesoporous range (diameter ~ 2.5 and ~ 2.9 nm), accessible through pore windows of 0.48×0.58 nm, for the small cage, and 0.86 nm, for the larger one. Finally, UiO-66 and UiO-67 are constituted by clusters of $Zr_6O_4(OH)_4(CO_2)_{12}$ connected through benzene-dicarboxylate and biphenyl-dicarboxylate linkers, respectively. The longer linker in the last case gives rise to larger tetrahedral and octahedral microporous cages, i.e. 0.75 nm and 1.2 nm, for UiO-66, and 1.2 nm and 1.6 nm, for UiO-67. **Figure 6.1** shows a schematic drawing of the evaluated MOFs.

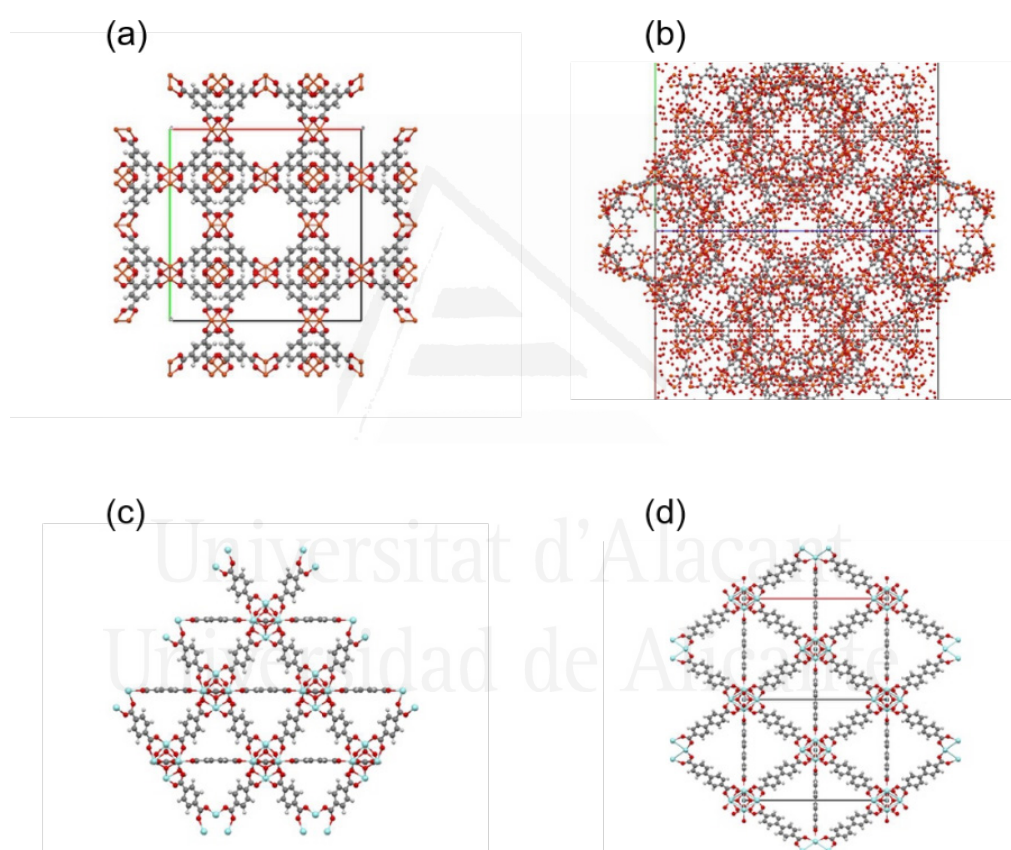


Figure 6.1. Schematic drawing of the MOFs evaluated: (a) HKUST-1, (b) MIL-100 (Fe), (c) UiO-66 and (d) UiO-67.

The textural characteristics of the synthesized materials have been evaluated using nitrogen adsorption at cryogenic temperatures. These measurements are mandatory to certify the validity of the synthesis method applied and to confirm the quality of the synthesized nanocrystals. **Figure 6.2** shows the N_2

adsorption/desorption isotherms at 77 K for the four samples evaluated. The nitrogen adsorption capacity for samples HKUST-1, MIL-100 (Fe) and UiO-66 is rather similar, i.e. around 350-400 cm³/g, although with some differences in the shape of the isotherm (knee at low relative pressures). While it is narrower for HKUST-1 and UiO-66 as corresponds to purely microporous materials, the knee is wider and associated with a significant slope in the mid-pressure region in the specific case of the micro/mesoporous MIL-100 (Fe). Compared to UiO-66, longer linkers in UiO-67 give rise to a two-fold increase in the adsorption capacity up to 800 cm³/g. The presence of larger cages (~1.6 nm) in the case of UiO-67 can be clearly appreciated by a sudden jump in the nitrogen adsorption isotherm at $p/p_0 \sim 0.2$ (right after the filling of the narrow cages).

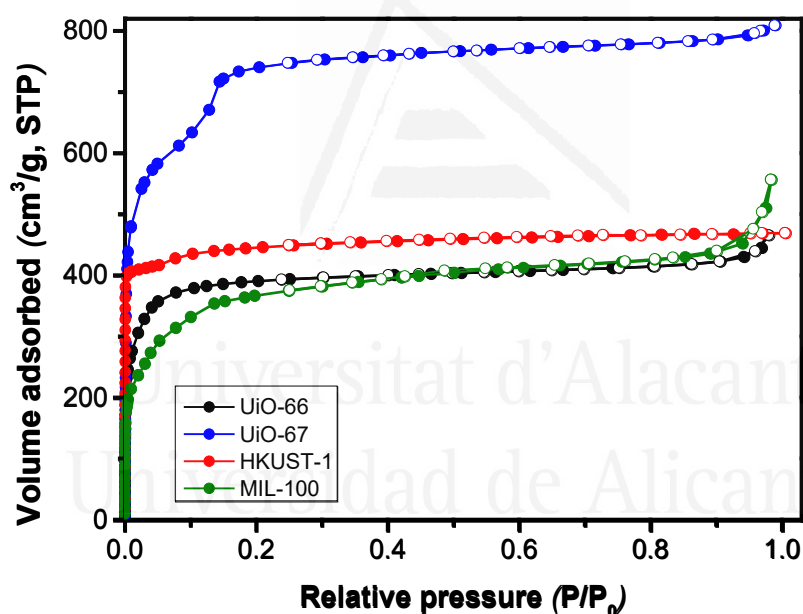


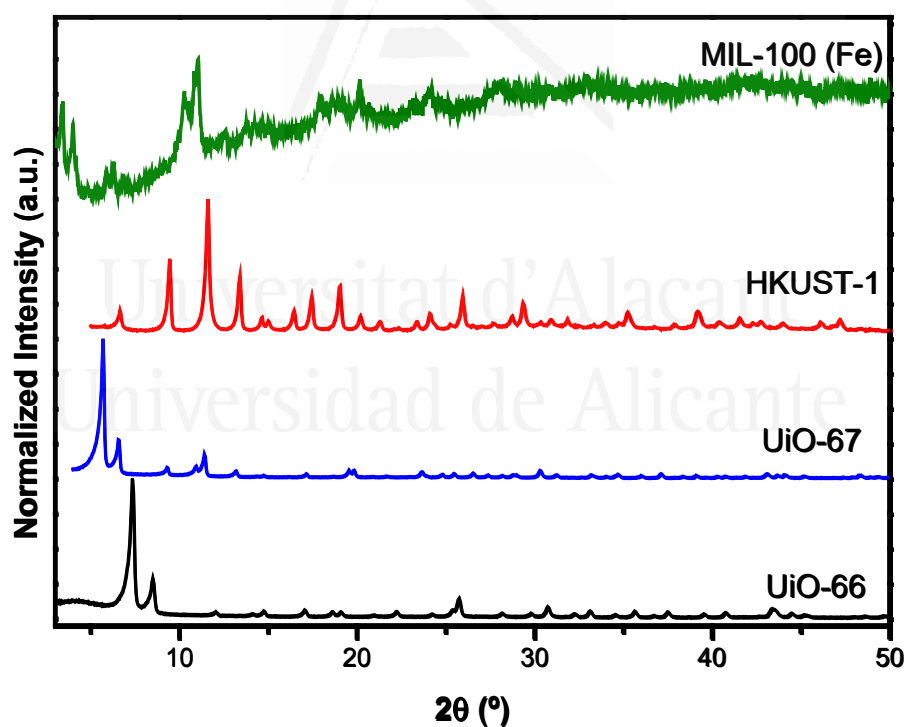
Figure 6.2. N₂ adsorption (full symbols)/desorption (empty symbols) isotherms at 77K for the different MOFs evaluated.

The textural characteristics obtained after application of the BET and the Dubinin-Radushkevich (DR) equations are collected in **Table 6.1**. The reported values are in close agreement with the literature, thus validating the synthesis procedure.

Table 6.1. Textural properties of the synthesized MOFs.

Sample	S_{BET} (m^2/g)	V_0 (cm^3/g)	V_t (cm^3/g)
HKUST-1	1690	0.65	0.72
MIL-100 (Fe)	1360	0.42	0.79
UiO-66	1465	0.53	0.69
UiO-67	2620	1.02	1.24

In addition to the textural properties, the crystallinity of the synthesized MOFs has been evaluated using X-ray diffraction. **Figure 6.3** shows the XRD pattern for each of the four MOFs evaluated in the 2θ range $2\text{-}50^\circ$. These patterns perfectly match those described in the literature for these materials, thus confirming the quality of the synthesized metal-organic frameworks.

**Figure 6.3.** X-ray diffraction pattern of the different MOFs evaluated.

The size and shape of the synthesized nanocrystals have been evaluated using FESEM. The morphology of the synthesized nanocarriers, preferentially the

crystal size, is of paramount importance in ophthalmological applications to minimize potential disruption in the visual field upon injection and/or undesired sedimentation in the ocular cavity. **Figure 6.4** shows representative images for the MOFs evaluated. As it can be observed, MIL-100 (Fe), UiO-66 and UiO-67 are constituted by nanometer size crystals (average crystal size 140 ± 30 nm, 80 ± 10 nm and 120 ± 20 nm, respectively). Only HKUST-1 exhibits larger crystals in the micrometer size range (average crystal size 3 ± 1 μ m).

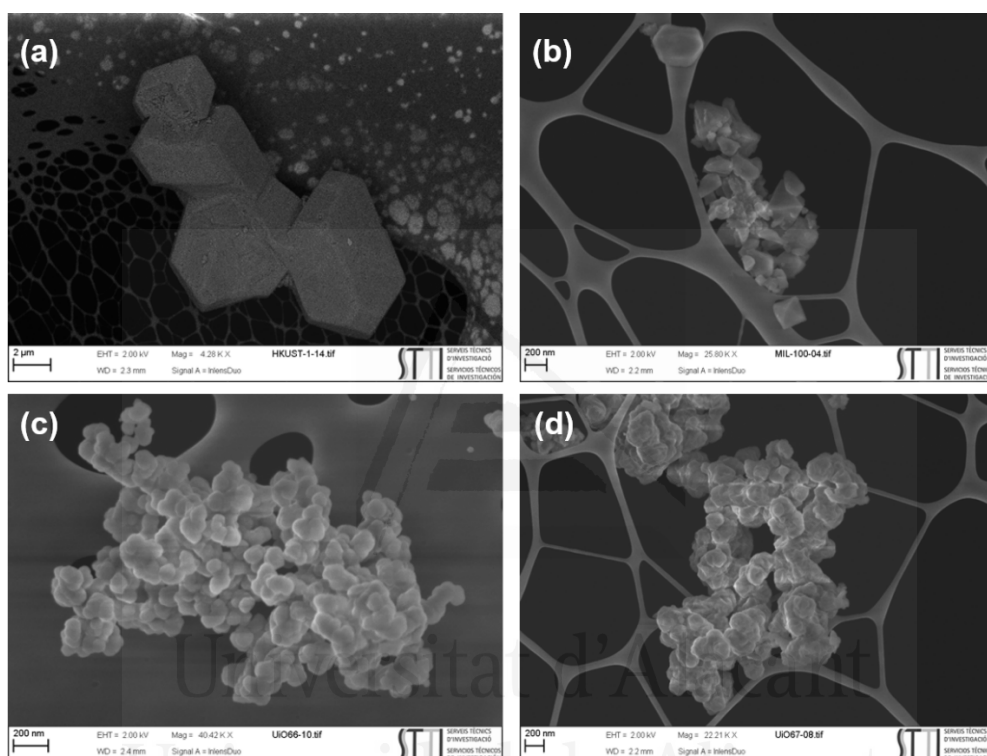


Figure 6.4. FESEM images of the MOFs evaluated: (a) HKUST-1, (b) MIL-100 (Fe), (c) UiO-66 and (d) UiO-67.

Last but not least, the vibrational modes of the synthesized MOFs have been evaluated using FTIR (**Figure 6.5**). FTIR spectra constitute a fingerprint to further certify the quality of the synthesized MOFs, including the surface functional characteristics. The four samples evaluated exhibit similar vibrational bands in the $1300\text{-}1700$ cm^{-1} range attributed to the structural carboxylate groups in the linkers.²⁹ More specifically, the peaks around 1368 cm^{-1} and 1448 cm^{-1} corresponds to symmetric stretching vibrations of the carboxylate group (O-C-O groups), whereas the asymmetric vibrations in the carboxylate appears close to $1550\text{-}1650$ cm^{-1} .³⁰

Vibration peaks corresponding to the aromatic ring (C=C) are shown at ca. 1500 cm^{-1} , whereas bands attributed to the metal cluster and the linkers appear at lower wavenumbers (1000-500 cm^{-1}).³¹ UiO-66 and UiO-67 exhibit longitudinal and transverse modes of Zr-O vibrations between 660 and 540 cm^{-1} and the OH and CH bending modes at 770-740 cm^{-1} . MIL-100(Fe) exhibits sharp peaks at 760 cm^{-1} and 709 cm^{-1} due to the linker bending modes and Fe-O cluster vibrations, while HKUST-1 shows a band at 727 cm^{-1} attributed to the Cu-O mode.^{30,32} Last but not least, the absence of significant peaks at 1710-1720 cm^{-1} attributed to the C=O stretching vibration of residual trimesic acid suggest the proper purification of the synthesized MOFs.

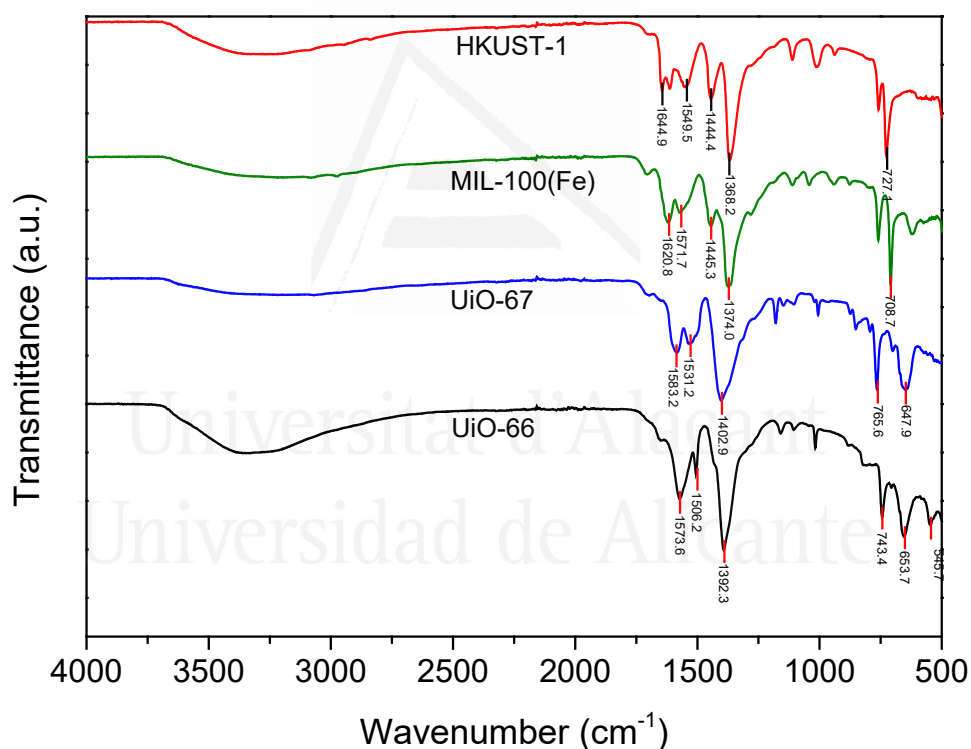


Figure 6.5. FTIR spectra of the MOFs evaluated: HKUST-1, MIL-100 (Fe), UiO-66 and UiO-67.

6.3.2. Brimonidine adsorption isotherms

Once the crystallographic structure and morphology of the different MOFs has been validated and the textural properties confirmed, these materials have been evaluated in the adsorption of brimonidine tartrate. Liquid phase adsorption

isotherms have been quantified at 298 K and at ranging concentrations using ultra-pure water as charging media. As it can be appreciated in **Figure 6.6** the amount of drug loaded increases with the concentration of brimonidine in the aqueous solution, except for HKUST-1 and UiO-66 materials where saturation is already reached at concentrations above 800 mg/L. Apparently, MOFs with narrow micropores become quickly saturated, the final loading capacity being around 0.16 g/g. The scenario changes completely for MOFs with larger micropores/small mesopores such as UiO67 and MIL-100 (Fe). In this specific case, the loading capacity increases with concentration with a loading capacity at 1400 mg/L as high as 0.31 g/g (31 wt.%), for MIL-100 (Fe), and 0.44 g/g (44 wt.%), for UiO-67. Previous studies described in literature for ibuprofen adsorption in MIL-100 (Cr) reported adsorption values around 0.35 g/g, in close agreement with our data.¹⁶ Extrapolation of the adsorption data reported in **Figure 6.6** using the Langmuir equation (dotted line) gives loading values at saturation as high as 0.49 g/g, for MIL-100 (Fe), and 0.63 g/g, for UiO-67. To our knowledge, these are among the best values described in the literature for the adsorption of drugs using metal-organic frameworks.

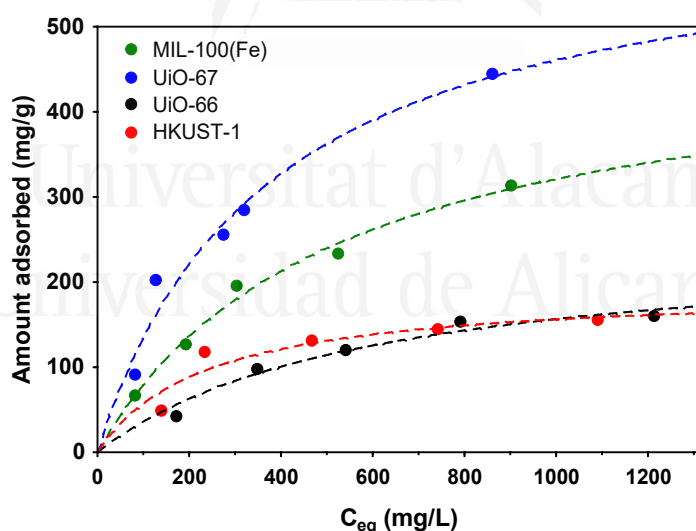


Figure 6.6. Liquid-phase adsorption isotherms for brimonidine tartrate at 298 K. Fitting to Langmuir equation is included (dotted line).

Adsorption results clearly show that UiO-67, with the larger BET surface area and pore volume (above 1 cc/g), is the best performing material over the whole concentration range evaluated with a loading capacity superior to the majority of

MOFs reported in the literature so far for similar drugs. Despite the significant surface area in HKUST-1, this material becomes saturated immediately with a poor performance at high concentrations. Last but not least, although MIL-100 (Fe) and UiO-66 exhibit similar textural properties (in terms of BET surface area and micropore volume), the presence of mesopores in the former MOF play a crucial role with a loading capacity more than double that of UiO-66. Consequently, these results clearly anticipate that microporous MOFs with a pore size below 0.8 nm are not appropriate for brimonidine adsorption due to the limited accessibility of the drug to the interior cavities. This can also be the reason for the lower loading in MIL-100 (Fe) compared to UiO-67 due to the limited accessibility of the small cages in the former (pore windows of 0.48 x 0.58 nm). In addition to the loading capacity, adsorption kinetics are also relevant. As it can be observed in **Figure 6.7**, for an initial concentration of 500 ppm, saturation is reached within 4-5 h, except for UiO-66 with narrow but accessible cavities with adsorption kinetics slightly above 5h. These results are very promising since only a few hours are required to load the materials before injection into the eye.

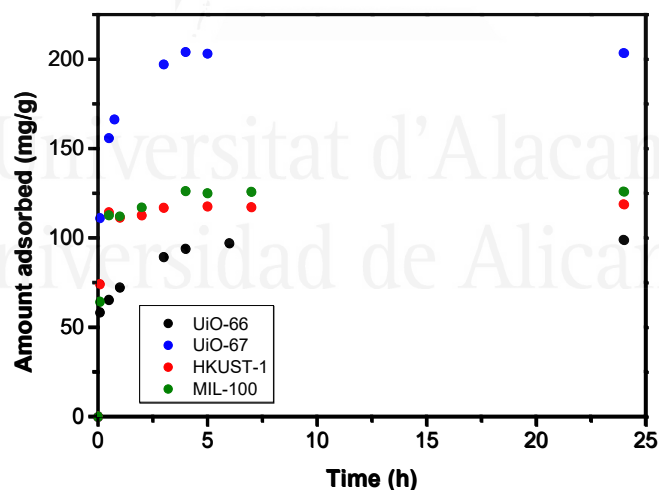


Figure 6.7. Brimonidine loading kinetics at 298 K in the different MOFs evaluated (initial brimonidine concentration in the aqueous solution 500 ppm) .

6.3.3. MOFs stability test

One of the most relevant issues in medical therapies, not frequently addressed in the literature, concerns the stability of the host structures in the loading

and discharging media, i.e. in aqueous solutions or physiological media (PBS). It is well-known in the literature that several MOFs exhibit structural deterioration upon exposure to a humid environment.^{33,34} The instability has been traditionally attributed to the nuclearity, coordination number of the metal, functionality of linker and framework dimensionality. In our case, we have evaluated the structural stability of the different MOFs at different time intervals from 1 day until 30 days using an aqueous solution as a charging media (see **Figure 6.8**). At this point it is important to highlight that similar results have been observed in the presence of a physiological solution of PBS as discharging media. As it can be appreciated, the structural stability highly depends on the nature of the metal-organic network. While HKUST-1 and UiO-67 exhibit a rapid deterioration in the first 24 hours, samples UiO-66 and MIL-100 (Fe) remain stable even after 30 days. The irreversible instability of HKUST-1 is in close agreement with previous findings in the literature in liquid and gas phase.^{35,36}

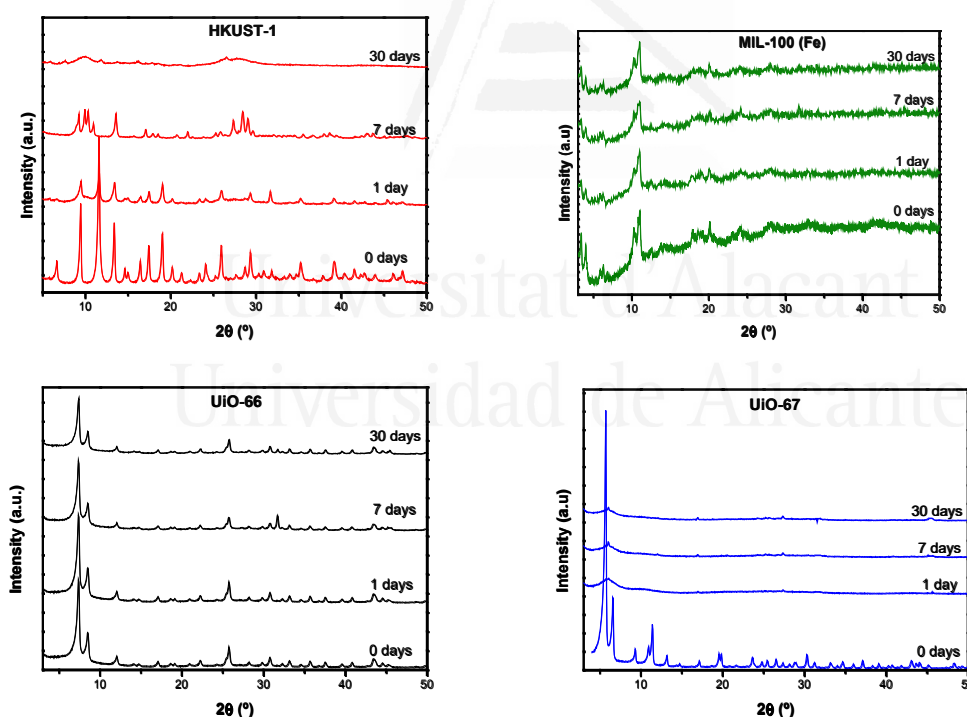


Figure 6.8. XRD pattern for the different MOFs evaluated after suspension in aqueous media at 298 K for different time periods (up to 30 days).

HKUST-1 suffers degradation due to the strong interaction between the open Cu(II) sites (the coordinatively unsaturated sites from the copper paddlewheel) and

water molecules. This irreversible instability can explain the low loading capacity for HKUST-1 (see **Figure 6.6**), despite the presence of a significant BET surface area in the as-synthesized material. However, the presence of limited accessibility for brimonidine to the inner micropores must also be considered to explain the adsorption results. Contrary to HKUST-1, the results for UiO-67 are more surprising since this material exhibits the best adsorption performance, despite the drastic instability observed in the first few hours. To confirm the potential role of brimonidine within the structure as a stabilizer, we have performed XRD analysis of the loaded material under aqueous solution right after complete saturation, i.e. after 24h. **Figure 6.9** compares the original XRD pattern and the ones after 24h in the presence and absence of the drug. As expected, although the XRD pattern of the loaded MOF already anticipates an important crystallographic deterioration (amorphization), this damage is lower than the one observed in the absence of the drug, i.e. the presence of the brimonidine within the structure seems to be crucial to preserve a certain crystallinity in UiO-67, thus explaining the excellent adsorption results achieved.

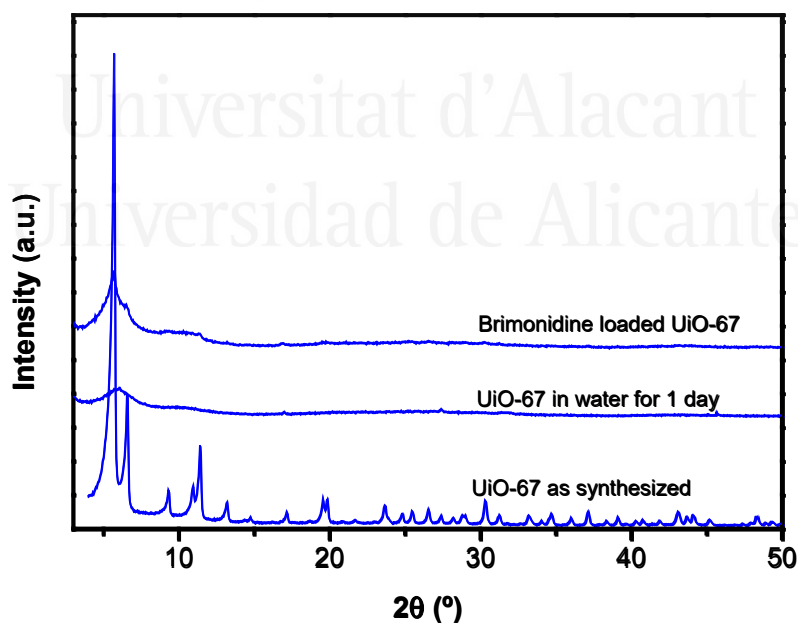


Figure 6.9. XRD pattern for UiO-67 evaluated after suspension in aqueous media at 298 K in the presence and absence of brimonidine.

6.3.4. Brimonidine release kinetics

Upon loading, the second open question concerns the delivery kinetics. Previous studies described in the literature for MOFs have shown that 3-5 days release is a common number for this kind of drugs.¹⁶⁻¹⁸ The main question at this point is the role that instability can exhibit in the release kinetics. Release kinetics were not evaluated for HKUST-1 due to the strong structural deterioration even in the presence of the drug. **Figure 6.10** shows the amount of brimonidine released in PBS (discharging media) versus time for the loaded UiO-66, UiO-67 and MIL-100 (Fe) materials (loading performed using a 500 ppm brimonidine aqueous solution). As it can be observed, all materials exhibit two regimes related to the location of the drug in the structure. An initial release for 3 days associated with brimonidine weakly bonded within the MOF structure (ca. 70-80% delivery for MIL-100 (Fe) and UiO-66) and a subsequent slow release of brimonidine, although quite limited up to 75-85% during next 6-8 days. The absence of complete release in these two MOFs clearly denotes the presence of brimonidine strongly interacting with the structural framework. Interestingly, the scenario changes completely in the specific case of UiO-67. The structural instability in aqueous and PBS media gives rise to an initial release within 4 days of around 43% and a subsequent and progressive release with time up to a 56% after 12 days. An extrapolation of these values suggests potentially more than 30 days of continuous release with the associated benefits for a chronic ocular disorder such as glaucoma. The beneficial role of the partial amorphization of MOFs in the release kinetics was recently described by Orellana-Tavra et al. for calcein released in mechanically deteriorated UiO-66.³⁷ More than 30 days controlled release could be obtained versus 2 days in the crystalline counterpart.

As described in the introduction, the final goal of this study is the design of metal-organic frameworks with a high potential to be applied in glaucoma treatment after injection in the intra-ocular cavity. From this perspective, the progressive deterioration of the MOF within the eye while releasing the drug can be anticipated as an optimum performance to promote the complete clearance of the ocular cavity (absence of disruptions in the visual field) upon completion of the job. To this end, there is a major issue that must be fulfilled, i.e. the MOFs and their respective

components (metal nodes and organic linkers) must exhibit a low toxicity towards ocular tissues.

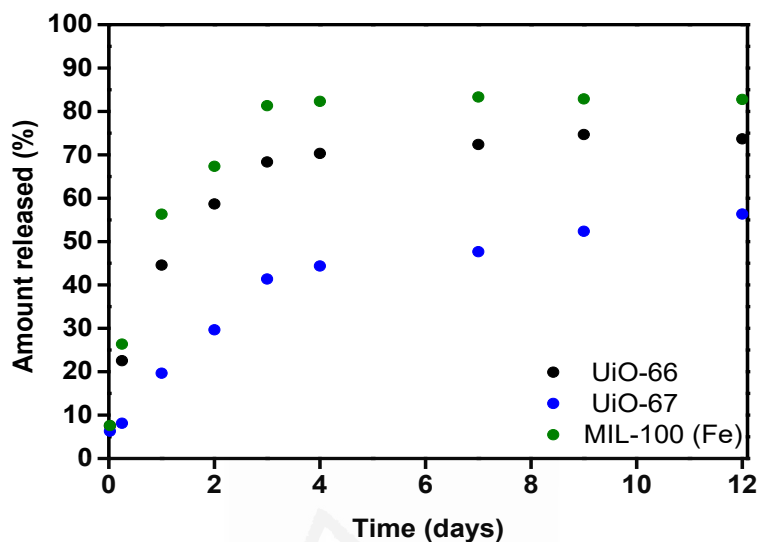


Figure 6.10. Brimonidine tartrate release kinetics at 298 K in physiological media PBS (loading concentration 500 ppm).

As described in the introduction, the final goal of this study is the design of metal-organic frameworks with a high potential to be applied in glaucoma treatment after injection in the intra-ocular cavity. From this perspective, the progressive deterioration of the MOF within the eye while releasing the drug can be anticipated as an optimum performance to promote the complete clearance of the ocular cavity (absence of disruptions in the visual field) upon completion of the job. To this end, there is a major issue that must be fulfilled, i.e. the MOFs and their respective components (metal nodes and organic linkers) must exhibit a low toxicity towards ocular tissues.

6.3.5. MOFs *in vitro* toxicity test

In vitro models based in cell cultures, instead of *in vivo* models, are the first choice to test toxicity of new compounds or nanoparticles, because of their low cost, time efficiency, their trustworthy results, and because they involve no ethical issues.³⁸

The 661W cell line (kindly provided by Dr. Muayyad Al-Ubaidi; University of Oklahoma) is derived from retinoblastoma, a mouse retinal tumour.³⁹ This cell line expresses several markers of photoreceptor cells,⁴⁰ that made them one of the most widely used cell line to screen safety and efficacy in a great number of drugs for ocular treatments.^{41–44} In fact, Januschowski *et al.* suggest that cell lines derived from retinal cells such 661W or ARPE19 cells are the most accurate to evaluate retinal toxicity.⁴⁵ Thus, cytotoxicity of MOFs and their components was assessed in 661W cells (**Figure 6.11**). As it can be appreciated in Figure 4, except in the specific case of HKUST-1, the cell viability evaluated after 48h exposure is, in all cases, very close to 100 %. These results anticipate that MIL-100 (Fe), UiO-66 and UiO-67 materials do not affect retinal photoreceptor cells viability. Only sample HKUST-1 is toxic for retinal photoreceptor cells (cell viability below 50 %), most probably due to the presence of copper and the important structural deterioration associated.

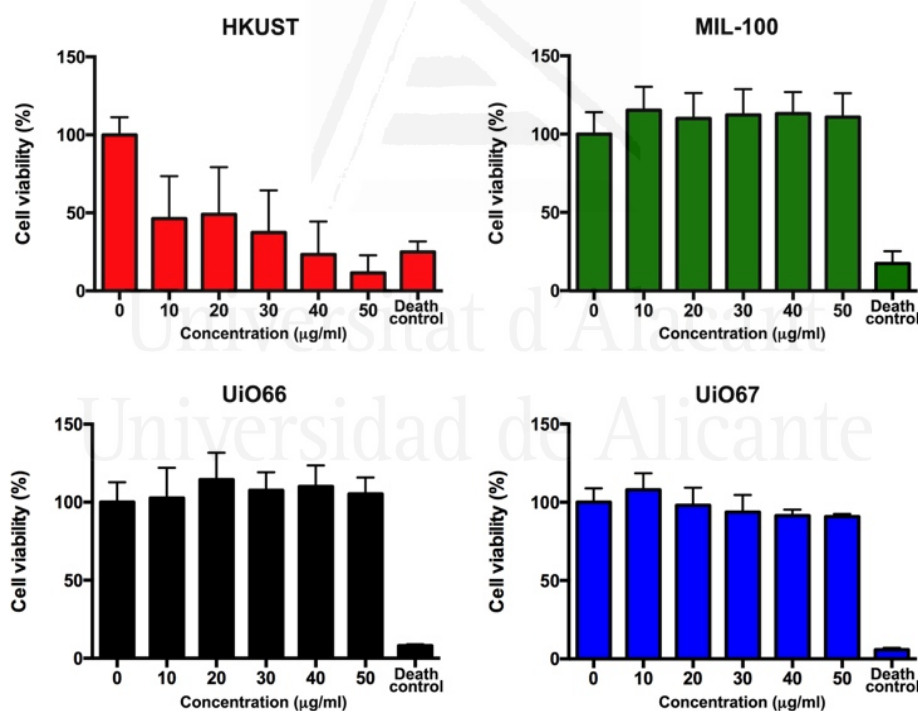


Figure 6.11. Cytotoxicity tests for the different MOFs evaluated using a retinal photoreceptor cell line (661 W) at 48h.

To confirm this point, the cytotoxicity assays have been extended to the different components of the MOF, i.e. metallic precursors and organic linkers (see **Figures 6.12-6.15**). These experiments confirm that, with the exception of HKUST-

1, cell viability is not affected by any of the MOF components. In addition, the effect of MIL-100 (Fe), UiO-66 and UiO-67 on cells is rather similar with different time incubations, i.e. the viability is maintained at 24h and 48h. This observation suggests that a prolonged interaction between MOFs and cells after intra-ocular injection will not be harmful for cell viability or proliferation. On the contrary, HKUST-1 present time-dependent effects, as a prolonged contact with cells drops cell viability at 48h, when compared to 24h (Figures S8). An evaluation of the HKUST-1 components clearly shows that the metal precursor (copper nitrate) is the one responsible for the high toxicity of the MOF.

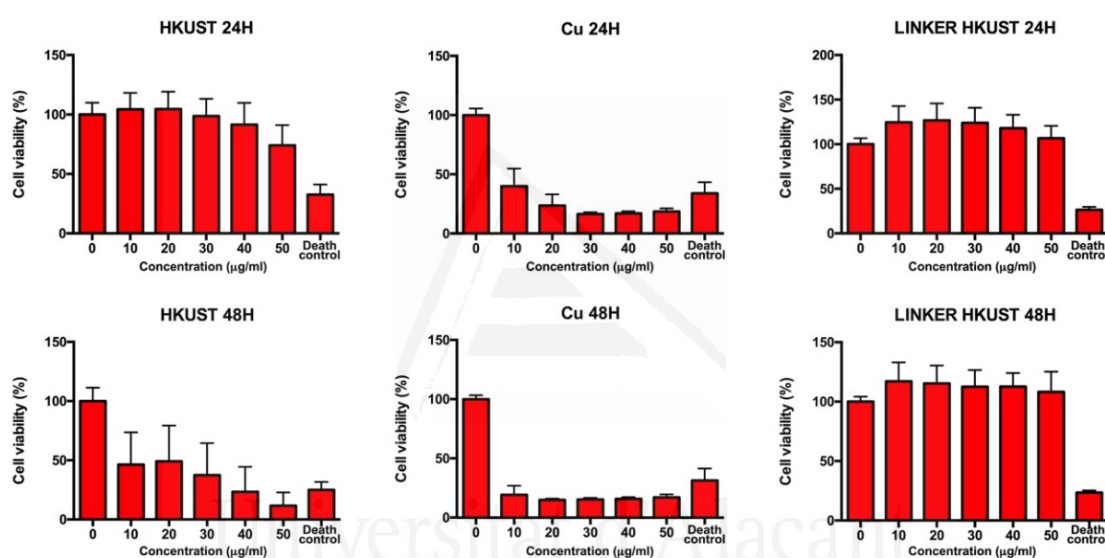


Figure 6.12. Cytotoxicity tests for the HKUST-1 using 661W retinal cells at 24h and 48h. The evaluation of the metallic precursors used (copper nitrate) and the organic linker (trimesic acid) is also included.

In summary, metal-organic frameworks can be anticipated as potential nanocarriers for drug delivery in ocular therapeutics. The proper selection of the metallic node and the organic linker allows to improve the loading capacity to values above 50 wt.%, in the specific case of UiO-67 and MIL-100 (Fe). Furthermore, the associated amorphization observed for UiO-67 in aqueous media becomes an advantage to extend the delivery kinetics up to 12 days or above. Taking into account that a patient with glaucoma requires 2-3 drops of brimonidine per day (2 mg/mL solution- ALPHAGAN), this corresponds to 0.3 mg per day or 4.5 mg every

15 days. Assuming a loading capacity for UiO-67 of 630 mg/g, patients will require the injection of 7 mg of loaded MOF every 15 days, i.e. 10 μl of MOF (considering the crystallographic density of 0.708 g/cm^3). Interestingly, these numbers are *a priori* within the theoretical threshold that human eye can hold. However, as the bioavailability of the drops is quite low ($< 10\%$), these numbers could be even reduced for an intra-ocular administration (considering 100% bioavailability) up to 1 order of magnitude, thus validating the potential of the proposed approach.

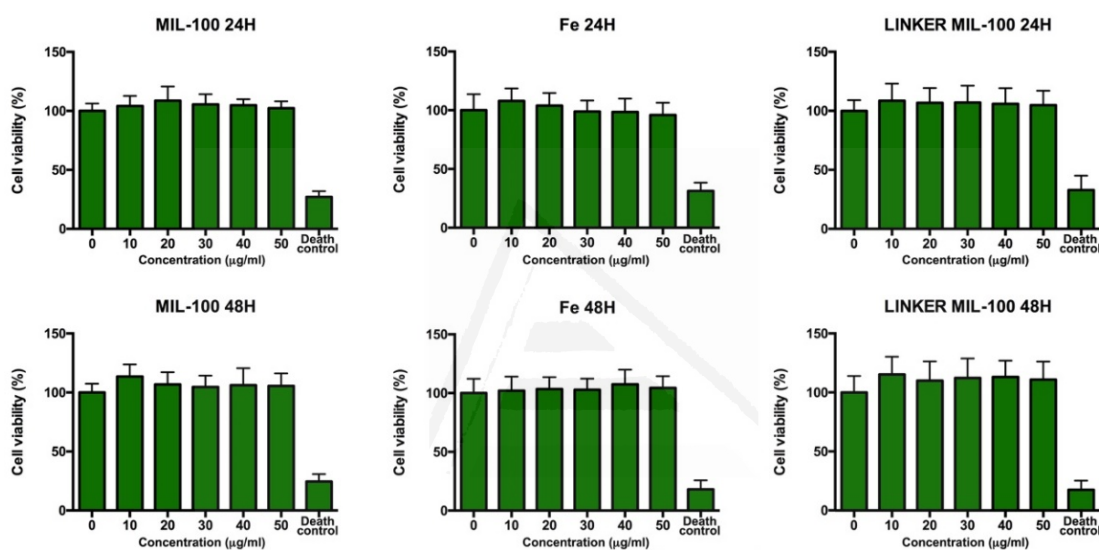


Figure 6.13. Cytotoxicity tests for the MIL-100 (Fe) using 661W retinal cells at 24h and 48h. The evaluation of the metallic precursors used (iron nitrate) and the organic linker (trimesic acid) is also included.

Furthermore, *in vitro* cytotoxicity results confirm the validity of our approach for drug delivery in intraocular treatments without inducing damage in photoreceptor retinal cells. These results are encouraging in terms of drug dosage and long-term delivery. However further experiments *in vivo* would be useful to assess the possible reaction of retinal tissue to MOFs, such as microglial activation or gliosis, due to an eventual accumulation of MOF metal nodes during long-term treatments.

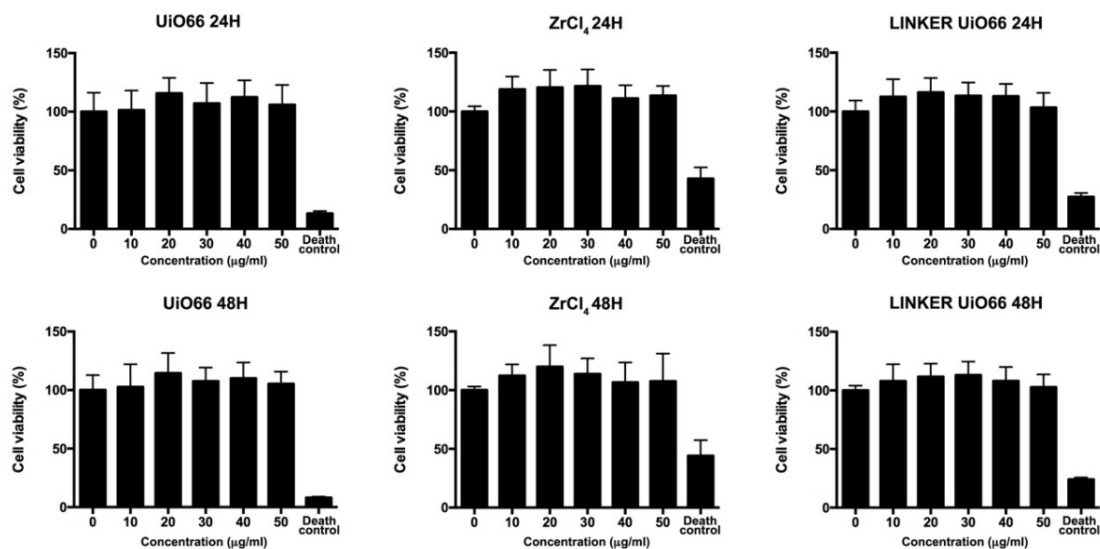


Figure 6.14. Cytotoxicity tests for the UiO-66 using 661W retinal cells at 24h and 48h. The evaluation of the metallic precursors used (zirconium chloride) and the organic linker (terephthalic acid) is also included.

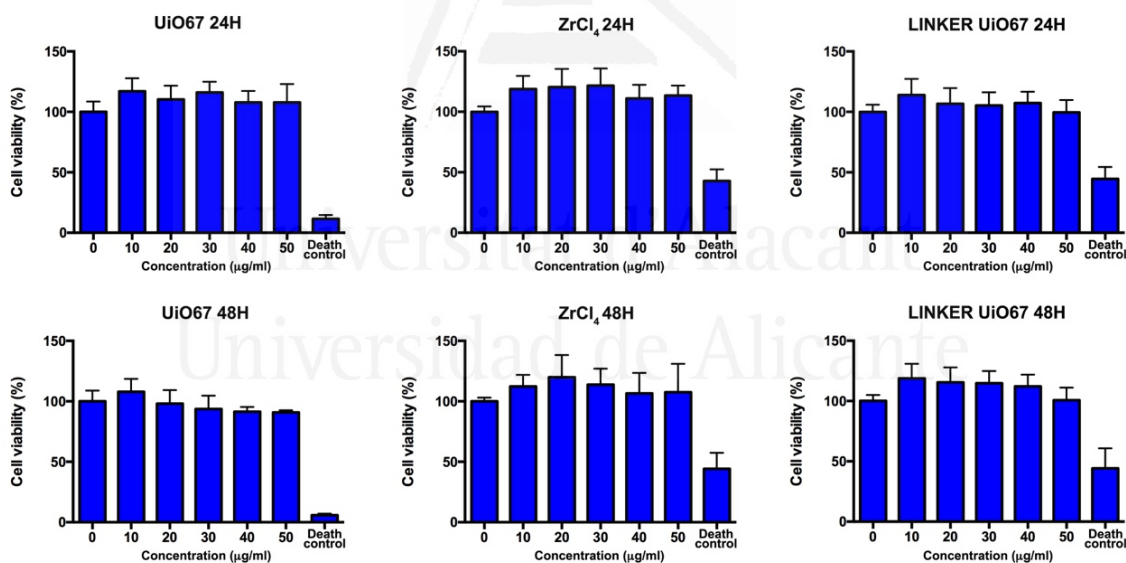


Figure 6.15. Cytotoxicity tests for the UiO-67 using 661W retinal cells at 24h and 48h. The evaluation of the metallic precursors used (zirconium chloride) and the organic linker (4,4'-biphenyldicarboxylic acid) is also included.

6.4. Conclusions

Metal-organic frameworks (MOFs) can be anticipated as promising nanodevices for drug delivery in ocular therapeutics. Experimental results have shown that samples combining wide micropores and/or small mesopores are able to achieve a high loading capacity, above 50 wt.% (MIL-100(Fe) and UiO-67), for an alpha-adrenergic receptor agonist such as brimonidine. Furthermore, delivery kinetics have shown that the associated amorphization in the case of UiO-67 upon ultrapure water or PBS exposure, as suggested by XRD measurements, can be very helpful to extend the delivery kinetic up to 12 days or above. Last but not least, cytotoxicity assays using retinal photoreceptor cells show a high biocompatibility for the MOFs evaluated, except HKUST-1, thus paving the way towards the application of MOFs in intra-ocular therapeutics.

6.5. References

1. Glaucoma Research Foundation. GRF. Available at: <https://www.glaucoma.org>.
2. Greenfield, D. S., Liebmann, J. M. & Ritch, R. Brimonidine: a new alpha2-adrenoreceptor agonist for glaucoma treatment. *J. Glaucoma* **6**, 250–258 (1997).
3. Beltramo, E. *et al.* Effects of the neuroprotective drugs somatostatin and brimonidine on retinal cell models of diabetic retinopathy. *Acta Diabetol.* **53**, 957–964 (2016).
4. Lambert, W. S., Ruiz, L., Crish, S. D., Wheeler, L. A. & Calkins, D. J. Brimonidine prevents axonal and somatic degeneration of retinal ganglion cell neurons. *Mol. Neurodegener.* **6**, 4 (2011).
5. Cho, I. S. *et al.* Thermosensitive hexanoyl glycol chitosan-based ocular delivery system for glaucoma therapy. *Acta Biomater.* **39**, 124–132 (2016).
6. Chiang, B. *et al.* Sustained reduction of intraocular pressure by supraciliary delivery of brimonidine-loaded poly(lactic acid) microspheres for the treatment of glaucoma. *J. Control. Release* **228**, 48–57 (2016).
7. Prabhu, P. *et al.* Preparation and Evaluation of Nano-vesicles of Brimonidine

- Tartrate as an Ocular Drug Delivery System. *J. Young Pharm.* **2**, 356–361 (2010).
8. Ibrahim, M. M., Abd-Elgawad, A.-E. H., Soliman, O. A. & Jablonski, M. M. Novel Topical Ophthalmic Formulations for Management of Glaucoma. *Pharm. Res.* **30**, 2818–2831 (2013).
 9. Manickavasagam, D. *et al.* Assessment of alkoxyphenacyl-based polycarbonates as a potential platform for controlled delivery of a model anti-glaucoma drug. *Eur. J. Pharm. Biopharm.* **107**, 56–66 (2016).
 10. Wadhwa, S., Paliwal, R., Paliwal, S. & Vyas, S. Nanocarriers in Ocular Drug Delivery: An Update Review. *Curr. Pharm. Des.* **15**, 2724–2750 (2009).
 11. Jiang, S., Franco, Y. L., Zhou, Y. & Chen, J. Nanotechnology in retinal drug delivery. *Int. J. Ophthalmol.* (2018). doi:10.18240/ijo.2018.06.23
 12. Bachu, R., Chowdhury, P., Al-Saedi, Z., Karla, P. & Boddu, S. Ocular Drug Delivery Barriers—Role of Nanocarriers in the Treatment of Anterior Segment Ocular Diseases. *Pharmaceutics* **10**, 28 (2018).
 13. Li, J. *et al.* Montmorillonite/chitosan nanoparticles as a novel controlled-release topical ophthalmic delivery system for the treatment of glaucoma. *Int. J. Nanomedicine* **Volume 13**, 3975–3987 (2018).
 14. Sun, J. *et al.* Sustained Release of Brimonidine from a New Composite Drug Delivery System for Treatment of Glaucoma. *ACS Appl. Mater. Interfaces* **9**, 7990–7999 (2017).
 15. Zhou, H.-C., Long, J. R. & Yaghi, O. M. Introduction to Metal–Organic Frameworks. *Chem. Rev.* **112**, 673–674 (2012).
 16. Horcajada, P. *et al.* Metal–Organic Frameworks as Efficient Materials for Drug Delivery. *Angew. Chemie Int. Ed.* **45**, 5974–5978 (2006).
 17. Horcajada, P. *et al.* Porous metal–organic-framework nanoscale carriers as a potential platform for drug delivery and imaging. *Nat. Mater.* **9**, 172–178 (2010).
 18. Abuçafy, M. P. *et al.* Supramolecular cyclodextrin-based metal-organic frameworks as efficient carrier for anti-inflammatory drugs. *Eur. J. Pharm. Biopharm.* **127**, 112–119 (2018).
 19. Katz, M. J. *et al.* A facile synthesis of UiO-66, UiO-67 and their derivatives. *Chem. Commun.* **49**, 9449 (2013).
 20. Zhang, F. *et al.* Facile synthesis of MIL-100(Fe) under HF-free conditions and its application in the acetalization of aldehydes with diols. *Chem. Eng. J.* **259**, 183–190 (2015).
 21. Bhagav, P., Deshpande, P., Pandey, S. & Chandran, S. Development and

- Validation of Stability Indicating UV Spectrophotometric Method for the Estimation of Brimonidine Tartrate in Pure Form, Formulations and Preformulation Studies. *Der Pharm. Lett.* **2**, 106–122 (2010).
22. Popaniya, H. S. & Patel, H. M. Simultaneous Determination of Brimonidine Tartrate and Timolol Maleate in Combined Pharmaceutical Dosage Form Using Two Different Green Spectrophotometric Methods. **3**, 1330–1340 (2014).
 23. U.S. National Library of Medicine. Toxicology Data Network. Available at: <https://toxnet.nlm.nih.gov/index.html>.
 24. Farha, O. K. *et al.* Metal–Organic Framework Materials with Ultrahigh Surface Areas: Is the Sky the Limit? *J. Am. Chem. Soc.* **134**, 15016–15021 (2012).
 25. McKinstry, C., Cussen, E. J., Fletcher, A. J., Patwardhan, S. V. & Sefcik, J. Scalable continuous production of high quality HKUST-1 via conventional and microwave heating. *Chem. Eng. J.* **326**, 570–577 (2017).
 26. Tian, T. *et al.* A sol–gel monolithic metal–organic framework with enhanced methane uptake. *Nat. Mater.* **17**, 174–179 (2018).
 27. Wang, S., Yang, Q. & Zhong, C. Adsorption and separation of binary mixtures in a metal-organic framework Cu-BTC: A computational study. *Sep. Purif. Technol.* **60**, 30–35 (2008).
 28. Getzschmann, J. *et al.* Methane storage mechanism in the metal-organic framework Cu₃(btc)₂: An in situ neutron diffraction study. *Microporous Mesoporous Mater.* **136**, 50–58 (2010).
 29. Lin, R., Ge, L., Diao, H., Rudolph, V. & Zhu, Z. Ionic Liquids as the MOFs/Polymer Interfacial Binder for Efficient Membrane Separation. *ACS Appl. Mater. Interfaces* **8**, 32041–32049 (2016).
 30. Tan, F. *et al.* Facile synthesis of size-controlled MIL-100(Fe) with excellent adsorption capacity for methylene blue. *Chem. Eng. J.* **281**, 360–367 (2015).
 31. Leclerc, H. *et al.* Infrared study of the influence of reducible iron(iii) metal sites on the adsorption of CO, CO₂, propane, propene and propyne in the mesoporous metal–organic framework MIL-100. *Phys. Chem. Chem. Phys.* **13**, 11748 (2011).
 32. Valenzano, L. *et al.* Disclosing the Complex Structure of UiO-66 Metal Organic Framework: A Synergic Combination of Experiment and Theory. *Chem. Mater.* **23**, 1700–1718 (2011).
 33. Karra, J. R., Jasuja, H., Huang, Y.-G. & Walton, K. S. Structural stability of BTTB-based metal–organic frameworks under humid conditions. *J. Mater. Chem. A* **3**, 1624–1631 (2015).

34. Qadir, N. ul, Said, S. A. M. & Bahaidarah, H. M. Structural stability of metal organic frameworks in aqueous media – Controlling factors and methods to improve hydrostability and hydrothermal cyclic stability. *Microporous Mesoporous Mater.* **201**, 61–90 (2015).
35. Al-Janabi, N. *et al.* Mapping the Cu-BTC metal–organic framework (HKUST-1) stability envelope in the presence of water vapour for CO₂ adsorption from flue gases. *Chem. Eng. J.* **281**, 669–677 (2015).
36. Gul-E-Noor, F. *et al.* Effects of varying water adsorption on a Cu₃(BTC)₂ metal–organic framework (MOF) as studied by ¹H and ¹³C solid-state NMR spectroscopy. *Phys. Chem. Chem. Phys.* **13**, 7783 (2011).
37. Orellana-Tavra, C. *et al.* Amorphous metal–organic frameworks for drug delivery. *Chem. Commun.* **51**, 13878–13881 (2015).
38. Bakand, S. Cell culture techniques essential for toxicity testing of inhaled materials and nanomaterials in vitro. *J. Tissue Sci. Eng.* **07**, (2016).
39. Bernstein, S. L., Kutty, G., Wiggert, B., Albert, D. M. & Nickerson, J. M. Expression of retina-specific genes by mouse retinoblastoma cells. *Invest. Ophthalmol. Vis. Sci.* **35**, 3931–3937 (1994).
40. Tan, E. *et al.* Expression of Cone-Photoreceptor–Specific Antigens in a Cell Line Derived from Retinal Tumors in Transgenic Mice. *Invest. Ophthalmol. Vis. Sci.* **45**, 764–768 (2004).
41. Chen, W.-J. *et al.* Nrf2 protects photoreceptor cells from photo-oxidative stress induced by blue light. *Exp. Eye Res.* **154**, 151–158 (2017).
42. Fan, B., Li, F.-Q., Zuo, L. & Li, G.-Y. mTOR inhibition attenuates glucose deprivation-induced death in photoreceptors via suppressing a mitochondria-dependent apoptotic pathway. *Neurochem. Int.* **99**, 178–186 (2016).
43. Wyse Jackson, A. C. & Cotter, T. G. The synthetic progesterone Norgestrel is neuroprotective in stressed photoreceptor-like cells and retinal explants, mediating its effects via basic fibroblast growth factor, protein kinase A and glycogen synthase kinase 3 β signalling. *Eur. J. Neurosci.* **43**, 899–911 (2016).
44. Nixon, E. & Simpkins, J. W. Neuroprotective Effects of Nonfeminizing Estrogens in Retinal Photoreceptor Neurons. *Investig. Ophthalmology Vis. Sci.* **53**, 4739 (2012).
45. Januschowski, K. *et al.* Retinal Toxicity of Medical Devices Used during Vitreoretinal Surgery: A Critical Overview. *Ophthalmologica* **240**, 236–243 (2018).

CHAPTER 7

MOF-based Composites as Drug Delivery Platforms

Chapter 7 presents the synthesis of novel MOF-based polymer nanocomposite films using Zr-based UiO-67 as a metal-organic framework (MOF) and polyurethane (PU) as a polymeric matrix. Synchrotron X-ray powder diffraction (SXRPD) analysis confirms the improved stability of the UiO-67 embedded nanocrystals and scanning electron microscopy images confirm their homogeneous distribution (average crystal size ~ 100-200 nm) within the 50 μm thick film. Accessibility to the inner porous structure of the embedded MOFs has been completely suppressed for N_2 at cryogenic temperatures. However, ethylene adsorption measurements at 25°C confirm that at least 45% of the MOF crystals are fully accessible for gas phase adsorption of non-polar molecules. UiO-67@PU nanocomposite exhibits a prolonged release of brimonidine (up to 14 days were quantified). Finally, the combined use of SXRPD, thermogravimetric analysis (TGA) and FTIR analysis confirmed the presence of the drug in the nanocomposite film, the stability of the MOF framework and the drug upon loading, and the presence of brimonidine in an amorphous phase once adsorbed.

7.1. Introduction

Glaucoma is a pathological eye disorder associated with an increase in the intraocular pressure (IOP) and one of the leading causes of irreversible blindness worldwide.¹ Approximately, 70 million middle-aged people and elderly are affected by its common form, open angle glaucoma whereof 10% ends in bilateral blindness.² Among the different drugs to treat glaucoma, brimonidine tartrate is one of the most widely applied. Brimonidine is an alpha-adrenergic agonist able to reduce the ocular pressure through the constriction in the blood vessels, ending in the decrease of the aqueous humour production.³

Conventional drug delivery systems such as eye droplets represent 90% of the marketed ophthalmic formulations.^{4,5} However, severe constraints are associated with this topical approach such as tear turnover, fast nasolacrimal drainage and reflex blinking, thus ending in a non-optimal dosage.⁶ Roughly, only 5% of the drug applied topically reaches the deeper ocular tissues, thus forcing pharmaceutical producers to increase the drug concentration, with the associated increase in the toxicity and, indirectly, the risk of side effects.⁷ Another limitation of these topical administration routes is the low compliance of patients, mainly elderly, to strictly follow the administration protocol (administration of a number of droplets several times per day).

The development of more efficient ocular drug delivery systems with well-designed and prolonged release kinetics remains a challenge in materials science and ophthalmology. Nanocarriers such as polyacrylic acid nanoparticles,⁸ chitosan nanoparticles,⁹ nano-vesicles,¹⁰ and layered double hydroxides (LDH)¹¹ have been reported as promising alternatives for topical brimonidine dosage. However, the main limitation of some of these materials for potential application falls in the physical (low gravimetric capacity for the drug) and textural properties.

Novel drug administration platforms to treat ocular disorders prepared from polymeric materials (solid or semi-solid inserts) have gained a large popularity in the last few years.¹²⁻¹⁴ The potential advantage of these polymeric devices is the accurate dosing, increased ocular residence time, reduction of systemic side effects

or better patient compliance, just to mention some.¹⁵ Due to the potential of these devices in ocular drug delivery, several companies have patented and commercialized them. For instance, one of the first marketed ocular insert has been commercialized by Alza (Vacville, CA) as Ocusert[®] which are used to dose anti-glaucoma drug pilocarpine for a maximum of 5-7 days.^{16,17} Although these are excellent numbers, the absence of a well-defined regular 3D network within these polymeric matrices limits their total drug uptake and hinders a controlled release.

Based on these premises, the design of novel functional ocular polymeric devices through the incorporation of perfectly designed high capacity nanofillers would be a key steppingstone to increase the versatility and impact of these inserts in nanomedicine. A potential approach not widely explored in the literature could be the incorporation of nanocarriers with an improved drug adsorption uptake and controlled release, provided that the incorporated guest structures does not alter the mechanical properties of the insert, while the porous structure of the nanofiller remains fully accessible in the mixed formulation.¹⁸⁻²⁰ Among the potential candidates, high-surface area porous materials such as metal-organic frameworks (MOFs) provide an avenue to achieve these requirements.²¹

MOFs are crystalline materials formed by the union of metal centres and organic linkers. The self-assembly of metal clusters (or nodes) and organic ligands allows the design of a large number of 1D to 3D networks characterized by high surface area, a large pore volume and tuneable host-guest interactions.²² Over the last few years, these materials have shown promise as a potential platform for drug delivery in powder form.^{23,24} Recent studies from Gandara-Loe *et al.* have shown that MOFs can store a large amount of brimonidine tartrate (up to 600 mg of drug per gram of MOF), and with an extended release time of up to 12 days, in the specific case of UiO-67. Furthermore, *in vitro* cytotoxicity assays have demonstrated the low toxicity of UiO-67 for retinal photoreceptor cells.²⁵ The excellent performance of UiO-67 is motivated by the presence of large tetrahedral and octahedral cages in the micro/mesoporous range.²⁶ Taking into account these excellent properties, the successful incorporation of these 3D porous networks in continuous polymeric matrix will offer a new perspective in nanomedicine with more suitable nanocomposite materials (instead of working with powders), with novel

functionalities (e.g., drug delivery properties), to be used either as micro-inserts (e.g. punctal plug in lacrimal or sub-tenon cavities) or as a component in contact lens.
27,28

Polymer-MOF nanocomposite materials have already been reported in the literature as potential candidates for gas adsorption/separation processes such as, CO₂/N₂ or CO₂/CH₄ separation or ethylene adsorption.^{29,30} There are recent studies on the use of HKUST-1/polyurethane nanocomposite membranes for drug encapsulation and controlled release.³¹ However, the understanding of molecular accessibility in liquid phase adsorption processes is still a challenge due to the different nature of the polymeric network and the MOF nanofiller. To the best of our knowledge, polymer-MOFs nanocomposite films have not yet been tested as a drug delivery carrier for ocular therapeutics.

Based on these premises, the main goal of this work is to report an optimal synthesis of functional MOF-based polyurethane thin films, and to evaluate the performance of these UiO-67@PU nanocomposites for brimonidine adsorption/release in liquid phase. The successful development of these functional materials (MOF@polymer) will open the gate towards the application of these devices in a number of ocular disorders that require a controlled and prolonged release of drugs, from glaucoma treatment to post-surgical treatments by anti-inflammatory drugs.

7.2. Experimental section

7.2.1. UiO-67 and films synthesis

7.2.1.1. UiO-67 synthesis

UiO-67 was synthesized based on the procedure reported in the literature by Katz et al.³² Briefly, 0.268 g of ZrCl₄ were dissolved in a mixture of 20 mL of N,N-dimethylformamide (DMF) and 2 mL of concentrated HCl. In a second vessel 0.360 g of 4,4'-biphenyldicarboxylic acid (BDPC) were dissolved in 40 mL of DMF. The two solutions were mixed and maintained under sonication for 30 min. The final

solution was transferred to a 200 mL glass jar, closed tightly and kept at 80°C overnight. The resulting white solid was filtered and washed first with DMF (2x30 mL) and then with ethanol (2x30 mL). The sample was activated first under low vacuum conditions (13×10^{-3} Pa) up to 90°C and, afterwards, at 150°C for 3 h under ultra-high vacuum conditions.

7.2.1.2. UiO-67@PU synthesis

The UiO-67@PU nanocomposite films were fabricated by following the procedures described below. Polyurethane (PU) solution was prepared by dissolving poly [4,4'-methylenebis (phenyl isocyanate)-alt-1,4-butanediol/di(propylene glycol)/polyurethane] pellets (purchased from Sigma Aldrich and used without further alterations) in tetrahydrofuran (THF) for 24-48 hours until complete dissolution of the polymer pellets. 30 wt.% UiO-67@PU nanocomposites and pristine PU films were produced by the dispersion of a specified amount of previously synthesized MOF particles (of a required wt.%) in a small amount of THF (930 mg of MOF per 1 mL of THF) before their incorporation into the PU-THF solution. The dispersion was performed by a combination of sonication (5 min) and magnetic stirring (20 min, 80 rpm). This strategy, followed by Cohen *et al.*³³, has proven to be a versatile approach for the preparation of homogeneous polymer-MOF nanocomposites. The thin films were subsequently cast onto a glass substrate *via* the doctor blade technique using a casting speed of 10 mm/s to achieve membranes of ~50 μm in thickness.^{30,34}

7.2.2. Materials characterization.

7.2.2.1. Synchrotron X-ray powder diffraction (SXRPD) analysis

Synchrotron X-ray powder diffraction data (SXRPD) were collected on the powder diffraction end station of the MSPD beamline at synchrotron ALBA in Spain, using a MYTHEN detector and a wavelength of 0.4227 Å. The experiments were performed in an *ad hoc* capillary reaction cell (fused silica capillary, inner diameter 0.7 mm, outer diameter 0.85 mm). SXRPD measurements were performed at 25°C to the as-synthesized UiO-67, PU and the UiO-67@PU films, and also to the UiO-

67@PU films after brimonidine adsorption. The reference spectra for brimonidine tartrate powder was also determined.

7.2.2.2. Thermogravimetric analysis (TGA)

Thermogravimetric analysis data of UiO-67, PU film and UiO-67@PU film were obtained using TG-DTA METTLER TOLEDO equipment model TG/SDTA851e/SF/1100. The samples were measured using an alumina sample holder and temperature range of 25°C-600°C with a heating rate of 5 °C/min under N₂ flow.

7.2.2.3. Scanning electron microscopy (SEM) evaluation

Cross-section micrographs were recorded using a Hitachi scanning electron microscope model S3000N. This microscope is equipped with Bruker brand X-ray detector (model Xflash 3001) for EDS microanalysis and mapping. Samples were kept under cryogenic conditions (liquid N₂) before the analysis in order to obtain a high-quality cross section and avoid surface alterations during the sectioning process.

7.2.2.4. Nitrogen and ethylene adsorption/desorption isotherms

Textural properties and gas phase accessibility of the different samples were evaluated by gas physisorption, i.e. nitrogen adsorption at -196°C and ethylene adsorption at 25°C. Nitrogen gas adsorption measurements were performed in a homemade fully automated manometric equipment designed and constructed by the Advanced Materials Group (LMA), now commercialized as N2GSorb-6 (Gas to Materials Technologies, www.g2mtech.com). Nitrogen adsorption data were used to calculate a) the total pore volume (V_t) at relative pressure of 0.95, b) the BET surface area (S_{BET}) and c) the micropore volume (V_{N_2}), after application of the Dubinin-Radushkevich (DR) equation. Ethylene adsorption experiments were performed in a home-built fully automated manometric equipment, now commercialized by Quantachrome Corp. as VSTAR. Before the experiments, samples were degassed at 100°C for 8 h under high vacuum conditions (10^{-5} torr).

7.2.2.5. Loading and release experiments

Brimonidine tartrate quantification was done based on the High Performance Liquid Chromatography method developed by Karamanos *et al.*³⁵ A stock solution of 1500 ppm of brimonidine tartrate was prepared by dissolving 1.5 g in 1000 mL of ultrapure water. Calibration curve was constructed by measuring concentrations from 2 to 15 ppm using chromatographic conditions, analytical column Supelcosil LC-18, 5 μm , 250 x 4.6 mm i.d. stainless steel (Supelco, Bellfonte, PA, USA) equipped with RP-18 precolumn, 20 x 4.6 mm i.d. (Supelco). The mobile phase was a mixture 9:1 (v/v) of 10 mM triethylamine pH 3.2 buffer and acetonitrile. The separation was performed at room temperature, at a flow rate of 1.0 mL/min, injection volume of 20 μL , and the detection of the brimonidine at 248 nm.

7.2.2.5.1. Brimonidine loading experiments

Brimonidine adsorption isotherms were performed at 25°C using a group of aqueous solution (pH = 7) prepared from the stock solution with an initial concentration of 250 ppm, 500 ppm, 750 ppm, 1000 ppm and 1500 ppm of brimonidine tartrate. The nanocomposite films were degassed at 100°C overnight before the experiment. Approximately, 100 mg of film were placed in contact with 50 mL of solution at each of the concentrations described above and left under stirring until equilibrium was reached. Aliquots were taken at different time intervals in order to evaluate the adsorption kinetics of the films.

The quantification of brimonidine was determined using High Performance Liquid Chromatography (HPLC) by diluting each aliquot 1:100 and using the method described above.

7.2.2.5.2. Brimonidine release experiments

100 mg of UiO-67@PU film, previously degassed, was loaded with brimonidine by contacting it with 50 mL of a 1500 ppm brimonidine tartrate aqueous solution. The system was left at 25°C under stirring for 24 h to ensure full equilibrium. After this time the film was separated from the solution and an aliquot was taken to determine the maximum loading amount. The brimonidine-loaded film was washed

several times with ultrapure water and dried under vacuum at 60°C for 6 h. The dried brimonidine loaded film was immersed in 50 mL of physiological solution (PBS) and aliquots were taken at different times up to 14 days. The aliquots were diluted 1:100 and brimonidine quantification was performed using the HPLC method described above.

7.3. Results

7.3.1. Characterization of the synthesized films and accessibility of the embedded MOFs

The crystallinity of the synthesized materials has been evaluated through synchrotron X-ray powder diffraction measurements (SXRPD). **Figure 7.1** shows the comparative SXRPD patterns for the as-synthesized UiO-67 crystals, obtained by solvothermal method, and the UiO-67@PU film. The SXRPD pattern of the UiO-67 sample perfectly fits with the simulated pattern and with those previously described in the literature, thus confirming the quality and reproducibility of the synthesized MOF.³² Concerning the UiO-67@PU nanocomposite material, the SXRPD pattern confirms the presence of a semi-crystalline system, with the combination of crystallinity due to UiO-67 nanoparticles and the amorphous background from the PU matrix.

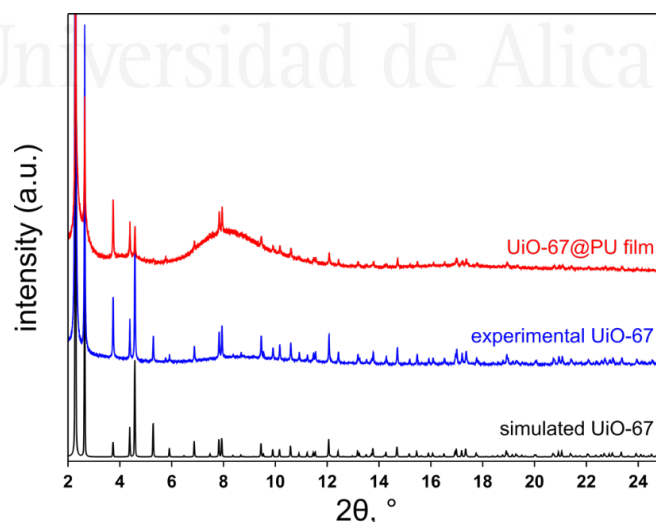


Figure 7.1. Synchrotron XRPD experimental patterns of UiO-67 and UiO-67@PU film accompanied by simulated pattern of UiO-67.

The PU matrix is characterized by a broad peak between $2\theta = 6^\circ - 11^\circ$ (see **Figure 7.2**), whereas the main diffraction peaks of the MOF can be clearly appreciated at $2\theta = 2.3^\circ - 2.6^\circ$. These results confirm the preservation of the 3D network in the UiO-67 nanocrystals upon incorporation in the polymeric matrix, and their excellent crystallinity.

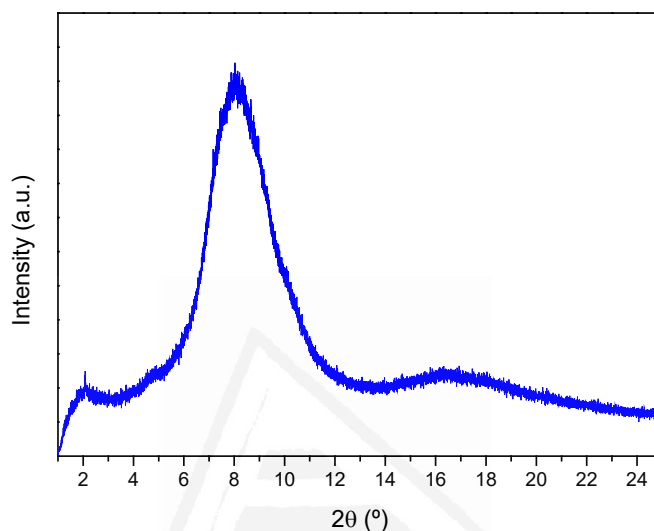


Figure 7.2. Synchrotron X-ray powder diffraction pattern of pure polyurethane film.

As it is observed in **Figure 7.3**, the morphology of UiO-67@PU film is a semi-transparent and flexible composite material with high versatility for the production of different ocular devices.

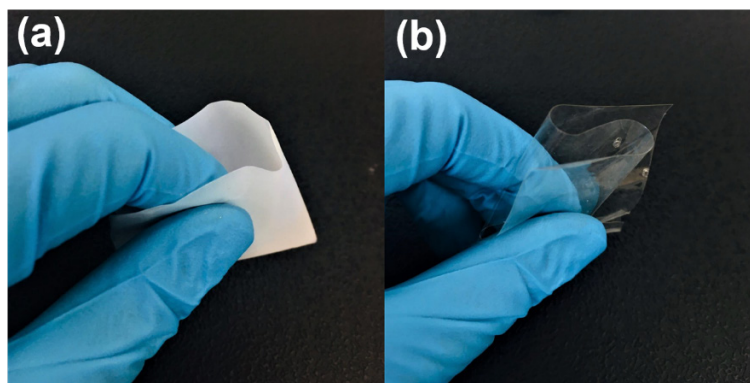


Figure 7.3. Photographs of the different samples prepared by doctor blading, (a) UiO67@PU and (b) PU films.

As it is shown in **Figure 7.4**, the nanocomposite film is formed by MOF nanocrystals (average crystal size 100-200 nm) embedded into the polyurethane matrix, giving a film of approximately 50 μm thick. **Figure 7.4c** shows the relatively uniform distribution of the UiO-67 nanocrystals within the PU matrix, an observation that was further confirmed by specific Zr-mapping experiments (**Figure 7.4d**). Previous results described in the literature for gas separation using similar composites have anticipated that the accessibility (permeation of gases) decreases with the thickness of the film.^{34,36} Based on this assumption and taking into account the objectives of this study (liquid phase adsorption processes usually possess lower kinetics compared to gas adsorption processes), we assume that a film of 50 μm can be considered as a good approach. Furthermore, 30 wt.% MOF loading can be considered as an upper limit to keep a good balance between thermomechanical and toughness properties for a potential future application.^{34,37}

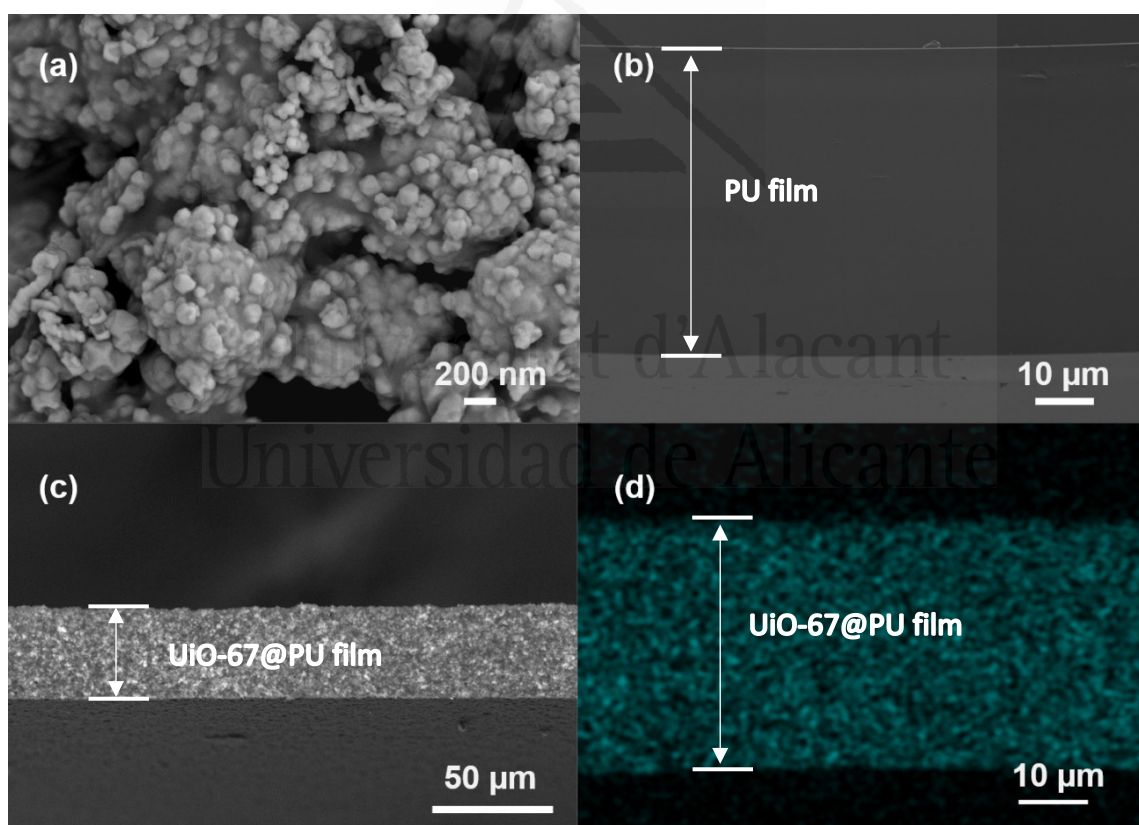


Figure 7.4. SEM micrograph of (a) as-synthesized UiO-67 nanocrystals, (b) cross-section of a 50 μm thick neat PU film, (c) cross-section of UiO-67@PU 50- μm film and (d) Zr EDX mapping (green colour) of a cross-section of UiO-67@PU nanocomposite film.

Thermogravimetric (TGA) analyses were used to evaluate the thermal stability of the nanocomposite film compared to the pure components (PU and UiO-67). Polyurethane and UiO-67 nanoparticles exhibit characteristic decomposition profiles with very sharp and symmetric decompositions peaks, as appreciated in **Figure 7.5**. For instance, the pure PU film exhibits a decomposition profile with a well-defined decomposition peak centred at 337°C and a small shoulder at 430°C, which is typical of polyurethane materials.³⁸

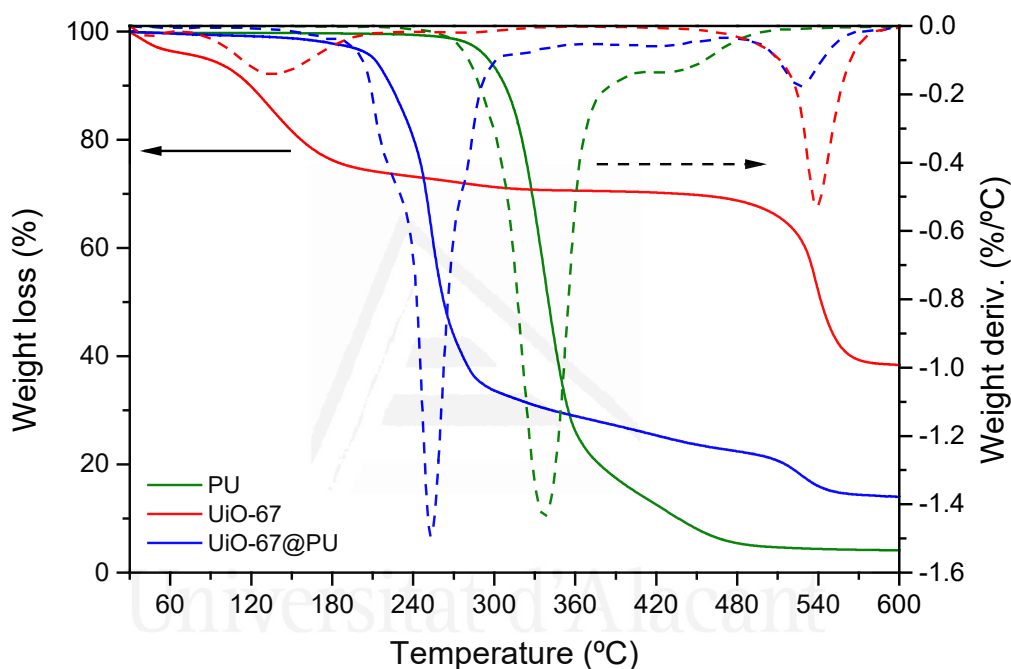


Figure 7.5. Thermogravimetric analysis (TGA and DTGA) of PU, UiO-67 and UiO-67@PU film.

In the case of UiO-67, the TGA profile shows the release of the solvent at 135°C and the main framework decomposition close to 550 °C.²⁶ **Figure 7.5** also shows the TGA profile for the UiO-67@PU nanocomposite film. In this case the scenario is more complex. As it can be appreciated, the nanocomposite material exhibits a broad decomposition profile with a main peak located in between 200 °C and 300 °C. Interestingly, this peak is not symmetric and clear shoulders can be appreciated at around 217°C and 278°C, in addition to the main contribution at 252°C. Taking into account that 70 wt.% of the composite corresponds to PU, the

main contribution at 252°C must be attributed to the decomposition of the polymeric matrix. Compared to the pure polymer (*ca.* 337°C), these results indicate a clear shift to lower temperatures upon incorporation of the MOF nanofillers, in close agreement with previous studies reported in the literature.³⁴ Apparently, the incorporation of the MOF nanocrystals limits the cross-linking between PU molecular chains, thus reducing their thermal stability.

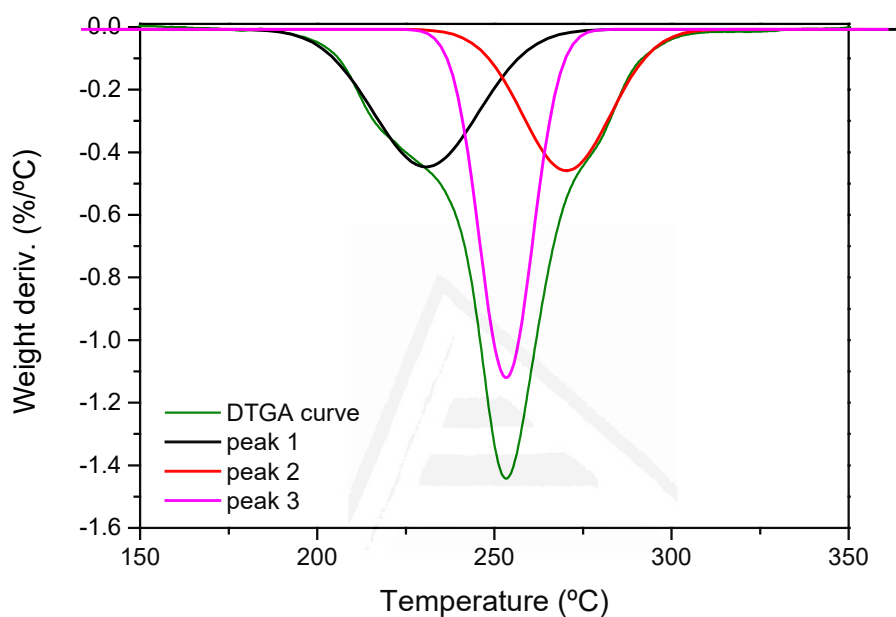


Figure 7.6. Deconvolution of the DTGA profile for UiO-67@PU film.

For the sake of clarity, a deconvolution of the DTGA profile for the nanocomposite system can be seen in **Figure 7.6**. In addition to the decomposition of the polymeric matrix, the aforementioned shoulders must be attributed to solvent removal (*ca.* 217°C) and to the secondary contribution in the decomposition of the PU matrix (*ca.* 278°C). Furthermore, the nanocomposite material exhibits an additional decomposition peak at 528°C, unambiguously attributed to the degradation of the embedded MOF. This finding constitutes another proof about the successful incorporation of the MOF crystals in the polymeric matrix. **Table 7.1** contains a summary of the TGA results for the three samples evaluated.

Table 7.1. Thermogravimetric results of the different samples evaluated.

Sample	1st stage		2nd stage		3rd stage		T_m (°C)
	ΔT	ΔW	ΔT	ΔW	ΔT	ΔW	
	(°C)	(wt.%)	(°C)	(wt.%)	(°C)	(wt.%)	
UiO-67	30-200	25.3	200-440	4.7	440-600	31.5	540
PU	30-190	0.4	235-500	94.7	500-600	0.7	337
UiO-67@PU	30-190	2.7	190-370	68.9	455-600	8.4	252

ΔT : temperature range of the thermal decomposition.

ΔW : Total weight loss at the main decomposition process

T_m : The degradation temperature corresponding to the maximum weight loss rate of DTG curve.

To check the accessibility of the 3D porous network in UiO-67@PU nanocomposite films to gas molecules, the nitrogen adsorption/desorption isotherm was performed at -196°C and compared to that of the pure MOF. As it can be appreciated in **Figure 7.7**, UiO-67 presents the typical adsorption-desorption isotherm already described elsewhere,³² with a large uptake at low relative pressures due to its highly microporous framework, and the associated step at $p/p_0 \sim 0.15$ attributed to the presence of wider pores (small mesopores). This observation is in close agreement with the presence of two kind of cavities in UiO-67, tetrahedral and octahedral cages with a diameter of 1.1 and 2.3 nm, respectively.³²

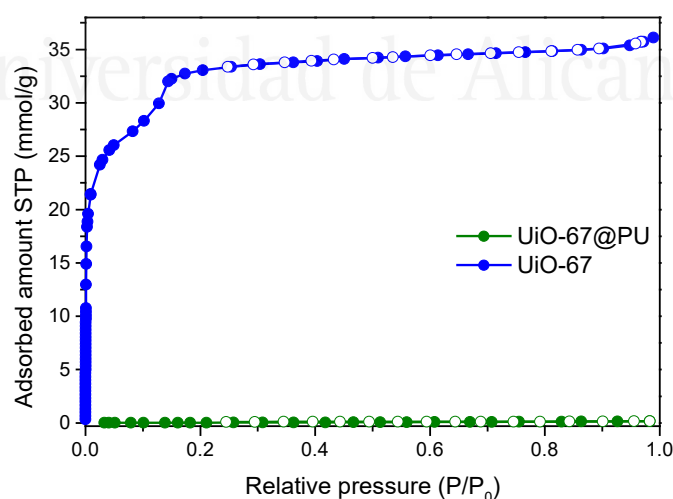


Figure 7.7. Nitrogen adsorption (filled symbols)-desorption (open symbols) isotherms at -196°C for UiO-67 and UiO-67@PU film.

Interestingly, in the specific case of the UiO-67@PU film the accessibility for nitrogen at cryogenic temperatures is completely suppressed over the whole relative pressure range evaluated. This observation is in close agreement with previous studies described in the literature for ZIF-8 and ZIF-7 loaded polymeric matrices.³⁷ Apparently, nitrogen with a quadrupolar moment is not able to diffuse through the rubbery polymeric network at cryogenic temperatures. Despite the inaccessibility of nitrogen to the embedded MOF crystals, this observation does not necessarily reflect the real scenario in the composite material. Based on our previous experience, adsorption of non-polar molecules (for instance, hydrocarbons) constitutes a complementary tool to evaluate the porous structure in these MOF@polymer nanocomposites.

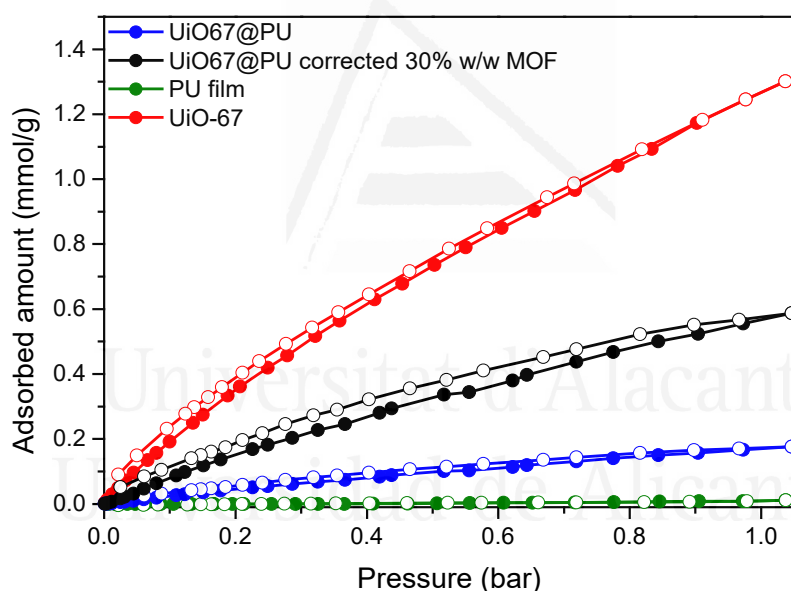


Figure 7.8. Ethylene adsorption (filled symbol)-desorption (open symbol) isotherms at 25°C in as-synthesized UiO-67, PU and UiO-67@PU films.

Figure 7.8 shows the ethylene adsorption/desorption isotherms at 25°C for the pure PU, UiO-67 and the nanocomposite. These results show that, contrary to N₂, ethylene is indeed able to access the inner porous structure in this kind of materials. Whereas the pure PU film exhibits an adsorption capacity close to 0 mmol/g, UiO-67 nanoparticles are able to adsorb up to 1.31 mmol/g at a pressure

of 1 bar. For the UiO-67@PU nanocomposite sample, the total adsorption capacity for ethylene at 1 bar is *ca.* 0.18 mmol/g. After a normalization to the total amount of MOF (considering that the composite contains *ca.* 30 wt.%), this value scales up to a total uptake of 0.59 mmol/g_{MOF}. Compared to the pure UiO-67, this result constitutes a reduction of 55% in the adsorption capacity of the embedded crystals, i.e. embedded nanocrystals are indeed accessible to gas molecules, although only partially.

7.3.2. Brimonidine adsorption and release

Brimonidine adsorption isotherms were performed in aqueous media (ultrapure water) and at room temperature in order to quantify the maximum amount of drug adsorbed in the porous structure of the synthesized films. As is shown in **Figure 7.9**, while the adsorption in the pure PU film is close to 0 mg/g, the maximum brimonidine adsorption capacity in the UiO-67@PU film (at an equilibrium time of 4h; see **Figure 7.10**) obtained from the Langmuir model achieves a value of 58.4 mg of brimonidine per gram of film, i.e. 194.7 mg of brimonidine per gram of UiO-67 (considering the nominal value of 30 wt.% of UiO-67 in the film). This value differs from that reported in the literature for pure UiO-67 nanoparticles (*ca.* 600 mg_{brimonidine}/g_{MOF}).²⁵

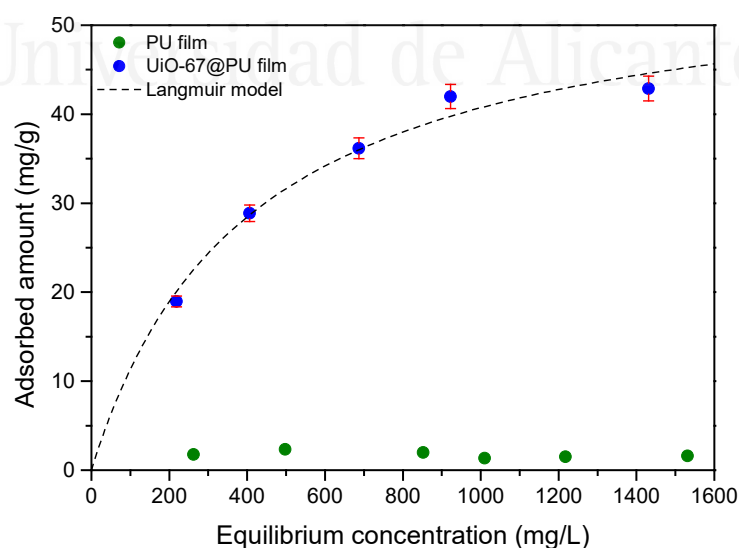


Figure 7.9. Brimonidine liquid-phase adsorption isotherm in PU and UiO-67@PU films at 25°C ($C_0 = 1500$ ppm).

The reduction in the adsorption capacity for the nanocomposite (around 67% reduction) is in close agreement with the gas-phase ethylene adsorption measurements described above (ethylene was able to access 45% of the porosity whereas brimonidine only 32.5% of the MOF porous network). Although these numbers must be optimized, this finding constitutes an important development elucidating the potential application of these MOF-doped polymeric matrices for liquid-phase adsorption/desorption processes. Even though these processes are performed in the presence of a solvent (for instance, an aqueous solution), the embedded MOFs are able to preserve a similar accessibility to the target molecule (e.g. ocular drug), compared to similar measurements in gas phase, i.e. in the absence of solvent. These results suggest that UiO-67 cavities are able to host both ethylene (molecular size of 4.7 x 9.8 Å) and brimonidine (3.28 x 4.18 x 4.84 Å) in a similar extend.^{39,40} Compared to the neat PU polymer, the incorporation of UiO-67 nanofillers gives rise to a 60-fold increase in the adsorption capacity for brimonidine tartrate.

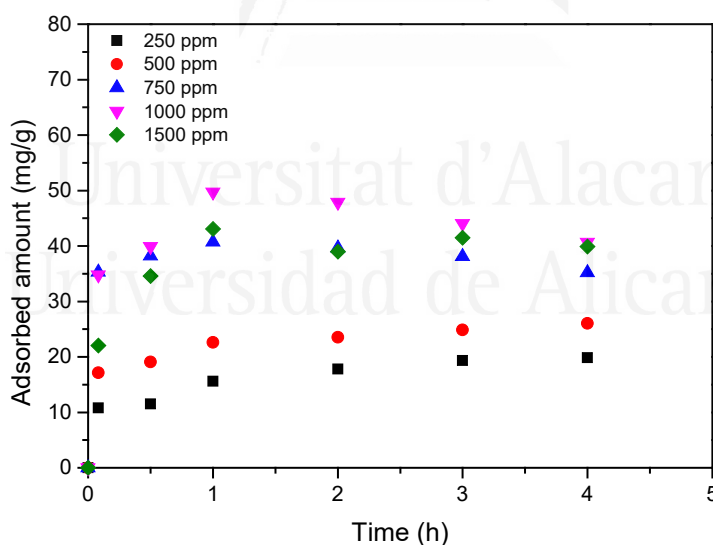


Figure 7.10. Brimonidine adsorption kinetics in the UiO67@PU film at different initial concentrations.

In order to mimic a potential application in human body, brimonidine release isotherms were performed in PBS solution at room temperature and neutral pH, **Figure 7.11**. As it can be observed, the UiO-67@PU nanocomposite exhibits a fast

release (up to 7 % of the total uptake) in the first minute of the experiment. Afterwards, there is a continuous release with time up to a maximum of 10% of the total brimonidine retained after 14 days exposure. The large release in the first few hours must be attributed to brimonidine weakly interacting with the nanocomposite and/or adsorbed in the external layers/pores of the film. Considering the traditional topical administration of brimonidine, i.e. a patient must take one droplet of brimonidine solution of 2 mg/mL (Alphagan P[®], Allergan) every 8h, this means 0.3 mg of brimonidine per day or 4.2 mg in 14 days.⁷ Taking into account the total uptake of 58.4 mg/g for our composite, a release of 10 % (5.8 mg/g) after 14 days is within the needs of a normal patient with glaucoma, thus validating our approach. At this point it is important to highlight that we cannot exclude the possibility that some brimonidine is already removed/released from the loaded film during the washing step performed after the loading and before the release experiment (this washing step was designed to remove exclusively the brimonidine retained in the external surface of the film).

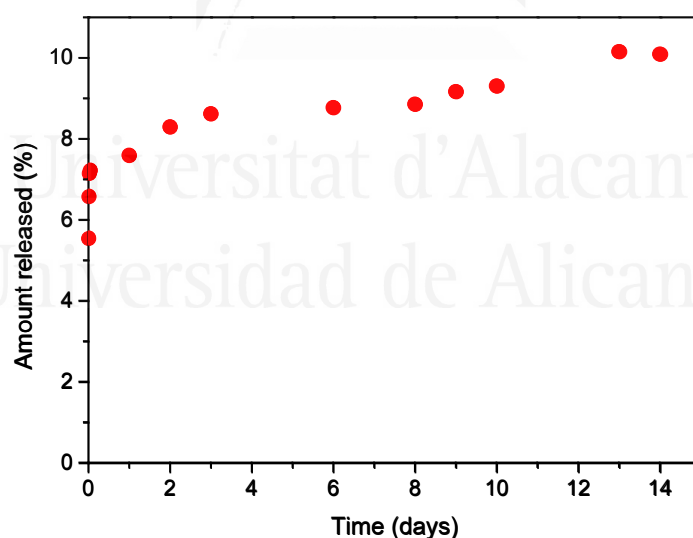


Figure 7.11. Brimonidine tartrate release kinetics at 25°C in physiological media PBS (loading concentration 1500 ppm)

At this point, the open questions remain the compatibility of the drug with the composite, the stability of the MOF structure after the loading process and finally,

the potential location of the drug molecule in the composite system. Next sections are devoted to answer all these questions.

7.3.3. Brimonidine-composite compatibility and stability studies

Structural stability of the MOF framework is an important parameter to be considered in liquid-phase adsorption processes. It is widely accepted in the literature that MOF materials can exhibit a limited stability in the presence of aqueous environments or after the incorporation of the drug.⁴¹ In the specific case of UiO-67, it is well-known that upon exposure to water or moisture, this system exhibits a large instability due to the hydrolysis of the linker-metal bonds, and the associated pore collapse.^{42–44} However, the partial amorphization of the UiO-67 nanoparticles during the adsorption/release of brimonidine has been very useful to extend the released kinetics beyond 12 days, as described before by some of us.²⁵

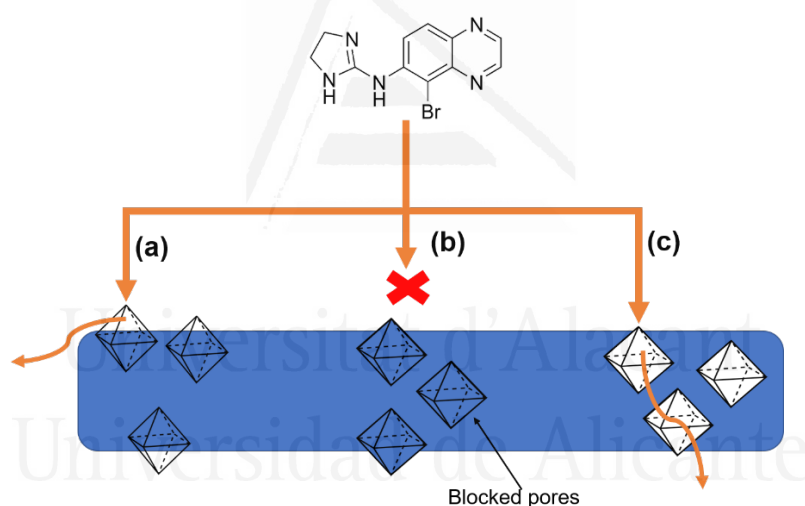


Figure 7.12. Scheme of possible scenarios for Brimonidine adsorption in MOF@polymer composites: (a) adsorption in the peripheric MOF crystals, (b) fully inaccessible and (c) fully accessible embedded MOF nanocrystals.

In addition to the structural stability, another concern is the adsorption mechanism. Adsorption of brimonidine into MOF-based polymeric films can be explained via three potential scenarios. As summarized in **Figure 7.12**, brimonidine can be adsorbed only in those MOF crystals located in the periphery of the PU film (option A), brimonidine can be adsorbed only in the polymeric matrix, i.e. MOF nanocrystals are completely blocked (option B) or it can be adsorbed equally in the

different crystals homogeneously distributed within the PU film (option C). To identify which of these options is the most plausible to explain the adsorption mechanism, the UiO-67@PU nanocomposite has been thoroughly evaluated before and after adsorption of brimonidine using synchrotron X-ray diffraction, thermogravimetry (TGA) and FTIR.

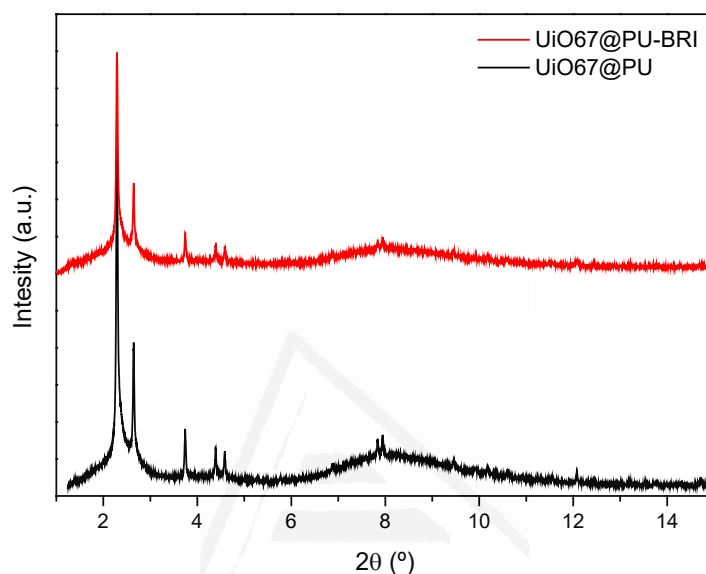


Figure 7.13. Synchrotron X-ray powder diffraction patterns of UiO-67@PU film before and after being exposed to the brimonidine solution.

Synchrotron X-ray diffraction measurements were performed in order to elucidate the structural parameters of the UiO-67 embedded crystals before and after the loading of brimonidine. As it can be observed in **Figure 7.13** both patterns are rather similar even after exposure to the brimonidine aqueous solution for several days. These results are contrary to the performance of the pure MOF (**Figure 7.14**), where a significant structural deterioration was identified after 1 day in contact with water and confirms the improved structural stability of UiO-67 upon encapsulation in the PU matrix. ²⁵

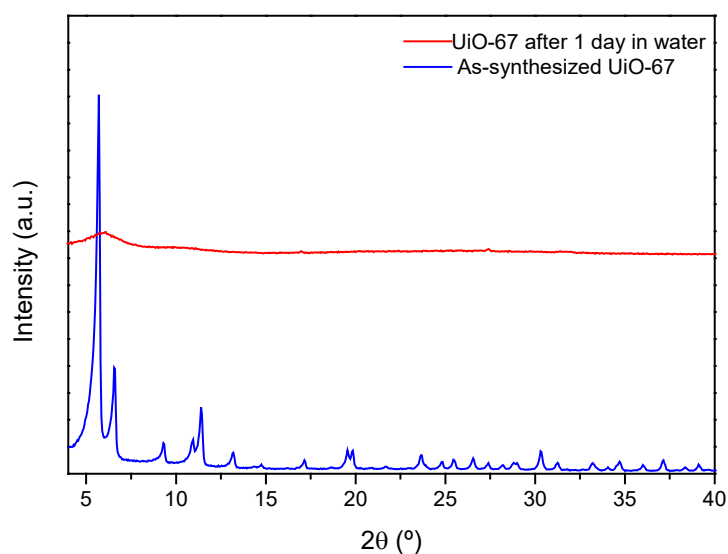


Figure 7.14. X-ray powder diffraction pattern of as-synthesized UiO-67 and after soaking in water for 1 day.¹

Although the cavities in UiO-67 (octahedral of 2.3 nm and tetrahedral of 1.15 nm) are large enough to accommodate the brimonidine molecule, the open question at this point is how to ascertain if brimonidine is able to take advantage of these cavities.³²

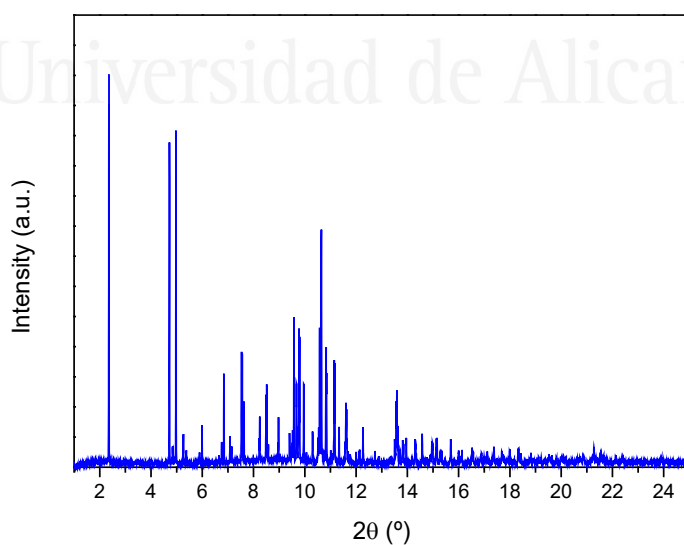


Figure 7.15. Synchrotron X-ray powder diffraction pattern of brimonidine tartrate.

Synchrotron X-ray diffraction measurements of the pure brimonidine tartrate (**Figure 7.15**) show a rich XRD pattern with a large number of peaks in the range 2 and 18°, confirming the high crystallinity of this molecule. The absence of these peaks in the SXRPD pattern of the brimonidine-loaded UiO-67@PU nanocomposite (**Figure 7.13**) could be *a priori* an evidence of the absence of brimonidine both in the polymeric network and in the embedded MOF nanocrystals. However, this observation would be in contradiction with brimonidine adsorption measurements reported in **Figure 7.9**. This inconsistency must be explained due to the amorphization of the drug upon adsorption, thus explaining the absence of peaks in the SXRPD pattern. This hypothesis would be in agreement with the encapsulation of the drug in the MOF cavities, with the associated limitation for these molecules to arrange in a periodic fashion. These conclusions are also supported by previous studies dealing with the adsorption/release of brimonidine through ocular devices suggesting the transformation of crystalline brimonidine into an amorphous phase once it is adsorbed into the material.^{45–47}

Table 7.2. Summary of structural parameters and adsorption performance of UiO-67, and UiO-67@PU film before and after loading with brimonidine.

	UiO-67	UiO-67@PU	UiO-67@PU-BRI
Cell parameter a (Å)	26.8447(9)	26.8306(6)	26.8252(6)
S_{BET} (m²/g)	2614	0	----
Ethylene adsorption (mmol/g)	1.31	0.18	----
Brimonidine adsorption (mg/g)	600 ²⁵	58.4	----
Brimonidine release (%)	50% (12 days)	10% (14 days)	----

The unit cell parameters deduced for the embedded UiO-67 crystals after Rietveld refinement are summarized in **Table 7.2**. Pure UiO-67 crystals have a cubic unit cell with lattice parameters $a = b = c = 26.8447(9)$ Å. As it can be observed, the lattice parameters remain rather similar after incorporation of the UiO-67 crystals in the polymeric matrix, in close agreement with the high quality of the crystals described in **Figure 7.1**. Interestingly, lattice parameters do not change after exposure of the UiO-67@PU nanocomposite to an aqueous solution of brimonidine. Although these results confirm the large stability of UiO-67 nanocrystals in an aqueous environment upon incorporation in the PU matrix, these are not conclusive

about the location of brimonidine upon adsorption. Unfortunately, Rietveld refinement analysis of the embedded crystals does not allow to answer this question due to the limited quality of the SXRPD pattern.

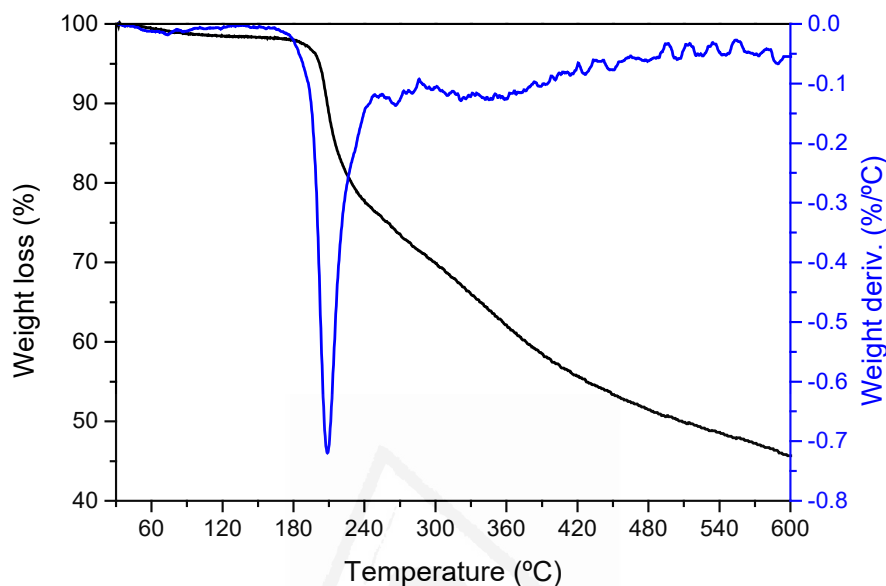


Figure 7.16. TGA-DTGA profiles for brimonidine tartrate.

To further ascertain the adsorption mechanism, TGA analysis was performed in the UiO-67@PU film after the loading of brimonidine. For clarity, the TGA of pure brimonidine tartrate has been included in **Figure 7.16**. Brimonidine tartrate exhibits a single decomposition peak at around 210 °C. A closer look to the TGA profile for the brimonidine-loaded UiO-67@PU nanocomposite (**Figure 7.17**) shows that the TGA peaks corresponding to the decomposition of the PU matrix and the UiO-67 crystals are shifted to higher temperatures upon adsorption. In addition, the thermogram shows an additional tinny peak at 210°C, not present in the un-loaded UiO-67@PU material, that can be attributed to brimonidine within the composite film (blue peak deconvoluted in **Figure 7.18**). Although the shifts observed in **Figure 7.17** for the decomposition of PU and UiO-67 upon brimonidine adsorption could be an indication of the presence of brimonidine in both domains, the real location of the drug remains an open question.

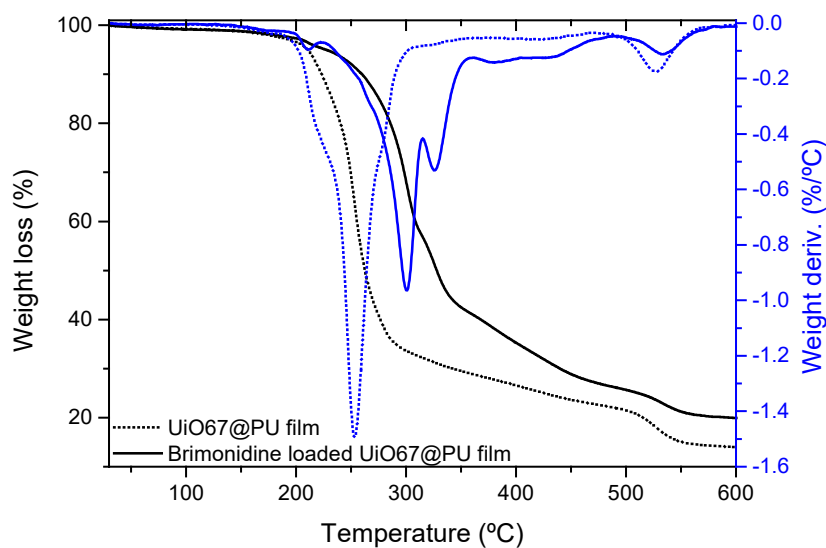


Figure 7.17. TGA-DTGA profiles for UiO-67@PU film before and after loading with brimonidine.

Last but not least, it is important to highlight that the quantification of the tinny peak at 210°C corresponds to ~ 23 mg Brimonidine/g_{composite film}. Although this is a rough estimation, we cannot exclude that around 40% of the brimonidine loaded at 1500 ppm (**Figure 7.9**) could be lost during the washing step applied before the TGA analysis. A similar hypothesis could be used to explain the low release achieved in **Figure 7.11**.

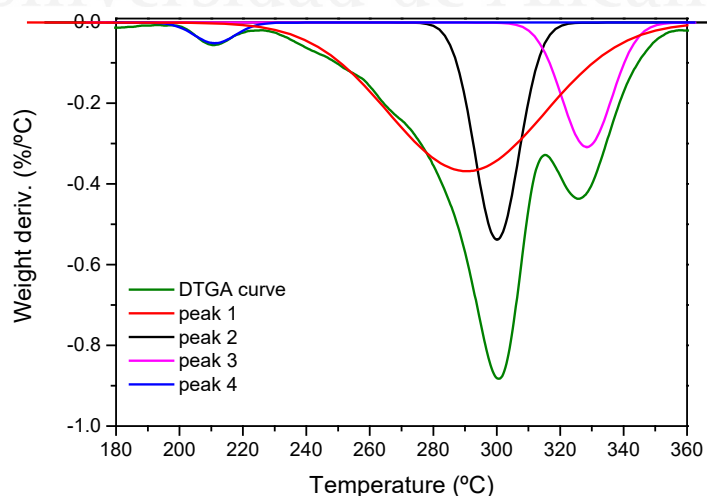


Figure 7.18. Deconvolution of the DTGA profile in brimonidine loaded UiO-67@PU films.

Finally, the presence of the drug has been evaluated using FTIR of the UiO-67@PU film before and after loading with brimonidine, **Figure 7.19**. The FTIR spectra for the individual components have also been included for clarity. As it can be observed, before loading, the FTIR spectra of the UiO-67@PU film shows the characteristic peaks of PU and UiO-67. PU has a characteristic peak at 3329 cm^{-1} attributed to the stretching of the NH bond (**Figure 7.19b**). In addition there are two contributions at 1724 cm^{-1} and 1696 cm^{-1} due to the poly(caprolactone) ester bond, and the -CH stretching vibration at 2944 cm^{-1} , among others.^{48,49} The characteristic peaks of UiO-67 can be observed at 1594 cm^{-1} , 1528 cm^{-1} and 1411 cm^{-1} due to the stretching vibrations of the carboxylate group of the ligands and, the peaks at 815 cm^{-1} , 766 cm^{-1} and 652 cm^{-1} due to the Zr-O stretching vibrations.^{50,51}

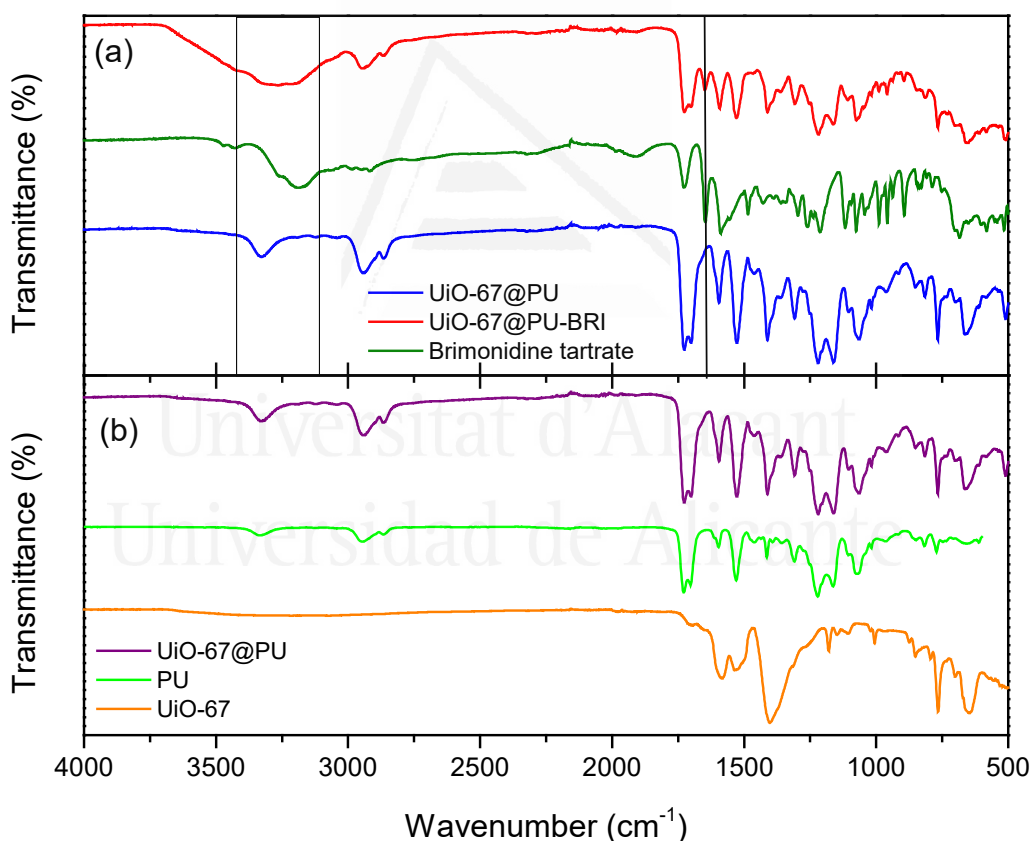


Figure 7.19. FTIR spectra of (a) UiO67@PU film before (bottom) and after (upper) loading with brimonidine, and (b) UiO-67 (bottom), PU (middle) and UiO67@PU film (upper).

As already reported in the literature, brimonidine tartrate also presents characteristic vibrations in the IR range. These characteristic vibrations include peaks at 3212 and 3268 cm^{-1} owing to N-H stretching vibration from the secondary amine groups (RR'-NH). Peaks around 1650 cm^{-1} are attributed to C=O stretching and -CN stretching appears at 1284 cm^{-1} .⁵²⁻⁵⁴

The most remarkable feature of the FTIR spectra of UiO-67@PU after loading brimonidine is, in addition to the bands described above due to PU and UiO-67, the presence of a wide contribution around 3575-3074 cm^{-1} . This broad contribution could be associated to the overlapping of signals from adsorbed H₂O (O-H stretching at 3404 cm^{-1}), and to the stretching -NH vibrations characteristics of urea and urethane bonds (3333 cm^{-1}) in PU.^{48,49} However, taking into account that the brimonidine-loaded sample has been vacuum dried at 60°C before the FTIR spectra, and the absence of this wide contribution in the drug-free nanocomposite film, the presence of this broad contribution must be unambiguously attributed to the presence of brimonidine chemically interacting with the composite via hydrogen bonding with surface oxygen and nitrogen groups. This finding is supported by the presence of a new peak at 1650 cm^{-1} (solid line in **Figure 7.19a**) in the loaded film due to the C=O groups of the brimonidine tartrate. These assignments are in perfect agreement with previous studies in NH₂-MIL-88(Fe) loaded with brimonidine.⁵³ In summary, FTIR spectra clearly confirm the presence of the drug in the UiO-67@PU film, although the real location, either in the polymeric matrix or in the UiO-67 network cannot be easily identified.

7.4. Conclusions

We have successfully developed a novel UiO-67-based polyurethane film with an excellent adsorption/release performance for an ocular drug such as brimonidine tartrate. Synchrotron X-ray powder diffraction measurements confirms the high quality of the MOF nanocrystals when embedded in a hydrophobic polymer such as PU and their improved stability in an aqueous environment, compared to the pure MOF. Although the inner porous structure is not accessible to nitrogen with a quadrupole moment, this is not the case for the adsorption of non-polar molecules (e.g., hydrocarbons) at room temperature. Although the partial accessibility of the

embedded MOFs limits the brimonidine adsorption performance, the UiO-67@PU composite gives rise to a 60-fold improvement compared to the neat PU film. Synchrotron XRPD, TGA and FTIR measurements of the composite before and after loading brimonidine confirm the presence of the drug within the UiO-67@PU film, although the real role of the polymer matrix and the UiO-67 nanocrystals cannot be conclusively confirmed. The total brimonidine uptake of the composite is as high as 58.4 mg_{BRI} per gram of composite or 194.7 mg_{BRI} per gram of MOF. These results in liquid-phase are highly promising and open the door to the design of novel polymeric inserts with functional properties and improved performance (for instance with drug delivery properties), to be applied in a number of ophthalmological disorders, either as a component of contact lens, in the composition of lacrimal stoppers (e.g., punctal plugs) or in sub-tenon inserts.

7.5. References

1. Hertzog, L. H., Albrecht, K. G., LaBree, L. & Lee, P. P. Glaucoma Care and Conformance with Preferred Practice Patterns: Examination of the Private, Community-based Ophthalmologist. *Ophthalmology* **103**, 1009–1013 (1996).
2. Quigley, H. A. & Broman, A. T. The number of people with glaucoma worldwide in 2010 and 2020. *Br. J. Ophthalmol.* **90**, 262 LP – 267 (2006).
3. Clineschmidt, C. M., Williams, R. D., Snyder, E. & Adamsons, I. A. A randomized trial in patients inadequately controlled with timolol alone comparing the dorzolamide-timolol combination to monotherapy with timolol or dorzolamide¹. *Ophthalmology* **105**, 1952–1959 (1998).
4. Bourlais, C. L. *et al.* Ophthalmic drug delivery systems--recent advances. *Prog. Retin. Eye Res.* **17**, 33–58 (1998).
5. Gulsen, D. & Chauhan, A. Ophthalmic drug delivery through contact lenses. *Invest. Ophthalmol. Vis. Sci.* **45**, 2342–7 (2004).
6. Gaudana, R., Ananthula, H. K., Parenky, A. & Mitra, A. K. Ocular drug delivery. *AAPS J.* **12**, 348–60 (2010).
7. Urtti, A. Challenges and obstacles of ocular pharmacokinetics and drug delivery. *Adv. Drug Deliv. Rev.* **58**, 1131–1135 (2006).
8. De, T. K., Rodman, D. J., Holm, B. A., Prasad, P. N. & Bergey, E. J. Brimonidine formulation in polyacrylic acid nanoparticles for ophthalmic delivery. *J. Microencapsul.* **20**, 361–374 (2003).

9. Singh, K. H. & Shinde, U. A. Chitosan nanoparticles for controlled delivery of brimonidine tartrate to the ocular membrane. *Pharmazie* **66**, 594–9 (2011).
10. Prabhu, P. *et al.* Preparation and Evaluation of Nano-vesicles of Brimonidine Tartrate as an Ocular Drug Delivery System. *J. Young Pharm.* **2**, 356–361 (2010).
11. Sun, J. *et al.* Sustained Release of Brimonidine from a New Composite Drug Delivery System for Treatment of Glaucoma. *ACS Appl. Mater. Interfaces* **9**, 7990–7999 (2017).
12. Ghate, D. & Edelhauser, H. F. Ocular drug delivery. *Expert Opin. Drug Deliv.* **3**, 275–287 (2006).
13. Diebold, Y. *et al.* Ocular drug delivery by liposome–chitosan nanoparticle complexes (LCS-NP). *Biomaterials* **28**, 1553–1564 (2007).
14. Sun, S. *et al.* Episcleral drug film for better-targeted ocular drug delivery and controlled release using multilayered poly- ϵ -caprolactone (PCL). *Acta Biomater.* **37**, 143–154 (2016).
15. Saettone, M. F. & Salminen, L. Ocular inserts for topical delivery. *Adv. Drug Deliv. Rev.* **16**, 95–106 (1995).
16. Brown, H. S. Visual Effects of Pilocarpine in Glaucoma. *Arch. Ophthalmol.* **94**, 1716 (1976).
17. POLLACK, I. P., QUIGLEY, H. A. & HARBIN, T. S. The Ocusert Pilocarpine System. *South. Med. J.* **69**, 1296–1298 (1976).
18. Mehta, P. *et al.* New platforms for multi-functional ocular lenses: engineering double-sided functionalized nano-coatings. *J. Drug Target.* **23**, 305–310 (2015).
19. Rosa dos Santos, J.-F. *et al.* Soft contact lenses functionalized with pendant cyclodextrins for controlled drug delivery. *Biomaterials* **30**, 1348–1355 (2009).
20. Verestiuc, L. *et al.* Functionalized chitosan/NIPAM (HEMA) hybrid polymer networks as inserts for ocular drug delivery: Synthesis, *in vitro* assessment, and *in vivo* evaluation. *J. Biomed. Mater. Res. Part A* **77A**, 726–735 (2006).
21. Sun, C.-Y., Qin, C., Wang, X.-L. & Su, Z.-M. Metal-organic frameworks as potential drug delivery systems. *Expert Opin. Drug Deliv.* **10**, 89–101 (2013).
22. Zhou, H.-C., Long, J. R. & Yaghi, O. M. Introduction to Metal–Organic Frameworks. *Chem. Rev.* **112**, 673–674 (2012).
23. Horcajada, P. *et al.* Metal–Organic Frameworks as Efficient Materials for Drug Delivery. *Angew. Chemie Int. Ed.* **45**, 5974–5978 (2006).

24. Sun, Y. *et al.* Metal–Organic Framework Nanocarriers for Drug Delivery in Biomedical Applications. *Nano-Micro Lett.* **12**, 103 (2020).
25. Gandara-Loe, J. *et al.* Metal–Organic Frameworks as Drug Delivery Platforms for Ocular Therapeutics. *ACS Appl. Mater. Interfaces* **11**, 1924–1931 (2019).
26. Chavan, S. *et al.* H₂ storage in isostructural UiO-67 and UiO-66 MOFs. *Phys. Chem. Chem. Phys.* **14**, 1614–1626 (2012).
27. Lee, V. H. L. & Robinson, J. R. Topical Ocular Drug Delivery: Recent Developments and Future Challenges. *J. Ocul. Pharmacol. Ther.* **2**, 67–108 (1986).
28. Xu, J. *et al.* A comprehensive review on contact lens for ophthalmic drug delivery. *J. Control. Release* **281**, 97–118 (2018).
29. Rodenas, T. *et al.* Metal–organic framework nanosheets in polymer composite materials for gas separation. *Nat. Mater.* **14**, 48–55 (2015).
30. Mahdi, E. M. & Tan, J.-C. Mixed-matrix membranes of zeolitic imidazolate framework (ZIF-8)/Matrimid nanocomposite: Thermo-mechanical stability and viscoelasticity underpinning membrane separation performance. *J. Memb. Sci.* **498**, 276–290 (2016).
31. Souza, B. E. *et al.* Elucidating the Drug Release from Metal–Organic Framework Nanocomposites via In Situ Synchrotron Microspectroscopy and Theoretical Modeling. *ACS Appl. Mater. Interfaces* **12**, 5147–5156 (2020).
32. Katz, M. J. *et al.* A facile synthesis of UiO-66, UiO-67 and their derivatives. *Chem. Commun.* **49**, 9449 (2013).
33. Denny Jr., M. S. & Cohen, S. M. In Situ Modification of Metal–Organic Frameworks in Mixed-Matrix Membranes. *Angew. Chemie Int. Ed.* **54**, 9029–9032 (2015).
34. Mahdi, E. M. & Tan, J.-C. Dynamic molecular interactions between polyurethane and ZIF-8 in a polymer-MOF nanocomposite: Microstructural, thermo-mechanical and viscoelastic effects. *Polymer (Guildf)*. **97**, 31–43 (2016).
35. Karamanos, N. K., Lamari, F., Katsimpris, J. & Gartaganis, S. Development of an HPLC method for determining the alpha2-adrenergic receptor agonist brimonidine in blood serum and aqueous humor of the eye. *Biomed. Chromatogr.* **13**, 86–88 (1999).
36. Bastani, D., Esmaeili, N. & Asadollahi, M. Polymeric mixed matrix membranes containing zeolites as a filler for gas separation applications: A review. *J. Ind. Eng. Chem.* **19**, 375–393 (2013).
37. Mahdi, E. M., Cuadrado-Collados, C., Silvestre-Albero, J. & Tan, J.-C.

- Polymer nanocomposites functionalised with nanocrystals of zeolitic imidazolate frameworks as ethylene control agents. *Mater. Today Adv.* **2**, 100008 (2019).
38. Trovati, G., Sanches, E. A., Neto, S. C., Mascarenhas, Y. P. & Chierice, G. O. Characterization of polyurethane resins by FTIR, TGA, and XRD. *J. Appl. Polym. Sci.* **115**, 263–268 (2010).
 39. Ball, D. W., Hill, J. W. & Scott, R. J. *The basics of general, organic, and biological chemistry*. (Saylor Foundation, 2011).
 40. Bao, Z. *et al.* Molecular Sieving of Ethane from Ethylene through the Molecular Cross-Section Size Differentiation in Gallate-based Metal–Organic Frameworks. *Angew. Chemie Int. Ed.* **57**, 16020–16025 (2018).
 41. Qadir, N. ul, Said, S. A. M. & Bahaidarah, H. M. Structural stability of metal organic frameworks in aqueous media – Controlling factors and methods to improve hydrostability and hydrothermal cyclic stability. *Microporous Mesoporous Mater.* **201**, 61–90 (2015).
 42. Lawrence, M. C., Schneider, C. & Katz, M. J. Determining the structural stability of UiO-67 with respect to time: a solid-state NMR investigation. *Chem. Commun.* **52**, 4971–4974 (2016).
 43. DeCoste, J. B. *et al.* Stability and degradation mechanisms of metal–organic frameworks containing the Zr₆O₄(OH)₄ secondary building unit. *J. Mater. Chem. A* **1**, 5642 (2013).
 44. Mondloch, J. E. *et al.* Are Zr₆-based MOFs water stable? Linker hydrolysis vs. capillary-force-driven channel collapse. *Chem. Commun.* **50**, 8944 (2014).
 45. Chandak, A. R. & Verma, P. R. P. Development and Evaluation of HPMC Based Matrices for Transdermal Patches of Tramadol. *Clin. Res. Regul. Aff.* **25**, 13–30 (2008).
 46. Aburahma, M. H. & Mahmoud, A. A. Biodegradable Ocular Inserts for Sustained Delivery of Brimonidine Tartarate: Preparation and In Vitro/In Vivo Evaluation. *AAPS PharmSciTech* **12**, 1335–1347 (2011).
 47. Nickerl, G. *et al.* Integration of accessible secondary metal sites into MOFs for H₂S removal. *Inorg. Chem. Front.* **1**, 325–330 (2014).
 48. Dias, R. C. M., Góes, A. M., Serakides, R., Ayres, E. & Oréface, R. L. Porous biodegradable polyurethane nanocomposites: preparation, characterization, and biocompatibility tests. *Mater. Res.* **13**, 211–218 (2010).
 49. Seymour, R. W. & Cooper, S. L. Thermal Analysis of Polyurethane Block Polymers. *Macromolecules* **6**, 48–53 (1973).
 50. Zhu, X. *et al.* Effective Adsorption and Enhanced Removal of

- Organophosphorus Pesticides from Aqueous Solution by Zr-Based MOFs of UiO-67. *ACS Appl. Mater. Interfaces* **7**, 223–231 (2015).
51. Pankajakshan, A., Sinha, M., Ojha, A. A. & Mandal, S. Water-Stable Nanoscale Zirconium-Based Metal–Organic Frameworks for the Effective Removal of Glyphosate from Aqueous Media. *ACS Omega* **3**, 7832–7839 (2018).
 52. Maiti, S., Paul, S., Mondol, R., Ray, S. & Sa, B. Nanovesicular Formulation of Brimonidine Tartrate for the Management of Glaucoma: In Vitro and In Vivo Evaluation. *AAPS PharmSciTech* **12**, 755–763 (2011).
 53. Kim, S.-N. *et al.* Metal-organic frameworks, NH₂-MIL-88(Fe), as carriers for ophthalmic delivery of brimonidine. *Acta Biomater.* **79**, 344–353 (2018).
 54. Emad Eldeeb, A., Salah, S. & Ghorab, M. Proniosomal gel-derived niosomes: an approach to sustain and improve the ocular delivery of brimonidine tartrate; formulation, in-vitro characterization, and in-vivo pharmacodynamic study. *Drug Deliv.* **26**, 509–521 (2019).



Universitat d'Alacant
Universidad de Alicante

CHAPTER 8

General Conclusions



Universitat d'Alacant
Universidad de Alicante

In this Doctoral Thesis, the large versatility of MOFs for gas and liquid phase adsorption processes has been studied using zeolitic imidazolate frameworks (ZIFs) and zirconium-based MOFs. A synergy between high sensitivity experimental equipment and molecular simulations has been achieved. The combined use of these approaches (experimental & modelling) has been very useful to understand structural changes in MOFs frameworks upon an external stimulus and the adsorption performance for several molecules under different conditions. These studies have been useful to highlight the versatility of MOFs in a number of potential applications, from gas to liquid phase adsorption processes.

Along the PhD thesis different specific conclusions of the main achievements have been described in each chapter. They can be summarized as follow.

1. *Chapter 3:* In summary, combination of synchrotron X-ray diffraction and inelastic neutron scattering measurements under operando conditions clearly show that ZIF-4 exhibits a breathing phenomenon upon nitrogen adsorption at ~30 kPa, associated with an 8-9% volume expansion in the unit cell. The transition from a narrow-pore (*np*) to an expanded-pore (*ep*) phase explains the complex behaviour of the nitrogen adsorption isotherm at cryogenic temperatures. The existence of an expanded ZIF-4 has been predicted by molecular simulations. First, the expanded ZIF-4 structure was predicted by MD simulations at higher temperatures, which increases entropic contributions to the free energy and stabilizes the expanded structure. Second, the expanded ZIF-4 structure with N₂ molecules was confirmed by MD and GCMC simulations at 77 K. Although CO₂ with a lower kinetic diameter and at a much higher adsorption temperature is able to access in the inner cavities in ZIF-4, this molecule is not able to promote the *np* to *ep* transition at ambient temperature. However, INS measurements show that at cryogenic temperatures (5 K) CO₂ is indeed able to promote certain structural changes.
2. *Chapter 4:* ZIF-62 was synthesized by solvothermal method and textural, and morphological characteristics were evaluated through

different physicochemical techniques. Large tetrahedral crystals with an average size of 5-20 μm and strong solvent-surface interactions in the structure evacuation process were successfully synthesized. Nitrogen and oxygen adsorption-desorption isotherms showed a similar performance at 298 K and 195 K but not at 77 K. At 77 K ZIF-62 is not able to adsorb nitrogen while oxygen can be easily adsorbed with a total uptake close to 8 mmol/g. Monte Carlo simulations for a rigid structure of ZIF-62 predict a framework with a large cavity of ca. 4.3 \AA and a small cavity of ca. 1 \AA . Simulated nitrogen and oxygen adsorption isotherms were able to predict the adsorption performance at 195 K and 298 K. However, at 77 K theoretical calculations predict a large adsorption capacity for nitrogen and oxygen with a similar uptake for both molecules (close to 5-6 mmol/g). The discrepancy between theoretical predictions and experimental evidences may suggest diffusional limitations for nitrogen at 77 K. SXRD experiment showed a structural transformation when the framework was loaded with oxygen or nitrogen at 90 K suggesting a certain structural flexibility. The Rietveld refinement performed in the SPXRD patterns at 90 K suggested a mixture of an expanded phase (phase I) and a contracted phase (phase II), these two phases prevailing up to 150 K. After this point the contracted phase disappears, and the cell parameter were close to those described for the blank structure. Even though experimental and simulated results could seem contradictory, synchrotron and particle size experiments are essential to understand the difference between these results. Even that nitrogen is not adsorbed as simulation experiments predicted, particle size and kinetic barriers experiments confirm the accessibility of nitrogen to the structure. However, the number of molecules accessing to the frameworks depends in external parameters such as, as kinetic barriers caused by particle size or equilibrium time. Expanding the potential applications of ZIF-62 for different industrial interest molecules, isotherms of small molecules such as, methane or carbon dioxide where were performed at 298 K.

C1-C4 paraffins and olefins adsorption isotherms in ZIF-62 at 298 K showed an inverse preferential adsorption behaviour which has been observed in other ZIF structures. Finally, ZIF-62 appeared to be an excellent material for separation of hexane isomers, showing a highly preference for linear alkane and non-adsorptive preference for bi-branched isomers.

3. *Chapter 5*: This chapter describes an alternative approach to the adsorption of NO in MOFs. Previous studies were based on the incorporation of open metal sites or the functionalization of the material with basic moieties. This study anticipates a third approach based on flexible MOFs. The presence of structural changes upon adsorption in ZIFs and the transition from low-to-high density phases and vice versa constitutes a promising alternative to store and deliver NO in a controlled way. By taking advantage of these phenomena, ZIF-4 can store up to 1.6 mmol/g NO and deliver it under humid conditions for more than 6h. Unfortunately, these excellent properties vanish after a thermal treatment at higher temperature (523 K) due to the partial amorphization and re-crystallization of ZIF-4 into the dense zni structure. In the specific case of ZIF-7, although the amount adsorbed is lower due to the inability of NO to breathe the structure, the presence of a dense-phase allows to control the delivery kinetics for more than 18h with a total amount released of more than 70 $\mu\text{mol/g}$ at 318 K. These excellent results together with the excellent structural stability of ZIFs, even under physiological solution, opens the gate towards the application of ZIFs in biomedical processes (e.g., NO storage and delivery).
4. Metal-organic frameworks (MOFs) can be anticipated as promising nanodevices for drug delivery in ocular therapeutics in *chapter 6*. Experimental results have shown that samples combining wide micropores and/or small mesopores are able to achieve a high loading capacity, above 50 wt.% (MIL-100(Fe) and UiO-67), for an alpha-adrenergic receptor agonist such as brimonidine. Furthermore,

delivery kinetics have shown that the associated amorphization in the case of UiO-67 upon ultrapure water or PBS exposure, as suggested by XRD measurements, can be very helpful to extend the delivery kinetic up to 12 days or above. Last but not least, cytotoxicity assays using retinal photoreceptor cells show high biocompatibility for the MOFs evaluated, except HKUST-1, thus paving the way towards the application of MOFs in intra-ocular therapeutics.

5. In *chapter 7*, we have successfully developed a novel UiO-67-based polyurethane film with an excellent adsorption/release performance for an ocular drug such as brimonidine tartrate. Synchrotron X-ray powder diffraction measurements confirm the high quality of the MOF nanocrystals when embedded in a hydrophobic polymer such as PU and their improved stability in an aqueous environment, compared to the pure MOF. Although the inner porous structure is not accessible to nitrogen with a quadrupole moment, this is not the case for the adsorption of non-polar molecules (e.g., hydrocarbons) at room temperature. Although the partial accessibility of the embedded MOFs limits the brimonidine adsorption performance, the UiO-67@PU composite gives rise to a 60-fold improvement compared to the neat PU film. Synchrotron XRPD, TGA and FTIR measurements of the composite before and after loading brimonidine confirm the presence of the drug within the UiO-67@PU film, although the real role of the polymer matrix and the UiO-67 nanocrystals cannot be conclusively confirmed. The total brimonidine uptake of the composite is as high as 58.4 mgBRI per gram of composite or 194.7 mgBRI per gram of MOF. These results in liquid-phase are highly promising and open the door to the design of novel polymeric inserts with functional properties and improved performance (for instance with drug delivery properties), to be applied in a number of ophthalmological disorders, either as a component of contact lens, in the composition of lacrimal stoppers (e.g., punctal plugs) or in sub-tenon inserts.



Universitat d'Alacant
Universidad de Alicante

Resumen en español



Universitat d'Alacant
Universidad de Alicante

- **Introducción general**

- **Adsorción y materiales porosos.**

La adsorción es un fenómeno superficial en el cual moléculas o átomos en fase líquida o gas se acumulan en la superficie de un material.¹ La adsorción física o fisisorción está generalmente controlada por tres mecanismos, estérico, cinético y de equilibrio. El primero hace referencia a los materiales con propiedades de tamizado molecular, es decir, solo las moléculas que tienen el tamaño apropiado podrán difundir en los poros. La separación cinética se lleva a cabo debido a las propiedades difusivas del adsorbato. Por último, la adsorción por equilibrio es aquella en la que ocurren la mayoría de los procesos y que considera las interacciones específicas debido a la química superficial del adsorbente y el adsorbato.²

Un gran número de procesos industriales hacen uso de la adsorción como herramienta para la separación de moléculas de alto interés industrial utilizando materiales adsorbentes como, carbón activado, zeolitas, arcillas, alúmina activada, etc.¹ Debido a la abundancia de materias primas para su producción, el carbón activado es uno de los adsorbentes más empleados en aplicaciones tales como, tratamiento de agua, separación de hidrocarburos, adsorción-liberación de fármacos, etc.³⁻⁶

El desarrollo de materiales porosos cristalinos ha significado un avance importante en el campo de la adsorción, debido a sus características y versatilidad ofrecen una mejora en el control y nivel de porosidad que se ve reflejada considerablemente en la optimización de procesos de adsorción. Uno de los primeros materiales cristalinos porosos descritos en la literatura fueron las zeolitas. Las zeolitas son aluminosilicatos cristalinos con estructura tridimensional que se conforman por redes de óxido de silicio, donde en ciertos puntos de la red, cargas negativas residuales se generan debido al reemplazo del Si^{4+} por Al^{3+} las cuales son compensadas con cationes.⁷ El incremento exponencial en el consumo anual de zeolitas en la industria ha motivado la investigación en el desarrollo y

diversificación de materiales porosos cristalinos, como sílice mesoporosa, redes covalente-orgánicas (COFs) y redes metal-orgánicas (MOFs).

○ Síntesis de redes metal-orgánicas

Las redes metal-orgánicas (MOFs) han emergido como una nueva clase de materiales porosos con gran potencial de aplicación gracias a su increíble versatilidad.⁸ Los MOFs se forman debido a la unión de ligandos orgánicos y átomos o núcleos metálicos (**Figura 1**).

El descubrimiento y desarrollo de las redes metal-orgánicas ha sido consecuencia de una comprensión e investigación continua en el ensamblaje de polímeros de coordinación a principios de los años noventa. Robson *et al.*, describieron por primera vez una red tridimensional con estructura tipo diamante e hicieron uno de los primeros estudios sobre la influencia del metal y los ligandos en la geometría de los polímeros de coordinación.⁹ El término “MOF” fue introducido por primera vez por Yaghi *et al.* en un artículo donde se informa de una estructura tridimensional tipo diamante formada por ligandos de 4,4'-bipiridina (4,4'-bpy) y cobre (II) como centro metálico.¹⁰ Solo un par de años después, los mismos autores describieron el primer polímero de coordinación con porosidad permanente utilizando ligandos basados en carboxilato (ácido tereftálico) y Zn^{2+} como centro metálico. En comparación con el sistema descrito anteriormente, este polímero de coordinación tiene la gran diferencia de ser una red neutral con solo moléculas de solventes que llenan los poros. La eliminación del solvente proporciona una red con accesibilidad y porosidad permanente a otras moléculas.¹¹

Los ligandos ampliamente utilizados en la síntesis de MOFs son aquellos que contienen grupos funcionales carboxilato. La gran abundancia de ligandos disponibles en el mercado permite una combinación ligando-metal casi infinita ofreciendo materiales con versatilidad en cuanto tamaño y forma de poro, y tamaño de cristal.¹² Los MOFs se caracterizan por tener una alta porosidad, estabilidad térmica y estabilidad estructural, lo que los hace altamente interesante para aplicaciones de almacenamiento/separación de gases, catálisis, liberación de fármacos, etc.

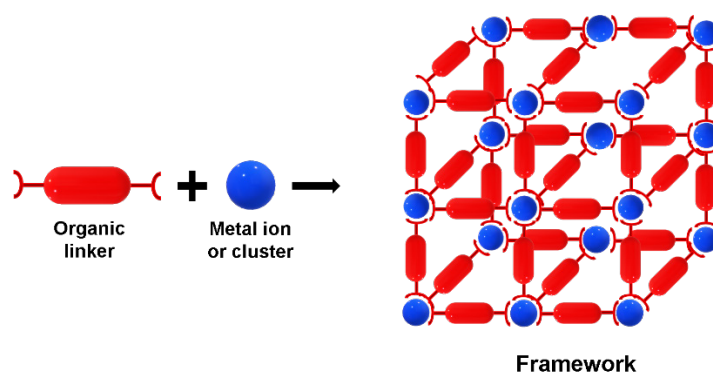


Figura 1. Esquema de formación de MOFs.

Las redes metal orgánicas formadas por ligandos imidazol (Zeolitic imidazolate frameworks, ZIFs) son un subgrupo de MOFs que se forman por la unión de Zn o Co con ligandos sustituidos o no sustituidos de imidazol, resultando en estructuras cristalinas 3D similares a las presentadas en las zeolitas.¹³ Dentro de la mayoría de los MOFs, los ZIFs ofrecen una sobresaliente capacidad de adsorción, estabilidad térmica y química.^{13,14}

La optimización de la metodología de síntesis en MOFs es una etapa fundamental en la búsqueda de propiedades específicas relacionadas con el tamaño de cristal, área superficial, forma de cristal, etc. Debido a esto, diferentes metodologías se han desarrollado, las cuales se pueden condensar en dos grandes grupos; las metodologías convencionales, que se llevan a cabo utilizando fuentes de calentamiento eléctrico o las no convencionales que son aquellas que utilizan fuentes alternas de calentamiento para promover la reacción como, la radiación de microondas, sonoquímica, electroquímica, mecanoquímica, etc.¹⁵

La síntesis solvotermal es una de las más empleadas para la obtención de MOFs debido a las ventajas que ofrece al escalar la reacción. Esta metodología hace referencia a la reacción que se lleva a cabo en autoclaves cerrados a temperatura cercana al punto de ebullición del solvente la cual promueve una presión autógena.¹⁶ Los parámetros que tienen un efecto importante en las características del producto final son, el radio metal/ligando, tipo de solvente, temperatura de síntesis, etc.¹⁷ MOFs, como el HKUST-1, ZIF-8, UiO-66 y UiO-67 han sido ampliamente sintetizados utilizando esta metodología.^{14,18-20}

○ **Flexibilidad en redes metal-orgánicas**

La flexibilidad estructural es una de las características de mayor interés en los polímeros de coordinación y la cual consiste en un cambio estructural de la red generalmente ocasionada por un estímulo externo como, temperatura, presión o moléculas depositadas en los poros.^{21,22}

Las primeras evidencias de flexibilidad en las redes metal-orgánicas se han asociado con un cambio drástico en la capacidad de absorción a una cierta presión de la curva de adsorción-desorción.²¹ Basados en esta propiedad, los MOF se han agrupado como rígidos y flexibles (cristales porosos blandos).²² Aunque la flexibilidad de los MOF se asocia comúnmente como resultado a un estímulo externo en la red, es importante mencionar que la flexibilidad puede ser intrínseca por la composición de la red.

Los factores intrínsecos de la red metal-orgánica que favorecen la flexibilidad en los MOF están relacionados con la composición estructural que incluye, el radio ion/clúster metálico y el ligando orgánico. Los grupos metálicos conocidos como unidades de construcción secundarias (SBU) o bloques de construcción moleculares (MBB) en los MOF son los responsables del movimiento de la red.^{23,24}

Los estímulos externos o desencadenador de la flexibilidad tienen un gran impacto en el cambio estructural de la red. Uno de los primeros estímulos descritos en los MOF flexibles fue el observado al eliminar el solvente de la red, que provoca un fenómeno de expansión/contracción o de respiración y que permite el intercambio de distintas moléculas huéspedes en la red.^{25,26}

Esta característica en MOFs ha sido ampliamente estudiada por distintas técnicas experimentales y de simulación molecular logrando una sinergia única para el entendimiento del fenómeno y la optimización de aplicaciones.

○ **Aplicaciones de redes metal-orgánicas**

Los MOF han brindado oportunidades únicas para una gran cantidad de aplicaciones. Debido a sus excelentes propiedades fisicoquímicas, como la alta porosidad, la versatilidad y estabilidad estructural, se han aplicado en distintas

áreas como, la administración de fármacos, catálisis, tecnología de sensores, almacenamiento y separación de gases, aplicaciones de sorción de agua, materiales luminiscentes, etc.²⁷

La separación y el almacenamiento de gases se han convertido en un área de investigación de gran importancia para los polímeros de coordinación como consecuencia del aumento de los problemas globales derivados de las actividades industriales, que emiten anualmente grandes cantidades de gases altamente contaminantes. Algunos ejemplos son, captura de CO₂, el almacenamiento de H₂ para combustible, la purificación de gas, etc.

La gran área superficial combinado con la estabilidad química en MOFs son algunos de los principales atractivos en la búsqueda de aplicaciones en estos materiales. En las últimas décadas, los MOFs se han considerado materiales adsorbentes ideales para la separación de CO₂ y otras moléculas polares en estado gas. Uno de los primeros estudios sugería que las redes metal-orgánicas con presencia de sitios metálicos insaturados son ideales para estas aplicaciones, ya que funcionan como sitios ácidos de Lewis.²⁸

Algunos otros ejemplos de separaciones en fase gas ampliamente descritas utilizando MOFs incluyen, la separación de N₂/O₂, almacenamiento de H₂ y CH₄, separación de hidrocarburos C1-C4, etc.²⁹⁻³² Por ejemplo, en el caso de la separación de N₂/O₂ se ha utilizado el principio de tamizado molecular en varios MOF. Recientemente, se informó una alta eficiencia de selectividad en MOF PCN-13 el cual contiene canales cuadrados de 3.5 Å x 3.5 Å y un volumen de poro de 0.3 cm³/g, permitiendo que las moléculas de oxígeno con un diámetro cinético de 3.45 Å pasen a través del material y excluyendo N₂ (diámetro cinético de 3.64 Å).³³

En la separación de hidrocarburos lineales con MOFs, los ZIF han resultado ser candidatos potenciales. Por ejemplo, Gascon *et al.* describieron el “breathing” en ZIF-7 como herramienta para la separación de etileno/etano.³⁴ De igual manera, las membranas basadas en ZIF-7 y ZIF-8 son algunos de los materiales más populares para la separación de hidrocarburos aromáticos y cíclicos como los isómeros de xileno, benceno o ciclohexano.³⁵⁻³⁷

En el área de la biomedicina los MOFs han sido ampliamente estudiados, encontrando resultados sobresalientes de estos materiales en la adsorción y liberación controlada de ciertos fármacos, como antiinflamatorios, contra el cáncer, pero también agentes biológicos importantes para ciertos procesos celulares, como el óxido nitroso³⁸⁻⁴⁰. El óxido nitroso es una molécula fundamental en ciertas actividades celulares de los seres humanos, por lo que agentes para dosificar pequeñas cantidades en el cuerpo han sido recientemente investigadas.^{41,42}

○ **MOFs en aplicaciones biomédicas y toxicidad**

La toxicidad de los MOFs es un tema que toma gran importancia para aplicaciones biológicas, ya que estos materiales están formados por ligandos orgánicos y metales que, la mayoría de las veces presentan alto nivel de toxicidad en bajas concentraciones en los seres humanos.^{43,44}

En la aplicación de MOFs como nuevos sistemas de administración de fármacos, la estabilidad y la biocompatibilidad son aspectos de gran importancia a tomar en consideración al momento de formular sistemas de liberación controlada. Como se informó recientemente, en un sistema de liberación controlada de fármacos se desea una cierta inestabilidad del MOF para ayudar al propio organismo en el proceso de degradación de la matriz después de la liberación y, en consecuencia, para evitar la acumulación endógena del material en el cuerpo.⁴⁵ La eficiencia de la liberación del fármaco se ve afectada por la degradación de la matriz que promueve la difusión del fármaco desde la matriz al cuerpo.⁴⁶ Sin embargo, también se requiere de cierto nivel de estabilidad en la estructura para garantizar la encapsulación adecuada y el almacenamiento de la molécula hasta que se libera en el cuerpo, por ejemplo, para el portador de fármacos contra el cáncer, se espera que la matriz conserve su estructura hasta el momento en que llegue al tejido tumoral.

Sin embargo, investigaciones han demostrado que la selección adecuado del ligando y del metal son parte fundamental para minimizar la toxicidad de estos materiales en las aplicaciones en biomedicina. MOFs con núcleos metálicos de hierro, calcio, circonio y, ligandos simples con grupos funcionales carboxilato han

demostrado ser excelente materiales para la liberación controlada de ciertos fármacos con bajo impacto toxicológico en los organismos estudiados.⁴³

○ **Materiales híbridos MOF-Polímero**

La comercialización de MOF para muchas aplicaciones se ha visto limitada debido a la morfología cristalina o microcristalina de estos materiales. Durante los últimos años se ha hecho un gran esfuerzo para incorporar y crear una sinergia entre polímeros orgánicos y nanopartículas de MOF. Se han utilizado diferentes enfoques para desarrollar metodologías de síntesis de materiales híbridos MOF-polímero. Estos se pueden resumir en dos, los enfoques de “arriba hacia abajo” que se realizan cuando los MOF se sintetizan inicialmente y luego se incorporan a la matriz polimérica, por el contrario, a lo que se hace en los enfoques de “abajo hacia arriba”, donde el material híbrido se sintetiza a medida que se forma el MOF.⁴⁷

Las membranas de matriz mixta (MMMs) consisten en la incorporación de materiales rígidos dispersos en una matriz polimérica flexible.^{48,49} El objetivo de este método es crear un material híbrido que combine la flexibilidad del polímero mientras las propiedades de la fase dispersa permanecen activas.^{48,50} Se han realizado esfuerzos para sintetizar MMMs basados en MOF para aplicaciones en separación de gases o líquidos. Debido a que con frecuencia en las membranas formadas exclusivamente de polímero, la selectividad y la permeabilidad están inversamente correlacionadas, es importante seleccionar el polímero apropiado para cada MOF a fin de maximizar la permeabilidad y selectividad de la molécula deseada a separar.^{51,52}

● **Objetivos generales del trabajo**

Teniendo en cuenta el panorama anteriormente expuesto sobre las redes metal-orgánicas y sus potenciales aplicaciones, este proyecto de Tesis Doctoral tiene como objetivo el estudio estructural de estos materiales en procesos de adsorción en fase líquida y fase gas.

Los objetivos planteados en este proyecto pueden condensarse en dos grandes bloques; el primero relacionado con el estudio estructural y de flexibilidad de distintos “Zeolitic imidazolate frameworks” ZIFs utilizando distintas técnicas de caracterización de alta resolución y, además, simulación molecular; así como el efecto en la adsorción de distintas moléculas en fase gas. El segundo bloque hace referencia al estudio de MOFs en aplicaciones biomédicas, en específico en el estudio de adsorción y liberación en fase líquida de fármacos para el tratamiento del glaucoma.

Por tanto, los objetivos establecidos en cada capítulo de este proyecto de Tesis Doctoral se condensan en los siguientes cinco puntos:

1. La flexibilidad ha sido una característica de gran interés en MOFs y especialmente en las redes metal-orgánicas formadas por ligandos imidazol (ZIFs). El *capítulo 3* tienen como objetivo el estudio a profundidad de la flexibilidad en el más simple de los ZIFs, el ZIF-4. Se plantea el uso de distintas técnicas de caracterización para lograr una sinergia que permita una descripción más clara del proceso de “breathing” en este ZIF tan especial. Se propone el estudio in-situ de la flexibilidad por medio de difracción de rayos X con luz sincrotrón el cual permitirá la elucidación de los parámetros de red y los cambios estructurales debido al “breathing”. Por último, simulación molecular se propone como herramienta para la descripción del cambio de fase en la estructura como resultado de adsorción de nitrógeno a 77 K.
2. El ZIF-62 es uno de los 105 ZIFs descrito en la literatura y el cual ha abierto paso a nueva área dentro del mundo de los MOFs, los cristales líquidos. El *capítulo 4* plantea el estudio estructural y las potenciales aplicaciones de un ZIF conformado por dos ligandos distintos. El ZIF-62 está conformado por núcleos metálicos de Zn^{2+} alternados entre ligandos imidazol y benzimidazol. Este capítulo presenta la

posible flexibilidad en este novedoso ZIF, así como la elucidación de los cambios estructurales por medio de simulación molecular.

3. Aunque el óxido nitroso por mucho tiempo fue considerado solo un compuesto altamente contaminante proveniente de la combustión en los automóviles, hace algunas décadas se describió como una molécula fundamental en distintos procesos biológicos, por lo que la adsorción de óxido nitroso para aplicaciones biomédicas ha resultado de gran interés en los últimos años. En el *capítulo 5* plantea el estudio de ZIFs flexibles (ZIF-4 y ZIF-7) en la adsorción y liberación de NO. Este capítulo contempla el efecto de distintos parámetros en la cantidad total de adsorción y liberación. Por último, se realiza un estudio del efecto de esta molécula en la flexibilidad de estos materiales.
4. El estudio de distintos MOFs en adsorción y liberación de brimonidina como alternativa a las formas de dosis convencionales. El *capítulo 6* plantea la síntesis de cuatro MOFs con centros metálicos de Fe, Zr, y Cu, la elucidación de las propiedades texturales y de morfología y además el estudio del efecto de las propiedades texturales en la capacidad de adsorción y liberación. Posteriormente el estudio de estabilidad estructural en medio acuoso de los cuatro materiales. Por último, se plantean estudios de toxicidad sobre líneas celulares oculares por medio de pruebas de viabilidad celular tanto en los materiales porosos como en los componentes orgánicos e inorgánicos.
5. Con el objetivo de expandir las aplicaciones de estos nanomateriales, el *capítulo 7* versa del estudio estructural de materiales híbridos poliuretano (PU) - MOFs y sus aplicaciones en biomedicina. Se plantea la síntesis de películas de PU y

nanopartículas de UiO-66 y; mediante distintas técnicas de caracterización se estudia la estabilidad de estos materiales compuestos, la accesibilidad de moléculas al composite, seguido del estudio de adsorción y liberación de brimonidina en fase acuosa y, por último, el estudio detallado de la localización del fármaco en el material híbrido.

- **Resultados y conclusiones más relevantes**

- **Capítulo 3. Entendiendo el fenómeno de respiración en ZIF-4**

La flexibilidad debido a la adsorción de gases en ZIFs se describe en el *capítulo 3*. La estructura de las redes metal-orgánicas formadas por ligandos imidazol están constituidas de forma general por centros metálicos de Zn coordinados tetraédricamente a través de enlaces de coordinación a ligandos con grupos imidazol. La más básica de estas estructuras, es decir, la constituida por un conector imidazol no sustituido, corresponde a ZIF-4. Este ZIF pertenece al grupo ortorrómbico con topología de red cristalina de “cag” y tamaño de ventana de poro de 0.21 nm de diámetro. Estudios recientes han demostrado que, a pesar del tamaño de cavidad tan pequeña predicha teóricamente, el ZIF-4 es capaz de adsorber N₂ e incluso hidrocarburos pequeños.

Con esto en mente, en este capítulo se sintetizó por metodología solvotermal ZIF-4, por la cual se aseguró la calidad de los cristales obtenidos y la ausencia de impurezas. En resumen, la combinación de difracción de rayos X de sincrotrón y las medidas de dispersión inelástica de neutrones muestran claramente que ZIF-4 exhibe un fenómeno de “breathing” tras la adsorción de nitrógeno a ~ 30 kPa, esto asociado con una expansión del volumen del 8-9% en la celda unitaria. La transición de una fase de poro estrecho (np) a una de poro expandido (ep) explica el comportamiento complejo de la isoterma de adsorción de nitrógeno a temperaturas criogénicas. La existencia de una fase de ZIF-4 expandido ha sido predicha por simulaciones moleculares. Primero, la estructura expandida fue predicha por

simulaciones MD a temperaturas más altas, lo que aumenta las contribuciones entrópicas a la energía libre y estabiliza la estructura expandida. En segundo lugar, la estructura expandida de ZIF-4 con la incorporación de moléculas de N₂ fue confirmada por simulaciones MD y GCMC a 77 K. Aunque el CO₂ que presenta un diámetro cinético más pequeño y una temperatura de adsorción mucho más alta es capaz de acceder a las cavidades internas en ZIF-4 pero no de promover la transición de fase de np a ep a temperatura ambiente. Sin embargo, las mediciones del INS muestran que solo a temperaturas criogénicas (5 K) CO₂ puede promover ciertos cambios estructurales.

- **Capítulo 4. Entendiendo la adsorción de gases en ZIF con ligando mixto.**

El *capítulo 4*, describe las características estructurales de un ZIF con ligandos mixtos. Recientemente, se han descrito los ZIFs formados por la combinación de dos o más ligandos como materiales potenciales para un gran número de aplicaciones debido a su propiedad de tamizado molecular como resultado de ligandos de diferentes tamaños. El ZIF-62 es una red metal-orgánica de ligando mixto con composición nominal Zn (Im)_{1.75}(blm)_{0.25} en el que Zn²⁺ se coordina con ligandos imidazolato (Im) (C₃H₃N₂⁻) y bencimidazolato (blm) (C₇H₆N₂⁻) en orientación alterna a lo largo de líneas tetraédrica.

Aunque las investigaciones relacionadas con ZIF-62 se han centrado en las propiedades resultantes de la de fusión de este material, ha permitido el desarrollo de un campo nuevo en los MOF llamados “liquid glass materials”, existe evidencia limitada de su accesibilidad porosa y propiedades de adsorción.

En base a esto, en el *capítulo 4* se describe por primera vez los fenómenos de adsorción de diferentes moléculas en ZIF-62 y sus modificaciones estructurales como resultado de estímulos externos. Además, mediante la simulación molecular, dilucidamos la accesibilidad porosa a las cavidades de este ZIF.

ZIF-62 se sintetizó por metodología solvotermal y se evaluaron las características texturales y morfológicas a través de diferentes técnicas fisicoquímicas. El material sintetizado presentaba cristales tetraédricos con un

tamaño promedio de 5-20 μm . Las isothermas de adsorción-desorción de nitrógeno y oxígeno muestran un comportamiento similar a 298 K y 195 K, pero no a 77 K, donde ZIF-62 se observa un comportamiento no adsorbente de nitrógeno mientras que la cantidad máxima de oxígeno adsorbido es cercana a 8 mmol/g. Las simulaciones por GCMC para una estructura rígida de ZIF-62 muestran una red tridimensional con dos tipos de cavidades, una grande de 4.3 Å y otra pequeña de 1 Å. Los resultados obtenidos para la simulación de las isothermas de adsorción-desorción de nitrógeno y oxígeno presentan un buen ajuste con los resultados experimentales de las isothermas a 195 K y 298 K, esto confirmando la fiabilidad del modelo desarrollado para este sistema. La isoterma de adsorción-desorción de nitrógeno y oxígeno a 77 K obtenidas por la simulación presentan un comportamiento similar, sugiriendo una capacidad máxima de adsorción de ambos gases aproximada a 8 mmol/g. El experimento de difracción de rayos X de sincrotrón (SPXRD) elucida los cambios de fase en el ZIF-62 cuando la estructura se carga con oxígeno o nitrógeno a 90 K, lo que sugiere cierta flexibilidad estructural. El refinamiento de Rietveld realizado en los difractogramas de rayos X de sincrotrón a 90 K sugiere una mezcla de una fase expandida (fase I) y una fase contraída (fase II), esta mezcla se observó hasta 150 K, después de este punto la fase contraída desaparece y el parámetro de celda se aproximan a los valores observados para la estructura a temperatura ambiente. Ampliando las potenciales aplicaciones de ZIF-62 para diferentes moléculas de interés industrial, las isothermas de moléculas pequeñas como el metano o el dióxido de carbono se realizaron a 298 K.

Las isothermas de adsorción- desorción de parafinas y olefinas de C1-C4 en ZIF-62 a 298 K muestran un comportamiento de adsorción preferencial inverso, fenómeno que se ha observado en otras estructuras de ZIF anteriormente. Finalmente, se demostró que el ZIF-62 es un material excelente para la separación de isómeros de hexano, mostrando una alta preferencia por alcanos lineales sobre los ramificados

○ **Capítulo 5. Adsorción de óxido nitroso en redes metal-orgánicas flexibles.**

El óxido nitroso (NO) es una molécula altamente reactiva con muchas funciones fisiológicas (por ejemplo, en el sistema cardiovascular) y el desarrollo de materiales nanoporosos capaces de almacenar y suministrar NO constituye un enfoque prometedor, por ejemplo, para evitar la formación de trombosis al incorporarlo en dispositivos médicos (por ejemplo, “stents” o catéteres) en el cuerpo humano. Sin embargo, debido a las bajas interacciones intermoleculares, la presión de vapor de saturación de NO es alta, es decir, 64,83 bar, con la complejidad asociada de almacenar una cantidad considerable de NO a presión atmosférica es alta.

El *capítulo 5* resume el estudio realizado en la adsorción y liberación de óxido nitroso, molécula en estado gas que desempeña una función de gran importancia en aplicaciones biomédicas. A pesar de la ausencia de sitios metálicos abiertos (OMS) y una química de superficie adecuada (por ejemplo, grupos básicos de amina) en los ZIFs, estos materiales exhiben un excelente rendimiento en términos de absorción total, irreversibilidad y la cinética de liberación. Estos excelentes resultados se deben atribuir a la presencia de cambios estructurales adecuados (p. Ej., “breathing” o efectos de apertura de la red) tras la adsorción que limitan/controlan la liberación de NO en condiciones específicas. Por ejemplo, ZIF-4 es capaz de adsorber hasta 1.6 mmol/g, mientras que su contraparte de bencilimidazolato (ZIF-7) está limitado a 0.5 mmol / g. Sin embargo, a pesar de la menor capacidad de adsorción exhibida por ZIF-7, la presencia de un poro estrecho (np), estructura altamente densa (fase II) permite controlar la liberación de NO en condiciones húmedas durante más de 15 h a temperatura fisiológica (310 K). La temperatura a la que se realiza la evacuación del solvente de la red es un parámetro determinante en la capacidad total de adsorción de NO en este tipo de materiales, por ejemplo, en el ZIF-4 estas excelentes propiedades desaparecen después de un tratamiento térmico a una temperatura más alta (523 K) debido a la amorfización parcial y recristalización de ZIF-4 en una fase amorfa. En el caso específico de ZIF-7, aunque la cantidad adsorbida es menor debido a la incapacidad del NO para promover un cambio estructural, la presencia de una fase densa permite controlar

la cinética de entrega durante más de 18 h con una cantidad total liberada de más de 70 $\mu\text{mol/g}$ a 318 K.

Teniendo en cuenta la gran estabilidad estructural de los ZIF, incluso en medios fisiológicos, estos materiales pueden anticiparse como candidatos prometedores para aplicaciones de suministro de fármacos bioquímicos (por ejemplo, liberación de NO), evitando procesos de lixiviación de metales no deseados en solución fisiológica y los efectos tóxicos asociados.

○ **Capítulo 6. MOFs como nuevos sistemas de liberación de fármacos para tratamientos oculares**

La búsqueda de plataformas de administración de fármacos de forma eficiente y controlada para tratamiento de enfermedades oculares ha crecido recientemente debido a la preocupación constante de efectos secundarios causados por la adsorción no óptima de fármacos. Esto ha llevado a explorar sistemas que ofrezcan una mayor biodisponibilidad del fármaco en el interior del ojo y minimicen los problemas asociados a las aplicaciones tópicas. Teniendo en cuenta el volumen limitado de la cavidad ocular ($< 3\text{-}4\text{ cm}^3$) y la cantidad limitada de líquido (el ojo humano puede contener solo 7-10 μl de líquido), cualquier plataforma de administración intraocular para tratamiento ocular debe cumplir aún más requisitos estrictos en comparación con los tratamientos tópicos como, i) la capacidad de carga debe ser extremadamente grande (en base gravimétrica (% en peso) y volumétrica (% en peso/v)) para mitigar cualquier interferencia en el campo visual después de la dosificación, ii) cinética de liberación debe ser lenta (dentro de días o semanas) para permitir una terapia a largo plazo, iii) alta biocompatibilidad del material con las células de la retina y, por último pero no menos importante, iv) degradabilidad estructural del material una vez que el material ha completado el trabajo.

El *capítulo 6* describe el estudio estructural y toxicológico de los MOFs, MIL-100 (Fe), HKUST-1 (Cu), UiO-66 (Zr) y UiO-67 (Zr) en la adsorción y liberación de brimonidina (fármaco utilizado para la reducción de presión intraocular causada por el glaucoma). Se realizó la caracterización estructural de los 4 MOFs elucidando el área superficial, la morfología y la estabilidad estructural en medio acuoso. En estos

resultados se observa que el MIL-100 (Fe) prolongaba su estabilidad estructural en medio acuoso hasta más de un mes, mientras que los otros 3 materiales sufrían un colapso estructural a los pocos días. Las isothermas de adsorción en fase líquida de brimonidina se desarrollaron a temperatura ambiente, en las cuales se observa una cinética de adsorción relativamente rápida, alcanzando el equilibrio después de 4 horas de contacto en la disolución líquida. El UiO-67 (Zr) presenta la mayor capacidad de adsorción alcanzando un total de ~600 mg de brimonidina por gramo de MOF. Las cinéticas de liberación de brimonidina se realizaron en solución biológica (PBS) a temperatura ambiente, se observa que la liberación en los cuatro materiales se desarrolla en 2 etapas, la primera en la cual se libera la mayor cantidad de fármaco y una segunda que se prolonga hasta 12 días y en la que se ralentiza la liberación del fármaco. Aunque el UiO-67 (Zr) había presentado la mayor cantidad de brimonidina adsorbida, el porcentaje de liberación es el más bajo (en términos totales) comparado con los otros 3 nanomateriales, pero se ve prolongada hasta 12 días posiblemente debido al proceso de amortización estructural observado con anterioridad en el estudio de estabilidad estructural en medio acuoso. Por último, estudios toxicológicos en líneas celulares oculares de retina 661W demuestran la dependencia en el nivel de toxicidad del material con el metal de la red. Los MOFs con centros metálicos de hierro y zirconio presentan una mayor viabilidad celular hasta después de 48 h de exposición, mientras que el HKUST-1 al tener poca estabilidad en medio acuoso y favorecer un lixiviado de los iones metálicos de Cu propician un mayor porcentaje de muerte celular después de 48 h de exposición.

Este estudio demuestra que los MOFs anteriormente descrito significan una alternativa relevante en la adsorción y liberación controlada de brimonidina para tratamientos oculares. De igual manera se demuestra que el porcentaje de adsorción y liberación depende de gran medida de las características superficiales del material y del nivel de estabilidad estructural en medio acuoso, por lo que cierto porcentaje de colapso estructural favorece la ralentización de la liberación del fármaco. Por último, estudios in vitro demuestran que estos MOFs MIL-100 (Fe), UiO-66 (Zr) y UiO-67 (Zr) presentan un bajo nivel de toxicidad tanto como red metal-

orgánica como sus componentes por separado, potenciando estos materiales como candidatos en formulaciones intraoculares para el tratamiento de glaucoma.

- **Capítulo 7. Películas híbridas MOF-poliuretano como potenciales sistemas de liberación de fármacos en dispositivos oculares**

Las nuevas plataformas de administración de medicamentos para tratar enfermedades oculares preparados a partir de materiales poliméricos (insertos sólidos o semisólidos) han ganado gran popularidad en los últimos años. Las potenciales ventajas de estos dispositivos poliméricos están relacionadas con, la dosificación precisa, el aumento del tiempo de residencia ocular, la reducción de los efectos secundarios sistémicos o el mejor cumplimiento del paciente, por mencionar algunos. Debido a las ventajas que ofrecen estos materiales frente a las formas de dosificación convencional de fármacos varias compañías los han patentado y comercializado en los últimos años. Por ejemplo, uno de los primeros insertos oculares comercializados ha sido por Alza (Vacville, CA) como Ocuser®^{53,54}, que se usa para dosificar el fármaco pilocarpina (fármaco anti-glaucoma) durante un máximo de 5-7 días. Aunque estos son números excelentes, la ausencia de una red porosa tridimensional dispersa dentro de estas matrices poliméricas limita la absorción total del fármaco y dificulta una liberación controlada.

El *capítulo 7* versa del estudio estructural de materiales compuestos preparados con nanopartículas de UiO-67 (Zr) y poliuretano como matriz polimérica para aplicaciones en biomedicina. Se caracterizaron por DRX, SEM e isothermas de N₂ a 77 K y, por último, se realizaron isothermas de adsorción de brimonidina y cinéticas de liberación del fármaco. El análisis de difracción de rayos X de sincrotrón (SXRPD) confirma la mejora en la estabilidad de las nanopartículas de UiO-67 dispersas en la matriz y las imágenes de microscopía electrónica de barrido confirman la distribución homogénea (tamaño de cristal promedio ~ 100-200 nm) dentro de la película de 50 µm de espesor. Tal como se observa en la isoterma de adsorción-desorción a 77 K, la accesibilidad a los poros del MOF embebido se suprime por completo para N₂ a temperaturas criogénicas. Sin embargo, las mediciones de adsorción de etileno a 298 K confirman que al menos el 45% de los cristales de MOF son totalmente accesibles para la adsorción en fase gaseosa de

moléculas no polares. Aunque este bloqueo parcial limita el rendimiento de adsorción de los MOF embebidos para fármacos oculares (tartrato de brimonidina) en comparación con el MOF puro, se observa una mejora de casi 60 veces en la capacidad de adsorción para la matriz de PU después de la incorporación de las nanopartículas de UiO-67. El nanocompuesto UiO-67 @ PU exhibe una liberación prolongada de brimonidina (se cuantificaron hasta 14 días). Finalmente, el uso combinado de SXRPD, el análisis termogravimétrico (TGA) y el análisis FTIR confirman la presencia del fármaco en la película de nanocompuestos, la estabilidad del MOF y el fármaco tras la carga y, por último, la presencia de brimonidina en una fase amorfa una vez adsorbida. Estos resultados abren la puerta hacia la aplicación de estas películas de nanocompuestos poliméricos para la administración de fármacos en terapias ópticas, ya sea como componente de lentes de contacto, en la composición de tapones lagrimales o en insertos oculares.

• Referencias

1. Desjonquères, M.-C. & Spanjaard, D. Adsorption Phenomena. in *Concepts in Surface Physics* 411–538 (Springer Berlin Heidelberg, 1996). doi:10.1007/978-3-642-61400-2_6
2. Yang, R. T. Introductory Remarks. in *Adsorbents: Fundamentals and Applications* 1–7 (John Wiley & Sons, Inc.). doi:10.1002/047144409X.ch1
3. Ali, I. & Gupta, V. K. Advances in water treatment by adsorption technology. *Nat. Protoc.* **1**, 2661–2667 (2006).
4. Sayılğan, Ş. Ç., Mobedi, M. & Ülkü, S. Effect of regeneration temperature on adsorption equilibria and mass diffusivity of zeolite 13x-water pair. *Microporous Mesoporous Mater.* **224**, 9–16 (2016).
5. Bonilla-Petriciolet, A., Mendoza-Castillo, D. I. & Reynel-Ávila, H. E. Introduction. in *Adsorption Processes for Water Treatment and Purification* 1–18 (Springer International Publishing, 2017). doi:10.1007/978-3-319-58136-1_1
6. Çeçen, F. & Aktaş, Ö. Water and Wastewater Treatment: Historical Perspective of Activated Carbon Adsorption and its Integration with Biological Processes. in *Activated Carbon for Water and Wastewater Treatment* 1–11 (Wiley-VCH Verlag GmbH & Co. KGaA, 2011). doi:10.1002/9783527639441.ch1
7. Maesen, T. & Marcus, B. Chapter 1 The zeolite scene—An overview. in *Introduction to Zeolite Science and Practice* 1–9 (2001). doi:10.1016/S0167-2991(01)80242-1

8. Corma, A., García, H. & Llabrés i Xamena, F. X. Engineering Metal Organic Frameworks for Heterogeneous Catalysis. *Chem. Rev.* **110**, 4606–4655 (2010).
9. Hoskins, B. F. & Robson, R. Design and construction of a new class of scaffolding-like materials comprising infinite polymeric frameworks of 3D-linked molecular rods. A reappraisal of the zinc cyanide and cadmium cyanide structures and the synthesis and structure of the diamond-rela. *J. Am. Chem. Soc.* **112**, 1546–1554 (1990).
10. Yaghi, O. M. & Li, G. Mutually Interpenetrating Sheets and Channels in the Extended Structure of [Cu(4,4'-bpy)Cl]. *Angew. Chemie Int. Ed. English* **34**, 207–209 (1995).
11. Yaghi, O. M. *et al.* Reticular synthesis and the design of new materials. *Nature* **423**, 705–714 (2003).
12. Llabrés i Xamena, F. X. & Gascon, J. CHAPTER 1. Introduction. in *Metal Organic Frameworks as Heterogeneous Catalysts* 1–5 (2001). doi:10.1039/9781849737586-00001
13. Park, K. S. *et al.* Exceptional chemical and thermal stability of zeolitic imidazolate frameworks. *Proc. Natl. Acad. Sci. U. S. A.* **103**, 10186–91 (2006).
14. Banerjee, R. *et al.* High-Throughput Synthesis of Zeolitic Imidazolate Frameworks and Application to CO₂ Capture. *Science (80-)*. **319**, 939–943 (2008).
15. Stock, N. & Biswas, S. Synthesis of Metal-Organic Frameworks (MOFs): Routes to various MOF topologies, morphologies, and composites. *Chem. Rev.* **112**, 933–969 (2012).
16. Rabenau, A. The Role of Hydrothermal Synthesis in Preparative Chemistry. *Angew. Chemie Int. Ed. English* **24**, 1026–1040 (1985).
17. Biemmi, E., Christian, S., Stock, N. & Bein, T. High-throughput screening of synthesis parameters in the formation of the metal-organic frameworks MOF-5 and HKUST-1. *Microporous Mesoporous Mater.* **117**, 111–117 (2009).
18. Küsgens, P. *et al.* Characterization of metal-organic frameworks by water adsorption. *Microporous Mesoporous Mater.* **120**, 325–330 (2009).
19. Garibay, S. J. & Cohen, S. M. Isorecticular synthesis and modification of frameworks with the UiO-66 topology. *Chem. Commun.* **46**, 7700 (2010).
20. Zhu, X. *et al.* Effective Adsorption and Enhanced Removal of Organophosphorus Pesticides from Aqueous Solution by Zr-Based MOFs of UiO-67. *ACS Appl. Mater. Interfaces* **7**, 223–231 (2015).
21. Devic, T. *et al.* Functionalization in Flexible Porous Solids: Effects on the Pore Opening and the Host–Guest Interactions. *J. Am. Chem. Soc.* **132**, 1127–1136 (2010).

22. Horike, S., Shimomura, S. & Kitagawa, S. Soft porous crystals. *Nat. Chem.* **1**, 695–704 (2009).
23. Férey, G. & Serre, C. Large breathing effects in three-dimensional porous hybrid matter: facts, analyses, rules and consequences. *Chem. Soc. Rev.* **38**, 1380 (2009).
24. Mellot-Draznieks, C., Serre, C., Surblé, S., Audebrand, N. & Férey, G. Very Large Swelling in Hybrid Frameworks: A Combined Computational and Powder Diffraction Study. *J. Am. Chem. Soc.* **127**, 16273–16278 (2005).
25. Uemura, K., Matsuda, R. & Kitagawa, S. Flexible microporous coordination polymers. *J. Solid State Chem.* **178**, 2420–2429 (2005).
26. Kitagawa, S. & Uemura, K. Dynamic porous properties of coordination polymers inspired by hydrogen bonds. *Chem. Soc. Rev.* **34**, 109 (2005).
27. Rungtaweivoranit, B., Diercks, C. S., Kalmutzki, M. J. & Yaghi, O. M. Spiers Memorial Lecture: : Progress and prospects of reticular chemistry. *Faraday Discuss.* **201**, 9–45 (2017).
28. Bao, Z., Yu, L., Ren, Q., Lu, X. & Deng, S. Adsorption of CO₂ and CH₄ on a magnesium-based metal organic framework. *J. Colloid Interface Sci.* **353**, 549–556 (2011).
29. Gygi, D. *et al.* Hydrogen Storage in the Expanded Pore Metal–Organic Frameworks M₂(dobpdc) (M = Mg, Mn, Fe, Co, Ni, Zn). *Chem. Mater.* **28**, 1128–1138 (2016).
30. Rosi, N. L. *et al.* Hydrogen Storage in Microporous Metal–Organic Frameworks. *Science (80-.)*. **300**, 1127 LP – 1129 (2003).
31. Orimo, S., Nakamori, Y., Eliseo, J. R., Züttel, A. & Jensen, C. M. Complex Hydrides for Hydrogen Storage. *Chem. Rev.* **107**, 4111–4132 (2007).
32. Wu, H., Gong, Q., Olson, D. H. & Li, J. Commensurate Adsorption of Hydrocarbons and Alcohols in Microporous Metal Organic Frameworks. *Chem. Rev.* **112**, 836–868 (2012).
33. Ma, S., Wang, X.-S., Collier, C. D., Manis, E. S. & Zhou, H.-C. Ultramicroporous Metal–Organic Framework Based on 9,10-Anthracenedicarboxylate for Selective Gas Adsorption. *Inorg. Chem.* **46**, 8499–8501 (2007).
34. Gücüyener, C., van den Bergh, J., Gascon, J. & Kapteijn, F. Ethane/Ethene Separation Turned on Its Head: Selective Ethane Adsorption on the Metal–Organic Framework ZIF-7 through a Gate-Opening Mechanism. *J. Am. Chem. Soc.* **132**, 17704–17706 (2010).
35. Demessence, A. *et al.* Adsorption properties in high optical quality nanoZIF-8 thin films with tunable thickness. *J. Mater. Chem.* **20**, 7676 (2010).
36. Diestel, L., Bux, H., Wachsmuth, D. & Caro, J. Pervaporation studies of n-hexane, benzene, mesitylene and their mixtures on zeolitic imidazolate framework-8 membranes. *Microporous Mesoporous Mater.* **164**, 288–293

- (2012).
37. Peralta, D. *et al.* The separation of xylene isomers by ZIF-8: A demonstration of the extraordinary flexibility of the ZIF-8 framework. *Microporous Mesoporous Mater.* **173**, 1–5 (2013).
 38. Lundberg, J. O., Gladwin, M. T. & Weitzberg, E. Strategies to increase nitric oxide signalling in cardiovascular disease. *Nat. Rev. Drug Discov.* **14**, 623–641 (2015).
 39. Bogdan, C. Nitric oxide and the immune response. *Nat. Immunol.* **2**, 907–916 (2001).
 40. Hambrecht, R., Berra, K. & Calfas, K. J. Managing Your Angina Symptoms With Nitroglycerin. *Circulation* **127**, (2013).
 41. Calabrese, V. *et al.* Nitric oxide in the central nervous system: neuroprotection versus neurotoxicity. *Nat. Rev. Neurosci.* **8**, 766–775 (2007).
 42. Chang, J. Y. H. *et al.* Role of nitric oxide in murine conventional outflow physiology. *Am. J. Physiol. Physiol.* **309**, C205–C214 (2015).
 43. Baati, T. *et al.* In depth analysis of the in vivo toxicity of nanoparticles of porous iron(III) metal–organic frameworks. *Chem. Sci.* **4**, 1597 (2013).
 44. Sajid, M. Toxicity of nanoscale metal organic frameworks: a perspective. *Environ. Sci. Pollut. Res.* **23**, 14805–14807 (2016).
 45. Sun, C.-Y., Qin, C., Wang, X.-L. & Su, Z.-M. Metal-organic frameworks as potential drug delivery systems. *Expert Opin. Drug Deliv.* **10**, 89–101 (2013).
 46. McKinlay, A. C. *et al.* BioMOFs: Metal-Organic Frameworks for Biological and Medical Applications. *Angew. Chemie Int. Ed.* **49**, 6260–6266 (2010).
 47. Kalaj, M. *et al.* MOF-Polymer Hybrid Materials: From Simple Composites to Tailored Architectures. *Chem. Rev.* [acs.chemrev.9b00575](https://doi.org/10.1021/acs.chemrev.9b00575) (2020). doi:10.1021/acs.chemrev.9b00575
 48. Chung, T.-S., Jiang, L. Y., Li, Y. & Kulprathipanja, S. Mixed matrix membranes (MMMs) comprising organic polymers with dispersed inorganic fillers for gas separation. *Prog. Polym. Sci.* **32**, 483–507 (2007).
 49. Bastani, D., Esmaeili, N. & Asadollahi, M. Polymeric mixed matrix membranes containing zeolites as a filler for gas separation applications: A review. *J. Ind. Eng. Chem.* **19**, 375–393 (2013).
 50. Zimmerman, C. M., Singh, A. & Koros, W. J. Tailoring mixed matrix composite membranes for gas separations. *J. Memb. Sci.* **137**, 145–154 (1997).
 51. Semino, R., Moreton, J. C., Ramsahye, N. A., Cohen, S. M. & Maurin, G. Understanding the origins of metal–organic framework/polymer compatibility. *Chem. Sci.* **9**, 315–324 (2018).
 52. Katayama, Y., Bentz, K. C. & Cohen, S. M. Defect-Free MOF-Based Mixed-

- Matrix Membranes Obtained by Corona Cross-Linking. *ACS Appl. Mater. Interfaces* **11**, 13029–13037 (2019).
53. Brown, H. S. Visual Effects of Pilocarpine in Glaucoma. *Arch. Ophthalmol.* **94**, 1716 (1976).
54. POLLACK, I. P., QUIGLEY, H. A. & HARBIN, T. S. The Ocusert Pilocarpine System. *South. Med. J.* **69**, 1296–1298 (1976).



Universitat d'Alacant
Universidad de Alicante



Curriculum Vitae

Universitat d'Alacant
Universidad de Alicante

Curriculum Vitae

Jesus Gandara-Loe was born on the 20th of November of 1989 in Guanajuato, Mexico. He earned his bachelor's degree in chemical engineering from the University of Guanajuato in 2014. His degree Thesis was devoted to the study of liquid adsorption of hazard metal ions from water effluents using alumina. After that, he started the master's in chemical science at the University of Guanajuato, where he was granted with a CONACYT Master fellowship. In 2016, he obtained the master's degree with Honorific Mention defending a Master Thesis related to the study of a transesterification reaction using Layered Double Hydroxides as catalysts. In 2016 he was granted with a Santiago Grisolia Fellowship from the Generalitat Valenciana (Regional Government in Spain) and he started his PhD studies in the Department of Inorganic Chemistry at University of Alicante. The PhD Thesis describes the study of liquid and gas adsorption processes in metal-organic frameworks.

List of Publications

- (1) **Gandara-Loe, J.**; Souza, B. E.; Missyul, A.; Giraldo, G.; Tan, J.-C.; Silvestre-Albero, J. MOF-Based Polymeric Nanocomposite Films as Potential Materials for Drug Delivery Devices in Ocular Therapeutics. *ACS Appl. Mater. Interfaces* **2020**, acsami.0c07517. <https://doi.org/10.1021/acsami.0c07517>.
- (2) Jarczewski, S.; Drozdek, M.; Michorczyk, P.; Cuadrado-Collados, C.; **Gandara-Loe, J.**; Silvestre-Albero, J.; Lityńska-Dobrzyńska, L.; Kuśtrowski, P. On the Catalytic Role of Superficial VO_x Species and Coke Deposited on Mesoporous MgO Replica in Oxidative Dehydrogenation of Ethylbenzene. *Appl. Surf. Sci.* **2020**, 504, 144336. <https://doi.org/10.1016/j.apsusc.2019.144336>.
- (3) **Gandara-Loe, J.**; Missyul, A.; Fauth, F.; Daemen, L. L.; Cheng, Y. Q.; Ramirez-Cuesta, A. J.; Ravikovitch, P. I.; Silvestre-Albero, J. New Insights into the Breathing Phenomenon in ZIF-4. *J. Mater. Chem. A* **2019**, 7 (24), 14552–14558. <https://doi.org/10.1039/C8TA09713E>.

- (4) Connolly, B. M.; Aragonés-Anglada, M.; **Gandara-Loe, J.**; Danaf, N. A.; Lamb, D. C.; Mehta, J. P.; Vulpe, D.; Wuttke, S.; Silvestre-Albero, J.; Moghadam, P. Z.; Wheatley, A. E. H.; Fairen-Jimenez, D. Tuning Porosity in Macroscopic Monolithic Metal-Organic Frameworks for Exceptional Natural Gas Storage. *Nat. Commun.* **2019**, *10* (1), 2345. <https://doi.org/10.1038/s41467-019-10185-1>.
- (5) **Gandara-Loe, J.**; Ortuño-Lizarán, I.; Fernández-Sánchez, L.; Alió, J. L.; Cuenca, N.; Vega-Estrada, A.; Silvestre-Albero, J. Metal–Organic Frameworks as Drug Delivery Platforms for Ocular Therapeutics. *ACS Appl. Mater. Interfaces* **2019**, *11* (2), 1924–1931. <https://doi.org/10.1021/acsami.8b20222>.
- (6) López-Salas, N.; Ferrer, M. L.; Gutiérrez, M. C.; Fierro, J. L. G.; Cuadrado-Collados, C.; **Gandara-Loe, J.**; Silvestre-Albero, J.; del Monte, F. Hydrogen-Bond Supramolecular Hydrogels as Efficient Precursors in the Preparation of Freestanding 3D Carbonaceous Architectures Containing BCNO Nanocrystals and Exhibiting a High CO₂/CH₄ Adsorption Ratio. *Carbon N. Y.* **2018**, *134*, 470–479. <https://doi.org/10.1016/j.carbon.2018.03.066>.
- (7) Jarczewski, S.; Drozdek, M.; Michorczyk, P.; Cuadrado-Collados, C.; **Gandara-Loe, J.**; Silvestre-Albero, J.; Kuśtrowski, P. Oxidative Dehydrogenation of Ethylbenzene over CMK-1 and CMK-3 Carbon Replicas with Various Mesopore Architectures. *Microporous Mesoporous Mater.* **2018**, *271*, 262–272. <https://doi.org/10.1016/j.micromeso.2018.06.007>.
- (8) **Gandara-Loe, J.**; Jacobo-Azuara, A.; Silvestre-Albero, J.; Sepúlveda-Escribano, A.; Ramos-Fernández, E. V. Layered Double Hydroxides as Base Catalysts for the Synthesis of Dimethyl Carbonate. *Catal. Today* **2017**, *296* (April), 254–261. <https://doi.org/10.1016/j.cattod.2017.04.047>.